Faculty of Health and Life Sciences
Oxford Brookes University
Oxford

and

Department of Pathology and Pathogen Biology
Royal Veterinary College
London

The ultrastructural morphology of *Eimeria tenella* exhibits striking natural variation and undergoes significant changes during the first few hours of infection.

Alana Burrell

A thesis submitted in partial fulfilment of the requirements of the award of Doctor of Philosophy

May 2019

Abstract

The data generated during this PhD provides novel insights into the biology of *Eimeria* parasites: protozoan organisms capable of causing enteric disease in a vast array of animals. Working with *Eimeria tenella,* a clinically and economically significant pathogen of chickens, I have quantified the fusion dynamics of the refractile bodies. Refractile bodies are non-membrane-bound organelles with immunogenic properties and unknown function. The structural and temporal dynamics of refractile body merger shares striking similarity with that of intrinsically disordered protein-containing droplet organelles; this comparison may help to direct future research into the character and function of these mysterious organelles. In an adjacent project, the organelle numbers and volumes for the *E. tenella* sporozoite stage were quantified. The resultant data shows a surprisingly high level of variability in cell morphometry; this could be due to genetic/epigenetic factors or may reflect an undiscovered maturation phase. The conoid is a cytoskeletal structure found in many important apicomplexan pathogens and is involved in host cell invasion and parasite motility. I have performed the first high resolution quantitative investigation of three-dimensional conoid structure and show that there is also a considerable level variability in conoid structure. Conoid fibre number was found to vary from 13 to 16 per conoid. This variation was seen in both freshly hatched and post-invasion sporozoites, suggesting that genetic factors are involved. Following analysis of structures within the conoid, my data suggests that secretory organelle protein release occurs through intra-conoidal transport, docking and fusion.

Acknowledgements

To my close friends, family and Ben, I am forever grateful for your continued support, kindness and for always putting a smile on my face.

I would like to aknowledge Sue, Fiona and Virginia for their many hours of advice, teaching and encouragement. I feel it is important to acknowledge the chickens used in the production of *E. tenella* oocysts, without which none of this work would have been possible. I am immensly thankful that I was selected to undertake this project; in the exploration of biological structures using electron microscopy I have found work that I am truly passionate for.

Contents

1. Introduction 12

1.1. Apicomplexa 12

1.2. Coccidia 13

1.3. Coccidial diseases 14

1.4. The life cycle of *E. tenella* 15

1.5. Structural biology of the *E. tenella* sporozoite 19

1.5.1. Overview 19

1.5.2. Apical complex: micronemes 21

1.5.3. Apical complex: rhoptries 22

1.5.4. Apical complex: conoid and conoid appendages 22

1.5.5. Refractile bodies 25

1.6. Aims and objectives 26

2. Methods 28

2.1. Mammalian cell culture 28

2.1.1. Preparation of cell-culture media 28

2.1.2. Cell defrosting 28

2.1.3. Preparation of cell-culture buffer 28

2.1.4. Cell passage 29

2.2. Parasite amplification 29

2.2.1. Infection of chickens 29

2.2.2. Oocyst harvest and purification 29

2.3. Sporozoite release and purification 30

2.3.1. Preparation of excysting solution 30

2.3.2. Preparation of eluting solution 30

2.3.3. Sporozoite release 30

2.3.4. Sporozoite purification 31

2.4. Assessment of temporal dynamics of anterior refractile body loss 31

2.4.1. Preparation of 0.2 M phosphate buffer stock solution 31

2.4.2. Preparation of 10% formaldehyde solution....32
2.4.3. Preparation of 4% buffered formaldehyde....32
2.4.4. In vitro *E. tenella* infections for light microscopy of fixed cells....32
2.4.5. Temporally-staggered fixation of MDBK/sporozoite samples....32
2.4.6. Preparation of Nile red stock solution....32
2.4.7. Preparation of Hoechst stock solution....32
2.4.8. Nile red and Hoechst staining....33
2.4.9. Quantification of anterior refractile body presence....33
2.5. Assessment of refractile body dynamics in live cells....33
2.5.1. Assessment of Nile red toxicity in live cells....33
2.5.2. Live cell imaging of anterior refractile body loss....34
2.6. Pharmacological inhibition of actin....34
2.6.1. Preparation of actin-inhibitor stock solutions....34
2.6.2. Culture of *E. tenella* in the presence of actin inhibitors....35
2.6.3. Preparation of Phalloidin 488 stock solution....35
2.6.4. Phalloidin 488, Nile red and Hoechst staining....35
2.6.5. Assessment of refractile body loss and host-cell actin morphology following actin inhibition....36
2.7. Sample preparation for electron microscopy....36
2.7.1. Preparation of 0.2 M cacodylate buffer....36
2.7.2. Preparation of primary fixative solution....36
2.7.3. Preparation of 2% uranyl acetate....36
2.7.4. Preparation of 4% osmium tetroxide....36
2.7.5. Preparation of 3% potassium ferrocyanide....37
2.7.6. Preparation of 1% thiocarbohydrazide....37
2.7.7. Single osmium processing of free sporozoites for electron microscopy....37
2.7.7.1. Primary fixation and osmium impregnation....37
2.7.7.2. Uranyl acetate staining, dehydration and resin embedding....37
2.7.8. Double osmium processing of free sporozoites for electron microscopy....38

2.7.9. Reduced double osmium and thiocarbohydrazide (ROTO) processing free sporozoites for electron microscopy 38
2.7.10. Preparation of infection samples (sporozoites and MDBK cells) for analysis by electron microscopy 38
2.7.11. Processing of infection samples (except the 2.5hr infection sample) 39
2.7.12. Processing of the 2.5hr infection sample 39
2.8. Section production for electron microscopy 39
2.8.1. Glass knife preparation 39
2.8.2. Semi-thin section assessment 40
2.8.3. Ultrathin section collection for transmission electron microscopy 40
2.8.4. Formvar coating of slot grids for three-dimensional transmission electron microscopy 40
2.8.5. Serial-section collection for three-dimensional transmission electron microscopy 41
2.9. Heavy metal staining of ultrathin sections 41
2.9.1. Preparation of Reynolds lead citrate 41
2.9.2. Uranyl acetate and lead staining 41
2.10. Transmission electron microscopy imaging 42
2.10.1. Transmission electron microscopy image acquisition 42
2.10.2. Transmission electron tomography image acquisition 42
2.10.3. Tomogram generation and structure segmentation 42
2.11. Serial block face scanning electron microscopy (SBF-SEM) imaging 43
2.11.1. SBF-SEM image acquisition 43
2.11.2. SBF-SEM data processing and structure segmentation 43
2.12. Statistical analysis 44
3. Quantitative analysis of sporozoite morphometrics and development 45
3.1. Introduction 45
3.2. Approach and method development 45
3.2.1. Optimisation of sample processing for the investigation of *E. tenella* ultrastructure 45
3.2.2. Evaluation of SBF-SEM imaging and three-dimensional structure segmentation 51
3.2.3. Evaluation of alternative methods for analysis of apical organelle morphometrics 56

3.3. Organelle morphometric quantification reveals wide variation in freshly-excysted sporozoite morphology....58
3.3.1. Whole cell morphometrics....59
3.3.2. Nucleus morphometrics....60
3.3.3. Refractile bodies morphometrics....62
3.3.4. Amylopectin granules morphometrics....64
3.3.5. Mitochondria morphometrics....66
3.3.6. Acidocalcisomes morphometrics....68
3.3.7. Microneme and rhoptry volumes....70
3.3.8. Organelle proportions....71
3.3.9. Summary of findings from quantitative ultrastructural analysis of freshly-excysted sporozoites....72
3.3.10. Sporozoite variation was also observed via light microscopy....73
3.4. Investigation of morphological changes during development of *E. tenella*....75
3.4.1. Sporozoite invasion of host cells....75
3.4.2. Schizont development within host cells....79
3.5. Morphometric changes within the first few hours of *E. tenella* sporozoite infection....82
3.5.1. Dynamic changes in cell shape, mitochondrial organisation and refractile body number in the initial hours after infection....82
3.5.2. Volumes of the whole cell, nucleus, refractile bodies and mitochondria increase during the early stages of infection. 85
3.5.3. Analysis of sporozoite morphometric changes by light microscopy before and after host cell invasion....90
4. Loss of the anterior refractile body occurs via actin-dependent organelle merger 92
4.1. Introduction....92
4.2. Nile red is a suitable marker for refractile bodies in *E. tenella*....92
4.3. Loss of the anterior refractile body occurs from approximately two hours following infection 94
4.4. Total refractile body volume increases following anterior refractile body loss....98

4.5. Anterior refractile body loss occurs through merger between the anterior and posterior refractile bodies 99

4.5.1. Addition of Nile red does not affect anterior refractile body loss 99

4.5.2. Refractile body merger was identified as the only mechanism of anterior refractile body loss 100

4.6. Sporozoite shape change and actin dynamics are associated with refractile body merger .. 105

4.6.1. Refractile body merger is dependent on sporozoite actin 105

4.6.2. Refractile body merger is associated with cell roundness 111

5. Diversity and temporal dynamics in *E. tenella* apical complex ultrastructure 115

5.1. Introduction 115

5.2. Three-dimensional organisation of the apical complex in *E. tenella* 115

5.3. Outer components of the apical complex 120

5.3.1. Variation in conoid fibre number 120

5.3.2. Increasing conoid fibre number is associated with increasing conoid diameter 122

5.3.3. Increasing conoid fibre number is associated with increasing apical polar ring diameter 125

5.3.4. Increasing conoid apex diameter is associated with increasing diameter of the pre-conoidal rings 127

5.3.5. Conoid fibre number varies between clonal sporozoites 129

5.3.6. Conoid fibre number varies between intracellular sporozoites 131

5.4. Inner components of apical complex 135

5.4.1. Micronemes and spherical vesicles attach to the plasma membrane in the centre of the conoid 135

5.4.2. The intra-conoidal microtubule pair is associated with secretory organelle positioning 137

5.4.3. Intracellular sporozoites interact directly with the host cell cytoplasm via a break in the parasitophorous vacuole membrane (preliminary data) 142

6. Discussion 145

6.1. Organelle morphometrics in *E. tenella* 145

6.1.1. Absence of dense granules in *E. tenella* 145

6.1.2. Rhoptries were found throughout the sporozoite....146
6.1.3. Microneme morphology and volume....146
6.1.4. *E. tenella* sporozoites possess multiple mitochondria....146
6.1.5. Evaluation of organelle quantification using SBF-SEM imaging....147
6.2. Cell-to-cell morphometric variation....148
6.2.1. Variation in cell shape and volume....148
6.2.2. Variation in conoid fibre number....149
6.2.3. Associated morphometric parameters of the apical complex ring structures....150
6.2.4. Sporozoite morphometric variation and single-cell heterogeniety....150
6.3. Morphological changes associated with early intracellular development....151
6.3.1. Cell and organelle shape and volume changes....152
6.3.2. Loss of the anterior refractile body....154
6.3.3. Increase in refractile bodies volume....154
6.3.4. Temporal regulation of anterior refractile body loss....154
6.3.5. Anterior refractile body loss occurs through fusion of the refractile bodies....155
6.3.6. Role of actin in cell shape change and refractile body merger....155
6.4. Structural insights into apical organelle secretion....158
6.4.1. Site of secretion for the apical organelles....159
6.4.2. Docking and secretion of a single microneme....159
6.4.3. Role of intraconoidal microtubules in apical organelle trafficking....160
6.4.4. Role and dynamics of the spherical vesicles....160
6.4.5. Interaction between rhoptry contents and host cell cytoplasm....161
6.5. Future work....162

1. **Introduction**

1.1. **Apicomplexa**

The phylum Apicomplexa contains an array of important parasitic species for both human and veterinary medicine (Fig. 1.1). This group belongs to the higher order 'Alveolata', which comprises over 17,000 biologically diverse microbial phyla (Grattepanche et. al. 2018) including predatory ciliates, parasitic apicomplexa and photosynthetic dinoflagellates. All species within the phylum Apicomplexa are parasitic protozoa which share a specialised set of cytoskeletal and secretory organelle structures known as the apical complex (Okamoto and Keeling 2014). This is later described at length with relation to the structural biology of *Eimeria tenella*. Two of the most clinically relevant groups of Apicomplexa are Haemosporidia (Danilewsky 1885, cited in Golemansky 2015) which contains the causative agents of malaria (*Plasmodium* spp.), and Coccidiasina (Leuckart 1879, cited in Levine 1980) within which *E. tenella* is found, together with other important parasites such as *Toxoplasma gondii* (Levine 1977).

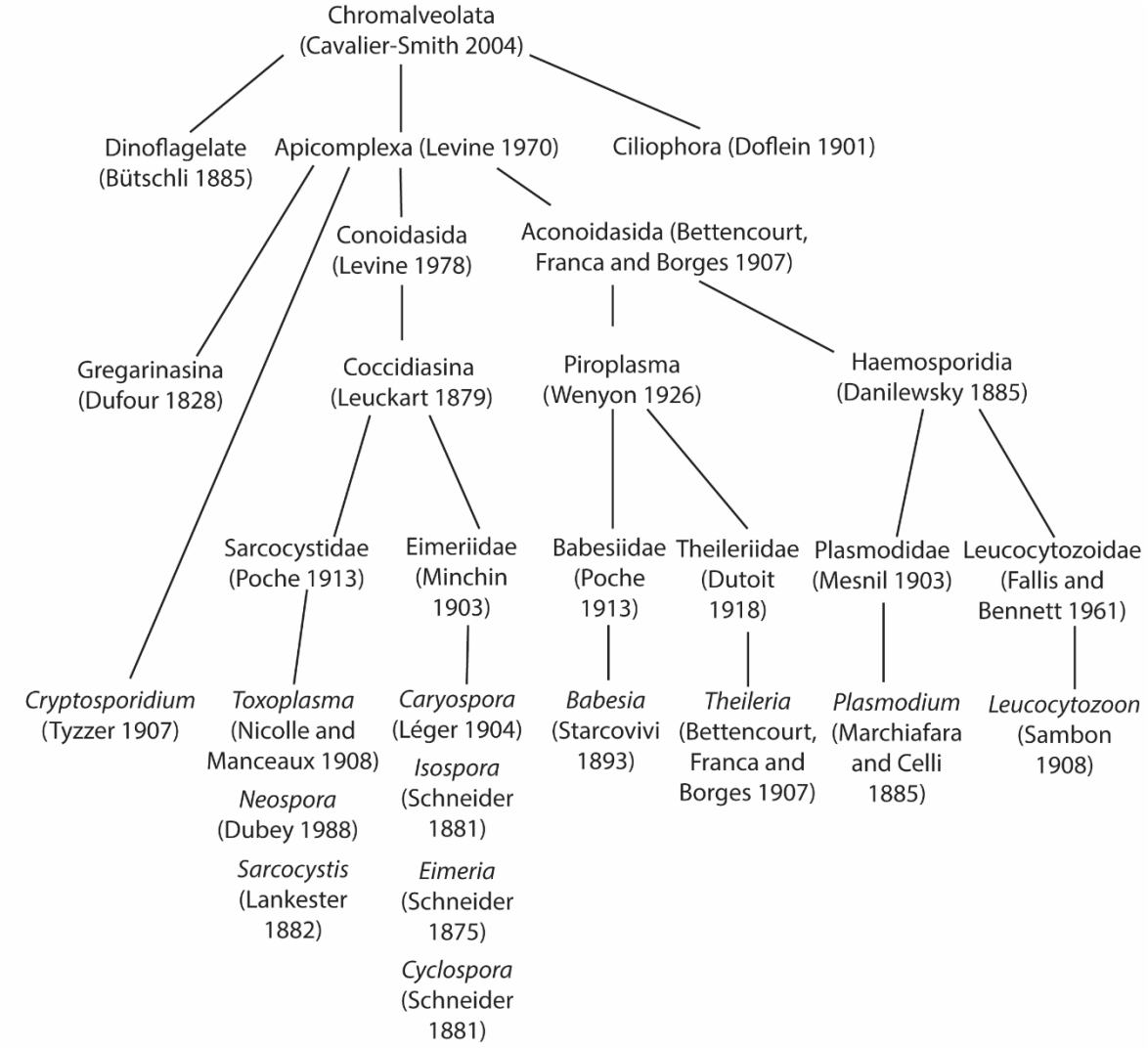


Figure 1.1. A phylogenetic tree showing the relationships between important apicomplexan species. This was constructed based on data from multiple sources (Adl *et. al.* 2007, Carreno et. al. 1999, Golemansky 2015, Jirků *et. al.* 2002, Lane and Archibald 2008, Levine 1984, Megía-Palma *et. al.* 2015, Tenter et. al. 2002, Tenter and Johnson 1997, West *et. al.* 2001).

1.2. **Coccidia**

Similarities between different species of the Coccidiasina were described by Leuckart in 1879 (cited in Levine 1980). At this stage they were grouped under the name Sporozoa based on the common feature of a protective 'spore' casing. Subsequent work by, biologists such as Fantham (1910) and Tyzzer (1929) provided key insights into the complex life-cycles of coccidian species. Through histological examination of infected tissues, it was discovered that the life-cycle of *Eimeria* species involved release of invasive infectious stages from the spore (now known as the oocyst), replication within intestinal cells of the infected host with formation of large multinuclear intermediate stages, generation of dimorphic sexual stages followed by the formation of oocysts, and additional oocyst development following release from the host (Fantham 1910). Other apicomplexan organisms, such as *T. gondii, Neospora caninum* and species of *Sarcocystis* were later found to share these life-cycle traits and were added to the group Coccidiasina (Hammond and Long 1973, Hutchison et. al. 1970).

1.3. **Coccidial diseases**

Diseases caused by parasites of the Coccidiasina are known as coccidial diseases. Another term, coccidiosis, is most commonly applied to enteric coccidial disease in production animals. With regards to human health, one of the most notable coccidial diseases is toxoplasmosis which is caused by the single species, *T. gondii* (Sabin 1939, Tenter et. al. 2000). The epidemiology of toxoplasmosis is complex. Seroprevalence of around 50% has been reported in several areas across the world including several regions in north Africa and certain subpopulations within the United States of America (Bissati et. al. 2018, Guigue et. al. 2018). Cases of acute disease are relatively rare but still represent a significant public health burden (Bissati et. al. 2018). There are several different manifestations of clinical toxoplasmosis. One form of the disease was widely publicised in relation to the American HIV epidemic of the 1980's. Patients suffering from immunodeficiency, such as those with HIV-AIDs, are at risk of tissue destruction due to proliferation of *T. gondii* parasites (Luft et. al. 1984). In this clinical scenario, the organism has a predilection for neural tissue and proliferation leads to the development of encephalitis which is often fatal (Pereira-Chioccola et. al. 2009). Other important clinical manifestations of toxoplasmosis include abortion or congenital deformities caused by pathology of the placenta or foetal tissues (Fallahi et. al. 2018, Robert-Gangneux et. al. 2011) and ocular disease found in immunocompetent or immunocompromised individuals (Butler et. al. 2013).

Due to both its significance in human disease and its amenability for maintenance in culture, *T. gondii* is a widely studied model organism (Szabo and Finney 2017). With its close phylogenetic relationship to the studied species of interest, *E. tenella*, data from work involving *T. gondii* has been used throughout this project to supplement data on *Eimeria* species and view the work in the broader context of coccidian biology. It is however important to note that there are numerous differences in both the structural and functional biology of these two parasites and where relevant these differences are acknowledged and referenced throughout this thesis.

Focusing on the impact of *Eimeria* species, one of the most clinically and economically relevant diseases caused by this genus is poultry coccidiosis (Blake and Tomley 2014). As previously mentioned, coccidiosis refers to enteric forms of the disease; in the case of poultry coccidiosis clinical signs of intestinal dysfunction can be seen, ranging from a failure to gain weight to severe diarrhoea with malnourishment, dehydration and death (Chapman 2014).

Seven recognised species of *Eimeria* are known to cause disease in chickens: *Eimeria acervulina, Eimeria brunetti, Eimeria maxima, Eimeria mitis, Eimeria necatrix*, *Eimeria praecox* and *Eimeria tenella* (Chapman 2014). *Eimeria* parasites are highly host specific, with each species capable of producing infection in only a single animal species (Vrba and Pakandl 2015). This is a key point of difference between *Eimeria* species and *T. gondii*. Whereas *Eimeria* species are host- and tissue-specific parasites, *T. gondii* can infect many different cell types in many different species (Sabin

1939, Sibley 1995). This suggests that there may be fundamental differences in the molecules or mechanisms used to invade and/or develop within the host. It has been hypothesised that the surface antigen protein (SAG) repertoire of *T. gondii* may be associated with this species' ability to invade diverse species and cell types (Lekutis et. al. 2001).

In addition to the estimated $3 billion cost of poultry coccidiosis annually (Blake and Tomley 2014), the global farming community suffers considerable losses due to coccidiosis in ruminants. As with the disease in poultry, *Eimeria* infection in cattle, sheep or goats can cause mild to severe intestinal dysfunction, in some cases leading to loss of life due to dysentery (Daugschies and Najdrowski 2005, Tafti and Mansourian 2008).

Despite their host specificity, *Eimeria* species have been incredibly successful at setting up parasitic niches throughout the animal kingdom. There are currently over 1800 known species of *Eimeria* (Duszynski 2001) including species affecting reptiles, amphibians and fish (Gjurčević et. al. 2017, McAllister et. al. 2014, 2017). An interesting point to note is that there has been no species of *Eimeria* found to parasitize man, however, the human pathogen *Cyclospora cayetanesis* is remarkably like *Eimeria* species in terms of both biology and pathogenesis (Ortega and Sanchez 2010).

1.4. **The life cycle of *E. tenella***

As previously mentioned, the coccidian life cycle is characterised by several intracellular replication stages in the intestines of a definitive host species, culminating in the production of resistant oocysts which are excreted with the faeces. Variations in the precise life cycle stages and events exist between different coccidia species; the book by Kheysin (2013) gives a good overview on different coccidian species affecting domestic animals. Here I describe the life cycle of *E. tenella* focusing on the aspects most relevant to this project, namely host cell invasion and early intracellular development.

To initiate infection, *E. tenella* is ingested by a chicken in the form of 'sporulated oocyst'. This stage consists of multiple parasites enclosed within a multi-layered protective egg-like casing. Within each sporulated oocyst there are eight infective sporozoites arranged as pairs (Fig. 1.2, Fig. 1.3.1). Each sporozoite pair is enclosed within another casing layer and the encased sporozoite pairs are known as sporocysts.

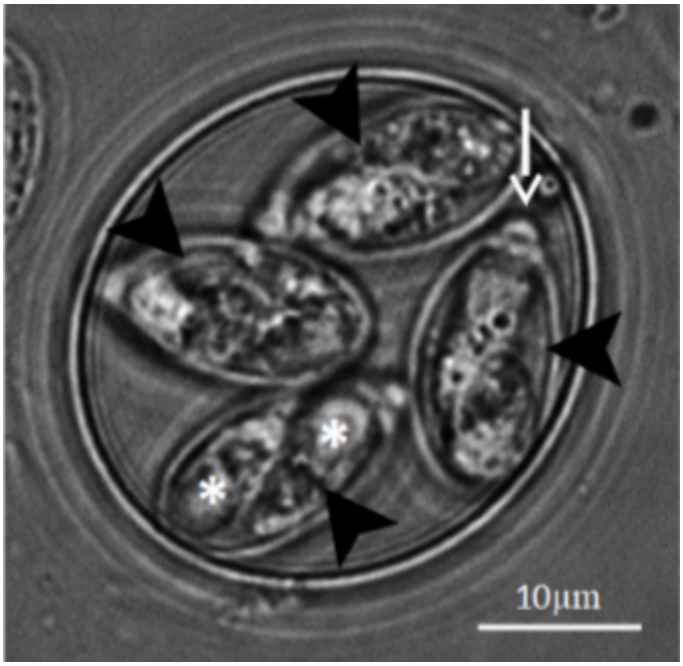


Figure 1.2. Sporulated oocyst of *Eimeria tenella*. This contains four sporocysts (arrowheads) each containing two sporozoites (asterisks) and a stieda body at each sporocyst apex (arrow). Light microscopy image courtesy of V. Marugan-Hernandez.

It is the sporozoites which are responsible for initial invasion of host tissues. Following mechanical and chemical disruption of the sporulated oocyst (Fig. 1.3.1) and sporocyst casings within the intestinal tract of the chicken, motile sporozoites escape into the intestinal lumen (Fig. 1.3.2). Attachment of sporozoites onto intestinal epithelial cells and movement across the epithelium surface involves multiple adhesive sporozoite proteins, transiently located on the cell surface and capable of attachment to host cell receptor proteins (Lai et. al. 2011). These proteins are delivered to the cell surface via regulated secretion from microneme organelles (Bumstead and Tomley 2000), which are part of the aforementioned 'apical complex'. Sporozoite motility is achieved through an apicomplexan-specific substrate-dependent mechanism, whereby directional force, generated from intracellular actin, is transmitted to surface-located microneme proteins connecting the parasite and substrate. The current model for apicomplexan motility, developed from work involving various apicomplexan species, suggests that the actin-generated force pushes against the microneme proteins, which are static with respect to the substrate but fluid with respect to the sporozoite membrane (Frénal et. al. 2017), leading to forward movement of the parasite and rearward movement of the microneme proteins with respect to the sporozoite cell. A key finding for the development of this model was the observation of microneme protein 'trails' deposited onto the surface behind motile sporozoites of *E. tenella* (Bumstead and Tomley 2000). More recently, work involving force measurement in motile apicomplexan cells points towards a variation of the original model, termed 'stick and slip motility' (Münter et. al. 2009). Here they showed that traction forces were not uniform across the length of the *Plasmodium berghei* sporozoite indicating that parasites were able to utilise elastic energy, generated by coupling rearward membrane flow and attachment site foci, to power rapid bursts of forward travel.

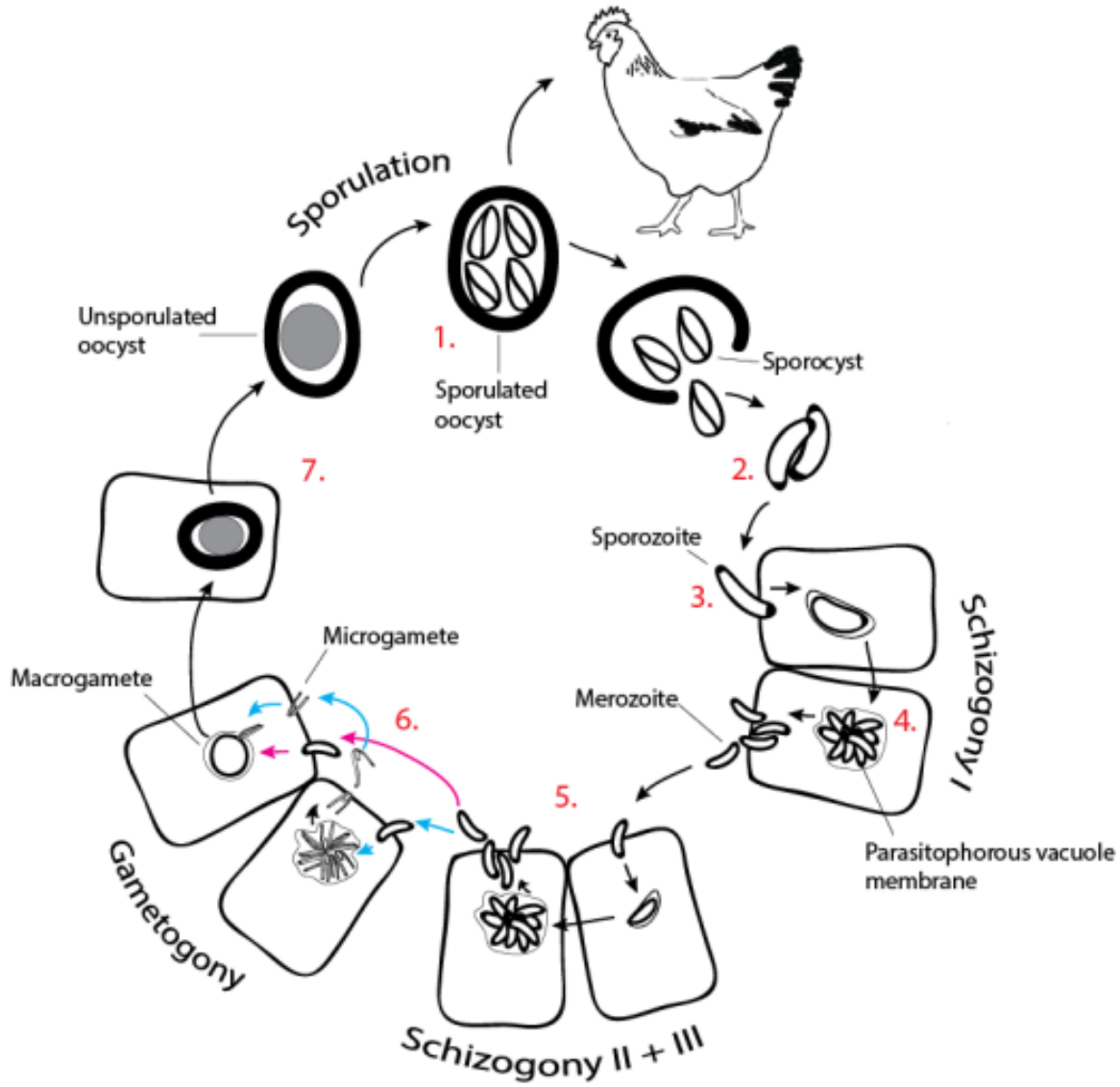


Figure 1.3. The life cycle of *E. tenella*
Numbered stages are referred to in the main body of text.

The process of host cell invasion in apicomplexans shares several features with that of substrate-dependent apicomplexan motility. Apicomplexan zoites (invasive apicomplexan cells) exhibit polarised invasion whereby the apical end initiates penetration (Aikawa et. al. 1978). When the apical tip is in contact with the host cell membrane, a ring-shaped structure is formed, containing proteins secreted from two classes of apical organelle, the micronemes and rhoptries (Alexander et. al. 2005). This ring-shaped structure, termed the moving junction, is anchored with respect to the host cell but fluid with respect to the parasite surface (Alexander et. al. 2005, Gonzalez et. al. 2009). Actin-dependent force generation allows the zoite to push against the moving junction, propelling itself towards the centre of the host cell (Riglar et. al. 2011).

Two important aspects of zoite invasion preceding intracellular development are that the invading cell does not breach the host cell (Chobotar and Entzeroth 1993), and that following invasion (Fig. 1.3.3) the intracellular zoite is contained within a membrane-bound compartment called the

'parasitophorous vacuole' (Fig. 1.3.4). The parasitophorous vacuole membrane is largely formed from the host cell plasma membrane but has been altered in its protein composition (Charron and Sibley 2004, Mordue et. al. 1999). During invasion, the moving junction is thought to be anchored to cytoplasmic host cell components, allowing membrane flow and invagination with the progressing zoite (Besteiro et. al. 2011). It is also known that apicomplexan invasion is distinct from host-cell generated endocytosis (Frénal et. al. 2017). Invasion, but not attachment, in *T. gondii* was shown to be parasite actin dependent (Dobrowolski and Sibley 1996), temporally and structurally different to phagocytosis of opsonised zoites (Morisaki et. al. 1995) and the parasitophorous vacuoles do not exhibit endosomal characteristics such as lysosome fusion (Mordue et. al. 1999).

Once inside the parasitophorous vacuole, *E. tenella* sporozoites undergo a change in cell shape. Prior to invasion, sporozoites appear as crescent-shaped cells (Ryley 1969), however in the first 24-35 hours post invasion they become progressively more rounded, lose the structures of the apical complex and are subsequently termed 'trophozoites' (McDougald and Jeffers 1976, Pacheco et. al. 1975). In the early stages of intracellular development, there are also changes to the parasite refractile bodies. These are two large, poorly understood, membrane-less structures seen as a pair in freshly excysted sporozoites. In trophozoites, a single refractile body is observed (Danforth and Augustine 1989). The dynamics of refractile bodies in early intracellular development is one of the focal points of this thesis; as such a more detailed review of their characteristics and dynamics can be found in a later section of this chapter.

From around 32 hr after infection nuclear division commences and the parasite becomes a 'schizont' (McDougald and Jeffers 1976, Pacheco et. al. 1975). Further mitotic divisions take place over the next ~12 hr until the resulting schizont contains up to around 200 nuclei (McDonald and Rose 1987). Daughter cell (merozoite) formation proceeds with the development of cytoskeletal structures which organise at the surface of the schizont and associate with the schizont membrane to form budding projections of immature merozoites (Pacheco et. al. 1975). Nuclei and organelles segregate into the developing merozoites and the merozoite buds elongate until they resemble distinct sickle-shaped cells, connected to remnants of the parent cell (residual body) at their posterior ends (McLaren 1969, Roberts et. al. 1970). Fission between merozoite and residual body occurs which completes merozoite formation. The process of merozoite formation, known as 'schizogony', is distinct from the process of cellular replication employed by the commonly studied tachyzoite stage of *T. gondii*. In *T. gondii* tachyzoites, daughter cell cytoskeletal formation commences prior to the loss of parent-cell apical complex structures and prior to the onset of nuclear division (Gavin et. al. 1962, Sheffield and Melton 1968). This form of replication is known as 'endodyogeny' and results in the production of just two daughter cells from each parent tachyzoite.

There is little data on how *Eimeria* spp. merozoites are released from the cell, however data from other apicomplexan species suggests the involvement of parasite perforins and proteases in

disruption of the parasitophorous membrane (Blackman and Carruthers 2013). Electron microscopy data has shown how *Plasmodium falciparum* gametocyte egress occurs in a two-step process, with lysis of the parasitophorous vacuole preceding lysis of the host cell membrane (Sologub et. al. 2011).

Following their release, *E. tenella* merozoites are capable of invading new host cells (Fig. 1.3.5). *In vivo*, three morphologically variant schizonts can be seen, with differing proportions present depending on time following infection (McDonald and Rose 1987). These schizont variants represent successive and distinct generations that originate from intracellular replication of the previous generation daughter merozoite (McDonald et. al. 1988, McDonald and Rose 1987).

At around four to five days post infection *in vivo*, two more morphological stages of the parasite can be seen. Host cells may contain microgametocystes, the stage within which a large number of flagellated 'microgametes' are formed, or macrogametocytes, from which an individual, rounded 'macrogamete is formed (McLaren 1969) (Fig. 1.3.6). These stages are responsible for the sexual life-cycle event. Fantham (1910) reports witnessing fertilisation, whereby the microgamete enters the macrogamete, however this is the sole reported observation of this event. In contrast to haploid macrogametes and microgametes, the subsequent parasitic life cycle stage, the zygote/ unsporoulated oocyst, is diploid (Cornelissen et. al. 1984), which supports the hypothesis that a fertilisation event occurs. Macrogametes undergo several developmental changes, involving fusion of peripheral 'wall forming bodies' to create the oocyst wall (Ferguson et. al. 2003). From around 6 days post infection, the first excreted oocysts can be seen in the faeces of the host (Cha et. al. 2018) (Fig. 1.3.7). These oocysts are 'unsporulated' and do not contain morphologically distinct sporozoites. If exposed to the correct environmental conditions, oxygen and a temperature between 20^0C and 30^0C (Edgar 1954, Wagenbach and Burns 1969), a final developmental stage (sporulation) occurs, culminating in the formation of eight haploid sporozoites (Cornelissen et. al. 1984, Wagenbach and Burns 1969) Fig. 1.3.1).

1.5. **Structural biology of the *E. tenella* sporozoite**

1.5.1. **Overview**

The fully-formed sporozoite is a crescent-shaped cell (Fig. 1.4) and in *E. tenella* is around 72 μm^3 in volume (Wagenbach 1969). The cell is bound by three membranous layers, collectively known as the pellicle. The outer-most layer of the pellicle is the plasma membrane and the two inner layers are opposing sides of flattened membranous sacs, or 'alveoli' (Dubremetz and Torpier 1978). Between the plasma membrane and the alveolar sacs, actin-myosin interactions are believed to occur, powering the force required for motility and invasion. In *T. gondii*, immuno- electron microscopy found that actin and myosin were located directly beneath the plasma membrane (Dobrowolski et. al. 1997). This localisation data is supported by subsequent works which have unravelled much of the molecular details behind motility in apicomplexan species (Boucher and Bosch 2015, Tosetti et.

al. 2019). Below the alveolar sacs (collectively known as the inner membrane complex) is situated an array of 24 microtubules, extending from the cell apex to roughly 2/3rds of the length towards the posterior (Roberts and Hammond 1970, Ryley 1969). An envelope-bound nucleus is located at the centre of the cell and both posterior to and anterior to the nucleus, there is a large globular structure known as a refractile body (Fig. 1.4) (covered in more detail later). The apical quarter of the sporozoite is filled with numerous elongated vesicles known as the micronemes and rhoptries (Ryley 1969) (Fig. 1.4) which form part of the 'apical complex' (structures of the apical complex are covered in more detail below). Dense granules are another type of specialised vesicle found in apicomplexan species such as *T. gondii* (Mercier and Cesbron-Delauw 2015). The presence of dense granules in *E. tenella* is yet to be verified and the genome of *E. tenella* contains few orthologues of known dense granule proteins (Reid et. al. 2014).

Scattered throughout the rest of the cell are ovoid-shaped granules of amylopectin (Fig. 1.4) which are thought to act as energy reserves (Matsubayashi et. al. 2013). In *T. gondii*, a link has been proposed between amylopectin content and stage conversion of the parasite (Coppin et. al. 2003), whether amylopectin levels play a role in developmental stage determination for *E. tenella* is unknown. Also dispersed throughout the cell are several osmophilic structures known as volutin granules or acidocalcisomes which are known to have a role in calcium homeostasis in *T. gondii* (Rohloff et. al. 2011). Mitochondria can also be seen throughout the cytoplasm with distinctly visible cristae when viewed by electron microscopy (Ryley 1969). Endoplasmic reticulum and Golgi apparatus can sometimes be seen near to the nucleus upon transmission electron microscopy observation (Ryley 1969). *Eimeria tenella* sporozoites also contain an apicoplast, an organelle which is specific to apicomplexa and was gained via secondary endosymbiosis (Lim and McFadden 2010). By electron microscopy, the apicoplast can be identified as four concentric membranous rings. In both *T. gondii* and *Plasmodium* spp., the apicoplast plays an essential role in fatty acid synthesis (Martins-Duarte et. al. 2016, Waller et. al. 2003).

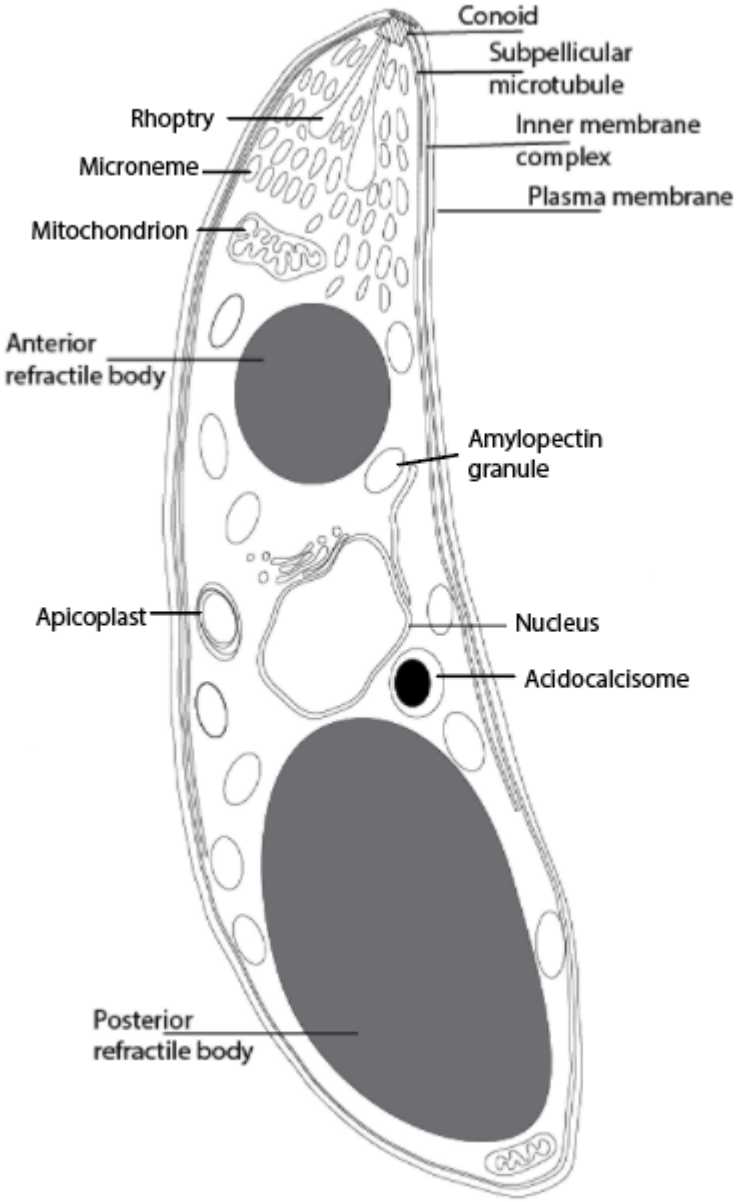


Figure 1.4. Subcellular structures of the *E. tenella* sporozoite.

1.5.2. **Apical complex: micronemes**

As previously mentioned, much of the anterior part of the cell is occupied by secretory organelles of the apical complex. The most abundant of these in *E. tenella* are the micronemes (based on qualitative assessment of electron microscopy data) (Ryley 1969). Micronemes are key organelles when it comes to pathogenesis of apicomplexan parasites. They have been shown to contain proteins that are essential for both motility and invasion (as described in section 1.4) and work in *T. gondii* has demonstrated the involvement of microneme proteins in host cell egress (Gras et. al. 2017).

Micronemes are approximately 400-500 nm in length and appear as elongated ovoid vesicles (Roberts and Hammond 1970). They are membrane bound and contain electron-opaque substance when viewed by transmission electron microscopy (Fig. 1.5A). Regulation of microneme secretion

in *T. gondii* has been shown to involve calcium signalling pathways (Carruthers and Sibley 1999); in both *T. gondii* and *E. tenella*, microneme secretion can be induced by exposure to serum albumin (Brown et. al. 2016, Bumstead and Tomley 2000) which interacts with intracellular calcium to stimulate microneme protein release (Brown et. al. 2016). There is some ambiguity in the literature as to the believed site for microneme secretion. Some have suggested that the micronemes fuse with another of the apical organelles (the rhoptries) (Bannister et. al. 2003, Scholtyseck and Mehlhorn 1970). More recent data in *T. gondii* and *P. falciparum* indicate that the micronemes fuse directly with the plasma membrane (Bullen et. al. 2016, Farrell et. al. 2012) however no microscopic evidence of this event exists.

1.5.3. **Apical complex: rhoptries**

The other known apical complex secretory organelles of *E. tenella* are the rhoptries. These are several times larger than the micronemes but present in smaller numbers (Ryley 1969). The rhoptries possess a characteristic club-shaped structure with a posterior rounded 'bulb' and elongated 'neck' that extends towards the parasite apex (Fig. 1.5B). Molecular data suggests that there is functional segregation between the neck and bulb components. Proteins localised to the rhoptry neck are involved in formation of the 'moving junction' in *T. gondii* and are secreted during the initial stages of invasion (Besteiro et. al. 2009, Lebrun et. al. 2005). In *T. gondii,* rhoptry bulb proteins have been found to mediate post-invasion processes such as interfering with host signalling (Saeij et. al. 2007) and modification of the parasitophorous vacuole (Håkansson et. al. 2001). Proteome analysis of gradient-purified rhoptry fractions from *E. tenella* sporozoites detected 12 proteins with homology to *T. gondii* rhoptry neck proteins, but only four with homology to rhoptry bulb proteins (Oakes et. al. 2013); the functional significance of the rhoptry bulb in *Eimeria* species remains unclear.

Another interesting rhoptry dynamic displayed in *T. gondii* is the ability to inject contents directly into the host cytosol through evacuoles (Nichols et. al. 1983). This occurs during the initial stage of invasion and is thought to play a role in delivering membrane constituents to the forming parasitophorous vacuole (Håkansson et. al. 2001).

1.5.4. **Apical complex: conoid and conoid appendages**

A structure that has much intrigued parasitologists is the apicomplexan conoid. The conoid sits at the anterior-most part of the apical complex, directly beneath the plasma membrane at the apical tip of the cell (Fig. 1.5A). It is a hollow cone-shaped structure, open at both ends and approximately 500 nm across (Roberts and Hammond 1970). The conoid is constructed from closely-apposed curved fibres which, in *T. gondii*, represent a novel arrangement of tubulin protofilaments (Hu et. al. 2002). Between the conoid and plasma membrane are two parallel pre-conoidal rings (Roberts and Hammond 1970) similar in diameter to that of the conoid (Fig. 1.5C). Running through the centre of the conoid is a pair of microtubules and encircling the conoid is the apical polar ring (Fig. 1.5C)

(Roberts and Hammond 1970). The apical polar ring refers to the ring that forms from the termination of the inner membrane complex and the ends of the subpellicular microtubules (Fig. 1.5C), which are anchored around the conoid. The conoid is thought to function in apical organelle secretion. Electron microscopy data shows what appears to be rhoptry necks passing into the conoid of *E. tenella* (Ryley 1969). Fluorescent light microscopy data in *E. tenella* has revealed that microneme and rhoptry secretion occurs from the apical end of the sporozoite (Bumstead and Tomley 2000, Entzeroth et. al. 1993). As the pellicle covering the apical end of the conoid lacks the inner membrane complex (Ryley 1969), it seems that this site is suited for secretion. It is currently uncertain whether the conoid has a purely structural function. Data from *T. gondii* has revealed that the conoid is capable of dynamic motions. When in the presence of mammalian cells or specific chemical cues, the conoid is seen to protrude from the apical tip of the cell (Chiappino et. al. 1984, Mondragon and Frixione 1996). Some have suggested that conoid extrusion acts as a 'gateway', for example by opening sites around the base of the conoid where microneme secretion is facilitated (Paredes-Santos et. al. 2012) or exposing protein domains that play a role in signal transduction (Katris et. al. 2014). Conflicting data suggest that conoid extrusion may not be essential to invasion as microneme protein secretion was detected following extrusion inhibition (Carey et. al. 2004). It has also been argued that the lack of consistency in the data may reflect the presence of more than one invasion strategy (Andenmatten et. al. 2013). Another point to consider is that many apicomplexan species, including *P. falciparum*, do not contain a conoid, yet do contain other apical complex structures and employ similar strategies of invasion (Preiser et. al. 2000).

As described in section 1.4, both sporozoite motility and invasion are highly polarised events. Both events involve the movement of molecules from the apex of the cell towards the posterior. During invasion, a key structure called the moving junction is formed at the point where the parasite apex interacts with the surface of the host cell. The polarised arrangement of organelles within sporozoite therefore reflects the polarisation of key events at this stage of the life cycle.

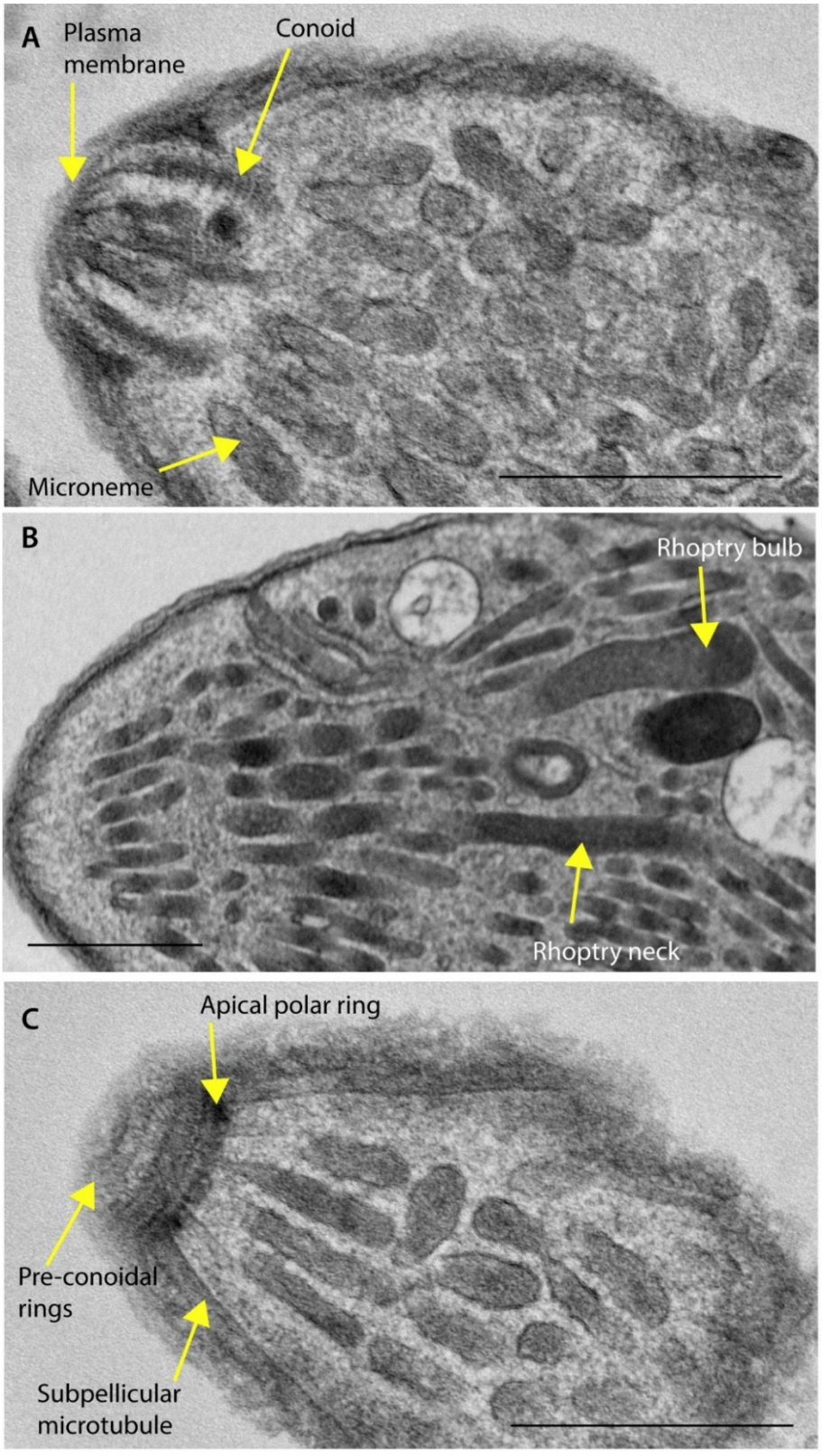


Figure 1.5. Apical complex of the *E. tenella* sporozoite.
A to C) Transmission electron microscopy images of the apical end of *E. tenella* sporozoites. Freshly-excysted sporozoites were fixed using aldehydes and processed for electron microscopy using a single osmium protocol. A) The conoid is positioned at the apical extreme of the cell. Numerous micronemes fill the apical portion of the cell. B) Rhoptries are comprised of elongated neck and rounded bulb portions. C) Subpellicular microtubules are attached to an apical polar ring which surrounds the conoid. Two pre-conoidal rings are situated just above the conoid. Scale ~ 500 nm.

1.5.5. **Refractile bodies**

As briefly mentioned in section 1.5.1, each *E. tenella* sporozoite contains two refractile body organelles (Fig. 1.4). The refractile bodies are a poorly studied class of organelle; I found just 13 papers focussing on this topic. One reason for a lack of research into these organelles may be because they are only present among members of the family 'Eimeriidae' (Lemgruber and Lupetti 2012). An argument for further research into the refractile bodies is their proven immunogenic capacity. One of the most promising vaccine candidates for the prevention of disease caused by *Eimeria* spp. is SO7 (Crane et. al. 1991, Kopko and Martin 2000, Song et. al. 2013), which is an antigen located in the refractile bodies (de Venevelles et. al. 2006).

In *E. tenella* sporozoites, the refractile bodies are the largest and most prominent organelles of the cell. Both refractile bodies are globular in shape; the anterior refractile body, located anterior to the nucleus, is roughly spherical (Fig. 1.4) and the posterior refractile body, located posterior to the nucleus, is ovoid in shape (Fig. 1.4). The posterior refractile body is the larger of the two, filling the posterior half of the cell. A peculiar feature of the refractile bodies is that they lack a limiting membrane or any discernible internal structure when chemically fixed and viewed by electron microscopy (Roberts and Hammond 1970). Histochemical investigations revealed that these compartments were lipid-rich (Frandsen 1968) and positive acridine orange staining indicates they are acidic and/or contain nucleic acids (Miranda et. al. 2008). A proteomic investigation of refractile body constituents found them to contain several enzymes including aspartyl protease and transhydrogenase, along with an array of proteins with unknown function (de Venevelles et. al. 2006). Microscopy investigations have described how the refractile bodies undergo dynamic changes throughout the life cycle. In the first 12 hours post invasion, several species of *Eimeria* appear to lose the anterior refractile body, either through fragmentation, shrinkage or combination with the posterior refractile body (Clark and Hammond 1969, Fayer 1969, Fayer and Hammond 1969, Roberts et. al. 1970). During the first generation of schizogony, the remaining refractile body appears to fragment and dissipate before emerging as a small globule in each of the resultant daughter merozoites (Danforth and Augustine 1989). As with several other structures in *Eimeria* spp. including the conoid, the function of the refractile bodies remains unknown. Due to their large size, lipid content and the presence of enzymes, some have hypothesised that the refractile bodies are either nutrient stores or involved in metabolising energy reserves (Chobotar and Scholtyseck 1982, Lemgruber and Lupetti 2012, de Venevelles et. al. 2006, Vermeulen et. al. 1993). This hypothesis raises several questions: why they are present in such large quantity prior to the first round of replication but not for the subsequent replication stages? Why are they not required in species such as *T. gondii*, even in the sporozoite stage which has a similar developmental pattern in felid species to that of the *E. tenella* sporozoite? And why does a small portion of refractile body specifically segregate to the daughter merozoites?

1.6. **Aims and objectives**

The aim of this PhD project was to investigate *E. tenella* structural and functional biology using high-resolution microscopy techniques. The methodology proposed included quantitative analysis of three-dimensional electron microscopy data and use of high-resolution fluorescence light microscopy. Through the comparative study of *E. tenella* ultrastructure at various developmental stages, this approach was expected to uncover temporally-associated organelle dynamics and reveal novel insights into the biology of this parasite.

To aid investigation, I was able to use a novel three-dimensional electron microscopy technique known as serial block face – scanning electron microscopy (SBF-SEM). In SBF-SEM for biological specimens, a resin-embedded sample is inserted into a scanning electron microscope. Automated removal of an ultrathin section from the surface of the sample is performed and the freshly-exposed surface is imaged using a scanning electron beam (Denk and Horstmann 2004). The sequence of section-removal and scanning electron microscopy imaging is repeated to build up a three-dimensional stack of images. The image stack often consists of hundreds of images and can include data about the subcellular structures of entire cells or regions of tissue; several examples of this are listed in the review by Peddie and Collinson (2014). The application of SBF-SEM for studying organelle morphometrics in protozoan parasites has recently been demonstrated (Hughes et. al. 2017), although its application for the investigation of coccidian species remains a novel endeavour.

Being a novel, specialised technique, the use of SBF-SEM in the investigation of diverse biological specimens and scientific questions is still being optimised. Application of biological SBF-SEM involves specific challenges associated with interactions between the electron beam and the resin-embedded sample. If too much electron current is applied to the surface of the sample, the sample can build up negative charge (Denk and Horstmann 2004, Titze and Denk 2013). Sample charging can damage the sample, inhibiting the smooth cutting of ultrathin sections (Pinali and Kitmitto 2014); it can also interfere with signal detection used to generate the electron microscopy image (Titze and Denk 2013). Reducing the electron current that reaches the sample can alleviate issues associated with sample charging, however insufficient current will mean that the resultant signal is insufficient for obtaining ultrastructural information (Denk and Horstmann 2004, Starborg et. al. 2013). Due to these challenges, specific protocols for the preparation of biological samples have been developed, with the aim of increasing sample stability under the electron beam whilst increasing the signal produced from sample-electron interactions (Mikula and Denk 2015, Pinali and Kitmitto 2014). As there is no existing data on the preparation of coccidian species for SBF-SEM, one of my objectives was the **optimisation of *E. tenella* sample preparation for SBF-SEM imaging**.

Following optimisation of the methodology for SBF-SEM imaging of *E. tenella*, I obtained three-dimensional data on the subcellular structures of multiple sporozoites. These data were used to fulfil

another objective, to **quantify the numbers and volumes of organelles in the *E. tenella* sporozoite stage**.

By collecting SBF-SEM data from both extracellular and intracellular sporozoites, it was possible to compare morphometric data to achieve my third objective to **investigate organelle dynamics associated with invasion and intracellular development**.

I was particularly interested in investigating changes associated with the refractile bodies because these organelles have so far received little detailed attention. As they contain at least one highly immunogenic peptide that shows promise as a vaccine candidate (Crane et. al. 1991), it would be useful to understand their role in *Eimeria* species development. Previous studies have shown that the anterior refractile body is lost following invasion of host cells (Clark and Hammond 1969, Fayer 1969, Fayer and Hammond 1969, Roberts et. al. 1970), yet the significance of this dynamic remains unknown. I therefore decided to pursue a further objective, to **investigate anterior refractile body loss in *E. tenella***.

The challenges and technical limitations involved with SBF-SEM imaging led to the consideration of alternative methods of three-dimensional electron microscopy. One such method is transmission electron tomography which uses a series of angle projections to reconstruct the three-dimensional architecture of a structure (Koster et. al. 1997) and can produce data with single nanometre resolution in both depth and axial planes (Scott et. al. 2012). Thus, transmission electron tomography could be used to assess secretory organelle morphology, and potentially **produce a quantitative, three-dimensional description of the apical complex in *E. tenella***. Such a detailed model could provide novel insights into the biomechanical features and dynamics of the apical complex.

Thus, in summary, the specific objectives for this PhD project were:

- to optimise *E. tenella* sample preparation for SBF-SEM imaging
- to quantify *E. tenella* sporozoite organelle numbers and volumes
- to investigate organelle dynamics associated with invasion and intracellular development
- to investigate anterior refractile body loss in *E. tenella*
- to produce a quantitative, three-dimensional description of the apical complex in *E. tenella.*

2. **Methods**

2.1. **Mammalian cell culture**[1, 2]

2.1.1. **Preparation of cell-culture media**

Cell-culture medium was prepared by supplementing a 500 ml bottle of Advanced Dulbecco's Modified Eagle Media (DMEM, high glucose – Gibco, Thermo Fisher) with 10 ml foetal calf serum (FCS – Gibco, Thermo Fisher) and 5 ml 10,000 U/ml Penicillin-Streptomycin (Gibco, Thermo Fisher). Media were stored in 50 ml alliquots at 4°C and warmed to 38°C before use. One month after opening, any unused medium was discarded.

2.1.2. **Cell defrosting**

A 2 ml cryogenic vial (Corning) containing $6x10^6$ Madin Darby Bovine Kidney (MDBK) cells stored in 1 ml 90% foetal calf serum and 10% dimethyl sulfoxide (DMSO - Sigma-Aldrich, Merck) was defrosted by mixing with 7.5 ml of cell-culture media within a culture flask (T25 - Falcon, Corning). The culture flask, containing MDBK cells and cell-culture medium was placed in a 38˚C incubator with 5% CO_2. After 24 hours (once cells had adhered to the surface of the flask) medium was poured off from the cell monolayer and replaced with 7.5 ml of fresh cell-culture media to remove any residual DMSO.

2.1.3. **Preparation of cell-culture buffer**

A 10x stock of cell-culture buffer was prepared by dissolving 80 g of sodium chloride (NaCl – Fisher Scientific), 3 g of potassium chloride (KCl - Sigma), 0.73 g of disodium hydrogen orthophosphate (Na_2HPO_4 – AnalaR, VWR), and 0.2 g of potassium phosphate (KPO_4H_2 – AnalaR, VWR) in 800 ml of double distilled water (ddH_2O). The pH was adjusted to 7.2 through dropwise addition of one molar sodium hydroxide (1M NaOH) and ddH_2O was added to give a final volume of 1,000 ml. Buffer was sterilised by autoclaving and stored at room temperature. Working solutions were generated by adding one-part stock solution to nine-parts autoclaved ddH_2O under aseptic working conditions.

---

[1] Mammalian cell culture was performed using aseptic techniques and conditions and all reagents were sterilised by autoclave or filtration prior to use.

[2] MDBK cells used in experiments were between passage 17 and passage 25

2.1.4. **Cell passage**

MDBK cell monolayers were washed once in 5 ml of cell-culture buffer then incubated with 2-3 ml 0.25% trypsin (trypsin-EDTA, 0.25%, buffered, with phenol red – Gibco, Thermo Fisher) for 2-3 min at 41^{0}C. Banging the sides of the flasks loosened the monolayers and 5 ml cell-culture media was then added and mixed with the cells by pipetting. The suspended cells were transferred to a 50ml centrifuge tube (Falcon, Corning) and centrifuged for 10 min at ~ 400 relative centrifugal force (RCF). Cell-culture medium was poured off from the pelleted cells. Ten ml of fresh cell-culture media was added and mixed with the cells by pipetting. One hundred microlitres of cell-suspension was mixed with 900 µl of media in a microcentrifuge tube (Camlab plastics). Cell number was calculated from a one in ten dilution of cells using a Fuchs-Rosenthal haemocytometer. Ten million cells were added to each new culture flask (T75 – Falcon, Corning) along with 15 ml cell-culture media.

2.2. **Parasite amplification**

2.2.1. **Infection of chickens**

Specified pathogen free Lohmann White chickens (obtained from APHA Weybridge at between 3 and 4 weeks old) were infected with 4,000 sporulated *E. tenella* Wisconsin strain oocysts. The oocysts used for dosing had been harvested within the previous three to six months and stored at 4^{o}C. Oral dosing was performed using a 1 ml syringe (BD) with oocysts suspended in 0.5-1 ml H_2O.

2.2.2. **Oocyst harvest and purification**

Seven days after dosing, all birds were culled by cervical dislocation. Oocyst harvest and purification was performed based on the protocols described by Long et. al. (1976) and Shirley (1995). The caeca, which were identified as paired blind-ending sacks attached to the distal intestine, were removed, cut open and scraped with a glass slide. Faecal content and scraped mucosal tissue were added to 300 ml water and mixed for 30 seconds in a tissue homogeniser (Waring).

The homogenised material was prepared to a concentration of 1.5% trypsin (Sigma) in water and the resulting solution incubated at 41^{0}C for 90 min, shaking every half hour. Oocysts were washed three times in water, pelleting each time by 10 min centrifugation (~ 600 RCF). The washed oocysts were counted using a Fuchs-Rosenthal haemocytometer and suspended in 2% aqueous potassium dichromate (5% potassium dichromate, Acros Organics, diluted to 2% in water) at a concentration of ~200,000 oocysts per ml. The oocyst solution was poured into 10 L conical flasks, each containing no more than ~ 3 L solution. A magnetic stirrer was added to each flask and flasks were placed onto magnetic stirring plates set to minimum stir-speed. Two 10 ml pipettes, attached to an air pump, were used to force a gentle bubble of air through the solution. Ambient temperature was adjusted to 27^{0}C and the oocysts were left in this condition to sporulate for 3-4 days. After microscopic confirmation

of sporulation (seen as characteristic changes to the appearance of internal oocyst material), oocysts were temporarily stored at 4^0C in 1000 ml of the sporulation solution. Sporulated oocysts were washed three times using H_2O, centrifuging for 10 min at ~ 600 RCF between each wash. Oocysts were then suspended in 20 ml of 1.2% aqueous sodium hypochlorite (12% sodium hypochlorite - VWR, diluted in H_2O) for precisely 10 min, kept on ice with intermittent swirling. Thirty ml of water were added to dilute the oocyst-containing sodium hypochlorite solution and oocysts were pelleted by 10 min centrifugation (~ 400 RCF). Chlorox solution was removed by pipette and oocysts were re-suspended in a saturated salt solution. Two millilitres of water were added to the salt solution so that it formed a thin layer above the salt. The oocyst solution was then centrifuged for 10 min at ~ 400 RCF and oocysts removed from the surface to another tube by pipetting. Water was added to the collected oocysts, ensuring that no more than 20% of the total volume was made up from the oocyst/salt solution. The collected oocysts were then washed a final three times in double-distilled H2O (ddH_2O); 10 min centrifugation was performed between each wash.

2.3. **Sporozoite release and purification**[3]

2.3.1. **Preparation of excysting solution**

Excysting solution comprised Hanks's balances salt solution (HBSS) (obtained as a pre-prepared solution from The Royal Veterinary College) supplemented with 0.25% trypsin (lyophilised trypsin powder from porcine pancreas - Sigma-Aldrich, Merck) and 1% taurocholic acid (taurocholic acid, sodium salt hydrate, 98% - ACROS organics, Thermo Fisher).

2.3.2. **Preparation of eluting solution**

A 4x concentrated stock of eluting buffer was prepared by adding 53.92 g of Na_2HPO_4, 3.12 g of NaH_2PO_4, and 17 g of NaCl to 800 ml of ddH_2O. The acidity was adjusted to pH 8 by adding 1 M NaOH in a dropwise manner. Double-distilled water was added to give a final volume of 1,000 ml. Stock buffer was sterilised by autoclaving and stored at room temperature.

To prepare working concentration eluting buffer, one-part stock buffer was mixed with three-parts sterile ddH_2O. Two and a half millilitres of filter-sterilised 20% glucose (≥99.5% glucose - Sigma-Aldrich, dissolved in ddH_2O) were added to 47.5 ml of working concentration eluting buffer.

2.3.3. **Sporozoite release**

Between 10 million and 50 million oocysts were washed in 50 ml of water and filtered through a 40 µm pore cell-strainer (Falcon, Corning) into a 50 ml centrifuge tube. Oocysts were pelleted by 10 min of centrifugation at ~ 400 RCF and water was removed down to the 2-3 ml mark. Oocysts were

[3] Sporozoite release and purification was performed under asceptic conditions and all reagents were sterilised by autoclave or filtration prior to use.

re-suspended by inverting the centrifuge tube several times. Number 8 glass beads (Jencons No. 8, 0.4-0.6 mm diameter range) were added to the oocyst suspension until they came to just below the waterline. The mixture of oocysts and beads was vortexed for 10 to 15 seconds (repeated if necessary) until most oocysts were cracked open to release the sporocysts. The extent of oocyst cracking was checked by microscopy after each vortex. The resulting mixture of beads and sporocysts and oocyst debris was washed four times with a total of 40 mls excysting solution. With each wash, sporocysts and oocyst debris, suspended in excysting solution, were poured into a conical flask, ensuring that glass beads remained in the 50 ml centrifuge tube. The flask was covered with parafilm and put into a 41˚C water-bath for 90 min. After 20 min incubation, 1M $MgCl_2$ was added to give a final concentration of 10 mM and the flask was swirled to mix. After 60 min incubation, the flask was swirled a second time. After 90 min incubation, the parasite-containing excysting solution was centrifuged for 10 min at ~ 400 RCF. Excysting solution was removed by pipette, ensuring not to disturb the pelleted parasites, and replaced by eluting solution.

2.3.4. **Sporozoite purification**

Preparation of the purification column involved filling a 20 ml syringe with knot-free nylon wool (Polysciences) up to the 5 ml mark. After sterilisation, the nylon-filled syringes were washed twice with 10 ml eluting solution and air bubbles were removed from the wool with a 1 ml serological pipette. DE-52 solution was added to the column, until the sediment reached the 10 ml mark, stoppering the syringe before it ran dry. DE-52 solution was obtained, pre-prepared, from the Royal Veterinary College London and consisted of washed and autoclaved diethylaminoethyl cellulose (Whatman pre-swollen microgranular anion exchange) in a pH8 phosphate buffered saline solution. The column was washed with 10 ml eluting solution and again stoppered before drying out. The sporozoite solution was added, dropwise, to the purification column and allowed to run through whilst ensuring that the cellulose matrix did not become dry. Flow through drops were collected on a slide to confirm the presence of purified sporozoites by microscopy. When the last millilitres of the sporozoites in eluting solution had reached the DE-52 sediment, a further 20 ml of eluting solution was added. This was continued up to a further two times, depending on whether sporozoites were still leaving the column and whether contaminating debris appeared.

2.4. **Assessment of temporal dynamics of anterior refractile body loss**

2.4.1. **Preparation of 0.2 M phosphate buffer stock solution**

Solution A was prepared by dissolving 69 g NaH_2PO_4 in 500 ml ddH_2O. Solution B was prepared by dissolving 8.9 g Na_2HPO_4 in 250 ml ddH_2O. Twenty-three-point-four ml of solution A was mixed with 91.5 ml of solution B and NaOH was added until the solution was pH 7.4. Double-distilled water was added up to 500 ml.

2.4.2. **Preparation of 10% formaldehyde solution**

Ten percent formaldehyde solution was prepared by adding 1 g of paraformaldehyde (PFA, 95% - Sigma-Aldrich, Merck) to 10 ml of ddH_2O. This was placed on a stirring hot plate, heated to 60^0C, and mixed using a magnetic stirrer. Three drops of 1 M NaOH were added using a 1 ml Pasteur pipette (Agar Scientific). Once all paraformaldehyde powder appeared to have dissolved, formaldehyde solution was filtered using a 10 ml syringe and 0.22 μm pore filter (Millex, Millipore).

2.4.3. **Preparation of 4% buffered formaldehyde**

Two millilitres of 10% formaldehyde was added to 5 ml 0.2 M phosphate buffer and topped up to 10 ml with ddH_2O.

2.4.4. **In vitro *E. tenella* infections for light microscopy of fixed cells**

Zero point two millilitres of cell-culture media, containing 100,000 MDBK cells, were deposited onto sterilised coverslips (13 mm diameter borosilicate coverglass - Agar scientific) within cell-culture-plate wells (24 well plate - Costar). Cells were left to settle for 15 min before an additional 0.3 ml of cell-culture media was added. Seeded cells were then incubated at 38˚C with 5% CO_2 for two to three hours. Purified sporozoites were suspended in cell-culture medium and added to the MDBK-cell seeded coverslips at a ratio of 0.5 sporozoites per MDBK cell. Infected monolayers were incubated in 0.5 ml of cell-culture media at 41˚C, 5% CO_2.

2.4.5. **Temporally-staggered fixation of MDBK/sporozoite samples**

Thirty minutes after the addition of sporozoites to MDBK cells, all wells were washed with fresh cell-culture medium and returned to incubation at 41˚C, 5% CO_2. At intervals of 30 min, 1 hr, 2 hr, 3 hr, 4 hr and 5 hr post infection, the wells were fixed by adding 4% buffered formaldehyde. Cells were incubated in fixative for 10 min at room temperature before being washed in 0.1 M phosphate buffer.

2.4.6. **Preparation of Nile red stock solution**

Zero-point-one gram of Nile red (Nile red powder 99% - ACROS Organics, Thermo Fisher) was dissolved in 50 ml of acetone and stored in the dark.

2.4.7. **Preparation of Hoechst stock solution**

Five milligrams of Hoechst (98% bisBenzimide H 33342 trihydrochloride – Sigma-Aldrich, Merck) were dissolved in 1 ml of ddH_2O and stored at -20^0C.

2.4.8. Nile red[4] and Hoechst[5] staining

For infected-monolayer samples, washes and incubations were all carried out within the cell-culture plates. For sporozoite-only samples, washes and incubations were performed in a 1.5 ml micro-centrifuge tube with 2 min of centrifugation (~ 800 RCF) between each step. Each wash step was performed for 5 min.

Fixed cells were washed three times in 0.1 M phosphate buffer, incubated for 10 min in 2 % buffered glycine (≥ 99.7% glycine – Millipore, Merck, dissolved in 0.1 M phosphate buffer) and washed a further three times in 0.1 M phosphate buffer. Cells were stained with 5 µl of Nile red stock solution in 1 ml of 0.1 M phosphate buffer for 15 min in the dark. Cells were washed three times in 0.1 M phosphate buffer then stained with 1 µl Hoechst stock solution in 1 ml of 0.1 M phosphate buffer for 15 min in the dark. Cells were washed a further six times in 0.1 M phosphate buffer.

2.4.9. Quantification of anterior refractile body presence

Fixed and stained samples were transferred to microscope slides with a drop of mounting medium (Vectashield antifade mounting medium - Vector Laboratories, Maraval LifeSciences). Slides were viewed using a widefield fluorescence microscope (AxioImager, Zeiss). Visualisation of Nile red signal was achieved using excitation light of wavelength 559 nm and detection of emission light of wavelength 636 nm. Slides were scanned in the standard zig-zag method. Each intracellular parasite was assessed for the presence or absence of an anterior refractile body until between 100 and 200 parasites were reached. Manipulation of focal height was performed when viewing each sporozoite to confirm that it resided within a host cell.

For visualisation of host-cell nuclei, light with a wavelength of 352 nm was used for excitation and emitted light at a wavelength of 455 nm was detected.

2.5. Assessment of refractile body dynamics in live cells

2.5.1. Assessment of Nile red toxicity in live cells

The effect of Nile red staining in living cells was assessed prior to investigation of refractile body dynamics using live cell light microscopy. This was to ensure that the presence of Nile red had no deleterious effect on the dynamics of anterior refractile body loss.

Nile red stock solution (2 mg/ml Nile red in acetone) was added to six microcentrifuge tubes, each containing 1 ml acetone, to create a series of dilutions containing 10 µg/ml, 20 µg/ml, 100 µg/ml,

[4] Nile red staining was used to improve visualisation of the refractile body organelles. Nile red is a lipophilic stain with fluorescent properties when present in a lipid-rich environment and was shown to selectively stain the refractile bodies of *Eimeria* species parasites (Hamid et. al. 2015).

[5] Hoechst specifically labels DNA (Darzynkiewicz et. al. 2004) and staining was used to highlight nuclei of the host cells.

200 µg/ml, 1000 µg/ml and 2000 µg/ml Nile red. Thirty minutes after performing *in vitro* infection of MDBK cells (see section 2.5.4), 25 µl of the Nile red dilutions were each added to individual culture-wells. For control samples, 25 µl of either water or acetone were added in the place of Nile red. The resulting wells, each containing MDBK cells, sporozoites and Nile red in the concentration of 0.5 µg/ml, 1 µg/ml, 5 µg/ml, 10 µg/ml, 50 µg/ml or 100 µg/ml (with 0 µg/ml Nile red in controls) were incubated at 41˚C, 5% CO_2. Four and a half hours after the addition of Nile red or control solution, medium was removed and 1 ml of 4% formaldehyde in 0.1 M phosphate buffer was added. After 10 min at room temperature, formaldehyde solution was removed, and wells were stained with both Nile red and Hoechst as described in section 2.4.8. The proportion of parasites possessing anterior refractile bodies in each condition was assessed using the methods described in section 2.4.9.

2.5.2. **Live cell imaging of anterior refractile body loss**

For light microscopy of living cells, 500,000 MDBK cells in 0.5 ml of cell-culture media were added to each well of a µ-Slide 2-well chambered coverslip (Ibidi). MDBK cells were incubated for one hour at 38˚C, 5% CO_2. Five-hundred-thousand freshly-purified sporozoites (see section 2.3 for sporozoite purification) in 0.5 ml of cell-culture media were added to each well. Sporozoites and MDBK cells were incubated for one hour at 41˚C, 5% CO_2. The µ-Slide was then placed onto the stage of a confocal microscope (LSM 880 AxioObserver – Zeiss) which was set at 41˚C, 5% CO_2. Fifty microlitres of 200 µg/ml Nile red in acetone were added to each well. Fluorescence imaging was performed using continuous z-stack acquisition encompassing all cell-containing focal planes. Images were acquired for both differential interference contrast (DIC) and fluorescence, using excitation light of wavelength 559 nm and detection of emitted light at wavelength 636 nm. Imaging was performed using either a 40x objective (experiment 1) or a 63x objective (experiment 2). For data collected at 40x, voxel size was 0.42 µm x 0.42 µm x (1-2) µm. For data collected at 63x, voxel size was 0.26 µm x 0.26 µm x 0.59 µm. Each field of view was imaged for a maximum of 15 min to minimise thermal damage to the cells.

2.6. **Pharmacological inhibition of actin**

2.6.1. **Preparation of actin-inhibitor stock solutions**

To create Cytochalasin D (CytoD) 1 mM stock solution, 1.97 ml of DMSO was added to a 1-mg vial of CytoD (Tocris) and shaken until all powder was dissolved.

To create Latrunculin A (LatA) 1 mM stock solution, 0.237 ml of DMSO was added to a 100-µg vial of LatA (Tocris) and shaken until all powder was dissolved.

2.6.2. **Culture of *E. tenella* in the presence of actin inhibitors**

Thirty thousand MDBK cells in 0.3 ml cell culture media were seeded onto sterilised 13 mm glass coverslips within wells of a 24-well cell culture plate. Madin Darby Bovine Kidney cells were incubated for one- to two- hours at 38˚C, 5% CO_2. Five million freshly-excysted and purified sporozoites, each in 1 ml cell culture medium, were added to the MDBK-cell-containing culture wells. Sporozoites and MDBK cells were incubated at 41˚C, 5% CO_2 for 30 min. Medium was removed from each well to remove extracellular sporozoites and replaced with 1 ml fresh cell culture medium. Aliquots of CytoD stock solution were diluted in DMSO to create one working solution with a concentration of 200 µM CytoD and one working solution with a concentration of 40 µM CytoD. Aliquots of LatA stock solution were diluted in DMSO to create one working solution with a concentration of 100 µM LatA and one working solution with a concentration of 40 µM LatA. Five microlitres of each CytoD or LatA working solution were added to individual wells containing sporozoites and MDBK cells in 1 ml cell culture medium. Experimental treatment conditions thus consisted of 1 µM CytoD, 200nM CytoD, 500nM LatA and 200nM LatA. Five microlitres of DMSO were added to additional wells (containing sporozoites and MDBK cells) as a control. Following treatment, samples were incubated for a further 4.5 hr at 41˚C and 5% CO_2 then fixed in 4% formaldehyde.

2.6.3. **Preparation of Phalloidin[6] 488 stock solution**

Three-hundred units of Phalloidin 488 (Alexa Fluor™ 488 Phalloidin - Invitrogen) were dissolved in 1.5 ml of methanol to create a 6.6 µM stock solution. Stock solution was stored at -20^{0}C and protected from light.

2.6.4. **Phalloidin 488, Nile red and Hoechst staining**

In vitro infection samples, prepared and fixed as described in section 2.6.2, were washed three times in 0.1M phosphate buffer for 5 min each. Cells were incubated for 15 min in one-part Triton X – 100 (Sigma) diluted in 1,000 parts 0.1 M phosphate buffer. They were then washed three times in 0.1M phosphate buffer for 5 min each. Cells were incubated in 1% glycine dissolved in 0.1 M phosphate buffer for 10 min then washed three times in 0.1M phosphate buffer for 5 min each. Cells were incubated in 10 µl of Phalloidin 488 stock solution and 400 µl of 0.1 M phosphate buffer for 45 min. Cells were washed three times in 0.1M phosphate buffer for 5 min each then incubated in 5 µl of Nile red stock solution and 1000 µl of 0.1 M phosphate buffer for 15 min. Cells were washed three times in 0.1M phosphate buffer for 5 min each then incubated in 1 µl of Hoechst stock solution and

[6] Phalloidin molecules conjugated to a fluorescent dye, such as AlexaFluor™ 488, can be used to specifically label filamentous actin in fixed cells (Peterson and Mitchison 2002).

1000 µl of 0.1 M phosphate buffer for 15 min. Cells were then washed a further six times in 0.1M phosphate buffer for 5 min each.

2.6.5. **Assessment of refractile body loss and host-cell actin morphology following actin inhibition**

Quantification of anterior refractile body presence in actin-inhibitor treated sporozoites was performed as described in section 2.4.9.

To visualise host-cell actin morphology, samples were concurrently imaged using excitation light of wavelength 493 nm with detection of emitted light at wavelength 517 nm.

2.7. **Sample preparation for electron microscopy**[7]

2.7.1. **Preparation of 0.2 M cacodylate buffer**

Twenty-one-point-four grams of sodium cacodylate powder (TAAB) were added to 400 ml of ddH_2O. Drops of 0.1 M HCl were added until the solution was at pH 7.4. The solution was topped up to 500 ml using ddH_2O.

2.7.2. **Preparation of primary fixative solution**

Two millilitres of freshly-prepared 10% formaldehyde solution (see section 2.4.2 for details), 1 ml of 25% electron microscopy grade glutaraldehyde (TAAB), 5 ml of 0.2 M sodium cacodylate buffer and 2 ml of ddH_2O were all added to a 10 ml centrifuge tube (Falcon, Corning).

2.7.3. **Preparation of 2% uranyl acetate**

Zero-point-four grams of uranyl acetate (Agar Scientific) were added to 20 ml of ddH_2O in a light-shielding container. The mixture was sonicated for 30 min to facilitate dissolution.

2.7.4. **Preparation of 4% osmium tetroxide**

A glass ampule containing 25 mg of osmium tetroxide (TAAB) was placed into a beaker of hot water to facilitate removal of the adhesive label. The outer label was removed, and the ampule was cleansed by wiping with a paper towel soaked in acetone. The ampule neck was snapped, and both pieces of glass were dropped into a glass stoppered container. Six-point-seven-five millilitres of ddH_2O were added into the vial by pipette. The stoppered container was sealed and sonicated for 30 min then left overnight to allow all osmium tetroxide to dissolve.

[7] All procedures involving aldehydes, cacodylate powder, osmium tetroxide, thiocarbohydrazide, uranyl acetate, solvents or resins were performed in a chemical fume hood equipped with the appropriate filter and all waste contaminated with these chemicals was disposed of in accordance with health and safety regulations.

2.7.5. **Preparation of 3% potassium ferrocyanide**

Zero-point-three grams of potassium ferrocyanide (AnalaR, VWR) were added to 10 ml of 0.2 M cacodylate buffer and mixed to dissolve.

2.7.6. **Preparation of 1% thiocarbohydrazide**

Thiocarbohydrazide solution was made just before use. One hundred milligrams of thiocarbohydrazide (Sigma-Aldrich) were added to 10 ml ddH_2O in a conical glass flask. After covering the top of the flask with foil, the mixture was heated to 60˚C for 1 hr and swirled every 10 min to aid dissolution.

2.7.7. **Single osmium processing of free sporozoites for electron microscopy**

2.7.7.1. **Primary fixation and osmium impregnation**

Freshly purified sporozoites were suspended in 1 ml of primary fix within a 1.5 ml microcentrifuge tube (Camlab plastics). Sporozoites were left in primary fixative for two hours at 4˚C. Fixed cells were washed five times in 0.1 M cacodylate buffer (made by diluting one-part 0.2 M cacodylate buffer in one-part ddH_2O) for 10 min each. Cells were pelleted by centrifugation for 2 min (~ 800 RCF) between each wash. Cells were incubated in 500 µl of 4% osmium tetroxide and 500 µl of 0.2 M cacodylate buffer for 60 min at 4ºC.

2.7.7.2. **Uranyl acetate staining, dehydration and resin embedding**

Following five washes in ddH20 for 10 min each (2 min centrifugation between each wash), cells were added to 1 ml molten 3% agarose (2-Hydroxyethyl agarose – Sigma-Aldrich, dissolved in ddH_2O by bringing to the boil in the microwave) in a 1.5 ml microcentrifuge tube and immediately centrifuged (2 min, ~ 10,000 RCF). Agarose and cells were transferred to 4ºC for 5 min to set. Approximately 1 mm^3 blocks were cut from the part of the agarose containing cells (this can be seen by eye due to sporozoite blackening from osmium impregnation). Cells and agarose blocks were incubated in freshly-filtered 2% uranyl in the dark at 4^0C overnight. Cells were washed three times in ddH20 for 10 min each then dehydrated by a series of 20 min incubations in acetone/ddH_20 solutions. Dehydration steps consisted of 30% acetone, 50% acetone, 70% acetone, 90% acetone, and three changes of 100% acetone. Acetone used for the final incubation was taken from a bottle of anhydrous acetone stored in contact with a molecular sieve. Cells were incubated for 2 hours in 25% epoxy resin (TAAB 812 resin premix kit, hard – prepared according to manufacturer's instructions) in acetone. Cells were then incubated in 50% resin in acetone overnight; 75% resin in acetone for six hours; 100% resin overnight and two changes of 100% resin for two hours each. Resin-infiltrated

pellets were embedded in embedding capsules (Beem capsules™) with fresh 100% resin and polymerised by incubation at 60˚C for 24 hours.

2.7.8. **Double osmium processing of free sporozoites for electron microscopy**

Cells were suspended in 1 ml of primary fix within a 1.5 ml microcentrifuge tube and left for two hours at 4˚C. Fixed cells were washed five times in 0.1 M cacodylate buffer for 10 min each, pelleting by centrifugation for 2 min (~ 800 RCF) between each wash. Cells were incubated in 500 µl of 3% potassium ferrocyanide in 0.2 M sodium cacodylate buffer, 250 µl of 4% osmium tetroxide and 250 µl of ddH_2O for 60 min at 4^0C. Following five washes in ddH20 for 10 min each (2 min centrifugation between each wash), sporozoites were incubated in 500 µl of 4% osmium tetroxide and 500 µl of ddH_2O for 60 min at 4^0C. From this point onwards, samples were processed according to the procedures described in section 2.7.7.2.

2.7.9. **Reduced double osmium and thiocarbohydrazide (ROTO) processing free sporozoites for electron microscopy**

Freshly purified sporozoites were suspended in 1 ml of primary fix within a 1.5 ml microcentrifuge tube. Sporozoites were left in primary fixative for two hours at 4˚C. Fixed cells were washed five times in 0.1 M cacodylate buffer for 10 min, pelleting by centrifugation for 2 min (~ 800 RCF) between each wash. Cells were incubated in 500 µl of 3% potassium ferrocyanide in 0.2 M sodium cacodylate buffer, 250 µl of 4% osmium tetroxide and 250 µl of ddH_2O for 60 min at 4^0C. Following five washes in ddH20 for 10 min each (2 min centrifugation between each), sporozoites were incubated in freshly made, filtered, 1% thiocarbohydrazide for 20 min under rotation. Following five washes in ddH20 (2 min centrifugation between each), sporozoites were incubated in 500 µl of 4% osmium tetroxide and 500 µl of ddH_2O for 30 min. From this point onwards, samples were processed according to the procedures described in section 2.7.7.2.

2.7.10. **Preparation of infection samples (sporozoites and MDBK cells) for analysis by electron microscopy**

Infections lasting for less than 10 hr. One millilitre of cell-culture medium containing 0.35 x 10^6 MDBK cells was added to wells of a 24 well culture plate. Cells were left to settle for up to 3 hr at 38 ^{0}C, 5% CO_2, prior to infection with sporozoites. Freshly-purified sporozoites were pelleted by centrifugation at ~ 600 RCF for 10 min and re-suspended in cell-culture medium at a concentration of 3.5 million sporozoites per ml. One millilitre of sporozoite suspension was added to each MDBK-cell containing well.

Infections lasting for more than 10 hr. One millilitre of cell-culture medium containing 0.35 x 10^6 MDBK cells was added to wells of a 24 well culture plate. Cells were left to settle for up to 3 hours at 38 ^{0}C, 5% CO_2, prior to infection with sporozoites. Freshly-purified sporozoites were pelleted by

centrifugation at ~ 600 RCF for 10 min and re-suspended in cell-culture medium at a concentration of 350,000 sporozoites per ml. One millilitre of sporozoite suspension was added to each MDBK-cell containing well.

2.7.11. **Processing of infection samples (except the 2.5hr infection sample)**

One-hundred microlitres of 25% electron microscopy grade glutaraldehyde were added to infection samples growing in 1 ml of cell-culture medium. Fifteen minutes after the addition of glutaraldehyde, cell-culture medium was removed and replaced by 1 ml of primary fix. Monolayers were washed five times in 0.1 M cacodylate buffer followed by a 60 min incubation in 500 µl of 4% osmium tetroxide and 500 µl of 0.2 M sodium cacodylate buffer. Fixed cells were washed five times in ddH_2O followed by an overnight incubation in 2% freshly-filtered aqueous uranyl acetate (at 4˚C and in the dark). Cells were washed three times in ddH20. Cells were then dehydrated by a series of 20 min incubations in increasing concentration of ethanol in ddH_20. Dehydration steps consisted of 30% ethanol, 50% ethanol, 70% ethanol, 90% ethanol, and 100% ethanol. One millilitre of propylene oxide (TAAB) was added to each well and left for 30 seconds. Agitating the solution using a Pasteur pipette resulted in detachment of the monolayer which could then be transferred to a 1.5 ml micro-centrifuge tube. Detached monolayers were then incubated in three changes of 100% anhydrous acetone, each for 10 min. Cells were incubated in 25% TAAB 812 resin in acetone for two hours, 50% resin overnight; 75% resin for six hours; 100% resin overnight and two changes of 100% resin, each for two hours. Infected-monolayer pellets were centrifuged for 20 min in fresh 100% resin and polymerised by incubation at 60˚C for 24 hours.

2.7.12. **Processing of the 2.5hr infection sample**

For the sample fixed at 2.5 hr post-infection, MDBK cells were detached from the culture-plate by incubation with 0.25% trypsin (2-3 min at 41^0C) and transferred to a 1.5 ml microcentrifuge tube prior to the addition of fixative. Subsequent processing was performed according to the double osmium protocol described in section 2.7.7.2.

2.8. **Section production for electron microscopy**

2.8.1. **Glass knife preparation**

Glass knives were made from glass rods (6 mm x 25.4 mm x 406 mm - Leica). Glass rods were split to form triangular knives with a glass knife maker (Boeckeler™ by RMC™) used according to the manufacturer's instructions. Section-collecting boats (6.4 mm, Electron Microscopy Sciences) were attached via superglue (Loctite) to glass knives designated for semi-thin section collection.

2.8.2. **Semi-thin section assessment**

Following polymerisation, the resin-embedded samples were removed from their moulds and any extra resin overlying the cells or tissue was shaved off with a razor blade. The shaved surface was then trimmed with a non-boated glass knife, using a PowerTome™ ultramicrotome (Boeckeler™ by RMC™). The knife angle was set to 6˚ and ~1 µm manual advances were made until the surface of the sample was level. The sample was then trimmed to form a quadrilateral-shaped block face, ~3-5 mm^2 in size. Sections of 800 nm thickness were cut by ultramicrotome with a boated glass knife filled with ddH_2O. A human eyelash tool (own eyelash attached to a cocktail stick using nail varnish) was used to transfer a section into a drop of ddH_2O on a glass microscope slide. The slide was left on a hot plate for ~5 min until the section had adhered.

A drop of 1% toluidine blue in 2% aqueous borax solution (obtained pre-prepared by Dr Louise Hughes, Oxford Brookes University) was added to the dried section and incubated on the hot plate for ~ 30 seconds. The slide was rinsed with water and left to dry before examination by bright-field light microscopy. After identifying an area of interest by microscopy, the block face was trimmed around the area of interest until the cutting-face was ~ 1 mm^2.

2.8.3. **Ultrathin section collection for transmission electron microscopy**

The trimmed block-face was sectioned by ultramicrotomy using a diamond knife (3 mm cutting-edge 35˚ wet ultra Diatome™ diamond knife). Microtome advance was set at 70 nm with a cutting speed of 1 mm/second and the knife boat was filled with ddH2O plus a single drop of 100% ethanol. Prior to section collection, an open bottle of chloroform was held next to the sectioning boat until sections were seen to stretch. A copper grid (TAAB G200) was pushed under the floating sections and lifted out of the water so that the resin sections became attached to the surface of the grid.

2.8.4. **Formvar coating of slot grids for three-dimensional transmission electron microscopy**

A glass slide (SuperFrost™, Thermo Fisher) was dipped into 0.5% formvar (TAAB) dissolved in choloroform (AnalaR, VWR) for ~1 second before it was pulled out quickly and steadily and held just above the chloroform for a few seconds before putting aside to dry. A rectangle was scored into the formvar layer which aids release of the formvar from the glass slide. The slide was then slowly lowered into a tub of ddH_2O so that the formvar layer floated off onto the water. Floating formvar appeared as a silvery-gold film. Three-millimetre copper slot-grids (Gilder) were dropped onto the floating formvar. The coated grids were collected onto a paper-label-covered microscope slide; using a scooping motion so that the formvar ended up on top of the grids. Once the formvar-coated grids were dry, a razor blade was used to detach the grids from surrounding formvar film.

2.8.5. **Serial-section collection for three-dimensional transmission electron microscopy**

The trimmed resin-embedded sample block-face was further trimmed until the height of the cutting-face was ~ 0.1 mm. The block-face was then sectioned by ultramicrotomy using a diamond knife; microtome advance was set at 150 nm or 200 nm (for serial section transmission electron tomography) or 70 nm (for serial section transmission electron microscopy) with a cutting speed of 1 mm/second. Ribbons of between 4 and 30 sections were lined up against a human hair that ran across the surface of the water and was attached to the diamond knife by adhesive tape. Sections were collected onto formvar-coated copper slot grids using the human hair to help line them up with the centre of the slot.

2.9. **Heavy metal staining of ultrathin sections**

2.9.1. **Preparation of Reynolds lead citrate**

One-point-three-three grams of lead nitrate (AnalaR, VWR) and 1.76 g of trisodium citrate (Fisher Scientific) were added to 30 ml of freshly-boiled ddH_2O in a glass stoppered container. The mixture was left for 30 min, shaking approximately every 5 min. One gram of NaOH was added to 25 ml of freshly-boiled ddH_2O. Five millilitres of the NaOH solution were added to the lead nitrate and trisodium citrate mixture. Drops of the NaOH solution were added to the lead citrate solution until the solution was pH 12.

2.9.2. **Uranyl acetate and lead staining**

Section-containing copper grids were placed section side down onto a drop of freshly filtered 2% uranyl acetate (see section 2.7.3 for preparation of uranyl acetate solution) on a sheet of parafilm for 15 min and covered from light. Grids were rinsed by dunking 20 times in a beaker of warm, pre-boiled ddH_2O, before resting on a drop of ddH2O. Water was drained from the grids by touching each grid to a piece of filter paper (Whattman) and grids were incubated for 5 min on a drop of freshly-filtered Reynolds lead citrate which was covered by a petri dish and surrounded by 5-7 pellets of NaOH. Grids were then rinsed by dunking 20 times in a beaker of warm, pre-boiled ddH_2O, before resting on a drop of ddH2O. Water was drained from the grids by touching each grid to a piece of filter paper. For the grids prepared for use by transmission electron tomography, grids were then placed onto drops of 10 nm unconjugated colloidal gold in H_2O (BBI Solutions) for 5 min and water was drained by touching to a piece of filter paper. Staining with colloidal gold was performed for both the front and reverse sides.

2.10. Transmission electron microscopy imaging

2.10.1. Transmission electron microscopy image acquisition

All two-dimensional electron microscopy imaging was performed using a Hitachi™ H-7560 transmission electron microscope with bottom mount camera (2k CCD, Advanced Microscopy Techniques) and manual tilt and rotation capabilities. Digital images were captured using either 1 or 4 integrations depending on sample stability.

2.10.2. Transmission electron tomography image acquisition

Transmission electron tomography was performed using one of several transmission electron microscopes: H-7560 (Hitachi™), Spirit (Tecnai™, FEI™/Thermo Fisher Scientific™) or Talos™ (FEI™/Thermo Fisher Scientific™). Sections cut at 150 nm thickness were generally used when operating at 120 kilovolts (kV) (Hitachi™ H-7560 or Tecnai™ Spirit electron microscopes); sections of 150 nm-200 nm thickness were used when operating at 200 kV (FEI™ Talos™ electron microscope). As the Hitachi™ H-7560 microscope was not compatible with automated tomography data-acquisition software, manual centring, focusing and adjustment of tilt angles were performed prior to collection of each image. Tomogram tilt series generated using the Hitachi™ H-7560 electron microscope were taken from -60˚ to +60˚ with intervals of +1˚. For tomography data acquisition using the Tecnai™ Spirit electron microscope, automated centring, focus adjustment, tilt setting, and image capture were performed through Xplore*3D*™ software by FEI™. For tomography data acquisition using the FEI™ Talos™ electron microscope, automated centring, focus adjustment, tilt setting, and image capture were performed using DigitalMicrograph™ (Gatan™) with SerialEM™ plug-in (Mastronarde, October 2005). Regardless of microscope used, dual axis tomograms were collected by rotating the grid by 90˚ and repeating the tilt series image collection.

2.10.3. Tomogram generation and structure segmentation

Tomogram image data series were processed using IMOD™ software (University of Colorado, Boulder) which was run through Cygwin™ command line interface. Data processing was performed as described in the IMOD tutorial videos created by the Mastronarde Group of the University of Colorado (these can be found by searching for the 'BL3DEMC' channel at youtube.com™). In brief, image series were converted to .mrc files using the command 'tif2mrc'; these were loaded into ETOMO™ (part of IMOD™ software) where they rough-aligned using automated image-processing algorithms. Fine-alignment was then performed using semi-automated adjustments involving fiducial-marker tracking. Tomogram generation was achieved using a back-projection algorithm. Serial tomograms, generated from imaging of serial resin-sections, were initially aligned using automated adjustments to rotation and translation and then manually transformed by matching of image overlays.

Structure segmentations (digital image partitioning) were performed using IMOD™ software. Conoid fibres were segmented with the help of the slicer window. X, Y and Z parameters were set so that the plane in view showed a sagittal cut through the selected fibre. A series of 'open contour' points were placed along the fibre and adjustments to X, Y and Z allowed the viewing plane to remain sagittal to the fibre whilst following along its helical trajectory. Globular objects, such as micronemes and rhoptries, were segmented using a series of closed contours. Depending on the size and complexity of the object, a new contour was added every one, to every 20, tomogram sections. Quantitative morphometric data was calculated as an average of two or more measurements. Measurements were generated using 'imodinfo' commands.

2.11. Serial block face scanning electron microscopy (SBF-SEM) imaging

2.11.1. SBF-SEM image acquisition

Serial block face – scanning electron microscopy (SBF-SEM) data was collected using a Zeiss™ Merlin scanning electron microscope with Gatan™ 3View™ automated sectioning and image capture system. Operation of the SBF-SEM system was performed by Dr Louise Hughes (Oxford Brookes University). Prior to imaging, samples were trimmed to ~1 mm^3 and mounted on 3view sample pins using an epoxy conductive adhesive from Circuitworks™. After insertion of the mounted block, the intra-microscope diamond-knife was advanced towards the block-face by 200 nm cutting-strokes until sectioning of the block face was observed. The block-face was then imaged using a scanning electron beam with 3-5 kV accelerating voltage. Electron signal was detected using a back-scatter electron detector (OnPoint, Gatan) and nitrogen gas was injected to raise chamber pressure to 30pa. A further 10 sections were cut at 100 nm before fine adjustments to magnification, focus and astigmatism were made. The SBF-SEM run was then initiated. Pixel size was between 3-7 nm with a section thickness from 60-100 nm. Dwell time was approximately two seconds per pixel with a scan area of around 4,000 x 4,000 pixels. Completed SBF-SEM data sets contained anywhere from 50 – 500 sections.

2.11.2. SBF-SEM data processing and structure segmentation

SBF-SEM data was processed using IMOD™ software, run through Cygwin™ command line interface. Image files were converted from .dm4 format to .mrc data stacks. Voxel size was adjusted in Z to reflect the slice thickness used, via the command 'alterheader'. Data was binned once (combining adjacent pixels to reduce the file size) and floated (scaling pixel values to a common mean and standard deviation) using 'newstack' commands and smoothed (averaging of pixels with their neighbours) and flipped using 'clip' commands. The image stack was then subject to automated alignment through the IMOD™ Etomo interface. Regions of interest were identified and trimmed using the command 'trimvol'.

2.12. **Statistical analysis**

Statistical analysis was performed using IBM™ SPSS™ version 25 software. Following appropriate numerical coding of data (where necessary) variables were assigned as either scale, nominal or ordinal type. Prior to testing for statistically-significant association between a continuous variable and a categorical variable, the distribution of the continuous variable in each of the categories was assessed. Histograms for each group were produced and visually determined as being either of normal or of skewed distribution. If normally distributed, parametric tests were subsequently used, if not-normally distributed then non-parametric tests were used. A t-test was used to test for an association between a continuous variable and a binary categorical variable where there was normal distribution for both groups. If testing for an association between a continuous variable and a binary categorical variable where one or both groups did not show normal distribution, the Mann-Whitney U test was used. If dealing with a continuous variable and a categorical variable with more than two groups, where the continuous data was normally distributed for all the groups, One-Way ANOVA was used followed by a post-hoc Turkey HSD test. If there was a continuous variable and a categorical variable with more than two groups, where data within at least one of the groups was not normally distributed, then the Kruskal-Wallis test was used. The Chi-squared test was used when assessing for a statistically significant association between two categorical variables.

3. Quantitative analysis of sporozoite morphometrics and development

3.1. Introduction

A primary aim of this project was to quantify the subcellular morphology of the *E. tenella* sporozoite. This required three-dimensional imaging of multiple cells with imaging resolution of ~100 nm or finer.

With advances in technology, x-ray, light and electron microscopy can all be used to investigate three-dimensional biological structures at sub-100 nm resolution. Both X-ray tomography and three-dimensional electron microscopy techniques can resolve subcellular structures. An advantage of using x-rays is that they can penetrate up to several microns, allowing entire cells to be imaged without the need for sectioning. However, the resolution achieved by x-ray imaging is still inferior to that of electron microscopy (Bushong et. al. 2015) meaning that the identification and segmentation of smaller organelles proves challenging (Parkinson et. al. 2008). For these reasons, three-dimensional electron microscopy is currently the only technique suitable for quantitatively characterising the subcellular morphology of sporozoites. Serial block face – scanning electron microscopy (SBF-SEM) is a novel three-dimensional electron microscopy technique that can be used to generate data with <5 nm lateral resolution and <100 nm axial resolution. Biological specimens stained with heavy metals and imaged by SBF-SEM, show enough contrast between subcellular compartments to distinguish various organelles. In addition, SBF-SEM can be used to image tens or even hundreds of cells with relatively little time or technical difficulty (Denk and Horstmann 2004).

3.2. Approach and method development

3.2.1. Optimisation of sample processing for the investigation of *E. tenella* ultrastructure

Eimeria species have not previously been imaged using SBF-SEM. To investigate whether individual organelles of *E. tenella* can be resolved by SBF-SEM imaging, I initially tested a sample containing both Madin-Darby Bovine Kidney (MDBK) cells and *E. tenella* sporozoites, fixed at 2.5hr post infection (Fig. 3.1). The sample was processed using a double osmium staining protocol, based on the method described by Starborg et. al. (2013), which was previously used for samples containing Trypanosoma species that were successfully imaged via SBF-SEM (Sue Vaughan, personal communication). Imaging was performed with lateral resolution of 7.1 nm and axial resolution of

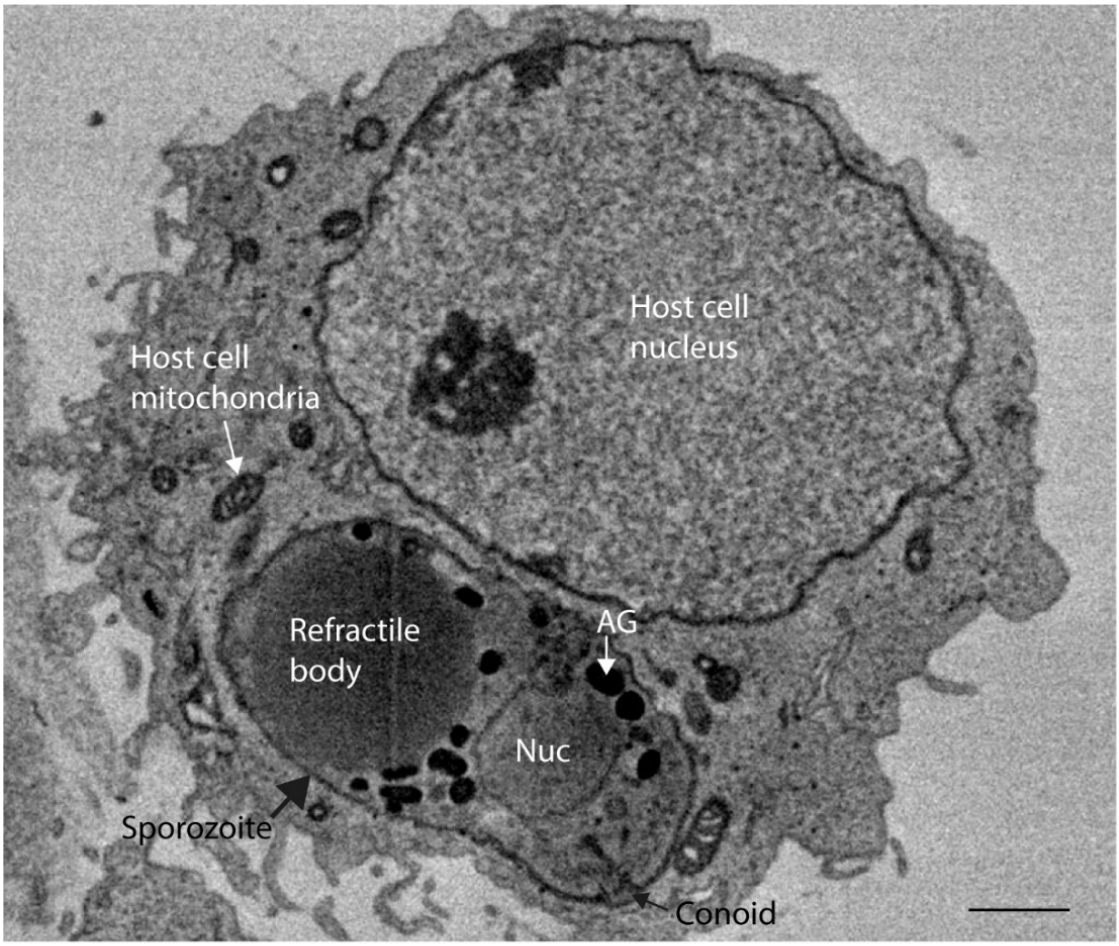


Figure 3.1. Sporozoite and host cell ultrastructures visualised by SBF-SEM.

A single section of SBF-SEM data following imaging of sporozoites and host cells fixed at 2.5 hr post infection and processed using the double osmium protocol. In the host cell, mitochondria and nucleus can be seen. A single sporozoite is contained within the host cell. Sporozoite structures including the nucleus, conoid, amylopectin granules (AG) and refractile bodies can be resolved. Scale ~1μm.

100 nm. The results of this pilot showed that both host-cell and parasite architecture could be resolved (Fig. 3.1). However, the microneme secretory organelles were difficult to distinguish from the surrounding cytoplasm.

To test whether adjusting the sample preparation would enable the resolution of apical organelle structures, three different processing protocols were tested on a sample of freshly-excysted (extracellular) *E. tenella* sporozoites. These were:

a) Single osmium

b) Double osmium (as performed on the 2.5hr post infection sample)

c) Reduced double osmium and thiocarbohydrazide (ROTO).

Variations of the single osmium protocol have been used extensively for imaging *Eimeria* sporozoites by transmission electron microscopy (TEM) (Jensen and Hammond 1975, Roberts et. al. 1970, 1971, Smith and Strout 1980). The ROTO protocol is specifically designed for generating high contrast samples and has been successfully used for other protozoan samples imaged by three-dimensional SEM (Sakaguchi et. al. 2016, Schneider et. al. 2017, Vidal et. al. 2016). For SBF-SEM imaging, sample preparation involving high amounts of heavy-metal impregnation, such as the ROTO protocol, are generally preferred over protocols involving lower amounts of heavy-metal impregnation, such as the single osmium protocol. This is because samples containing large amounts of atoms with high atomic mass are less susceptible to charge build-up and subsequent sample damage or data interference when imaged using scanning electron microscopy (Friedman and Ellisman 1981, Tapia et. al. 2012). Transmission electron microscopy was used to screen the samples and assess which of the three protocols would be most suitable for further investigation by SBF-SEM.

Nuclei, refractile bodies and acidocalcisomes were well visualised in all three samples (Fig.3.2A-D, G-H, K-L; Fig.3.3A-D, G-I, L-M; Fig.3.4A-D, G-H, K-L). Of the three protocols tested, sample preparation using the single osmium protocol resulted in the greatest contrast between apical secretory organelles (micronemes and rhoptries) and surrounding cytoplasm (Fig.3.2M-R). Apical organelles were also visible in samples prepared using the double osmium protocol, however microneme and rhoptry contents were of a similar density to that of the surrounding cytoplasm (Fig.3.3N-R). In samples prepared using the ROTO protocol, micronemes were generally indistinguishable from the surrounding cytoplasm (Fig.3.4M-N). Highly electron opaque structures resembling rhoptries could still be seen (Fig.3.4Q-R, arrowheads). Mitochondria were most contrasted in the ROTO-prepared sample (Fig.3.4I-J) and amylopectin granules were best visualised in the single osmium sample (Fig.3.2E-F) or double osmium sample (Fig.3.3E-F).

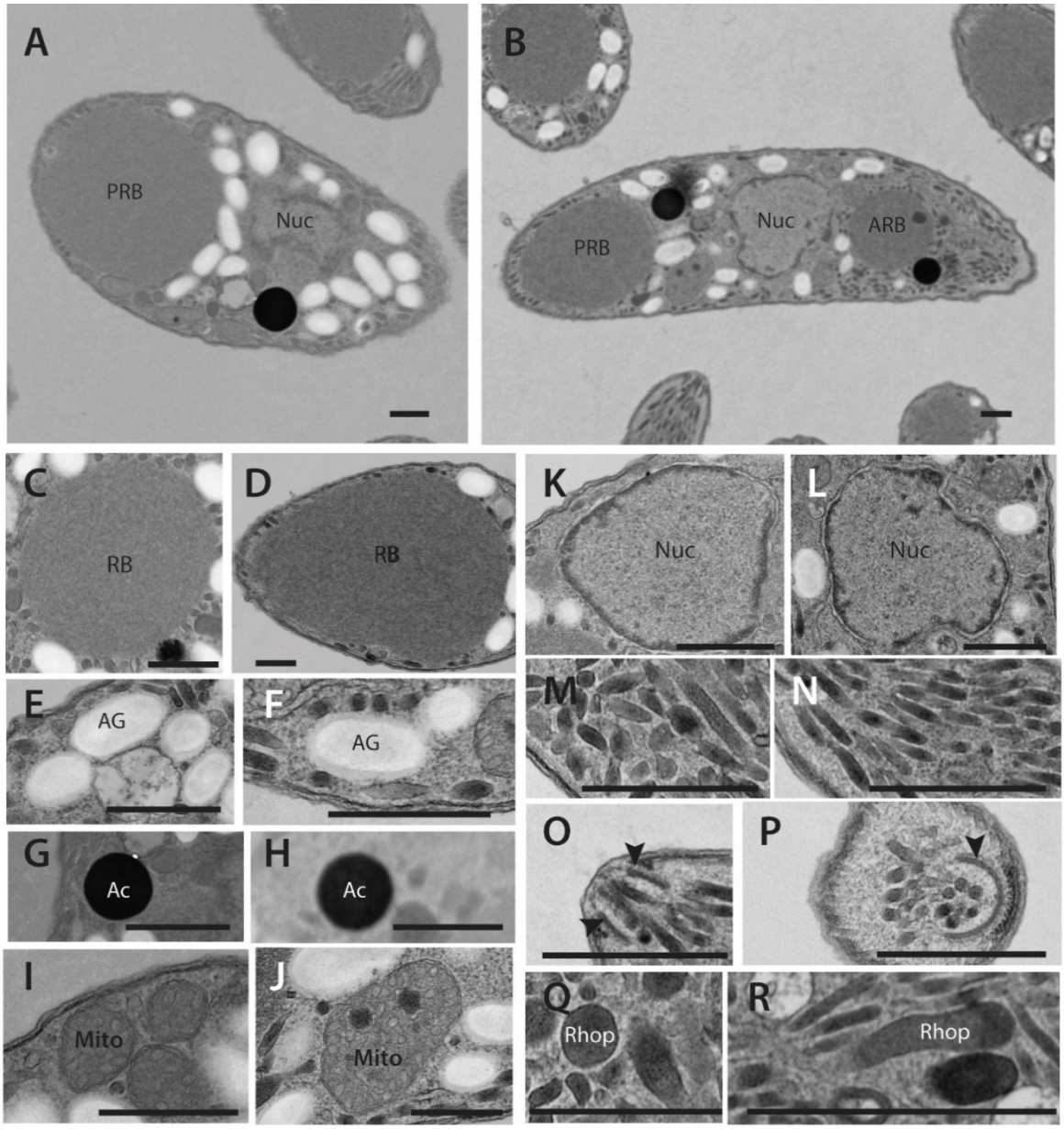


Figure 3.2. *Eimeria tenella* sporozoite utrastructure resolved following sample preparation using a single osmium protocol.

A-R) Transmission electron microscopy images of freshly-excysted sporozoite structures following processing using the single osmium protocol. A and B) Whole cells (ARB = anterior refractile body; PRB = posterior refractile body; Nuc = nucleus). C and D) Refractile bodies (RB). E and F) Amylopectin granules (AG). G and H) Acidocalcisomes (Ac). I and J) Mitochondria (Mito). K and L) Nuclei (Nuc). M and N) Micronemes. O and P) conoids (arrows). Q and R) and rhoptries (Rhop). Scale bar ~ 500 nm.

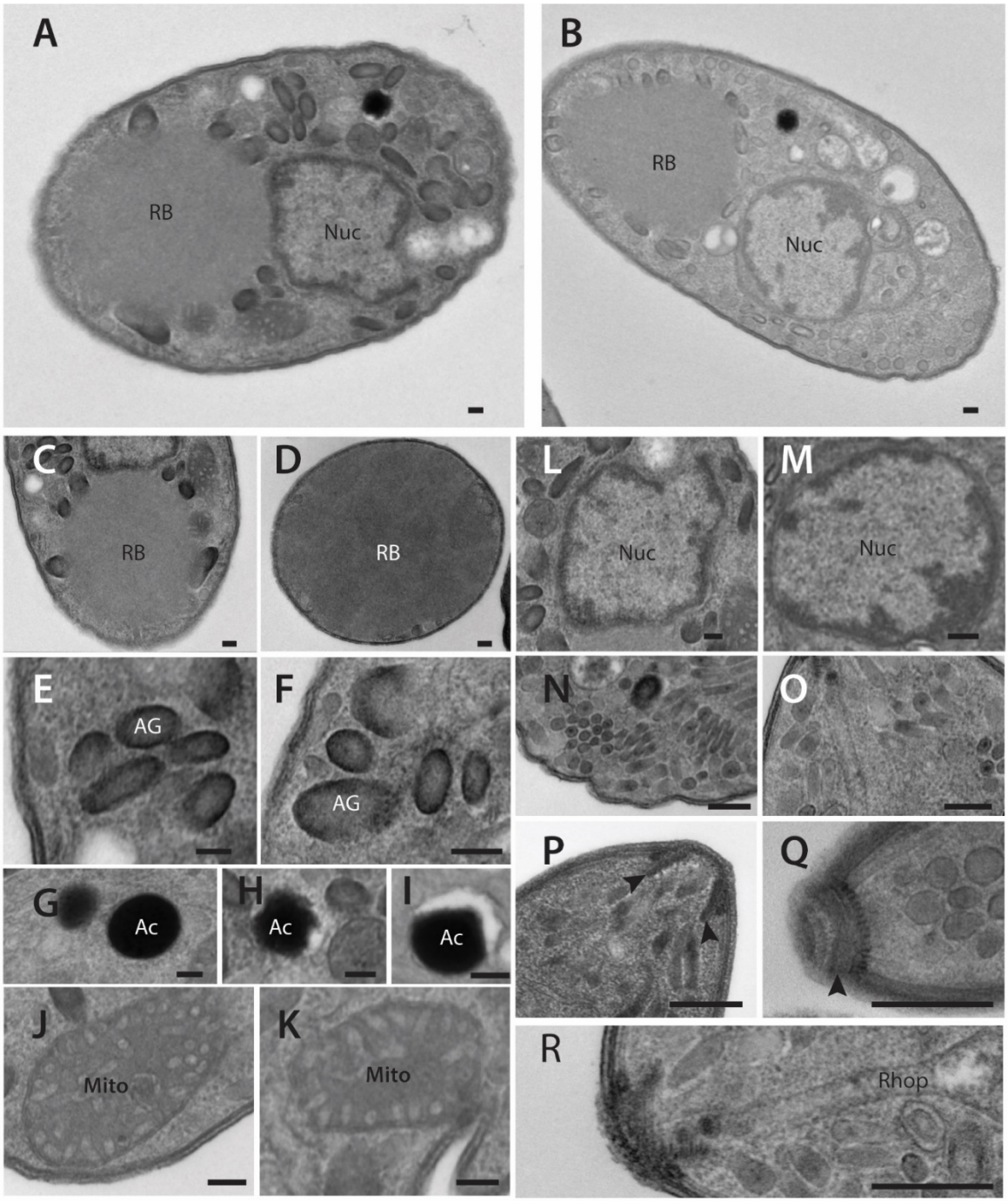


Figure 3.3. *Eimeria tenella* sporozoite utrastructure resolved following sample preparation using a double osmium protocol.

A-R) Transmission electron microscopy images of freshly-excysted sporozoite structures following processing using the double osmium protocol. A and B) Whole cells (RB = refractile body; Nuc = nucleus). C and D) Refractile bodies (RB). E and F) Amylopectin granules (AG). G, H and I) Acidocalcisomes (Ac). J and K) Mitochondria (Mito). L and M) Nuclei (Nuc). N and O) Micronemes. P and Q) conoids (arrowheads). R) and rhoptry (Rhop). Scale bar ~ 500 nm.

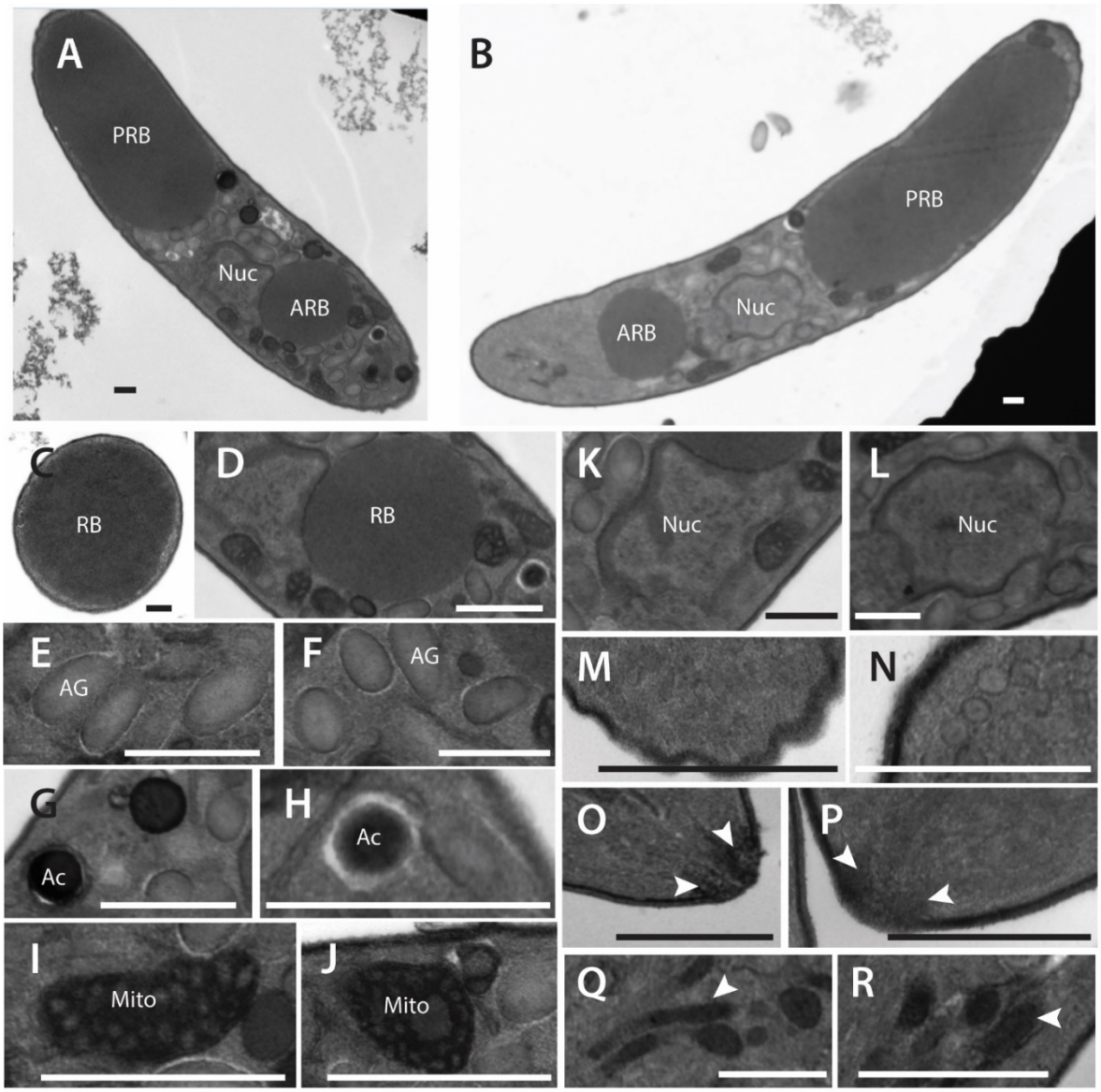


Figure 3.4. *Eimeria tenella* sporozoite utrastructure resolved following sample preparation using a double osmium and thiocarbohydrazide (ROTO) protocol.
A-R) Transmission electron microscopy images of freshly-excysted sporozoite structures following processing using the ROTO protocol. A and B) Whole cells (ARB = anterior refractile body; PRB = posterior refractile body; Nuc = nucleus). C and D) Refractile bodies (RB). E and F) Amylopectin granules (AG). G and H) Acidocalcisomes (Ac). I and J) Mitochondria (Mito). K and L) Nuclei (Nuc). M and N) Micronemes. O and P) conoids (arrows). Q and R) and rhoptries (arrowheads). Scale bar ~ 500 nm.

The transmission electron microscopy analysis indicated that preparation of sporozoites using a single osmium protocol is most likely to yield SBF-SEM data amenable to apical secretory organelle morphometric analysis. With regards to other subcellular organelles, preparation of sporozoites using either a double or single osmium protocol is likely to be suitable for morphometric analysis following SBF-SEM. This data also suggested that the preparation of sporozoite samples using high levels of heavy metals, such as in the ROTO protocols, reduces the contrast between subcellular compartments due to increased electron opacity of the cytoplasm.

3.2.2. **Evaluation of SBF-SEM imaging and three-dimensional structure segmentation**

Following the results of the TEM screen, described above, SBF-SEM was performed on both the single osmium sporozoite sample (which exhibited the highest contrast between cytoplasm and apical organelles) and the double osmium sporozoite sample (predicted to have greater stability under the electron beam due to higher heavy-metal content). In total, four series of SBF-SEM image stacks were generated. Series one was performed on the sample processed using double osmium and consisted of 737 slices with lateral resolution of 4.5 nm, axial resolution of 100 nm and lateral area of 35.7 μm^2; series two was performed on the sample processed using single osmium and consisted of 643 slices with lateral resolution of 3.7 nm, axial resolution of 50 nm and lateral area of 22.2 μm^2; series three was performed on the sample processed using single osmium consisted of 137 slices with lateral resolution of 2.4 nm, axial resolution of 60 nm and lateral area of 12 μm^2 and series four was performed on the sample processed using single osmium and consisted of 301 slices with lateral resolution of 2.4 nm, axial resolution of 60 nm and lateral area of 12 μm^2. Seventeen entire cells were contained within the SBF-SEM data collected from imaging the double osmium sporozoite sample (series one). Eight entire cells were contained within the SBF-SEM data collected when imaging the single osmium sporozoite sample (series two to four). Morphometric analysis was achieved through structure segmentation and volumetric calculations using AMIRA^{TM} software. Organelle identification in the SBF-SEM data set (Fig.3.5A) was aided by comparison with previous high resolution TEM analysis (Fig.3.5B).

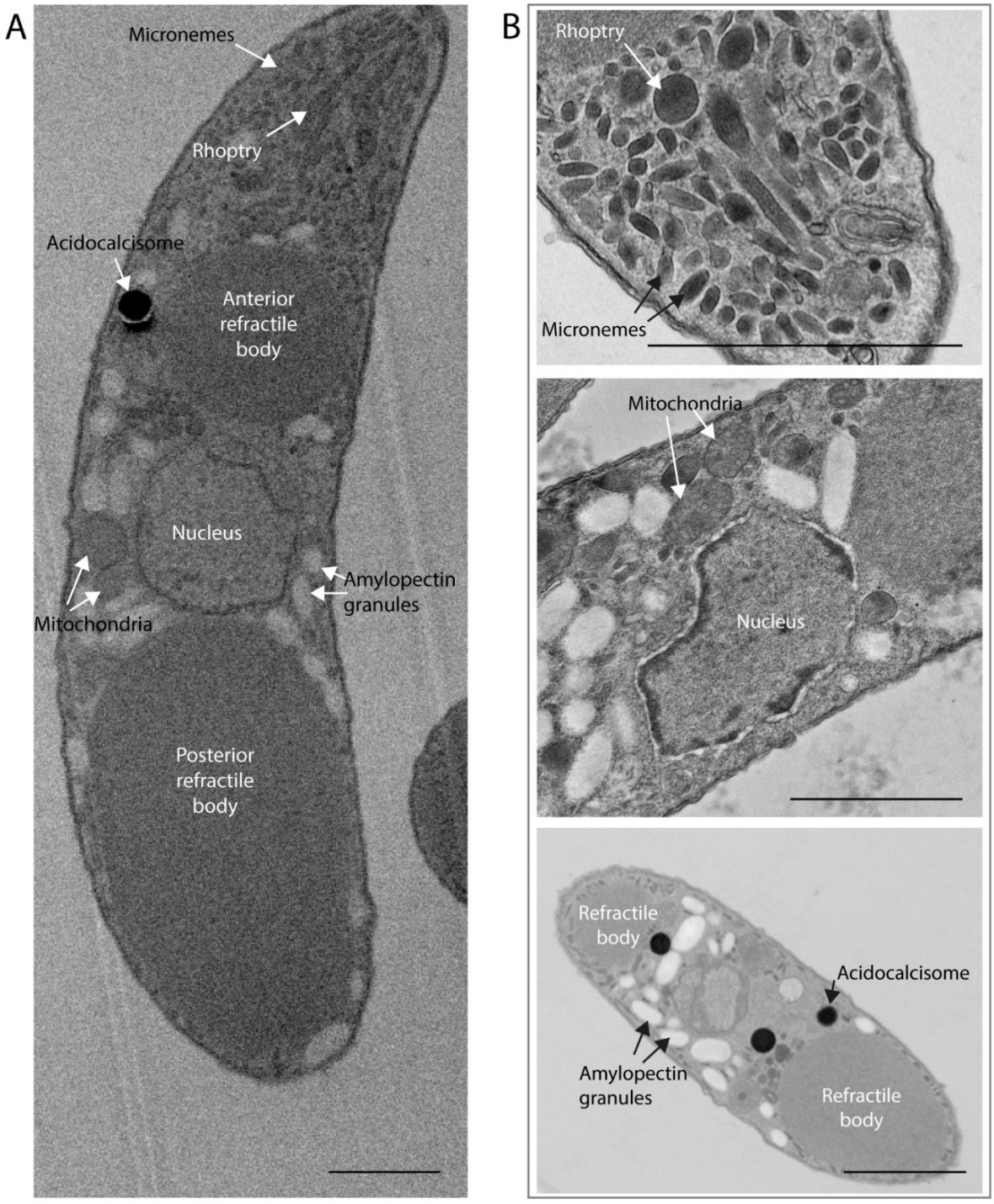


Figure 3.5. Comparison of sporozoite organelle appearance between SBF-SEM and TEM data.

A) A representative slice from SBF-SEM data of freshly-excysted sporozoites. B) Examples of freshly-excysted sporozoites as viewed by TEM. In both the SBF-SEM (A) and TEM (B) data, micronemes, rhoptries, acidocalcisomes, anterior refractile bodies, posterior refractile bodies, nuclei, mitochondria and amylopectin granules can be seen. Scale ~ 1 μm.

In addition to whole cell volumes (Fig.3.6A), refractile bodies (Fig.3.6B), mitochondria (Fig.3.6C), amylopectin granules (Fig.3.6D), nuclei (Fig.3.6E) and acidocalcisomes (Fig.3.6F) were all amenable to individual organelle segmentation through both lateral and axial planes. All segmentation of these structures was performed manually. Nineteen cells were included for each data

point. Figure 3.7 contains six examples of the surface rendered models produced following individual organelle segmentation of the sporozoites.

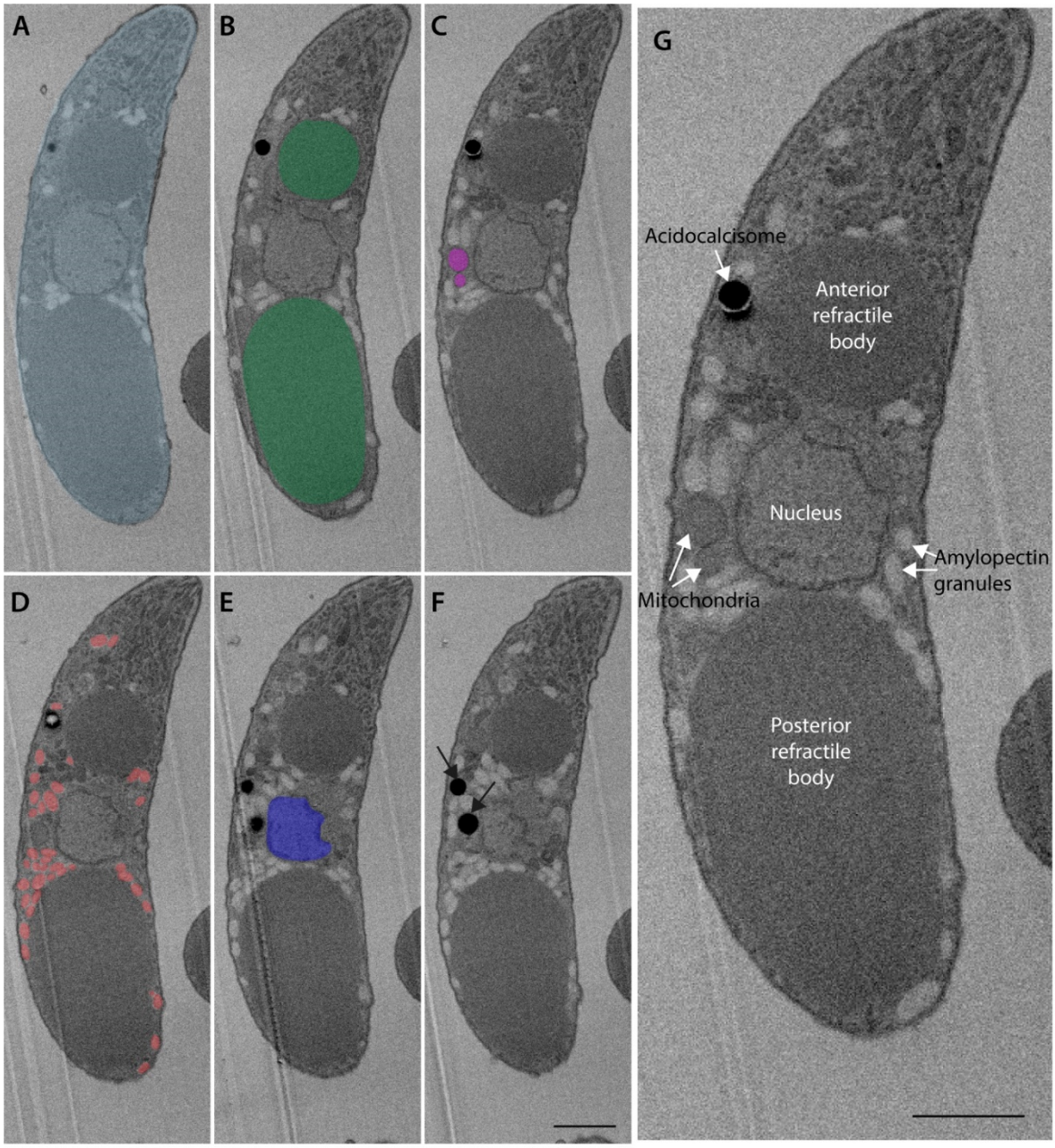


Figure 3.6. Serial block face SEM imaging allows identification and three-dimensional segmentation of sporozoite organelles.

A-F) Serial SBF-SEM images through part of a freshly-excysted sporozoite with lateral resolution of 2.4 nm and axial resolution of 60 nm (series three of SBF-SEM imaging using the single osmium processed sample). G) Same as in Fig.3.5A.

Key: light blue = whole cell (A), green = refractile bodies (B), pink = mitochondria (C), red = amylopectin granules (D), dark blue = nucleus (E). Black arrows indicate acidocalcisomes (F). Scale bar ~ 1 µm.

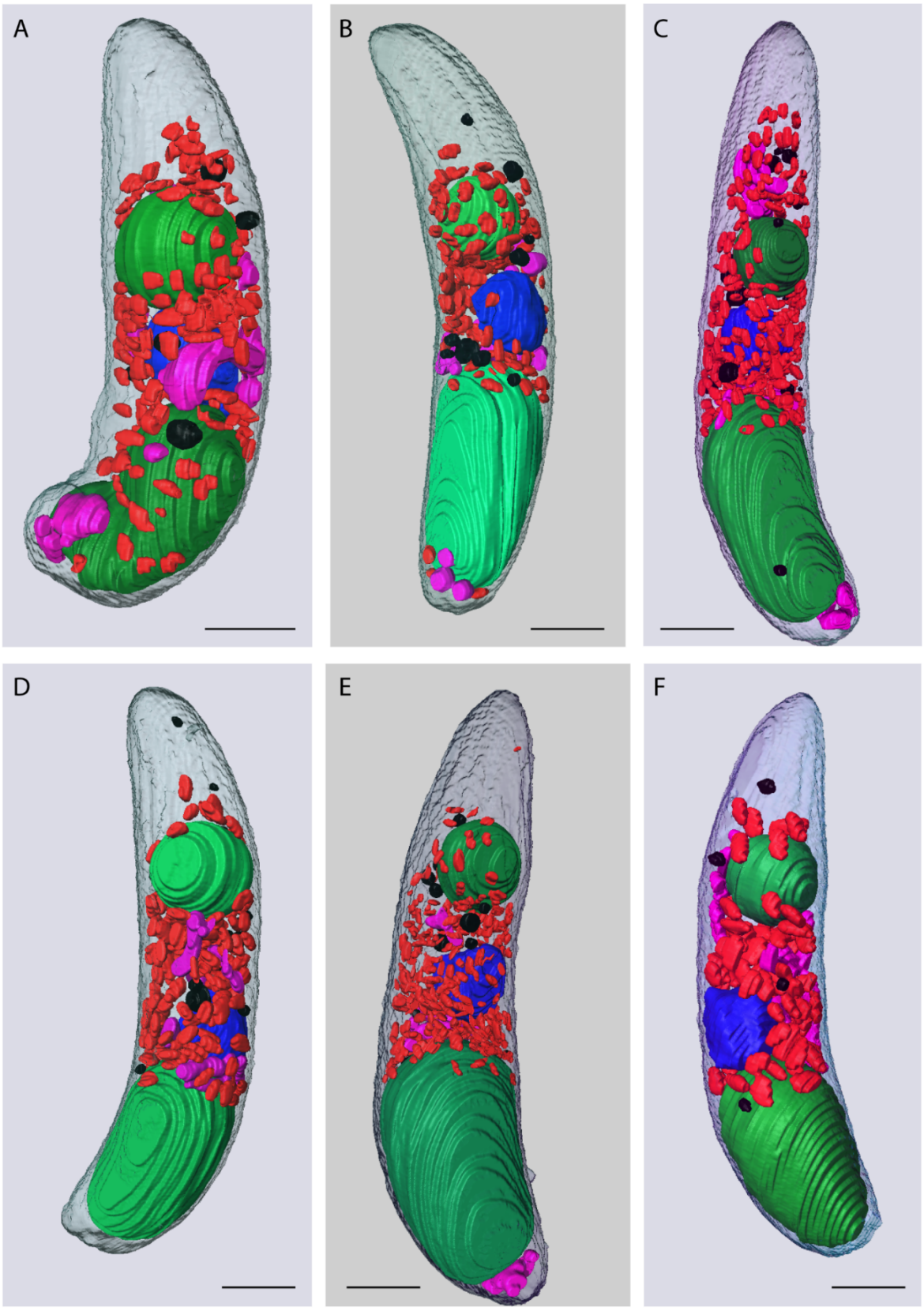


Figure 3.7. Surface-rendered models from freshly-excysted sporozoites.

A-F) Individual sporozoite models generated following segmentation of SBF-SEM data, showing nuclei (blue), refractile bodies (green), amylopectin granules (red), mitochondria (pink) and acidocalcisomes (black). Scale ~ 1μm.

Microneme and rhoptry segmentation was more complicated than that of the aforementioned structures. Micronemes are present in vast numbers, closely positioned to one another and the width of a microneme is around 50 nm, which is less than the axial resolution of the SBF-SEM data sets. Rhoptries can be difficult to distinguish from micronemes in SBF-SEM images; the rhoptry necks can appear identical to micronemes when viewed in cross-section.

Despite these challenges, a successful method for approximate microneme volume quantification was developed. A median filter of value three (AMIRA^{TM}) was applied to the SBF-SEM data collected from the single osmium processed sample. This enabled microneme-corresponding pixels to be selected (Fig.3.8A) via a combination of pixel density thresholding and manual area selection. When surface rendered, this segment is mostly comprised of elongated ovoid structures (Fig.3.8B). Based on previous electron microscopy analysis, the model appears as expected for microneme structures. When selecting microneme-containing areas, structures that resembled the larger diameter rhoptry bulbs were excluded; nevertheless, it is likely that some data corresponding to rhoptry necks were included in the microneme segmentation.

Rhoptries were identified based on their bulb portions, which are considerably larger than micronemes. Rhoptry bulbs were manually segmented by selecting the corresponding pixels in each SBF-SEM slice. Where rhoptries were sectioned lengthways during the SBF-SEM imaging, rhoptry necks could be clearly seen extending from the rhoptry bulbs, which facilitated segmentation of entire rhoptries. In some cases where rhoptries were sectioned on their short axes during SBF-SEM imaging, segmentation of the rhoptry neck was not possible; in this instance the rhoptry bulb alone was segmented.

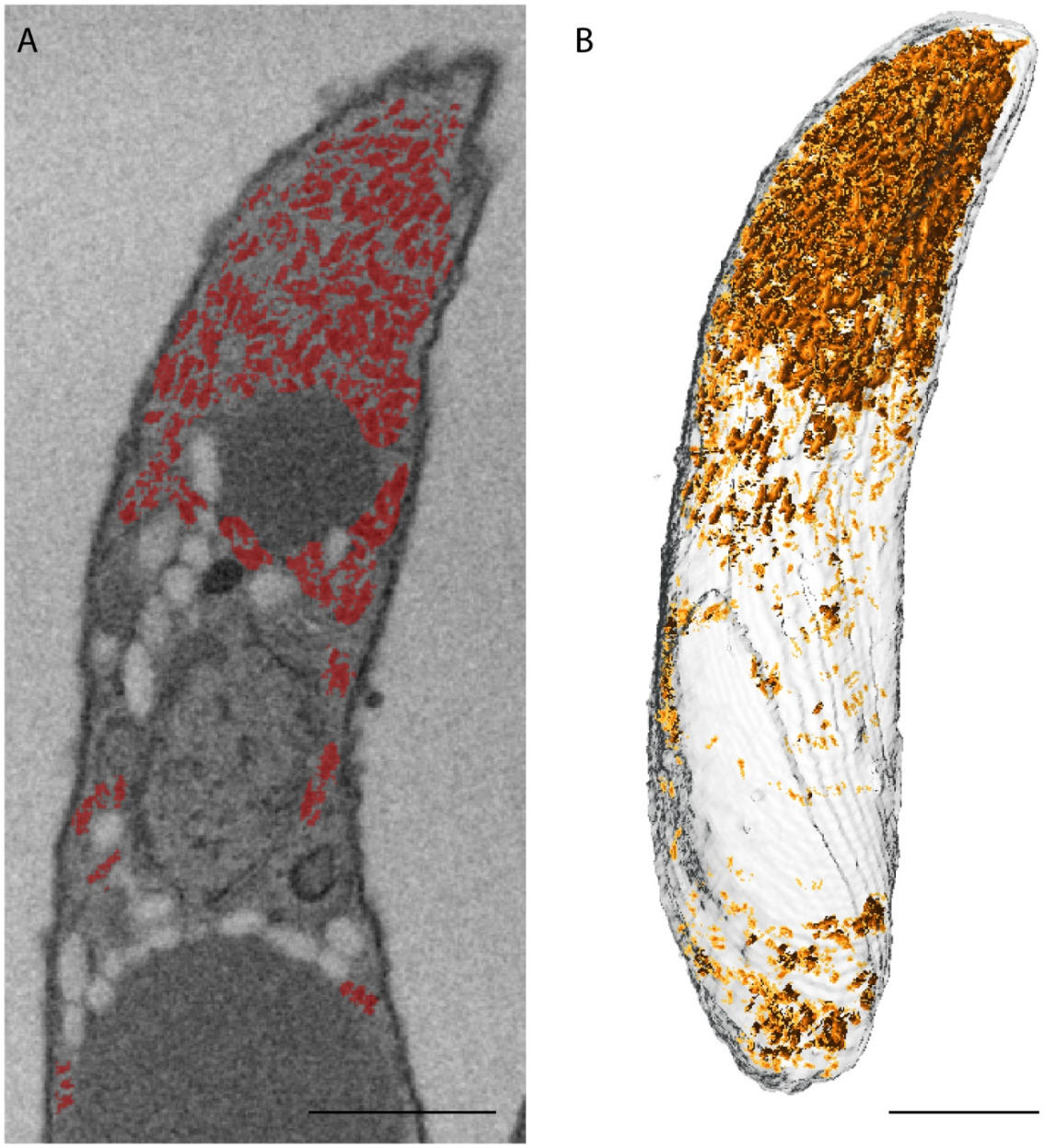


Figure 3.8. Pixel density thresholding (AMIRA™) enables semi-accurate microneme segmentation.

A) Pixels corresponding to microneme organelles (red) were selected from SBF-SEM data using a combination of a median-3 image filter, thresholding mask and manual area selection. B) Surface-rendered micronemes (gold) are seen as rod-shaped structures following segmentation, as shown in (A). Scale ~ 1 µm.

3.2.3. Evaluation of alternative methods for analysis of apical organelle morphometrics

As explained in section 3.2.2, segmentation of microneme and rhoptry volumes from SBF-SEM data proved to be more challenging than that of the larger organelles. To assess whether an alternative method could be used for apical organelle morphometric analysis, the use of serial-section transmission electron microscopy was explored.

Serial 70 nm sections were cut from the single-osmium sporozoite sample and collected onto formvar coated slot-grids. Two serial-section data sets were generated using transmission electron

microscopy. The first data set consisted of 29 serial sections (Fig. 3.9A-D) and the second data set consisted of 23 serial sections (Fig. 3.9E-F). In both data sets, sporozoite organelles can be clearly visualised (Fig. 3.9A, C, D and E). Both data sets included the majority of a single whole-sporozoite cell volume (Fig. 3.9B and F), however neither data set captured the entire sporozoite cell. Unless entire sporozoite volumes are imaged, reliable data on individual-cell organelle morphometrics cannot be generated. Due to the technical difficulty and time required to collect whole-cell serial-section transmission electron microscopy data, it was decided not to perform any further investigations using this method.

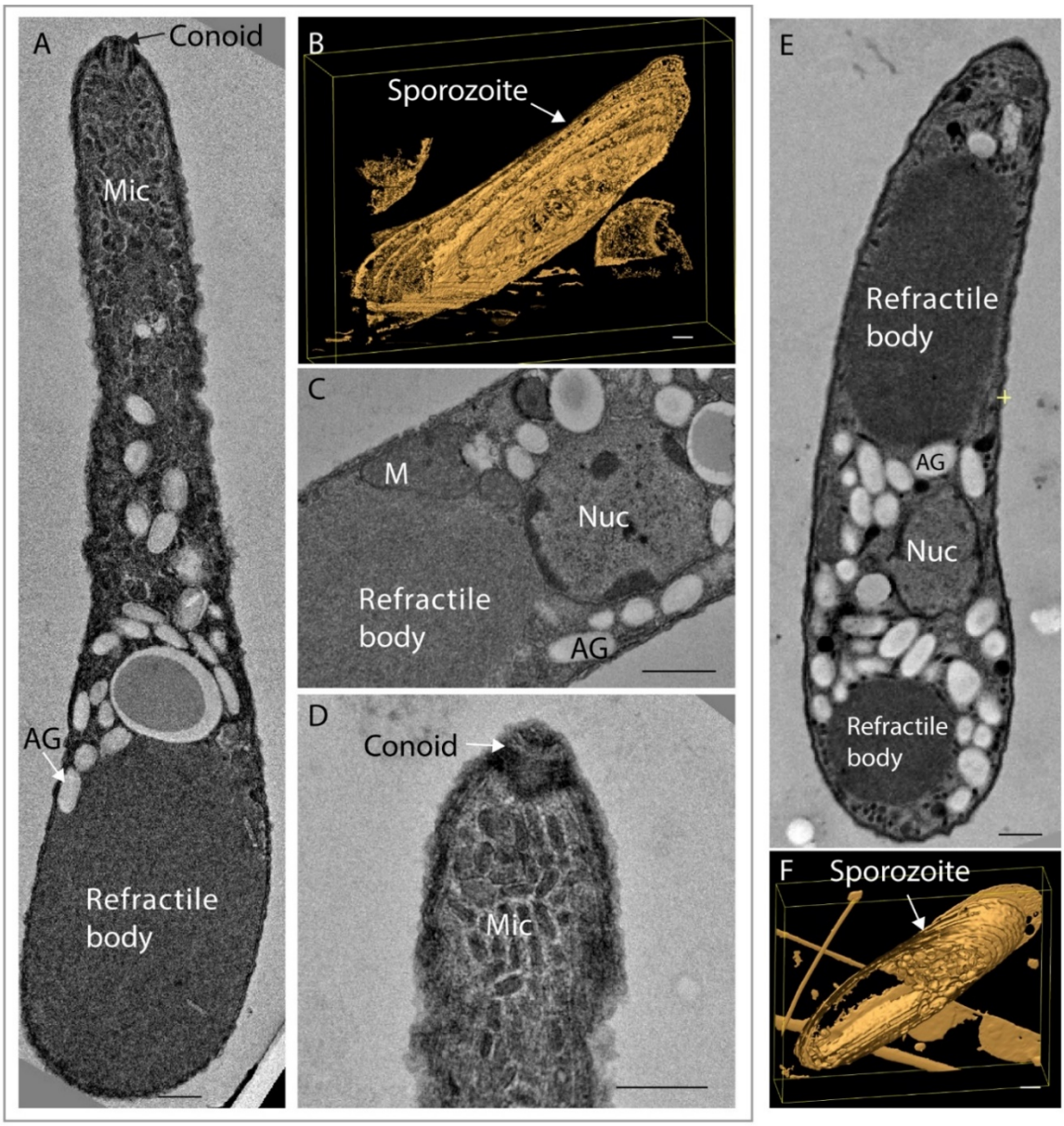


Figure 3.9. Application of serial section transmission electron microscopy to study *E. tenella* sub-cellular structure.

Serial section transmission electron microscopy was performed on one sporozoite over 29 x 70 nm sections (A-D) and another sporozoite over 23 x 70 nm sections (E+F). A) An example transmission electron microscopy image of the sporozoite imaged over 29 sections. B) Automated surface model generated in IMOD from the 29-serial-section data shows the sporozoite outer surface. C+D) Ultrastructural details from one of the 29 sections. E) An example transmission electron microscopy image of the sporozoite imaged over 23 sections. F) Automated surface model generated in IMOD from the 23-serial-section data. Mic = micronemes, M = mitochondria, AG = amylopectin granule. Scale ~ 500 nm.

3.3. Organelle morphometric quantification reveals wide variation in freshly-excysted sporozoite morphology

In *E. tenella*, the sporozoite is the stage that forms inside the oocyst during oocyst maturation in the environment (Allen and Fetterer 2002). Following ingestion of oocysts by a new host, sporozoites

are released into the intestine and invade intestinal epithelial cells before commencing endogenous replication (Lal et. al. 2009, Rose et. al. 1984). I sought to compare morphometrics of sporozoites, both prior to and following host cell invasion, to determine the physical changes occurring during this critical life cycle event.

As described in the previous section, it was possible to digitally segment individual structures from within the three-dimensional image data collected by SBF-SEM. Thus for 19 sporozoites, the whole cell, nucleus, refractile bodies, amylopectin granules, mitochondria and acidocalcisomes were all segmented. Micronemes were segmented from four sporozoites and rhoptries were segmented from three sporozoites. To quantify freshly-excysted sporozoite morphometrics, volumetric values were calculated from segmented data using AMIRA™.

3.3.1. **Whole cell morphometrics**

The sporozoite is a polarised, sickle-shaped cell, with a specialised set of secretory organelles at one end known as apical secretory organelles (Gubbels and Duraisingh 2012, Ryley 1969). Segmentation of the plasma membrane was carried out for 19 freshly excysted sporozoites (Fig.3.10A) and whole cell volume was quantified from surface rendered models of each cell (Fig.3.10B). Mean sporozoite cell volume was found to be 61.27 +/- 10.9 μm^3 (Fig.3.10C). This number is 11 μm^3 less than the mean cell volume found following Coulter Counter analysis of *E. tenella* sporozoites (Wagenbach 1969). Coefficient of variation, which is the standard deviation displayed as a percentage of the mean, was found to be 17.7% (Fig.3.10C). The smallest sporozoite had a whole cell volume of 36.5 μm^3 and the largest sporozoite had a whole cell volume of 72.4 μm^3 (Fig.3.10C).

These data revealed a wide variation in size (volume) between individual sporozoites. These are non-dividing sporozoites collected immediately after excystation and purification and wide variations in individual sporozoites have not previously been documented.

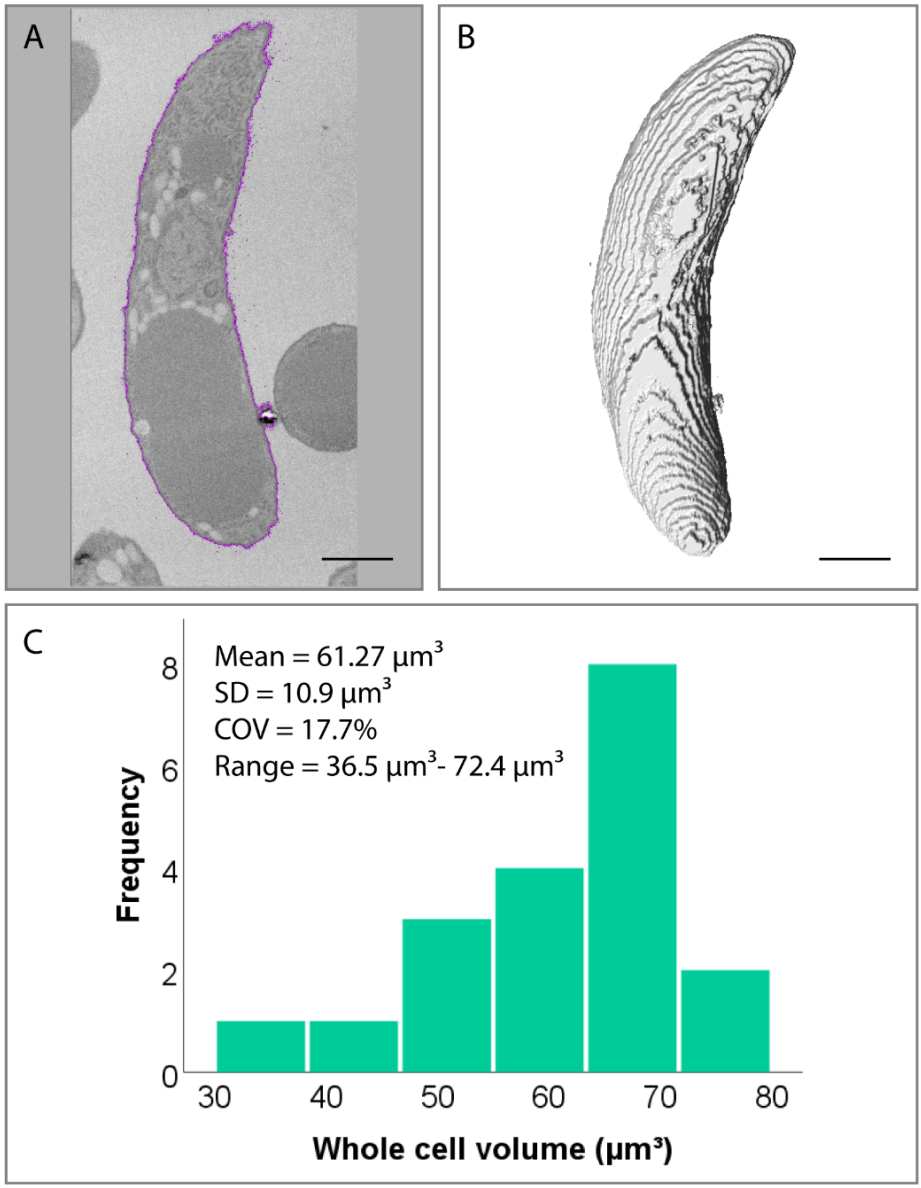


Figure 3.10. Mean cell volume in freshly-excysted sporozoites.

A) Single slice from SBF-SEM data on freshly-excysted sporozoites. Whole cell areas (outlined in purple) were manually segmented. B) Surface model of a whole sporozoite rendered from SBF-SEM segmentation data. C) Distribution of whole cell volumes from 19 freshly-excysted sporozoites. Volumes were calculated in AMIRA™ using the segmentation data. SD = standard deviation, COV = coefficient of variation. Scale ~ 1 µm.

3.3.2. Nucleus morphometrics

The *E. tenella* sporozoite nucleus is roughly spherical in shape and is in the centre of the cell, positioned between the two refractile bodies. Following segmentation (Fig.3.11A) and surface rendering (Fig.3.11B) of nuclei from 19 sporozoites imaged by SBF-SEM, mean nucleus volume was found to be 2.3 +/- 0.4 µm³ (Fig.3.11C). Coefficient of variation was found to be 17.2% and nuclei volumes ranged from 1.58 µm³ to 2.83 µm³ (Fig.3.11C). Increasing nucleus volume was

statistically associated with increasing sporozoite cell volume (Pearson's correlation coefficient (r) = 0.737, $p < 0.0005$) (Fig.3.11D).

These data show that there is a wide variation in nucleus volume between individual *E. tenella* sporozoites. It was also revealed that larger sporozoites contain larger nuclei.

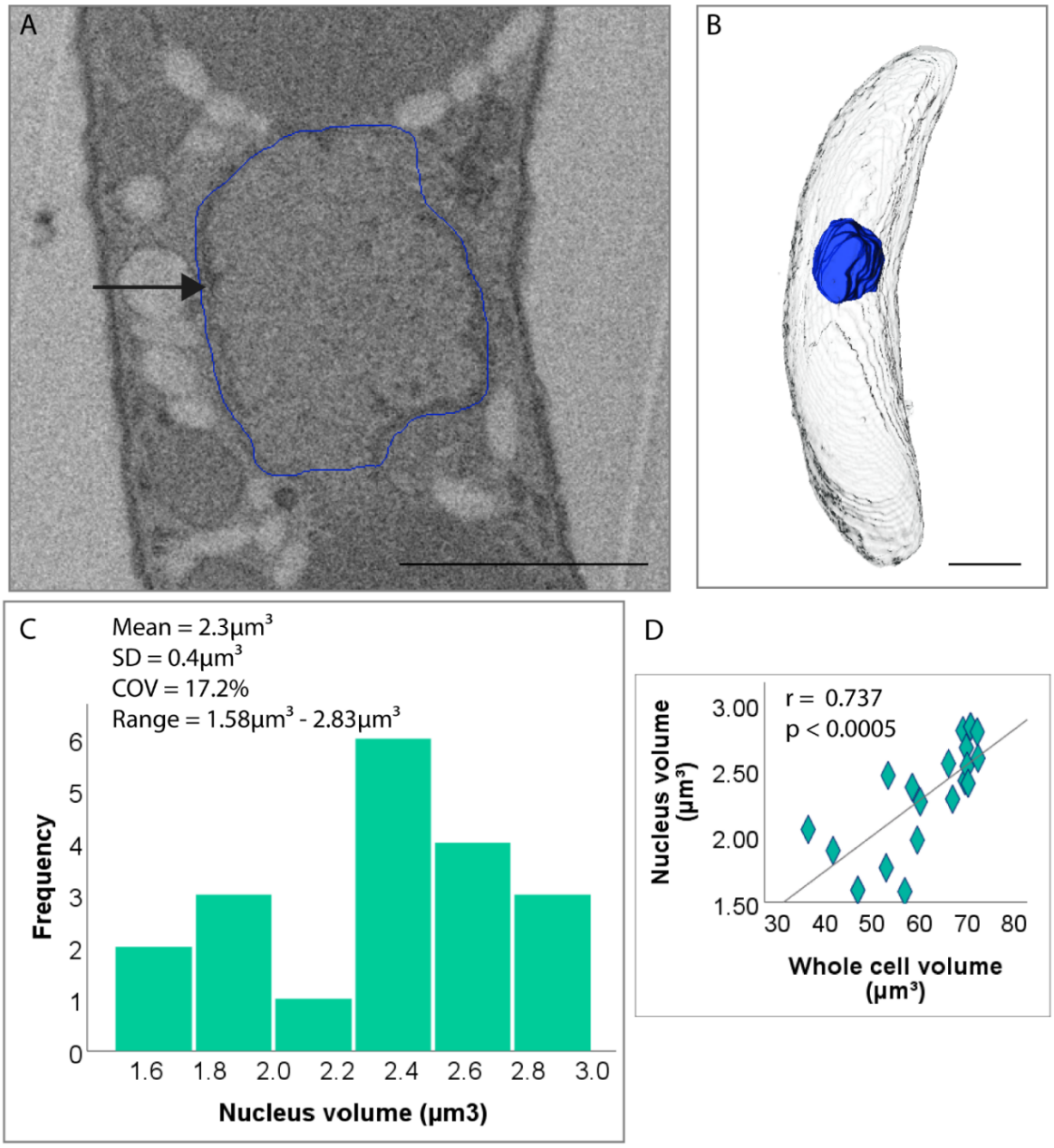


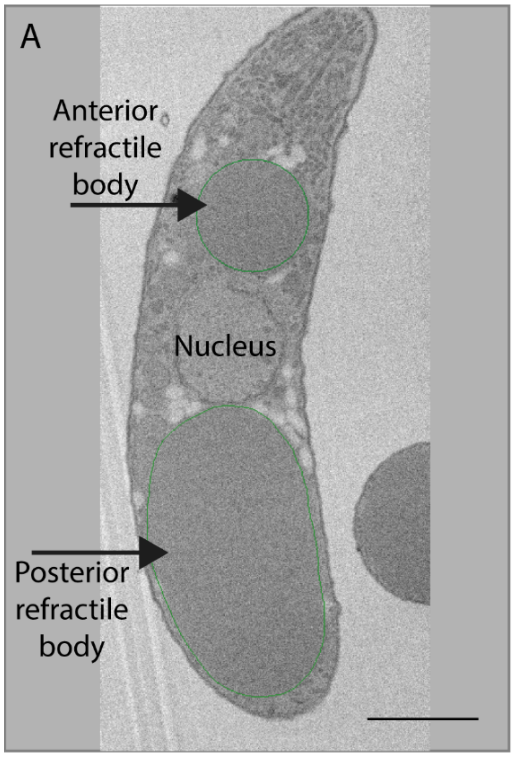
Figure 3.11. Mean nucleus volume in freshly-excysted sporozoites.

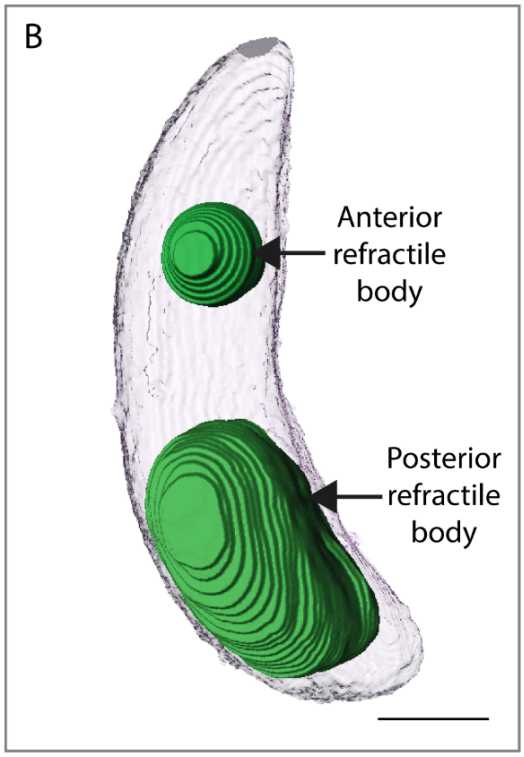
A) Single slice from SBF-SEM data on freshly-excysted sporozoites. Nuclei areas (outlined in blue and indicated by arrow) were manually segmented. B) Surface model of a nucleus (blue) within a sporozoite (transparent) rendered from SBF-SEM segmentation data. C) Distribution of nuclei volumes from 19 freshly-excysted sporozoites. SD = standard deviation, COV = coefficient of variation. D) Correlation analysis of nucleus volume with whole cell volume (r = Pearson correlation coefficient). Volumes were calculated in AMIRA™ using the segmentation data. Scale ~ 1 µm.

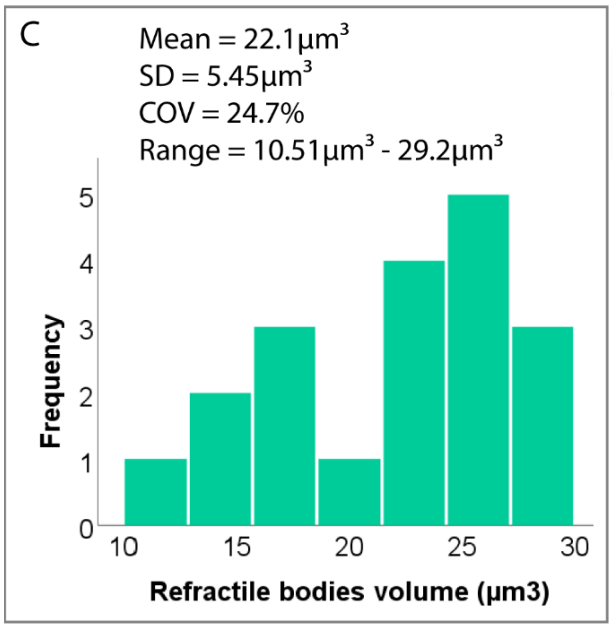
3.3.3. **Refractile bodies morphometrics**

There are generally two refractile bodies in freshly excysted sporozoite cells (see later for further analysis). The posterior refractile body appears larger than the anterior refractile body, is roughly ovoid in shape and fills much of the posterior third of the cell (Fig.3.12A and B). The anterior refractile body is roughly spherical in shape and sits just anterior to the nucleus (Fig.3.12A and B). Anterior and posterior refractile bodies were segmented from SBF-SEM data of 19 freshly-excysted sporozoites. Refractile bodies volume (anterior refractile body volume plus posterior refractile body volume) was calculated for each cell. On average, refractile bodies volume was found to be 22.1 +/- 5.45 μm^3, and coefficient of variation was 24.7% (Fig.3.12C). The smallest refractile bodies volume was 10.51 μm^3 and the largest refractile bodies volume was 29.2 μm^3 (Fig.3.12C). Sixteen of the 19 sporozoites contained two refractile bodies (one anterior refractile body and one posterior refractile body) and three sporozoites contained three refractile bodies (Fig.3.12D). In all sporozoites containing three refractile bodies, at least one refractile body was found anterior to the nucleus and at least one refractile body was found posterior to the nucleus. Greater refractile bodies volume was strongly associated with greater sporozoite cell volume (Pearson's correlation coefficient (r) = 0.984, $p < 0.0005$) (Fig.3.12E).

These data show that there is a wide variation in refractile bodies volume between individual sporozoites and that refractile body number per cell can vary. It also shows that there is a strong connection between cell size and total refractile body volume.







D

Refractile body number	Number of sporozoites
2	16
3	3

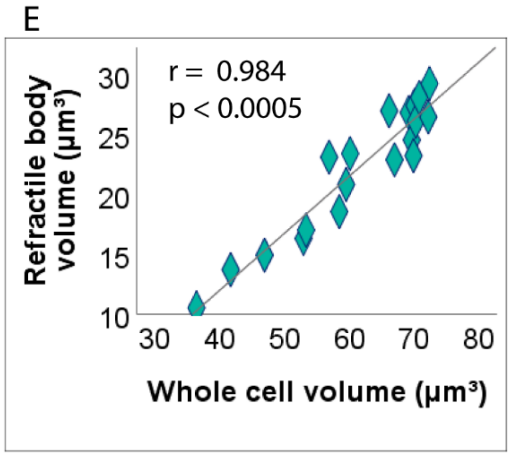


Figure 3.12. Mean refractile bodies volume in freshly-excysted sporozoites.

A) Single slice from SBF-SEM data on freshly-excysted sporozoites. Refractile body areas (outlined in green and indicated by arrows) were manually segmented. B) Surface model of refractile bodies (green) within a sporozoite (transparent) rendered from SBF-SEM segmentation data. C) Distribution of refractile bodies volumes from 19 freshly-excysted sporozoites. SD = standard deviation, COV = coefficient of variation. D) Counts from the 19 SBF-SEM - imaged sporozoites containing either two or three refractile bodies. E) Correlation analysis of refractile bodies volume with whole cell volume (r = Pearson correlation coefficient). Volumes were calculated in AMIRA™ using the segmentation data. Scale ~ 1 µm.

3.3.4. **Amylopectin granules morphometrics**

Amylopectin granules are ovoid structures present in large numbers in *E. tenella* sporozoites (see later for quantification). They exist as a form of polysaccharide storage and are hypothesised to function as long-term energy reserves (Nakai and Ogimoto 1987, Uboldi et. al. 2015).

Following single osmium processing, amylopectin granules appear electron lucent when viewed by transmission electron microscopy (Fig.3.2E and F) but following double osmium processing they appear as electron opaque structures (Fig.3.3E and F; Fig.3.4E and F). Amylopectin granules were segmented from SBF-SEM data of 19 sporozoites (Fig.3.13A). Inspection of three-dimensional models generated from segmentation data (Fig.3.13B) showed that amylopectin granules were found throughout the cell, with the greatest density of amylopectin granules present in the central part, surrounding the nucleus. The anterior and posterior thirds of the cell contained fewer amylopectin granules; these areas are occupied by the apical organelles and posterior refractile body respectively (Fig.3.13B).

The average volume of amylopectin granules per sporozoite was found to be 2.66 +/- 1.22 μm^3, with a coefficient of variation of 46% (Fig.3.13C). Amylopectin granules volume ranged from 1.01 μm^3 to 5.15 μm^3 (Fig3.13C). Amylopectin granules volume was not found to be associated with sporozoite cell volume (Fig.3.13D). On average, sporozoites contained 196 amylopectin granules (+/- 63) (Fig.3.13E). Coefficient of variation for amylopectin granule number was 32.3% and amylopectin granule number ranged from 86 to 294 (Fig.3.13E). Amylopectin granule number was not correlated with cell volume (Fig.3.13F).

These data reveal that there is a wide variation in amylopectin granules number and volume between individual sporozoites. It also shows that there is no correlation between amylopectin granules number or volume and sporozoite cell volume.

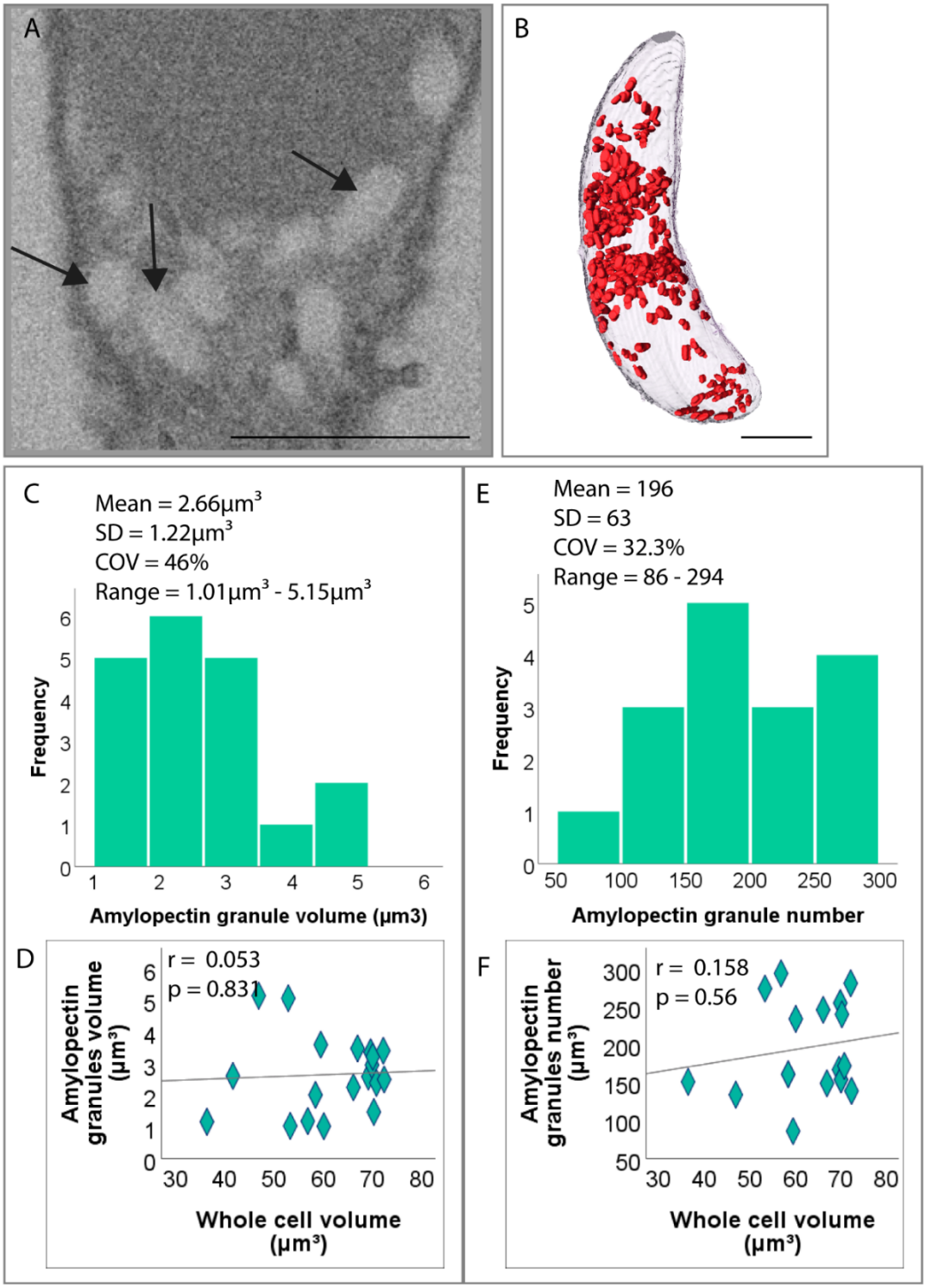


Figure 3.13. Mean amylopectin granules volume in freshly-excysted sporozoites.

A) Single slice from SBF-SEM data on freshly-excysted sporozoites. Amylopectin granules (three are indicated by arrows) were manually segmented. B) Surface model of amylopectin granules (red) within a sporozoite (transparent) rendered from SBF-SEM segmentation data. C) Distribution of amylopectin granules volumes from 19 freshly-excysted sporozoites. SD = standard deviation, COV = coefficient of variation. D) Correlation analysis of amylopectin granules volume with whole cell volume (r = Pearson correlation coefficient). Volumes were calculated in AMIRA™ using the segmentation data. E) Distribution of amylopectin granule number from 17 freshly-excysted sporozoites. F) Correlation analysis of amylopectin granule number with whole cell volume. Scale ~ 1 µm.

3.3.5. **Mitochondria morphometrics**

Assessment of mitochondrial morphology in *T. gondii* tachyzoites revealed that each cell possesses a single, branched mitochondrion which extended throughout much of the cell (Melo et. al. 2000). It was not known whether *Eimeria* species sporozoites possess a single mitochondrion or multiple mitochondria.

Mitochondria (Fig.3.14A) were segmented from SBF-SEM data of 19 sporozoites. Inspection of surface rendered models from segmented data revealed that *E. tenella* sporozoites possess multiple mitochondria (Fig.3.14B). Volumetric analysis of surface rendered models showed that average total mitochondria volume per cell was 1.14 +/- 0.31 μm^3 (Fig.3.14C). Coefficient of variation for mitochondria volume was 27.1% (Fig.3.14C) and range was 0.47 μm^3 to 1.82 μm^3. Increasing mitochondria volume was found to be associated with increasing sporozoite cell volume (Pearson's correlation (r) = 0.561, p = 0.013) (Fig.3.14D). On average, sporozoites contained 14 mitochondria per cell (+/- 5.4) (Fig.3.14E). Coefficient of variation for mitochondria number was 38.7% and mitochondria number ranged from eight to 26 (Fig.3.14E). No correlation between mitochondria number and cell volume was found (Fig.3.14F).

In summary, *E. tenella* sporozoites were found to contain multiple mitochondria, in contrast to *T. gondii* tachyzoites which contain a single mitochondrion. Both the number and volume of mitochondria was found to vary considerably between sporozoites. Increasing mitochondria volume, but not number, was associated with increasing sporozoite cell volume.

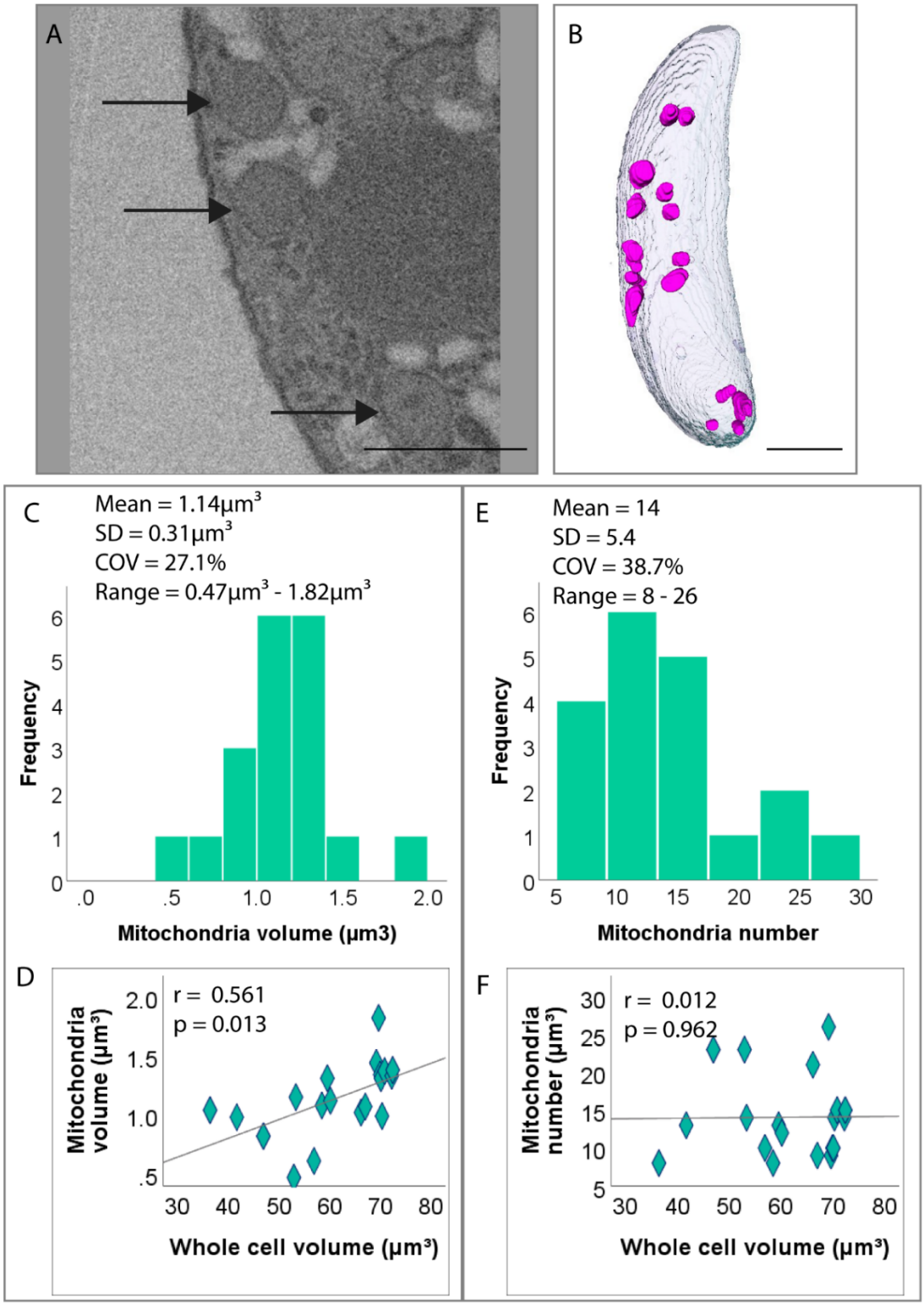


Figure 3.14. Mean mitochondria volume in freshly-excysted sporozoites.

A) Single slice from SBF-SEM data on freshly-excysted sporozoites. Mitochondrial areas (indicated by arrows) were manually segmented. B) Surface model of a mitochondria (pink) within a sporozoite (transparent) rendered from SBF-SEM segmentation data. C) Distribution of mitochondrial volumes from 19 freshly-excysted sporozoites. SD = standard deviation, COV = coefficient of variation. D) Correlation analysis of mitochondria volume with whole cell volume (r = Pearson correlation coefficient). Volumes were calculated in AMIRA™ using the segmentation data. E) Distribution of mitochondria number from 19 freshly-excysted sporozoites. F) Correlation analysis of mitochondria number with whole cell volume. Scale ~ 1 µm.

3.3.6. **Acidocalcisomes morphometrics**

As their name suggests, acidocalcisomes are acidic calcium stores that are found in a variety of protozoa including trypanosomatids and apicomplexans (Docampo 2016). Until recently, these structures in *Eimeria* species were referred to as volutin granules; they are now recognised to be acidocalcisomes since they were shown to possess analogous chemical and structural characteristics (Soares Medeiros et. al. 2011). In chemically prepared specimens viewed by electron microscopy, acidocalcisomes appear as round compartments, filled to varying extents with highly electron opaque material (Docampo 2016). In *T. gondii*, acidocalcisomes are thought to play an important role in the calcium signalling events involved in host cell invasion and egress (Lourido and Moreno 2015, Soares Medeiros et. al. 2011).

Acidocalcisomes were identified in SBF-SEM images (Fig.3.15A), manually segmented and three-dimensional models were produced for each of the 19 sporozoites (Fig.3.15B). Quantification of total acidocalcisomes volume per cell revealed that mean total acidocalcisomes volume was 0.32 +/- 0.09 μm^3 (Fig.3.15C). Coefficient of variation for acidocalcisomes volume was found to be 26.8% and range was 0.19 μm^3 to 0.5 μm^3 (Fig.3.15C). Increasing acidocalcisomes volume was statistically associated with increasing sporozoite cell volume (Pearson's correlation (r) = 0.5, p = 0.029) (Fig.3.15D). On average, sporozoites contained 13 acidocalcisomes per cell (+/- 3.7) and coefficient of variation for acidocalcisome number was 28.9% (Fig.3.15E). Minimum acidocalcisome number was six per cell and maximum acidocalcisome number was 21 per cell (Fig.3.15E). Increasing acidocalcisome number was also found to be associated with increasing sporozoite cell volume (Pearson's correlation (r) = 0.492, p = 0.032) (Fig.3.15F).

These data show that acidocalcisomes volume and number varies considerably between sporozoites. It also revealed that larger sporozoites contain a greater number and volume of acidocalcisomes.

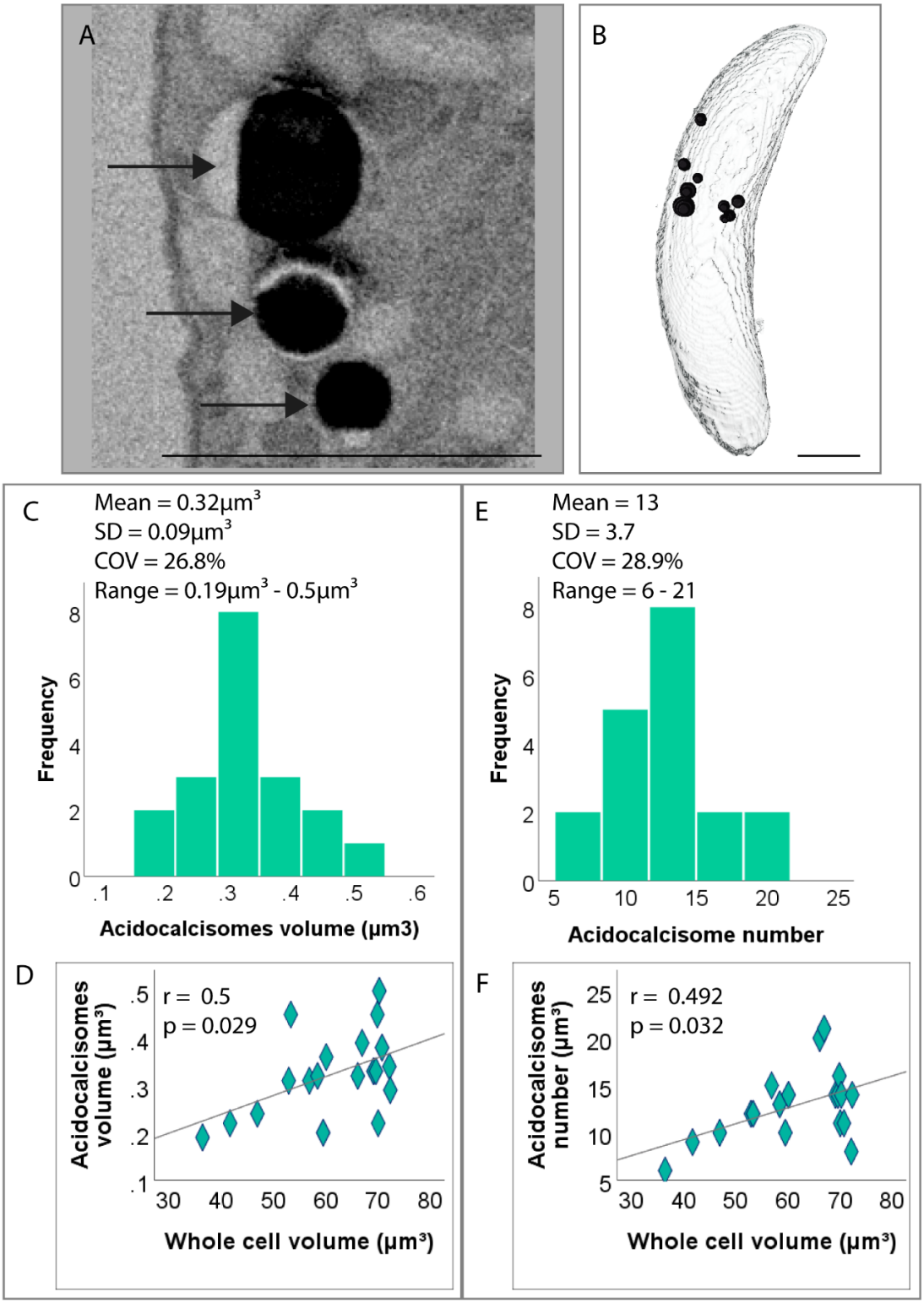
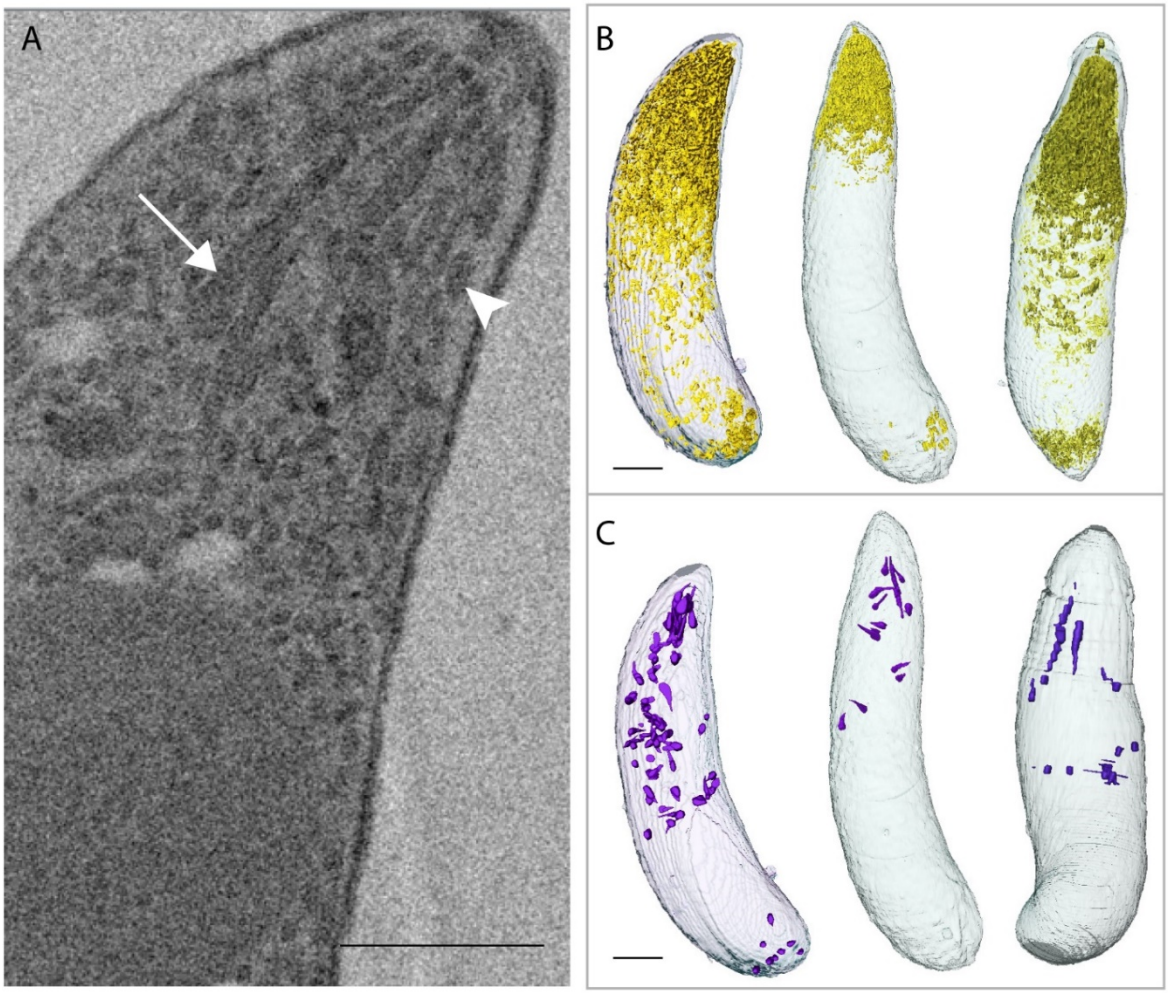


Figure 3.15. Mean acidocalcisomes volume in freshly-excysted sporozoites.

A) Single slice from SBF-SEM data on freshly-excysted sporozoites. Acidocalcisome areas (indicated by arrows) were manually segmented. B) Surface model of acidocalcisomes (black) within a sporozoite (transparent) rendered from SBF-SEM segmentation data. C) Distribution of acidocalcisome volumes from 19 freshly-excysted sporozoites. SD = standard deviation, COV = coefficient of variation. D) Correlation analysis of acidocalcisomes volume with whole cell volume (r = Pearson correlation coefficient). Volumes were calculated in AMIRA™ using the segmentation data. E) Distribution of acidocalcisome number from 19 freshly-excysted sporozoites. F) Correlation analysis of acidocalcisome number with whole cell volume. Scale ~ 1 µm.

3.3.7. **Microneme and rhoptry volumes**

Microneme volumes were calculated from SBF-SEM data of four freshly-excysted sporozoites and rhoptry volumes were calculated from SBF-SEM data of three freshly-excysted sporozoites. Micronemes were observed in SBF-SEM data as ovoid structures, approximately 50- to 100- nm in size (Fig. 3.16A, arrowhead). Rhoptries were observed as club-shaped structures, with a rounded 'bulb' part and an elongated 'neck' part (Fig. 3.16A, arrow). Micronemes were segmented using a combination of pixel-density thresholding and manual area selection (as described in section 3.2.2) (Fig. 3.8). The majority of micronemes were found in the apical third of the parasite, although some organelles conforming to the size and shape of micronemes were found throughout the cell (Fig. 3.16B). Rhoptries were also mostly found towards the sporozoite apex, although some rhoptries were present in the central and posterior parts of the cell (Fig. 3.16C). Mean micronemes volume was found to be 3.18 +/- 1.01 μm^3 and mean rhoptries volume was found to be 0.26 +/- 0.26 μm^3. These data are best interpreted as volumetric estimations due to the low number of samples included in this analysis and limitations in resolution of SBF-SEM imaging when analysing these small, poorly-contrasted structures.



D

	Cell 1	Cell 2	Cell 3	Cell 4	Mean	Standard deviation
Microneme volume (µm³)	3.66	3.14	1.78	4.12	3.18	1.01

E

	Cell 1	Cell 2	Cell 3	Mean	Standard deviation
Rhoptry volume (µm³)	0.1	0.56	0.12	0.26	0.26

Figure 3.16. Micronemes and rhoptries volumes.

A) Single slice from SBF-SEM data on freshly-excysted sporozoites. Arrow indicates a rhoptry, arrowhead indicates a microneme. B) Surface-rendered models of micronemes (yellow) generated from SBF-SEM data. C) Surface-rendered models of rhoptries (purple) generated from SBF-SEM data. D) Quantification of micronemes volumes from segmented SBF-SEM data of four freshly-excysted sporozoites. E) Quantification of rhoptries volumes from segmented SBF-SEM data of three freshly-excysted sporozoites. Scale bars ~ 1 µm.

3.3.8. Organelle proportions

To understand the relative contributions of each organelle to the whole cell volume, I used the volumetric data described above to calculate organelle proportions in relation to whole cell volume. As displayed in Figure 3.17, I found that on average, refractile bodies comprised 36% of whole cell volume, nucleus and amylopectin granules each comprised 4% of whole cell volume, mitochondria comprised 2% of whole cell volume, acidocalcisomes comprised 1% of whole cell volume, micronemes comprised 5% of whole cell volume and rhoptries comprised <0.5% of whole cell volume.

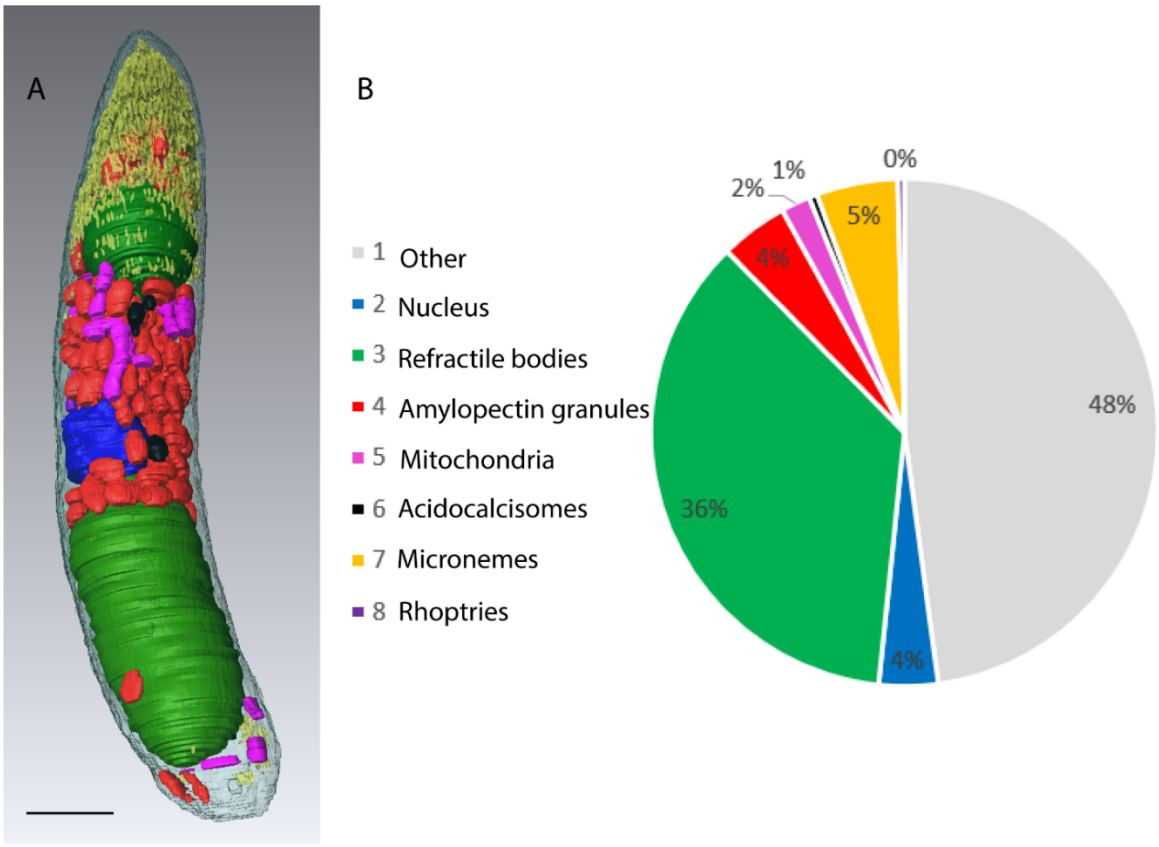


Figure 3.17. Volumetric organelle composition of freshly-excysted sporozoites.

A) Surface-rendered model generated from SBF-SEM data of a freshly-excysted sporozoite. The nucleus (blue), refractile bodies (green), amylopectin granules (red), mitochondria (pink), acidocalcisomes (black), micronemes (gold) and rhoptries (not visible) were all segmented. B) Volumetric organelle composition of freshly-excysted sporozoites. Percentages were calculated using the mean value from all sporozoites segmented and with 100% representing the average whole cell volume. For nucleus, refractile bodies, amylopectin granules, mitochondria and acidocalcisomes, n = 19 sporozoites; for micronemes, n = 4 sporozoites and for rhoptries, n = 3 sporozoites. Scale ~ 1 µm.

3.3.9. Summary of findings from quantitative ultrastructural analysis of freshly-excysted sporozoites

To summarise the results displayed in sections 3.3.1 to 3.3.8, investigation of whole cell and organelle morphometrics using SBF-SEM imaging revealed that there is considerable morphological variation between freshly-excysted sporozoites (Figs.3.10-15). Morphometric variation was assessed using both coefficient of variation (standard deviation as a percentage of the mean) and range. For each morphometric parameter assessed, coefficient of variation was greater than 17% (Table 3.1, COV) and data ranged by a factor of ≥ 1.79 (Table 3.1, min/max). Sporulated coccidian oocysts represent a static biological state, and freshly-excysted sporozoites are non-dividing cells. For these reasons, the extent of morphological variation observed in these data was surprising.

Greater nucleus, refractile bodies, mitochondria and acidocalcisomes volumes were all associated with a larger overall sporozoite cell volume. Comparison of mean organelle volumes with mean

whole cell volume revealed that the refractile bodies occupy 36% of the entire cell volume (Fig.3.17B).

Table 3.1. Whole cell and organelle morphometric data following SBF-SEM imaging and quantitative analysis of 19 freshly-excysted sporozoites

Cell identity	Whole cell volume (µm³)	Nuclear volume (µm³)	Refractile bodies volume (µm³)	Refractile body number	Amylopectin granules volume (µm³)	Amylopectin granules number	Mitochondria volume (µm³)	Mitochondria number	Acidocalcisomes volume (µm³)	Acidocalcisomes number	Micronemes volume (µm³)	Rhoptries volume (µm³)
8	36.46	2.05	10.51	2	1.16	151	1.04	8	0.19	6		
21	41.72	1.89	13.69	2	2.61	NA	0.98	13	0.22	9	3.14	
22	46.95	1.59	14.9	2	5.15	134	0.82	23	0.24	10	1.78	0.12
19	52.95	1.76	16.29	2	5.07	NA	0.47	23	0.31	12	4.12	0.1
3	53.35	2.46	16.99	3	1.03	274	1.15	14	0.45	12		
5	56.9	1.58	23.07	2	1.18	294	0.61	10	0.31	15		
2	58.46	2.37	18.52	2	2.01	161	1.08	8	0.32	13		
9	59.54	1.97	20.79	2	3.6	86	1.31	13	0.2	10		
15	60.14	2.26	23.37	3	1.02	234	1.12	12	0.36	14		
6	66.15	2.55	26.93	2	2.25	246	1.02	21	0.32	20		
12	66.99	2.28	22.85	2	3.48	149	1.07	9	0.39	21		
1	69.17	2.8	26.78	2	2.59	NA	1.44	26	0.33	14		
11	69.63	2.42	24.5	2	3.36	167	1.82	9	0.33	14		
10	69.91	2.67	23.19	2	2.96	255	1.34	10	0.45	16		
14	70.07	2.53	27.37	2	3.22	154	1.31	10	0.22	11		
7	70.28	2.4	26.07	2	1.47	240	0.99	14	0.5	14		
13	70.8	2.83	28.04	3	2.39	172	1.37	15	0.38	11		
20	72.2	2.79	26.42	2	3.41	281	1.33	14	0.34	8	3.67	0.56
4	72.38	2.59	29.2	2	2.5	139	1.38	15	0.29	14		
Mean (µm³)	61.27	2.30	22.08	2.16	2.66	196.06	1.14	14.05	0.32	12.84	3.18	0.26
Standard deviation (µm³)	10.86	0.40	5.45	0.37	1.22	63.30	0.31	5.44	0.09	3.72	1.01	0.26
COV ((SD/mean)*100)	17.7	17.2	24.7	17.4	46.0	32.3	27.1	38.7	26.8	28.9	31.9	100.0
Min	36.46	1.58	10.51	2	1.02	86	0.47	8	0.19	6	1.78	0.1
Max	72.38	2.83	29.2	3	5.15	294	1.82	26	0.5	21	4.12	0.56
Max/min	1.98519	1.7911	2.77831	1.5	5.0490196	3.418605	3.87234	3.25	2.631579	3.5	2.31461	5.6

By visualising the electron microscopy data and three-dimensional models generated using segmentation data I was able to confirm that cells had healthy ultrastructural appearances and that no drastic errors in segmentation had been made. In addition, only cells that were capable of active excystation were included in the sample which indicates a good degree of biological functionality.

This is the first time that organelle volumes have been quantified for a species of *Eimeria*. These quantitative, descriptive data may be useful to many aspects of coccidiosis research. To give some examples, the data could be used for predicting organelle, molecule or chemical quantities per unit of cells or as a reference for studies exploring morphological changes associated with life cycle progression or experimental perturbation.

3.3.10. **Sporozoite variation was also observed via light microscopy**

To confirm the prior assessment of freshly-excysted sporozoite morphometric variability and to generate more robust data, a light microscopy investigation of cell lengths and widths was carried out on a fresh set of parasites that were excysted and purified specifically for this experiment. Fifty

additional cells were measured to determine if this independent population also displayed a wide variation in cell size. Sporozoites were fixed using formaldehyde, imaged using phase contrast, and captured images were analysed using ImageJ ™ software.

Sporozoite cell length and width measurements were taken across the central axes (Fig.3.18A). Cell length ranged from 8 µm to 13.5 µm and cell width ranged from 2.7 µm to 4.5 µm. Average cell length was found to be 11.1 +/- 1.3 µm (Fig.3.18B) and average cell width was found to be 3.3 +/- 0.3 µm (Fig.3.18C). Length divided by width (length/width) was also calculated for each cell to provide a measure of cell shape. This ranged from 1.78 to 4.78. The coefficients of variation for length, width and length/width were 12.1%, 10.4% and 17.5% respectively.

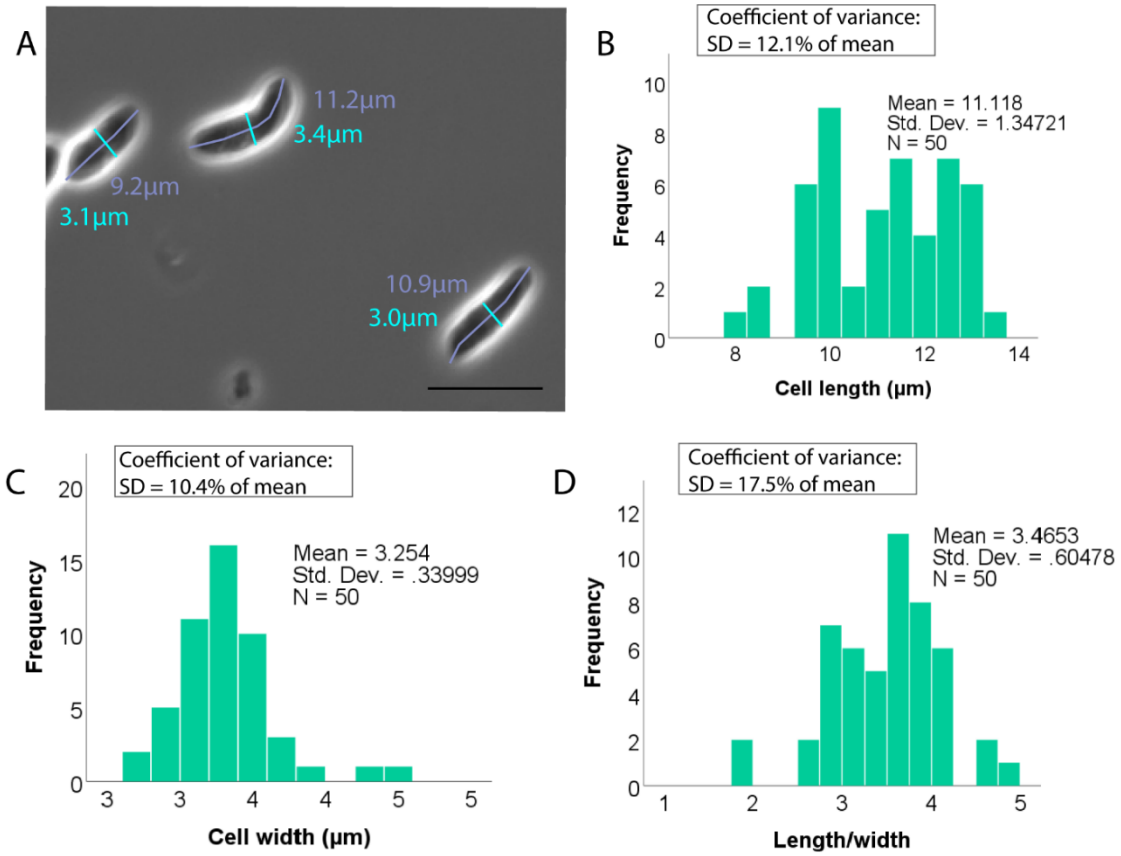


Figure 3.18. Light microscopy investigation of sporozoite morphometric variation.

A) Light microscopy image showing three freshly-excysted sporozoites. Sporozoite length and width measurements were taken from the centre of both the long and short cell axes and calculated using ImageJ ™ software. Scale bar ~ 10 µm. B) Distribution of cell lengths from 50 sporozoites. C) Distribution of cell widths from 50 sporozoites. D) Distribution of cell length/width values for 50 sporozoites.

These findings, in association with the SBF-SEM morphometric data, show that there is considerable variation in both cell size and shape within a single population of freshly-excysted sporozoites. Coefficient of variation values for sporozoite morphometrics obtained via light microscopy (Fig.3.18) were comparable to the coefficient of variation for sporozoite volume obtained following SBF-SEM investigation (Table 3.1). The presence of considerable sporozoite morphometric variation is thus demonstrated using multiple populations of sporozoites and multiple investigation methods.

3.4. **Investigation of morphological changes during development of *E. tenella***

3.4.1. **Sporozoite invasion of host cells**

In addition to the production of quantitative morphometric data on the subcellular structure of the *E. tenella* sporozoite, one of the aims of this project was to investigate dynamic morphological events that occur in the parasite and/or host cell during intracellular development of *E. tenella*. To qualitatively assess early post-invasion development, electron microscopy analysis of intracellular *E. tenella* sporozoites that had invaded MDBK-cells and were fixed at 2.5 hr post infection (same samples used to test the feasibility of SBF-SEM investigation) was performed.

On examination by electron microscopy, ultrastructural features including endoplasmic reticulum, mitochondria and nuclei could be visualised within the mammalian cells (Fig. 3.19A and B). In some of the cells, invaded sporozoites were present (Fig. 3.20A and B), contained within a parasitophorous vacuole membrane (Fig. 3.20A). Within the parasites, organelles such as the rhoptries (Fig. 3.20A), micronemes (Fig. 3.20A), amylopectin granules (Fig. 3.20A and B), nucleus (Fig. 3.20B) and refractile bodies (Fig. 3.20B) could be seen.

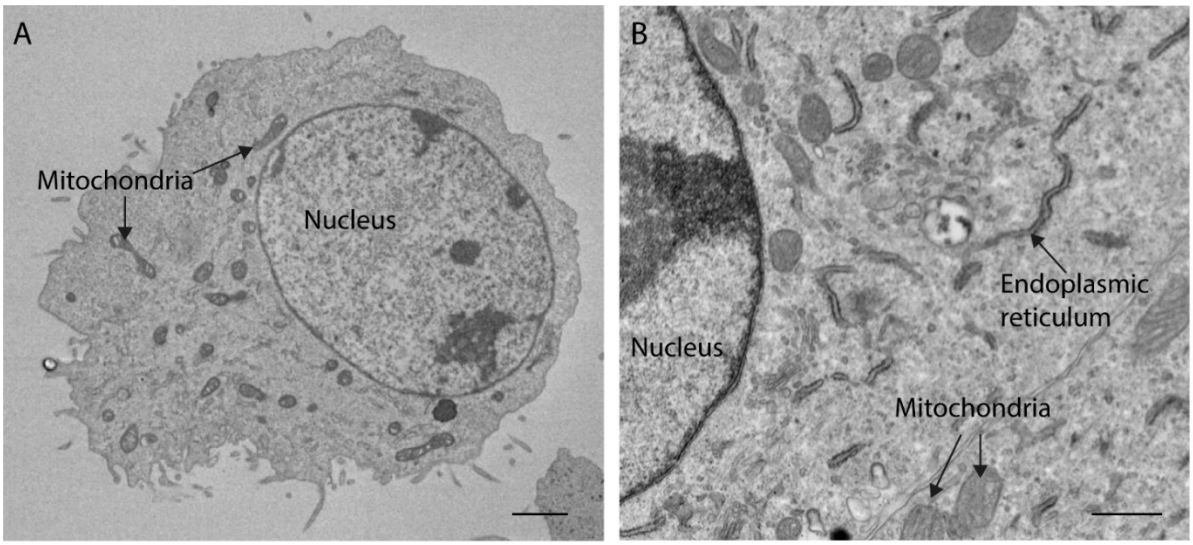


Figure 3.19. MDBK-cell ultrastructure observed by electron microscopy.

A) Single slice from SBF-SEM data showing an MDBK cell. The nucleus and mitochondria can be clearly seen. Scale ~ 1 µm. B) Transmission electron microscopy image from a 70 nm section of an MDBK cell. The nucleus, mitochondria and endoplasmic reticulum can all be discerned. Scale ~ 500 nm.

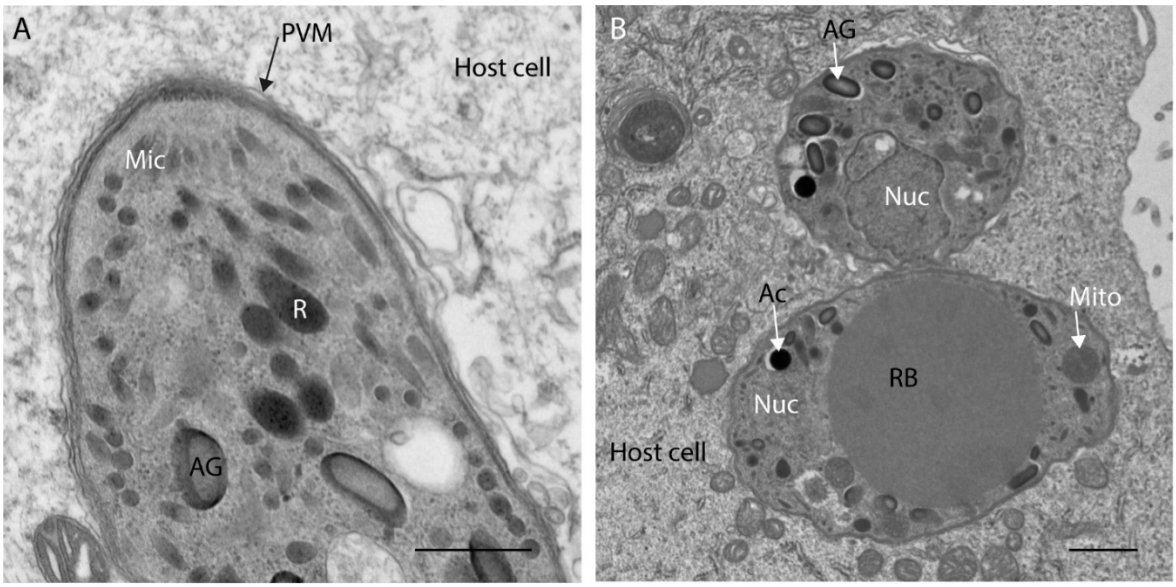


Figure 3.20. Sporozoite and host cell ultrastructure at 2.5hr post infection.

A) Transmission electron microscopy image of the apical tip of an intracellular sporozoite fixed at 2.5 hr following infection of MDBK cells. The sporozoite is contained within a specialised compartment bound by a parasitophorous vacuole membrane (PVM). Apical organelles, the micronemes (Mic) and rhoptries (R), can be seen. Amylopectin granules (AG) are also shown. B) Transmission electron microscopy image of two intracellular sporozoites at 2.5 hr post infection. Both sporozoites are found within a single host cell. Sporozoite organelles, including the nucleus (Nuc), refractile bodies (RB), acidocalcisomes (Ac), amylopectin granules (AG) and mitochondria (Mito), are shown. Scale ~ 500 nm.

The SBF-SEM data generated from the 2.5 hr post-infection sample consisted of two series; series one contained 326 slices with lateral resolution of 7.1 nm, axial resolution of 100 nm and lateral area

of 56.9 x 35.6 μm²; series two contained 365 slices with lateral resolution of 6.8 nm, axial resolution of 100 nm and lateral area of 54.6 μm². Within these data sets a total of 13 sporozoites were analysed (Fig. 3.21). In some cases (Fig. 3.21E and H), sporozoites were orientated so that their apical tip was near the host cell nucleus. Collectively, sporozoite orientation within the host cell appears to be random (Fig. 3.21A-M). When imaged by SBF-SEM, delineation of the parasitophorous vacuole was not visible. In general, a single refractile body was observed in intracellular sporozoites.

As described for the SBF-SEM data collected on freshly-excysted sporozoites, morphometric analysis was achieved through structure segmentation and volume calculations using AMIRA™ software. Figure 3.22 shows surface rendered models built from segmented data from six of the nine segmented intracellular sporozoites.

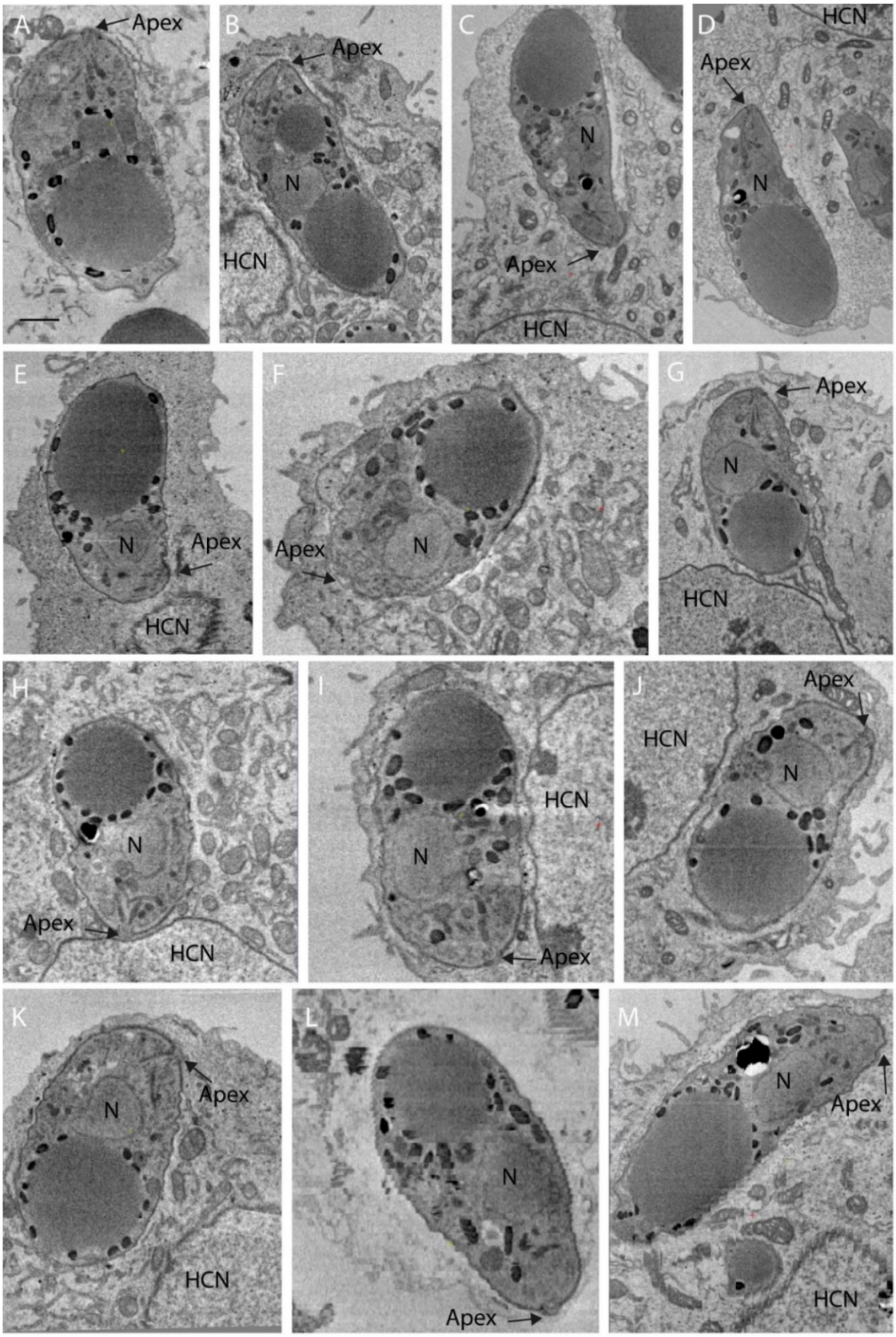


Figure 3.21. Thirteen 2.5hr post-infection sporozoites imaged by SBF-SEM.

A-M) SBF-SEM images showing the appearance of each sporozoite and, where possible, its orientation and location in relation to the host cell nucleus. In some cases, A, E, H, K, L + M, demonstration of parasite orientation was achieved through angled three-dimensional data sectioning using the slicer window in IMOD software (University of Colorado, Boulder). HCN = host cell nucleus, N = parasite nucleus, Apex = parasite apex. Scale ~ 1 μm.

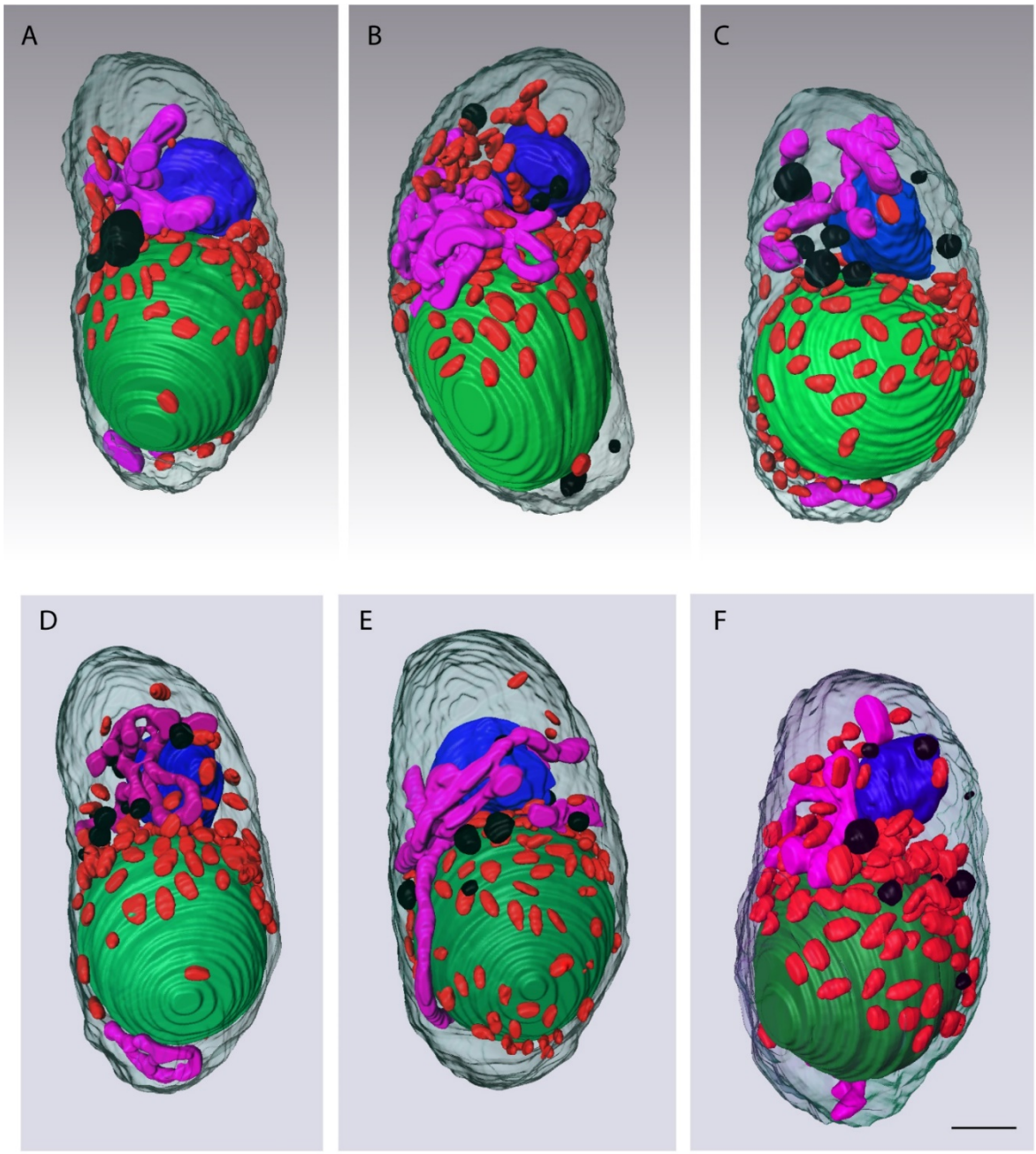


Figure 3.22. Surface-rendered models from sporozoites fixed at 2.5hr post infection.

A-F) Individual sporozoite models generated following segmentation of SBF-SEM data, showing nuclei (blue), refractile bodies (green), amylopectin granules (red), mitochondria (pink) and acidocalcisomes (black). Scale ~ 1 μm.

3.4.2. Schizont development within host cells

To qualitatively assess the ultrastructural characteristics of schizont development, sporozoites were added to MDBK cell monolayers and incubated at 41 ^{0}C and 5% CO_2 for 48- or 64- hr before fixation.

Developing schizonts can be observed in the 48hr sample (Fig. 3.23). Organelles such as endoplasmic reticulum and mitochondria, could be seen in the MDBK cells when viewed by transmission electron microscopy (Fig. 3.23A). Schizonts (Fig. 3.23B and C) containing multiple nuclei were seen within some of the host cells. These were contained within large parasitophorous vacuoles, delineated by a

parasitophorous vacuole membrane (Fig. 3.23B-E). Immature merozoite structures, such as the early conoid (Fig. 3.23D) could be seen at the periphery of some of the schizonts. Other intra-schizont structures were visualised, including microtubules and multi-laminar apicoplasts (Fig. 3.23E and F).

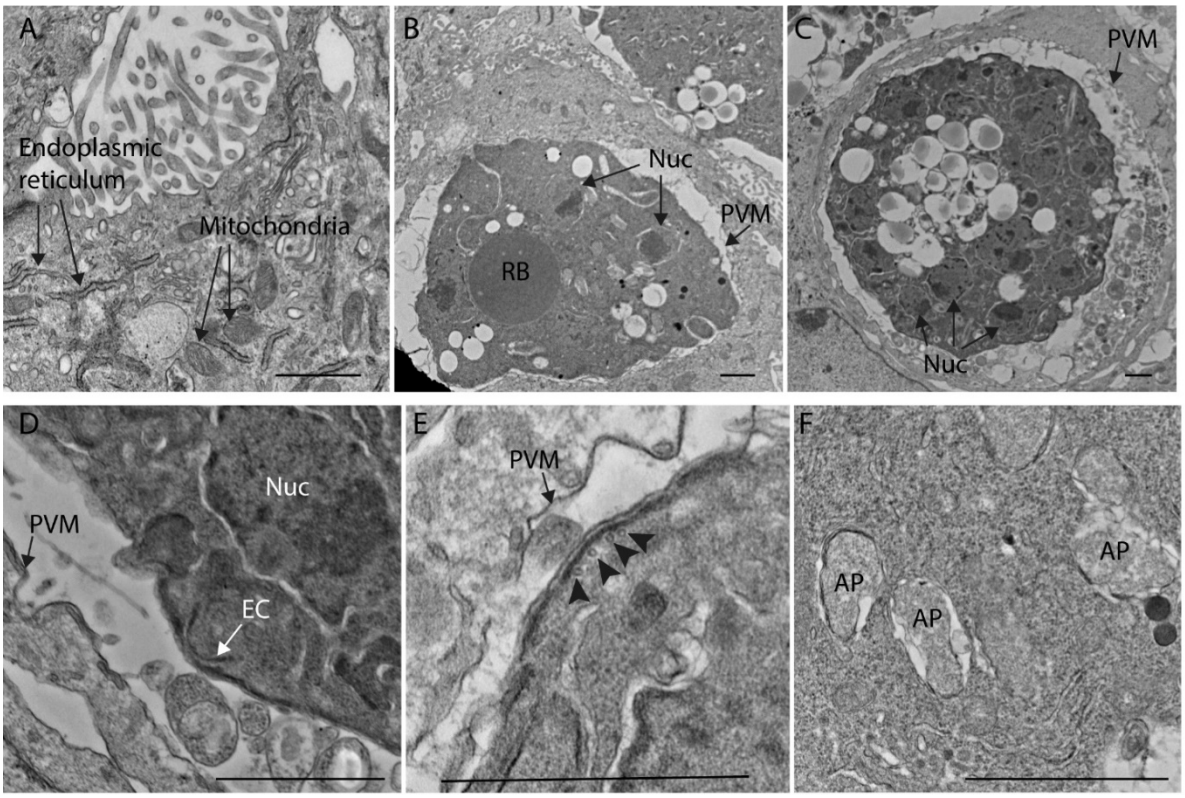


Figure 3.23. Schizont and host cell ultrastructure at 48hr post infection.

A) Transmission electron microscopy image of a host cell at 48hr post infection. Organelles including mitochondria and endoplasmic reticulum can be seen. B+C) Transmission electron microscopy images of parasite stages at 48hr post infection. Parasites contain multiple nuclei (Nuc) and reside within a specialised compartment in the host cell which is bound by a parasitophorous vacuole membrane (PVM). D) Transmission electron microscopy image showing early merozoite formation at the surface of a schizont, close to the parasitophorous vacuole membrane (PVM). A structure resembling the formation of an early conoid (EC) is seen near one of the schizont nuclei (Nuc). E) Transmission electron microscopy image of the surface of a schizont close to the parasitophorous vacuole membrane (PVM). Microtubules can be seen running below the multi-laminar schizont surface (arrowheads). F) Transmission electron microscopy image showing multiple apicoplasts (AP) within the cytoplasm of a schizont. Scale ~ 1 μm.

In the SBF-SEM data collected from the 48-hr sample, which consisted of 836 slices with lateral resolution of 8 nm, axial resolution of 75 nm and lateral area of 63.6 μm², a total of three schizonts were found (Fig. 3.24). By SBF-SEM, the parasitophorous vacuole membrane (Fig. 3.24A), schizont nuclei (Fig. 3.24A) and a single refractile body (Fig. 3.24A) could be identified. One of the schizonts was found to contain two nuclei (Fig. 3.24B), one schizont contained four nuclei (Fig. 3.24C) and one schizont contained 16 nuclei (Fig. 3.24D). As these nuclei numbers are all within a doubling sequence (e.g. 1, 2, 4, 8, 16 …) this preliminary data suggests co-ordinated nuclear division. As I was only able to collect data on nuclei from three schizonts, further analysis is required to assess this hypothesis.

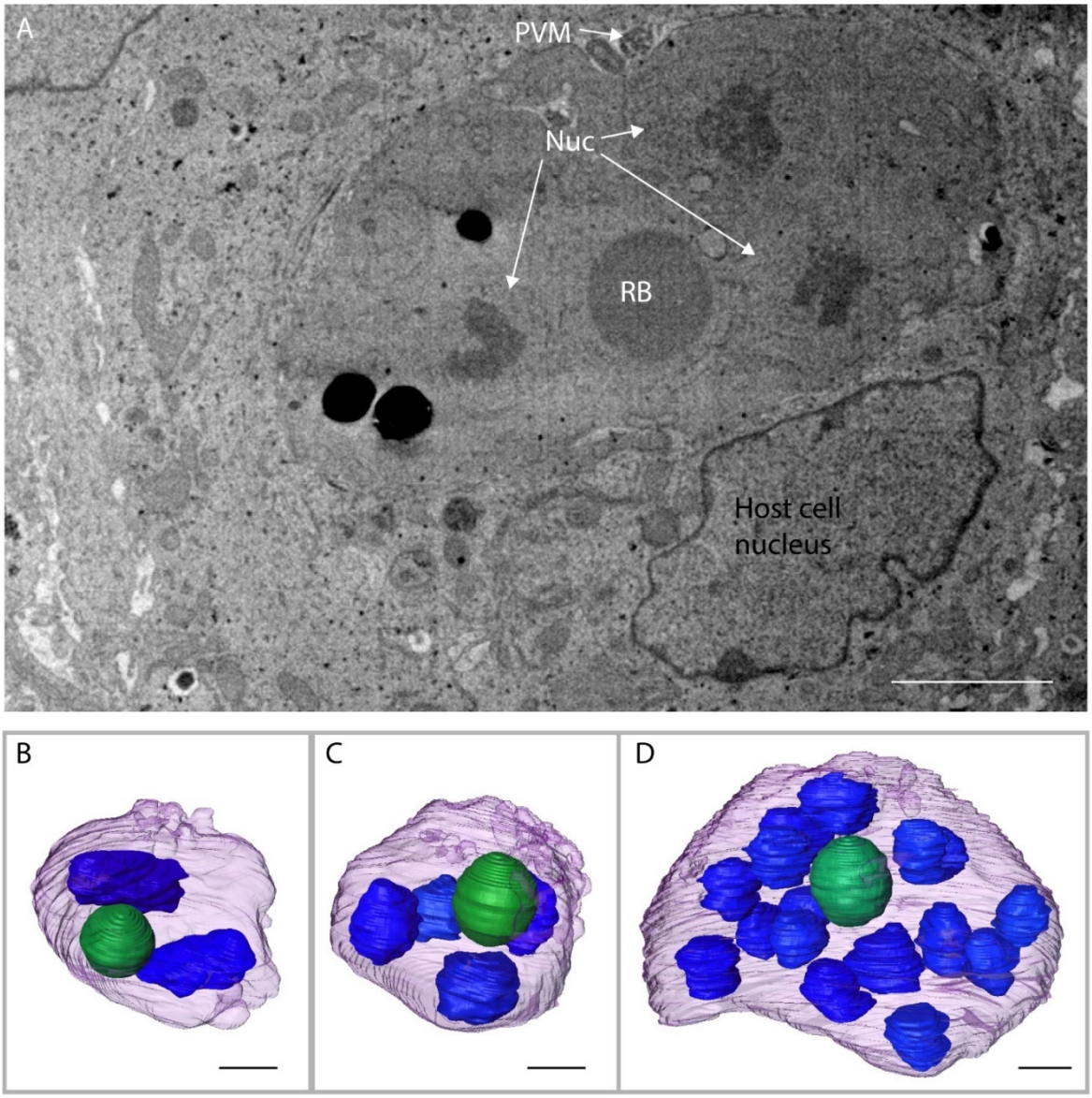


Figure 3.24. Nuclei numbers of the three schizonts imaged by SBF-SEM.

A) Single slice from SBF-SEM data showing a multi-nuclear schizont developing within a host cell at 48 hr post infection. (RB = refractile body, Nuc = nuclei, PVM = parasitophorous vacuole membrane). B - D) Surface-rendered models of the three schizonts found following SBF-SEM imaging of the 48hr post infection sample. B) Surface-rendered model of a schizont containing two nuclei (blue) and a single refractile body (green). C) Surface-rendered model of a schizont containing four nuclei (blue) and a single refractile body (green). D) Surface-rendered model of a schizont containing 16 nuclei (blue) and a single refractile body (green). Schizont outer surface is shown in purple. Scale ~ 2 μm.

Mature schizonts with early first generation merozoites were found at 64 hr of infection (Fig. 3.25). At this time point, damage to the monolayer is common with merozoite egress resulting in host cell rupture. In addition, prolonged incubation at 41^{o}C, although essential for parasite development, is sub-optimal for MDBK cells. Despite these limitations, successful harvesting and processing of a sample at 64 hr post-infection was achieved. Careful inspection of semi-thin sections by light microscopy enabled the detection of a maturely developed schizont. Subsequent imaging by

transmission electron microscopy revealed the presence of multiple merozoites (Fig. 3.25) contained within the parasitophorous vacuole membrane (Fig. 3.25A). Within the merozoites, apical complex structures including the micronemes (Fig. 3.25B) and conoid (Fig. 3.25B) were seen. These data suggest that the infection conditions used in my experiments were conducive to schizont development and merozoite formation.

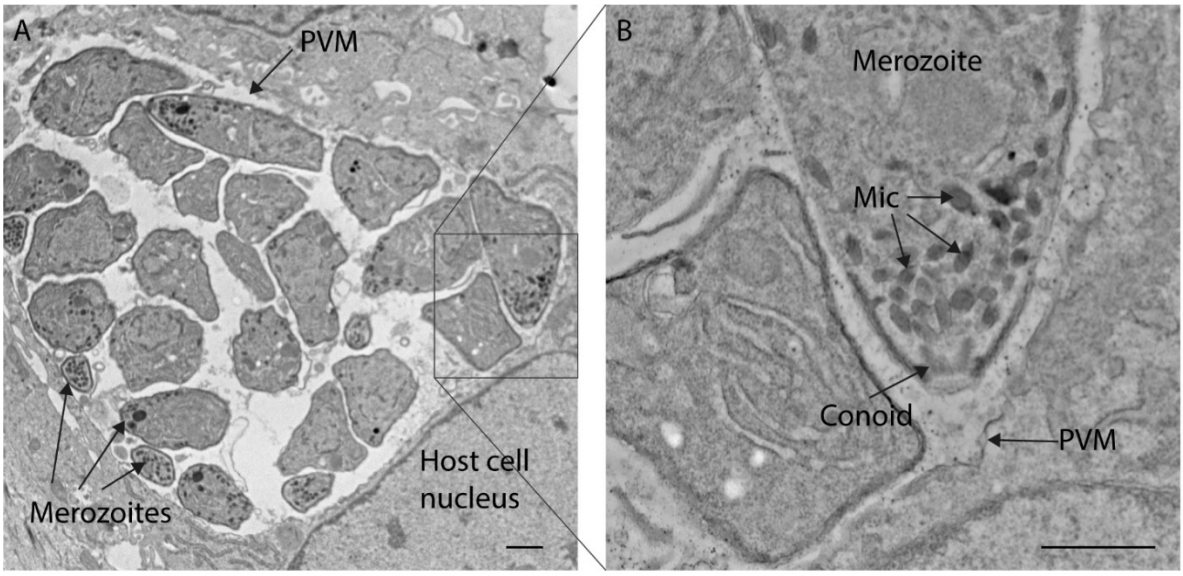


Figure 3.25. A mature *E. tenella* schizont seen at 64 hr post infection of cultured cells.

A) Transmission electron microscopy image of a mature schizont encased within a parasitophorous vacuole membrane (PVM) containing well-developed merozoites. Three merozoites are indicated by arrows. B) Higher magnification image from the schizont in (A). Merozoite organelles can be seen, including the micronemes (Mic) and conoid. Scale ~ 1 μm.

3.5. Morphometric changes within the first few hours of *E. tenella* sporozoite infection

3.5.1. Dynamic changes in cell shape, mitochondrial organisation and refractile body number in the initial hours after infection

To investigate morphological changes occurring in early sporozoite development, SBF-SEM-generated data on 2.5 hr post-infection parasites were compared with SBF-SEM-generated data on freshly-excysted sporozoites.

On visual comparison of surface rendered models of freshly-excysted sporozoites (Fig.3.7) with those of intracellular sporozoites (Fig.3.22), it was evident that significant morphological changes had occurred. In addition to cells appearing more elongated at 0 hr post infection (Fig. 3.26A and B) compared with those at 2.5 hr post infection (Fig. 3.26C and D) there was a reduction in the number of refractile bodies per cell (Fig.3.65E-G). Sixteen of the 19 freshly-excysted sporozoites analysed contained two refractile bodies with the remaining three sporozoites each containing three refractile bodies (Fig.3.26E). Of the nine intracellular sporozoites, seven contained a single refractile body and two contained two refractile bodies (Fig.3.26E). The refractile bodies of intracellular sporozoites

(Fig.3.26G) also appeared rounder in shape compared to those of the freshly-excysted cells (Fig.3.26F).

There were also changes to mitochondrial morphology. In freshly-excysted sporozoites, the mitochondria appeared to be more fragmented, with cells containing numerous globular mitochondrial units (Fig.3.26F). In intracellular sporozoites, large, branched mitochondria were frequently seen (Fig.3.26G).

These data suggest that despite a lag time of nearly two days before nuclear division is first observed (Pacheco et. al. 1975), sporozoites undergo highly dynamic cellular processes within the first few hours of infection.

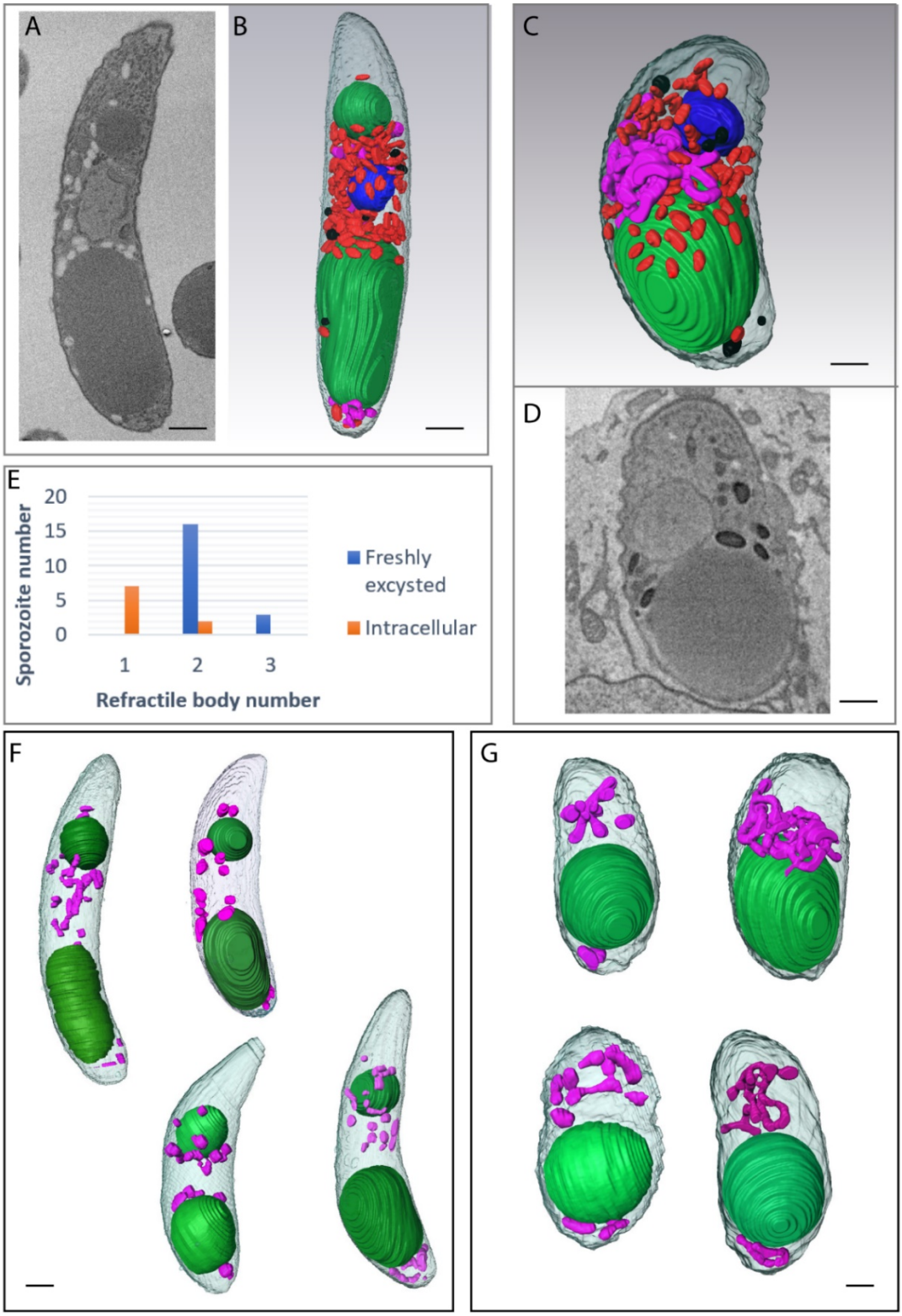


Figure. 3.26. Sporozoite morphology changes within the first 2.5 hr of infection.

A) Single slice from SBF-SEM data of a freshly-excysted sporozoite. B) Three-dimensional model from SBF-SEM data of a freshly-excysted sporozoite. C) Three-dimensional model from SBF-SEM data of a sporozoite at 2.5 hr post infection. D) SBF-SEM image of a sporozoite at 2.5 hr post infection. E) Numbers of freshly-excysted or intracellular (2.5 hr post infection) sporozoites containing either one, two or three refractile bodies. F) Three-dimensional models of freshly-excysted sporozoites showing refractile bodies (green) and mitochondria (pink). G) Three-dimensional models of sporozoites at 2.5 hr post infection showing refractile bodies (green) and mitochondria (pink). Scale bars ~ 1 µm.

3.5.2. **Volumes of the whole cell, nucleus, refractile bodies and mitochondria increase during the early stages of infection.**

To quantitatively assess the morphological differences observed between freshly-excysted and intracellular sporozoites, statistical comparisons on organelle volumes for the two types of sporozoite samples were performed.

Serial block face SEM data on nine 2.5 hr post-infection sporozoites were segmented using AMIRA^{TM}. Values for whole cell volume, nuclear volume, refractile bodies volume, mitochondrial volume, amylopectin granules volume and acidocalcisomes volume were generated for each cell. These values were compared to the values obtained for freshly-excysted sporozoites (Fig. 3.10-3.15). Statistical analysis revealed that the whole cell volume, nuclear volume, refractile bodies volume and mitochondrial volume all significantly increase during the first 2.5 hr of infection. Freshly excysted sporozoites (Fig.3.27A) had a mean cell volume of 61.3 μm^3 (Fig.3.27C) whereas intracellular sporozoites (Fig.3.27B) had a mean cell volume of 70.6 μm^3 (Fig.3.27C) ($p = 0.046$, Mann Whitney U).

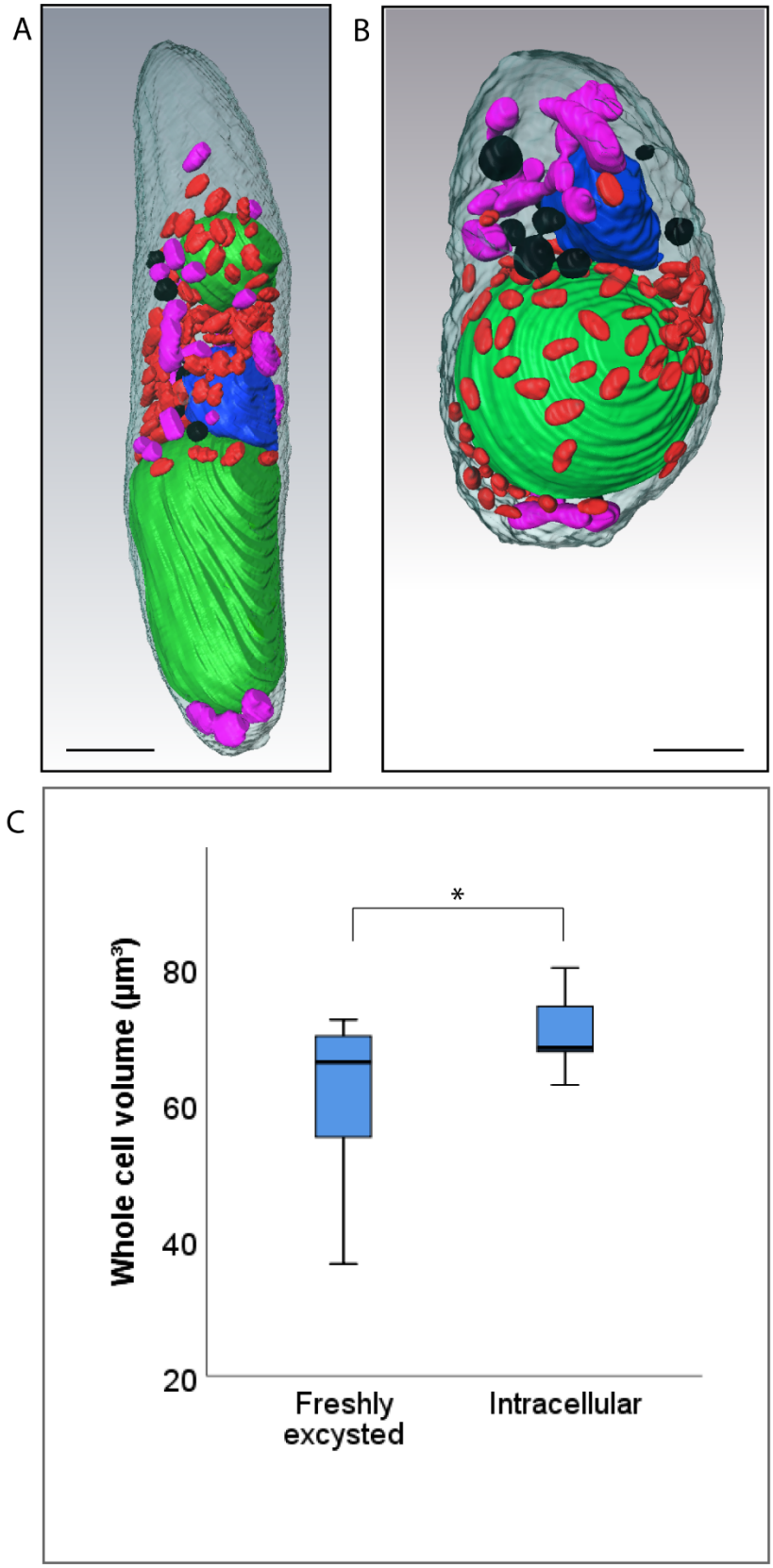


Figure. 3.27. Cell volume increase in sporozoites over the first 2.5 hr of infection.

A) Surface-rendered model of a freshly-excysted sporozoites. B) Surface-rendered model of an intracellular sporozoite at 2.5 hr post infection. C) Comparison of whole cell volumes between freshly-excysted sporozoites (n=19) and intracellular sporozoites (n=9). Statistical test = Mann-Whitney U, * = $p \leq 0.05$. Scale ~ 1 µm.

Mean nuclear volume for freshly excysted sporozoites (Fig.3.28A) was 2.3 μm^3 (Fig.3.28C) compared to 3.4 μm^3 in intracellular sporozoites (Fig.3.28B and C) (T-test, $p < 0.001$). Mean refractile bodies volume in freshly excysted sporozoites (Fig.3.28D) was 22.1 μm^3 (Fig.3.28F) compared to 26.9 μm^3 in intracellular sporozoites (Fig.3.28E and F) (T-test, $p = 0.02$). Freshly-excysted sporozoites (Fig.3.28G) had a mean mitochondrial volume of 1.1 μm^3 (Fig.3.28I) whereas intracellular sporozoites (Fig.3.28H) had a mean mitochondrial volume of 1.6 μm^3 (Fig.3.28I) (T-test, $p = 0.001$). A slight decrease in amylopectin granule volume from 0 hr to 2.5 hr post infection was also seen (Fig.3.29C) as well as an increase in acidocalcisome volume (Fig.3.29F), however neither of these changes were found to be statistically significant.

These data suggest that sporozoites undergo active developmental changes during the first few hours of infection.

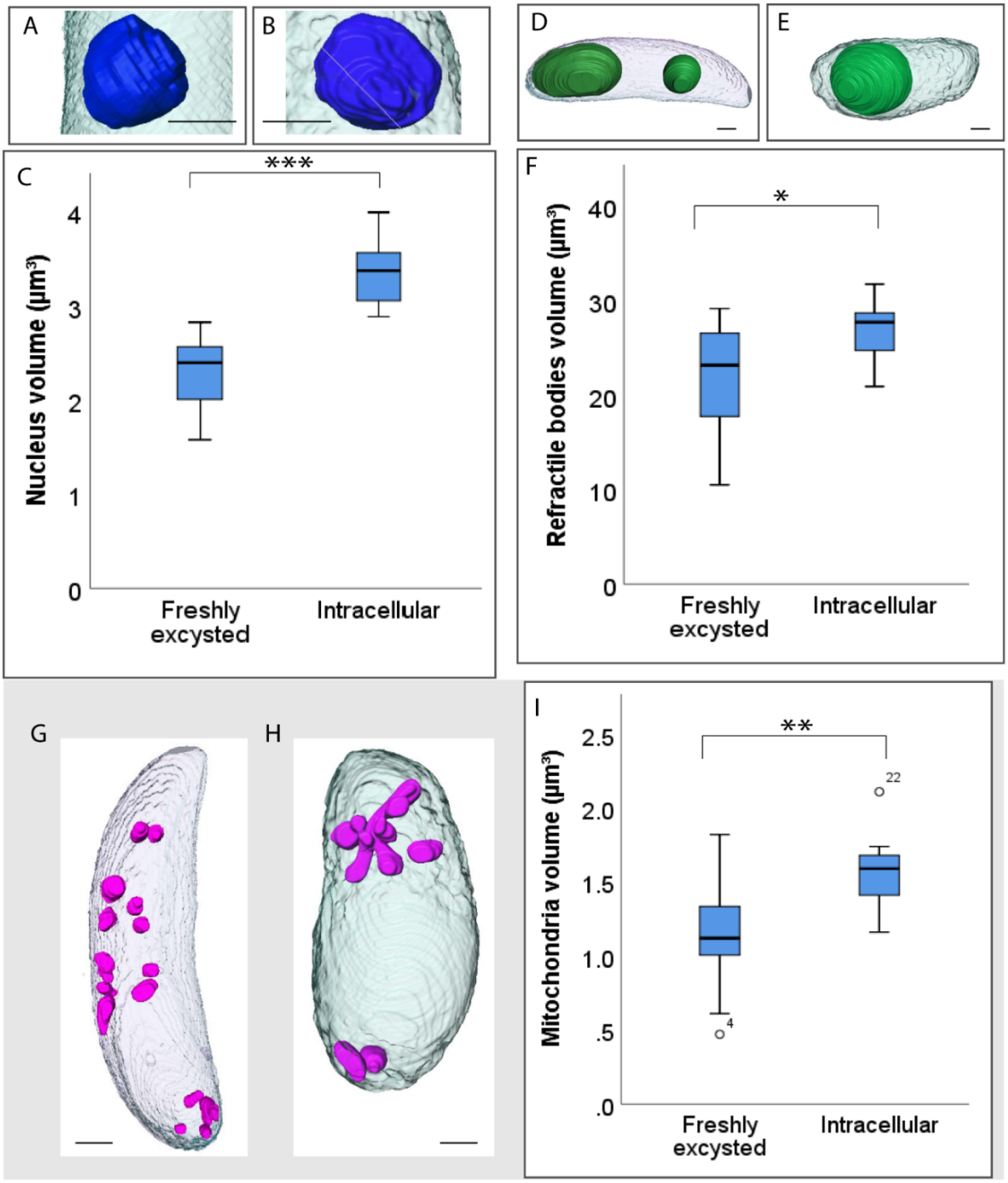


Figure 3.28. Changes in sporozoite nucleus, refractile bodies and mitochondria volumes within the first 2.5 hr of infection.

A) Three-dimensional model of a nucleus from SBF-SEM data of a freshly-excysted sporozoite B) Three-dimensional model of a nucleus from SBF-SEM data of a sporozoite at 2.5 hr post infection C) Comparison of nuclear volumes for freshly-excysted sporozoites (n=19) and intracellular sporozoites (n=9) calculated from segmented SBF-SEM data. D) Three-dimensional model of refractile bodies from SBF-SEM data of a freshly-excysted sporozoite E) Three-dimensional model of refractile bodies from SBF-SEM data of a sporozoite at 2.5 hr post infection F). Comparison of refractile bodies volumes for freshly-excysted sporozoites (n=19) and intracellular sporozoites (n=9) calculated from segmented SBF-SEM data. G) Three-dimensional model of mitochondria from SBF-SEM data of a freshly-excysted sporozoite H) Three-dimensional model of refractile bodies from SBF-SEM data of a sporozoite at 2.5 hr post infection I). Comparison of mitochondrial volumes for freshly-excysted sporozoites (n=19) and intracellular sporozoites (n=9) calculated from segmented SBF-SEM data. Statistical test = T-test; ** = $p \leq 0.01$, *** = $p \leq 0.001$. Scale bars ~ 1 µm.

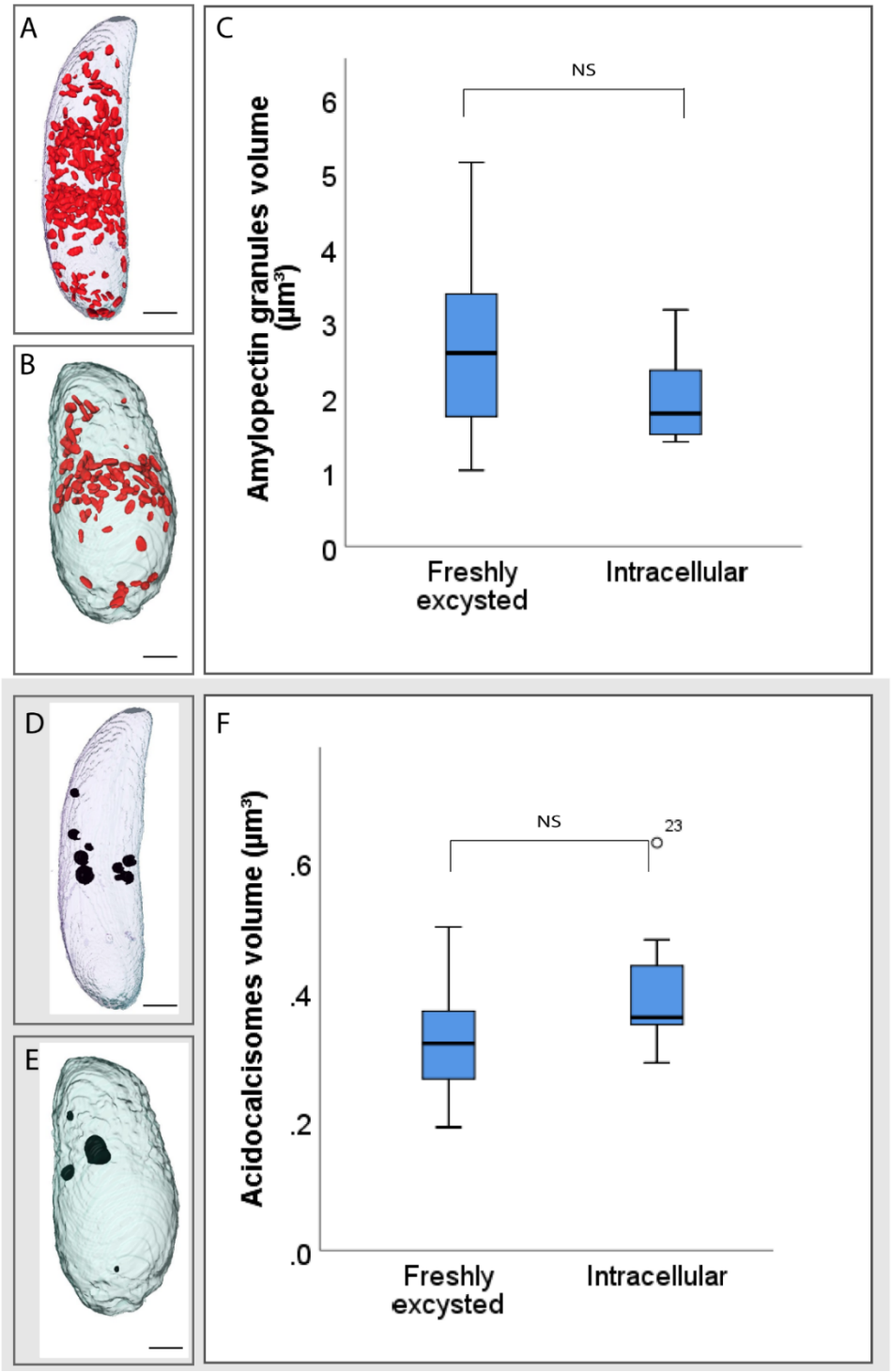


Figure 3.29. No significant changes to volumes of amylopectin granules and acidocalcisomes during the first 2.5 hr of infection.

A) Three-dimensional model of amylopectin granules from SBF-SEM data of a freshly-excysted sporozoite. B) Three-dimensional model of amylopectin granules from SBF-SEM data of a sporozoite at 2.5 hr post infection C) Comparison of amylopectin granules volumes for freshly-excysted sporozoites (n=19) and intracellular sporozoites (n=9) calculated from segmented SBF-SEM data. D) Three-dimensional model of acidocalcisomes from SBF-SEM data of a freshly-excysted sporozoite E) Three-dimensional model of acidocalcisomes from SBF-SEM data of a sporozoite at 2.5hr post infection. F) Comparison of acidocalcisomes volumes for freshly-excysted sporozoites (n=19) and intracellular sporozoites (n=9) calculated from segmented SBF-SEM data. Statistical tests = Mann Whitney U (C) and T-test (F); NS = not significant at significance level 0.05. Scale bars ~ 1 µm.

3.5.3. **Analysis of sporozoite morphometric changes by light microscopy before and after host cell invasion**

Throughout the comparisons of freshly-excysted and intracellular sporozoites, it was assumed that the changes in morphology observed were dependent on parasite invasion of a host cell. To confirm that sporozoite morphological changes are dependent on host cell invasion, sporozoite morphometric values were compared following incubation of freshly excysted sporozoites in cell-culture medium (DMEM) with or without the presence of host cells. Widefield microscopy was used to capture images of sporozoites in each sample and morphometric measurements were made using ImageJ software. Length and width measurements were taken along the central axes of sporozoites from three samples generated in parallel: a control sample of sporozoites fixed in formaldehyde immediately following purification (Fig.3.30A) (n=50), a sample where sporozoites were incubated in medium without host cells for 6 hr (Fig.3.30B) (n=19) and a sample where sporozoites were incubated with cultured MDBK cells for 5 hr (Fig.3.30C) (n = 21).

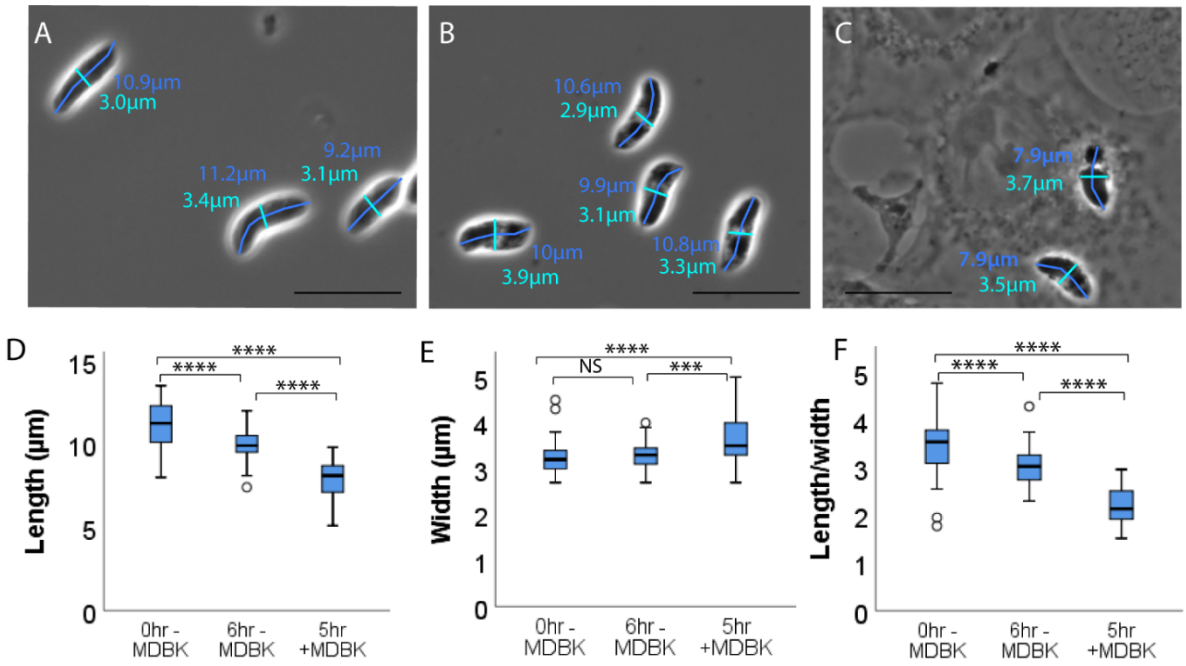


Figure 3.30. Sporozoite morphometric changes are dependent on the presence of host cells.

A) Light microscopy image of freshly excysted sporozoites added to DMEM and immediately fixed. B) Light microscopy image of sporozoites incubated in cell-culture medium for 6 hr prior to fixation. C) Light microscopy image of intracellular sporozoites at 5 hr post infection of MDBK cells. A to C) Sporozoite length and width measurements were taken from the centre of both the long and short cell axes. D to F) Comparison of cell morphometrics between sporozoites fixed without incubation in medium (0 hr -MDBK; n=50), sporozoites fixed following 6 hr incubation in medium without host cells (6 hr -MDBK; n=19) and sporozoites fixed at 5 hr following infection of host cells (5 hr +MDBK; n=21). Statistical test = One-way ANOVA, NS = not significant at 0.05 level, *** = $p \leq 0.001$, **** = $p \leq 0.0005$. Scale bars ~ 10 µm.

Mean sporozoite length was 11.12 +/- 1.35 µm in freshly-excysted sporozoites, 9.96 +/- 0.67 µm in sporozoites incubated for 6 hr in cell-culture medium and 7.94 +/- 1.14 µm in intracellular

sporozoites. Mean sporozoite width was 3.25 +/- 0.34 μm in freshly-excysted sporozoites, 3.23 +/- 0.28 μm in sporozoites incubated for 6 hr in cell-culture medium and 3.67 +/- 0.62 μm in intracellular sporozoites. Mean sporozoite length/width was 3.47 +/- 0.6 in freshly-excysted sporozoites, 3.11 +/- 0.33 in sporozoites incubated for 6 hr in cell-culture medium and 2.21 +/- 0.43 in intracellular sporozoites.

Statistical analysis revealed that intracellular sporozoites were significantly shorter compared to both freshly-excysted sporozoites ($p < 0.0005$, One-way ANOVA and post-hoc Turkey HSD) and sporozoites incubated for 6 hr in medium ($p < 0.0005$, One-way ANOVA and post-hoc Turkey HSD) (Fig. 3.30D). Sporozoites incubated in medium were also significantly shorter compared to freshly-excysted sporozoites ($p < 0.0005$, One-way ANOVA and post-hoc Turkey HSD) (Fig. 3.30D). Intracellular sporozoites were significantly greater in width compared to both freshly-excysted sporozoites ($p < 0.0005$, One-way ANOVA and post-hoc Turkey HSD) and sporozoites incubated for 6 hr in medium ($p = 0.001$, One-way ANOVA and post-hoc Turkey HSD) (Fig. 3.30E). No significant difference in cell width was found between freshly excysted sporozoites and sporozoites incubated in medium (One-way ANOVA and post-hoc Turkey HSD) (Fig. 3.30E). There were significant differences in length/width values between all three samples ($p < 0.0005$ for each comparison, One-way ANOVA and post-hoc Turkey HSD) (Fig. 3.30F).

These data suggest that morphological differences between freshly-excysted sporozoites and intracellular sporozoites, as investigated using SBF-SEM (Fig. 3.26, Fig. 3.27, Fig. 3.28), are partially dependent on sporozoite-host cell interaction. Significant differences in sporozoite morphology were found between each sporozoite sample (freshly-excysted sporozoites, sporozoites incubated in medium and intracellular sporozoites) (Fig. 3.30). Cell-shortening was found to occur independently of host-cell invasion (Fig. 3.30D), however intracellular sporozoites were still significantly shorter, wider and rounder compared to sporozoites incubated in cell-culture medium (Fig. 3.30D, E and F).

4. Loss of the anterior refractile body occurs via actin-dependent organelle merger

4.1. Introduction

Refractile bodies occupy more volume than any other organelle of *E. tenella* sporozoites, comprising on average 36% of the whole cell volume (Fig.3.17). They undergo significant changes in both volume and cellular configuration within the first few hours after infection (Fig.3.26, Fig.3.28F). Despite these intriguing properties, few studies have investigated the origins, functions or biological dynamics of refractile bodies. In freshly-excysted sporozoites, the refractile bodies are generally observed as a pair, one located anterior to the nucleus and termed the anterior refractile body and the other located posterior to the nucleus and termed the posterior refractile body. It is postulated that anterior refractile body loss can occur through a variety of mechanisms; merger of the anterior and posterior refractile bodies, fragmentation of the anterior refractile body and shrinkage of the anterior refractile body have all been described (Clark and Hammond 1969, Fayer 1969, Roberts et. al. 1970). In this investigation, the aim was to increase the understanding of refractile body dynamics in the early stages of infection using high resolution imaging and quantitative data analysis.

4.2. Nile red is a suitable marker for refractile bodies in *E. tenella*

As refractile bodies are large, micron-scale organelles, light microscopy can be used to investigate their structural dynamics. In a study investigating lipid dynamics of *Eimeria bovis* (Hamid et. al. 2015), Nile red was found to localise to the refractile bodies. I hypothesised that the use of Nile red would facilitate light-microscopy investigation of refractile bodies in *E. tenella.*

To confirm that Nile red is a suitable refractile body marker in *E. tenella,* a population of freshly excysted sporozoites were fixed in 4% formaldehyde and stained with 10 µg/ml Nile red. The Nile red signal was assessed for 200 cells using widefield fluorescence microscopy (excitation 559, emission 636).

When viewed by three-dimensional electron microscopy, a typical sporozoite contains a posterior refractile body, which is ovoid and fills the posterior half of the cell (Fig. 4.1A, PRB), and an anterior refractile body, which is spherical and situated at approximately one quarter of the cell length posterior to the apical tip of the sporozoite (Fig. 4.1A, ARB). In 93% of sporozoites analysed by light microscopy, Nile red was localised to an oval structure filling the posterior half of the cell (Fig. 4.1B, PRB) and a smaller, round structure at approximately one quarter of the cell length posterior to the apical tip of the sporozoite (Fig. 4.1B, asterisk). Based on morphological characteristics and homology between what was observed by light- and electron- microscopy, the large, oval structure corresponds to the posterior refractile body and the smaller, round structure corresponds to the anterior refractile body. In 6% of sporozoites analysed by light microscopy, Nile red localisation indicated an absence of the anterior refractile body (Fig. 4.1C) and in 1% of sporozoites, Nile red localisation indicated the presence of an additional anterior refractile body (Fig. 4.1D).

These data confirm that Nile red localises to the refractile bodies in *E. tenella*. It also shows that a small proportion of freshly-excysted sporozoites exhibit atypical refractile body configurations.

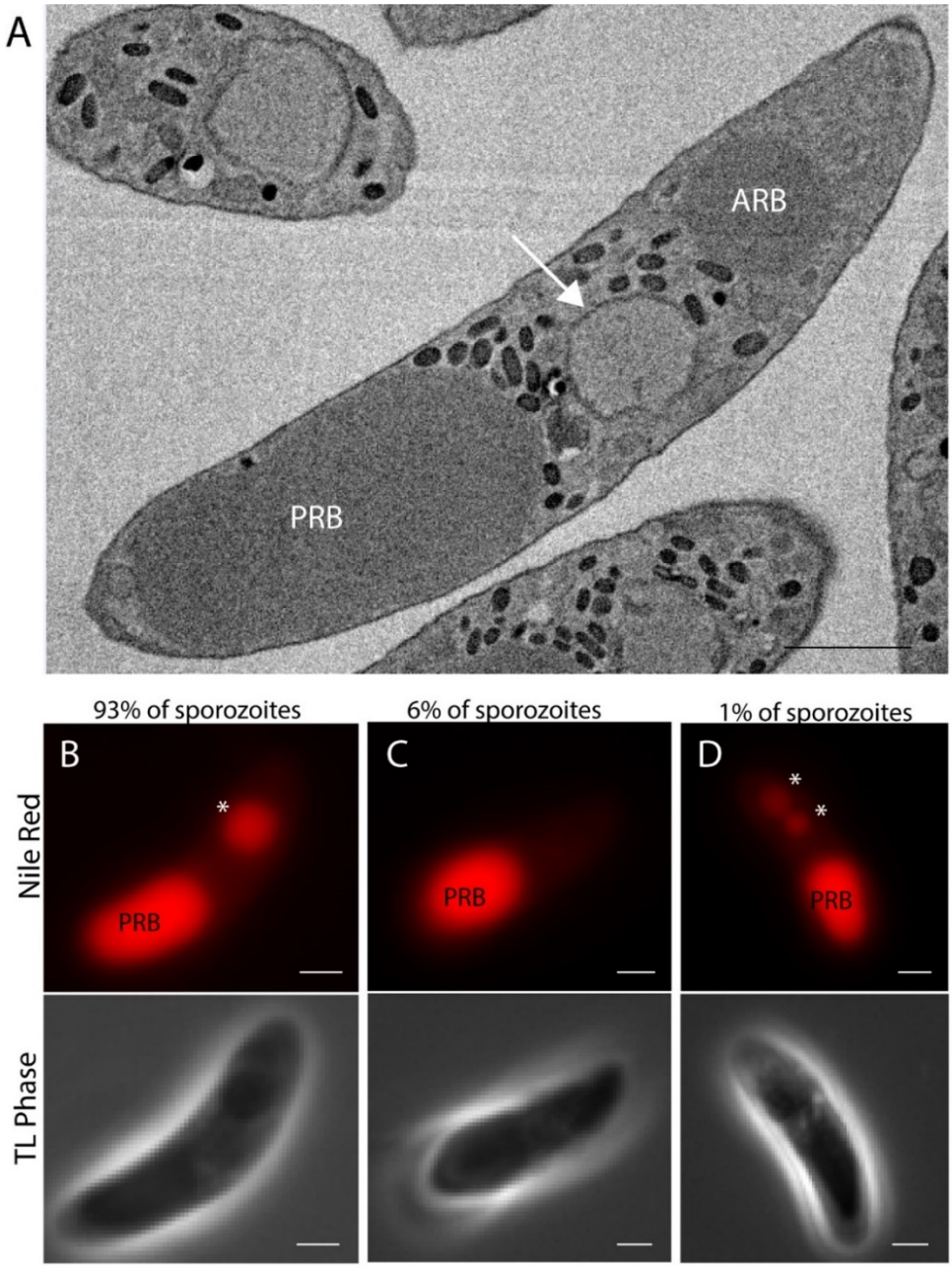


Figure 4.1. Localisation of Nile red staining in sporozoites.

A) Single section of SBF-SEM data showing a typical sporozoite which contains a large ovoid refractile body situated just posterior to the centrally located nucleus (arrow) and fills the posterior half of the cell (the posterior refractile body - PRB) and a smaller spherical refractile body situated just anterior to the nucleus (the anterior refractile body - ARB). B-D) Light microscopy images of freshly purified sporozoites stained with Nile red. B) Ninety-three percent of sporozoites showed Nile red localisations which correspond to the refractile body configuration seen in A. C) Six percent of sporozoites contained only the posterior refractile body. D) One percent of sporozoites contained an additional anterior refractile body. Anterior refractile bodies are indicated by asterisks; PRB = posterior refractile body. Scale bars ~ 1 μm.

4.3. **Loss of the anterior refractile body occurs from approximately two hours following infection**

Previous works by Fayer, Speer and Hammond have shown that *Eimeria* sporozoites lose their anterior refractile body following invasion of cultured cells (Fayer 1969, Fayer and Hammond 1969, Speer and Hammond 1970). This dynamic was temporally analysed for sporozoites of *E. bovis, E. meleagrimitis, E. adenoeides* and *E. callospermophi.* At 6 hr post infection, 58% of *E. meleagrimitis* were found to contain only the posterior refractile body, for *E. adenoeids* 53% were found to contain only the posterior refractile body at 3 hr post infection (Fayer 1969). A loss of anterior refractile body was also observed for sporozoites of *E. tenella,* however the exact temporal regulation of this has not been described (Fayer 1969).

To measure when anterior refractile body loss occurs for *E. tenella***,** MDBK cells were infected with freshly-excysted *E. tenella* sporozoites and fixed at 30 min, 1 hr, 2 hr, 3 hr, 4 hr and 5 hr post-infection. After staining with Nile red, intracellular sporozoites (Fig. 4.2A, arrows) were assessed for anterior refractile body presence (Fig. 4.2C, ARB) or anterior refractile body absence (Fig. 4.2, boxed in yellow).

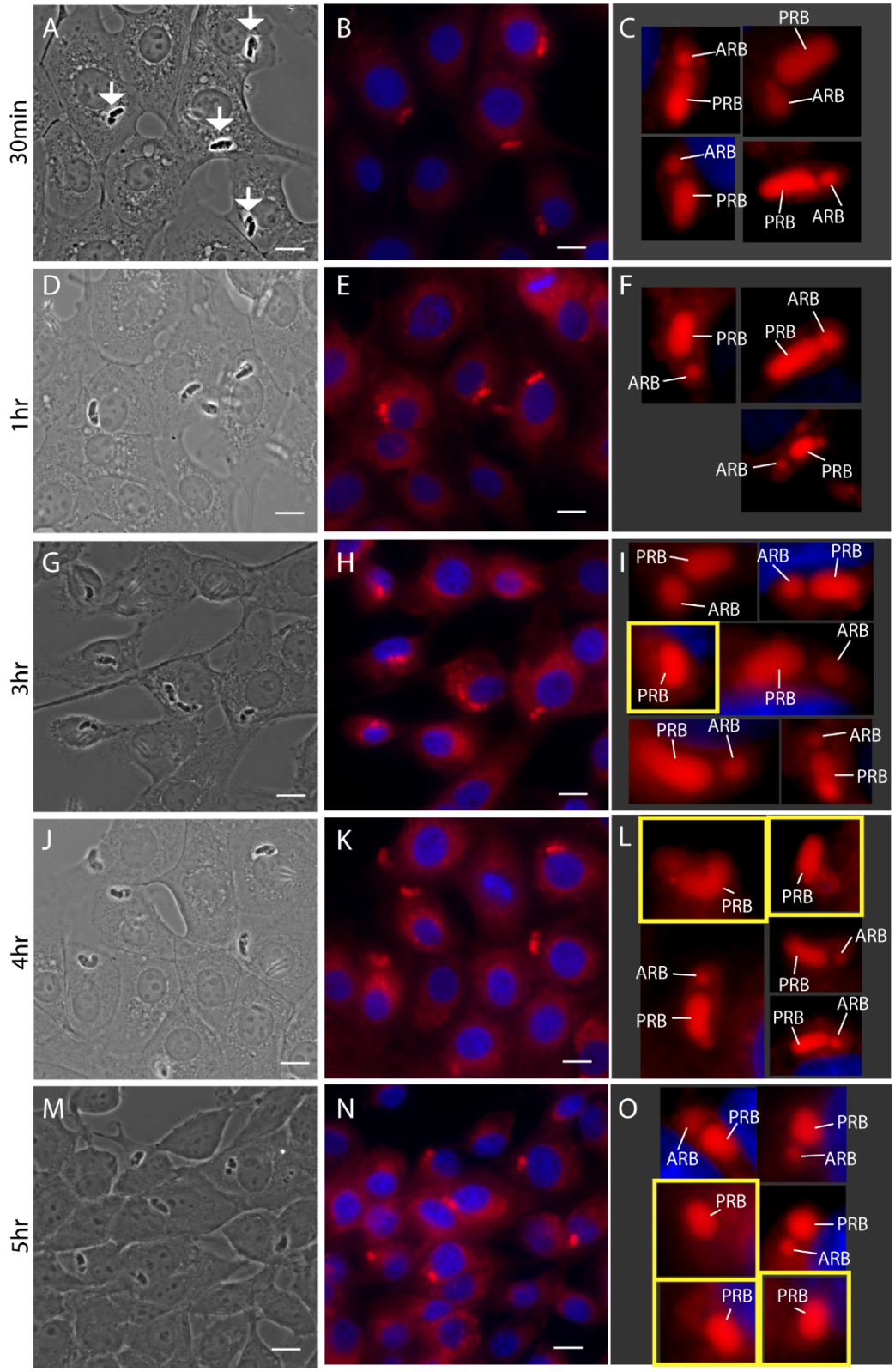


Figure 4.2. Loss of the anterior refractile body following host cell infection.

A to O) Light microscopy of sporozoites (arrows) within MDBK cells fixed at various time points following infection. Hoechst staining localises to host cell nuclei (blue), Nile red staining (red) localises to the anterior refractile body (ARB) and posterior refractile body (PRB). A to C) Cells fixed at 30 min post infection. D to F) Cells fixed at 1 hr post infection. G to I) Cells fixed at 3 hr post infection. J to L) Cells fixed at 4 hr post infection. M to O) Cells fixed at 5 hr post infection. After a few hours of incubation, sporozoites containing just the posterior refractile body (boxed in yellow) were found. Scale bars ~ 10 µm.

This experiment was performed twice, with triplicate samples in Experiment 1 (Fig. 4.3A) and duplicate samples in Experiment 2 (Fig 4.3B). Each data point was generated from analysis of at least 100 sporozoites.

Experiment1:

From 0 hr to 2 hr post infection, anterior refractile body presence decreased from 96% to 78% ($p = 0.04$, T-test). Between 2 hr and 5 hr post infection, anterior refractile body presence decreased from 78% to 22% ($p = 0.001$, T-test) (Fig. 4.3A).

Experiment2:

From 0 hr to 2 hr post infection, anterior refractile body presence changed from 92% to 93%. Between 2 hr and 5 hr post infection, anterior refractile body presence decreased from 93% to 56% ($p = 0.009$, T-test) (Fig. 4.3B).

For both experiments, there was little change in the percentage of parasites possessing an anterior refractile body from 0 hr to 2 hr post infection (Fig. 4.3A and B). In both experiments, there was a significant decrease in the percentage of cells containing an anterior refractile body from 2 hr to 5 hr post infection (Fig. 4.3A and B).

We conclude that anterior refractile body loss in *E. tenella* is likely to occur from ~2 hr post infection. This data also suggests that the majority of anterior refractile body loss occurs by ~5 hr post infection.

Of the three control samples, one was fixed immediately post-purification (Experiment 1) (Fig. 4.3A), one was incubated in host-cell-free medium for 3 hr (Experiment 1) (Fig.4.3A) and the third was incubated in host-cell-free medium for 5 hr (Experiment 2) (Fig. 4.3B). All three controls were at 0 hr post infection of host cells.

The percentage of sporozoites possessing an anterior refractile body for each control was 94%, 98% and 92% respectively. When compared to the percentages of anterior refractile body presence at 3 hr or 5 hr post infection of host cells (Fig. 4.3A and B), this data suggests that anterior refractile body loss only occurs in association with host-cell infection.

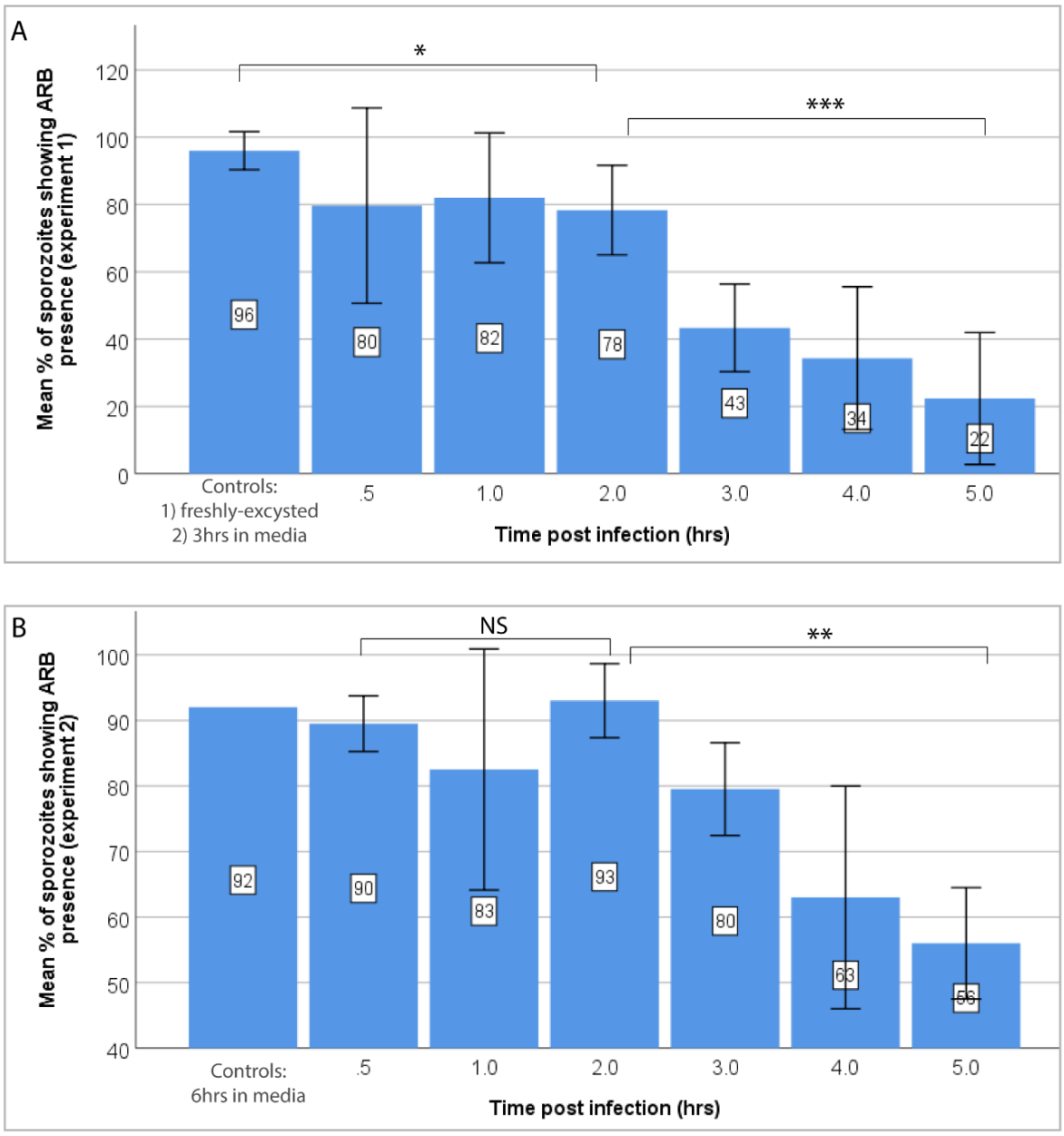


Figure 4.3. Temporal analysis of anterior refractile body loss.

Sporozoites, fixed at various times post infection of host cells, were assessed for anterior refractile body presence or absence (n ~ 100 for each count). A) Temporal dynamics of the percentage of sporozoites containing anterior refractile bodies for experiment 1. Anterior refractile body presence decreased from 96% to 78% over the first 2 hr of infection ($p = 0.04$, T-test). From 2-5 hr post infection, anterior refractile body presence decreased from 78% to 22% ($p = 0.001$, T-test). B) Temporal dynamics of the percentage of sporozoites containing anterior refractile bodies for experiment 2. There was little change in anterior refractile body presence over the first 2 hr (NS = no significant change between 0.5 hr and 2 hr). From 2 hr to 5 hr, anterior refractile body presence decreased from 93% to 56% ($p = 0.009$, T-test).

4.4. Total refractile body volume increases following anterior refractile body loss

In Chapter 3, morphometric changes associated with sporozoite infection and early intracellular development were investigated. Most freshly-excysted sporozoites contained two refractile bodies (21 out of 24, analysed by SBF-SEM) whereas most sporozoites at 2.5 hr contained a single posterior refractile body (7 out of 9, analysed by SBF-SEM) (Fig. 3.26E). The mean total refractile bodies volume was greater at 2.5 hr post-invasion compared to freshly-excysted sporozoites (Fig. 3.28F). This finding was unexpected and contradicts previous reports that size of the refractile bodies decreases following invasion of *Eimeria* species (Fayer and Hammond 1969, Speer and Hammond 1970).

To assess whether anterior refractile body loss leads to a change in refractile bodies volume, SBF-SEM imaging data from the freshly excysted and 2.5 hr post-infection sporozoites (described in more detail in chapter 3) was analysed further**.**

The refractile bodies volumes from all freshly excysted sporozoites containing both anterior and posterior refractile bodies (Fig.4.4A) (n=21) were compared with refractile bodies volumes from all sporozoites at 2.5 hr post invasion which contained only the posterior refractile body (Fig.4.4B) (n=13). Three freshly-excysted sporozoites were not included due to the presence of two anterior refractile bodies and two sporozoites at 2.5 hr post invasion were not included as they had not lost their anterior refractile body. Mean refractile bodies volume was significantly greater in sporozoites containing one refractile body at 2.5 hr post infection (26.3 +/- 3.7 µm²) than in freshly excysted sporozoites containing two refractile bodies (20.3 +/- 5.6 µm²) ($p = 0.002$) (Fig. 4.4C).

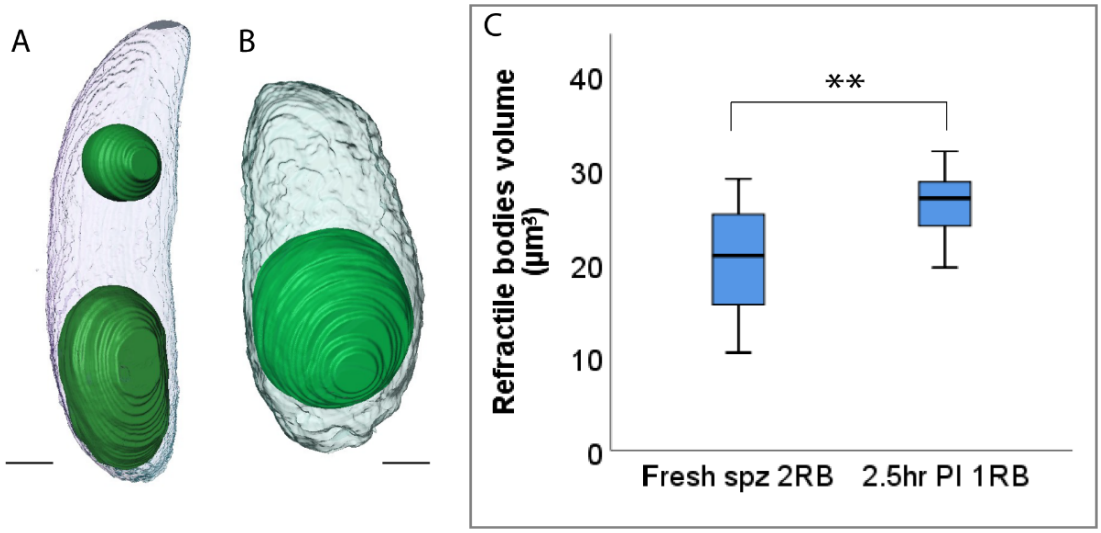


Figure 4.4. Refractile bodies volume increases following loss of the anterior refractile body.

A) Surface-rendered model of refractile bodies (green) from SBF-SEM data of a freshly-excysted sporozoite. B) Surface-rendered model of refractile bodies (green) from SBF-SEM data of a sporozoite at 2.5 hr post infection. C) Comparison of mean refractile bodies volume for freshly-excysted sporozoites containing two refractile bodies (n = 21) against sporozoites at 2.5 hr post infection containing one refractile body (n=13). Statistical test = T-test, ** = $p \leq 0.01$. Scale bars ~ 1µm.

These data confirm that anterior refractile body loss is associated with an increase in total refractile bodies volume.

Refractile body merger, as demonstrated in the work by Fayer (Fayer 1969), would partly explain this result, as it means anterior refractile body loss may occur without the loss of refractile body material from the cell. It is not clear what causes an *increase* in total refractile body volume (as opposed to remaining static) but possible explanations include a change in molecular conformation or increased refractile body protein synthesis.

4.5. Anterior refractile body loss occurs through merger between the anterior and posterior refractile bodies

4.5.1. Addition of Nile red does not affect anterior refractile body loss

In the studies described in sections 4.2 and 4.3, it was found that addition of Nile red greatly facilitated the assessment of anterior refractile body presence or absence.

To determine the feasibility of using Nile red staining to investigate refractile body dynamics in live cells and assess whether Nile red had any deleterious effect on sporozoite development, live sporozoites were treated with a series of Nile red dilutions. Sporozoites were added to MDBK cells in the presence 0.5 µg/ml, 1 µg/ml, 5 µg/ml, 10 µg/ml, 50 µg/ml or 100 µg/ml Nile red in 50 µl of acetone, with 50 µl of H_2O or acetone used as controls. Each condition was performed in duplicate and after 5 hr incubation each sample was fixed using formaldehyde. Widefield microscopy was used to assess anterior refractile body presence or absence for over 100 parasites per sample (Fig. 4.5).

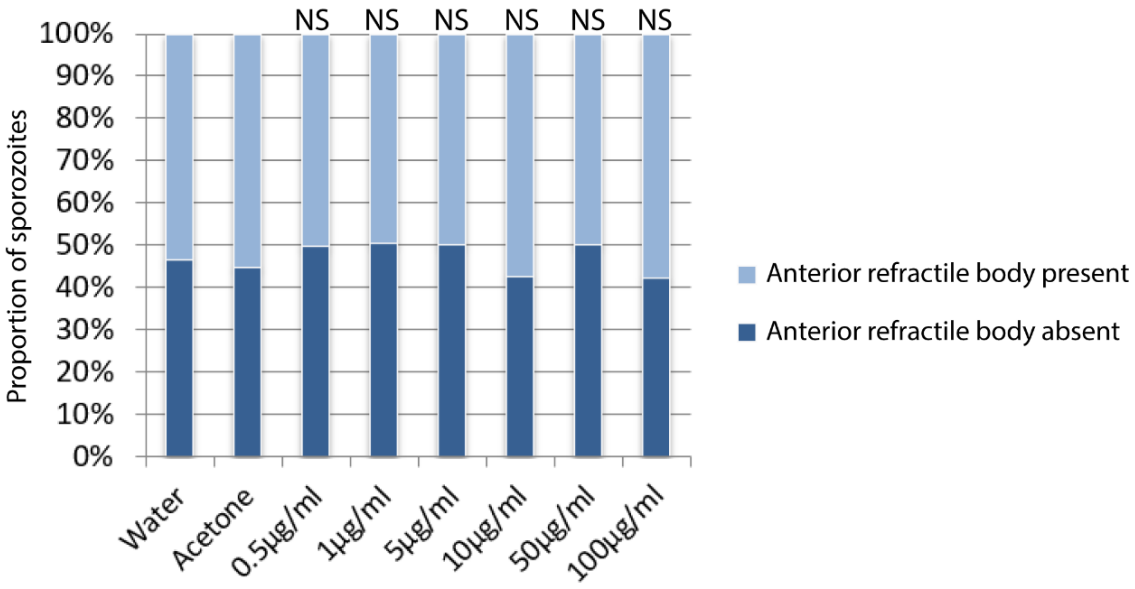


Figure 4.5. Effect of Nile red on anterior refractile body loss in live parasites.

Host cells were infected with sporozoites and incubated in the presence of varying concentrations of Nile red (or control) for 5 hr. Each column (n > 100 parasites) represents the proportion of anterior refractile body presence for a given dilution of Nile red (or control). No significant differences in anterior refractile body presence were found between the samples (NS) (Chi-squared analysis).

There were no significant differences in anterior refractile body presence between Nile-red treated samples and controls (Fig. 4.5, NS) (Chi-squared test). This data suggests that the addition of Nile red (between 0.5 µg/ml and 100 µg/ml) does not affect anterior refractile body loss. Nile red staining can therefore be used in live cells for the investigation of refractile body dynamics.

4.5.2. **Refractile body merger was identified as the only mechanism of anterior refractile body loss**

Anterior-refractile-body loss is hypothesised to occur through a variety of mechanisms, as both chemically fixed and live cell light microscopy investigations have described anterior refractile body shrinkage, fragmentation and merger with the posterior refractile body (Clark and Hammond 1969, Fayer 1969, Roberts et. al. 1970).

To describe and quantify the mechanisms of anterior refractile body loss in *E. tenella*, MDBK cells were infected with freshly-excysted sporozoites and stained with 10 µg/ml of Nile red. Live-cell confocal imaging was performed whilst appropriate incubation conditions were maintained (41^{0}C, 5% CO_2). In the first experiment, cells were imaged at 40x magnification, with continuous imaging from 2-4 hr post infection. Each field of view was changed after approximately 15 min of imaging to reduce the effect of thermal damage. In the initial experiment, seven sets of time-series data were generated, with frame rates between 4 and 9 seconds. In a second experiment, images were captured using 60x magnification, rather than 40x, with a frame rate of 7.6 seconds.

To detect events of anterior refractile body loss, I first identified which sporozoites did not contain an anterior refractile body at the end of each time series (Fig. 4.6A, blue arrows). The initial frame was then assessed to see which of these sporozoites had contained both an anterior refractile body (Fig. 4.6A, yellow arrows) and a posterior refractile body (Fig. 4.6A, white arrows) at the start of imaging. Over the seven time-series collected at 40x magnification, 19 sporozoites were captured undergoing anterior refractile body loss. By moving through the temporal data for each cell, I was able to find the frames capturing the moment of each anterior refractile body loss.

Time-lapse light microscopy data of each anterior refractile body loss event is shown in Fig.4.6, with each row (Fig. 4.6Ai-Axix) representing data from a single cell. For each cell, the first frame shows a time point where both the anterior refractile body (Fig. 4.6A, yellow arrows) and posterior refractile body (Fig. 4.6A, white arrows) are visible. For each cell, the final frame shows a time point where only a single refractile body is present (Fig. 4.6A, blue arrows). Time from the first frame is given in seconds, in the bottom right hand corner of each subsequent frame.

From the data collected at 60x magnification, one sporozoite was captured undergoing anterior refractile body loss (Fig. 4.6B). In the first few frames, both an anterior refractile body (Fig. 4.6B, yellow arrow) and a posterior refractile body (Fig. 4.6B, white arrow) can be seen. At around 60 seconds after the first frame, this same parasite contains just a single refractile body (Fig. 4.6B, blue arrow).

In all 20 cases observed (Fig. 4.6A and B), the mechanism of anterior refractile body loss was found to be merger/fusion between the anterior and posterior refractile bodies (Fig. 4.6A and B). No events of anterior refractile body loss by dissolution, shrinkage or fragmentation were observed.

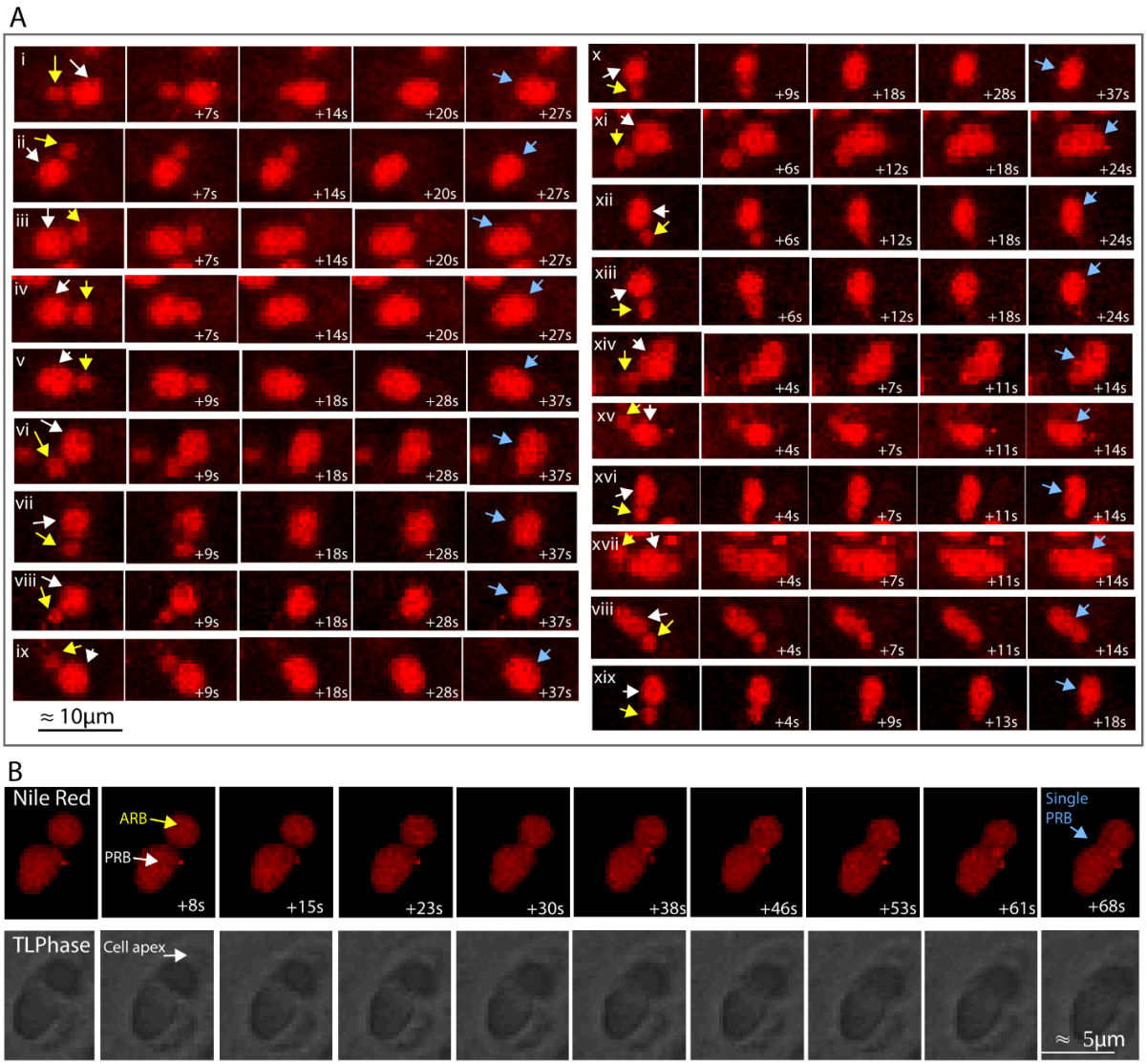


Figure 4.6. Refractile body merger is the predominant mechanism behind anterior refractile body loss.

Freshly purified sporozoites were added to MDBK cell cultures along with 10 µg/ml Nile red. During imaging, cells were maintained at 41°C and 5% CO_2. A) Light microscopy data of all events of anterior refractile body loss seen in a sample imaged from 2-4 hr post infection. In all 19 cases, the mechanism of anterior refractile body loss was fusion/merger with the posterior refractile body. In all 19, the first time point shown sees a smaller anterior body (yellow arrow) positioned close to the large posterior body (white arrow). In under 40 seconds, the anterior body has completely fused with the posterior body, leaving the cell with a single refractile body (blue arrow). B) Light microscopy data of a single event of refractile body merger captured at 60x magnification.

In freshly-excysted sporozoites, the anterior refractile body (Fig. 4.7A and B, ARB) is situated a couple of microns anterior to the posterior refractile body (Fig. 4.7A and B, PRB) with the nucleus situated between the two refractile bodies (Fig. 4.7B). In the minutes prior to merger, the anterior refractile body (Fig. 4.6A, yellow arrows; Fig. 4.7C, ARB) was observed to be close to the posterior refractile body (Fig. 4.6A, white arrows, Fig.4.7C, PRB). Once the 2 refractile bodies make contact, completion of merger (as determined by smooth outline of the posterior refractile body) occurred within 60 seconds (Fig.4.6A and B).

Transmission electron microscopy investigation of a sample fixed at 3 hr post infection also showed a sporozoite where the anterior refractile body (Fig. 4.7D, ARB) was close to the posterior refractile body (Fig. 4.7D, PRB). In this image, the anterior refractile body (Fig. 4.7D, ARB) is situated adjacent to the nucleus.

In summary, these data establish that anterior refractile body loss in *E. tenella* occurs through refractile body merger and this involves movement of the anterior refractile body towards the posterior refractile body. The process of merger occurs over a 60 second time window and refractile body merger is most likely to occur between 2 hr and 5 hr following invasion of host cells.

This is the first detailed assessment of how anterior refractile body loss occurs in *E. tenella* sporozoites. Nineteen events of anterior refractile body loss were captured and each event was shown to occur through refractile body merger; from here on in I can confidently describe anterior refractile body loss as refractile body merger or fusion. This is also the first study to establish the speed of refractile body merger; this is the time taken from first contact between the anterior and posterior refractile bodies to completed structural merger.

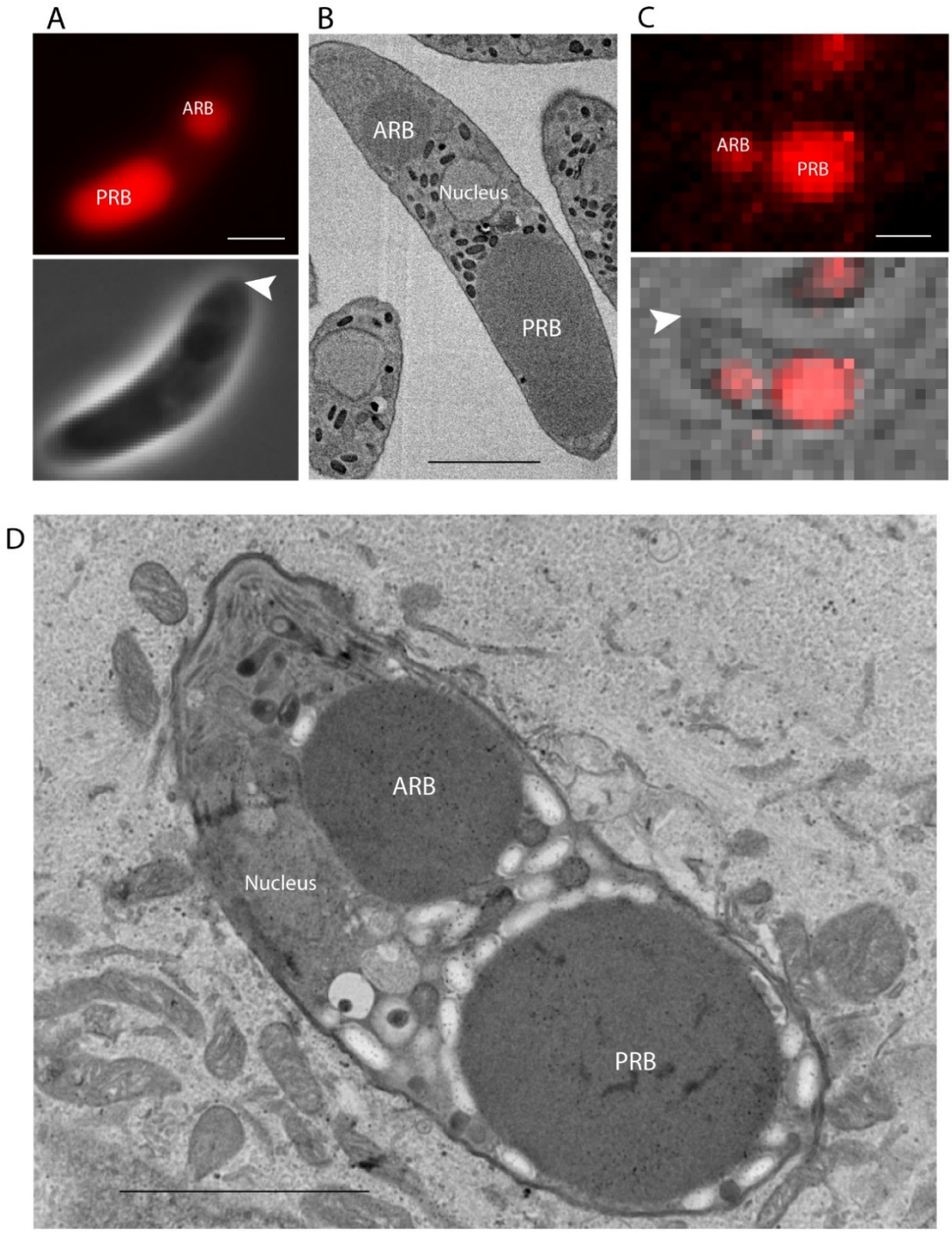


Figure 4.7. Prior to refractile body merger, the anterior refractile body (ARB) adopts a position close to the posterior refractile body (PRB).

A) Light microscopy of a freshly-excysted sporozoite, stained with Nile red, where there is an ~ 2 µm gap separating the anterior refractile body (ARB) and posterior refractile body (PRB) (arrowhead indicates cell apex). B) SBF-SEM image of a freshly-excysted sporozoite where there is an ~ 2 µm gap separating the anterior refractile body (ARB) and posterior refractile body (PRB). The nucleus resides between the two refractile bodies. C) Light microscopy data of a sporozoite stained with Nile red and captured prior to undergoing refractile body merger (taken from figure 4.6Ai). There is less than 1 µm between the anterior refractile body (ARB) and posterior refractile body (PRB). D) Transmission electron microscopy image of an intracellular sporozoite at 3 hr post infection of host cells. There is less than 1 µm between the anterior refractile body (ARB) and posterior refractile body (PRB). The anterior refractile body (ARB) is situated alongside the nucleus. Scale ~ 2 µm.

4.6. **Sporozoite shape change and actin dynamics are associated with refractile body merger**

4.6.1. **Refractile body merger is dependent on sporozoite actin**

Having established that the primary cause for anterior refractile body loss is merger between the anterior and posterior refractile bodies, I wanted to investigate the biological mechanisms that are involved in this merger. In recent years, there have been several investigations into 'proteinaceous membrane-less organelles' (PMLO's) (Nott et. al. 2015, 2016, Uversky 2017, Zaslavsky et. al. 2018), sometimes known as 'droplet organelles' (Courchaine et. al. 2016) or 'biomolecular condensates' (Banani et. al. 2017). One paper defines PMLO's as being 'characterized by liquid-like behaviour, being able to drip, fuse, wet, and relax to spherical structures upon fusion' (Darling et. al. 2018). According to this definition, I hypothesised that refractile bodies would fall into this category; they do not possess a limiting membrane (Fig.4.8A), and when viewed by electron microscopy posses similar morphology to droplet organelles synthesised in vitro (Li et. al. 2012) (Fig.4.8B). Droplet organelles are spherical in shape when static and exhibit fluid-like dynamics of fusion (Li et. al. 2012) (Fig.4.8C), these properties are also apparent in the refractile bodies of *E. tenella* (Fig.4.8D).

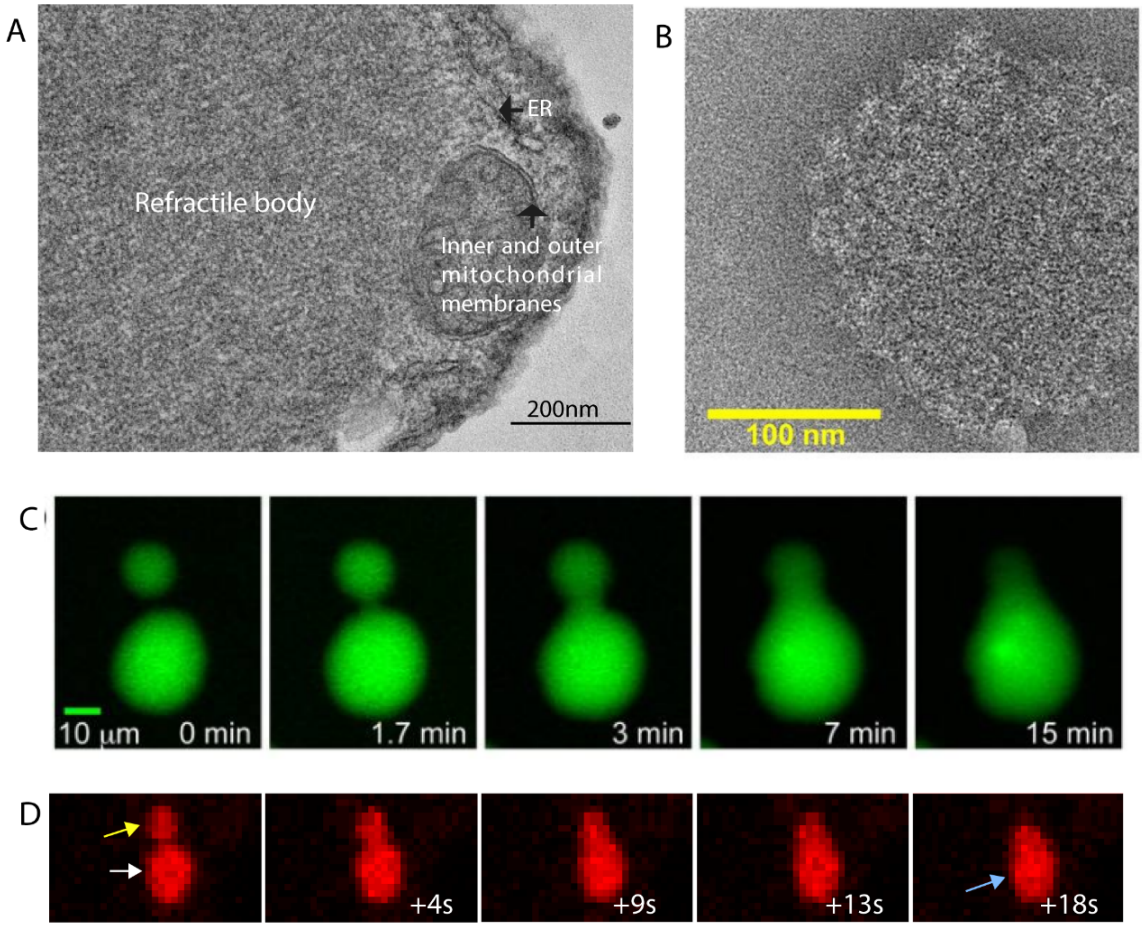


Figure 4.8. Refractile bodies share key characteristics with PMLO's.

A) Transmission electron microscopy image of a chemically fixed sporozoite. The refractile body appears to have a granular matrix which is not bound by a limiting membrane. Membranes of nearby mitochondria and endoplasmic reticulum (ER) are visible. B) Transmission electron microscopy image of an in-vitro synthesised droplet organelle (Li et. al. 2012). C) Light microscopy data of droplets of the protein mixture shown in (B). D) Light microscopy images of refractile bodies undergoing merger. The dynamics of refractile body merger (example panel taken from Fig.18) are remarkably similar to that of the coalescing droplets seen in (C).

Feric and Brangwynne (2013) studied the mechanisms behind fusion of nuclear PMLO's in oocytes of *Xenopus laevis*. They found that in untreated cells, a nuclear actin scaffold suspends the PMLO's, preventing their coalescence. On chemical disruption of filamentous actin, the nuclear PMLO's moved ventrally and fused together, resulting in less numerous, larger PMLO's. Reflecting on these findings with respect to the current investigations, I hypothesised that actin dynamics are associated with refractile body merger. An additional argument for proposing the involvement of actin, is that during extensive electron microscopy investigations of sporozoites, microtubules (the other main polymer involved in biomechanical movements in eukaryotic cells) were only ever observed at the parasite periphery and never in association with the refractile bodies.

To test the hypothesis that actin is involved in refractile body merger, anterior refractile body presence was assessed following actin disruption, at 5 hr post infection.

It is well established that filamentous actin is required for host cell invasion in apicomplexan species (Sibley 2004) and invasion by *E. tenella* sporozoites is blocked by the presence of actin-inhibiting drugs (Bumstead and Tomley 2000). Thus, assessing the impact of actin inhibitors on refractile body merger must be differentiated from their effects on invasion. In addition, the use of classical actin inhibitors to elucidate roles in parasite dynamics becomes more complex, as off-target effects on host cell must also be accounted for.

Since apicomplexan actin is divergent from other eukaryotic organisms (Dobrowolski et. al. 1997, Schmitz et. al. 2005, Skillman et. al. 2011) it is possible to use chemicals with differential effects on parasite and host actin. To my knowledge, there are no reports of drugs that specifically target apicomplexan actin without affecting the host; however, drugs affecting host-cell actin and not apicomplexan actin have been described. In *T. gondii* it was reported that when applying the actin inhibitors, Cytochalasin D (CytoD), Latrunculin A (LatA) and Jasplakinolide (Jas), both CytoD and Jas altered the parasite phenotype whereas LatA did not (Periz et. al. 2017, Whitelaw et. al. 2017). By comparing the effects of host and parasite actin inhibition with the effect of host-only actin inhibition, conclusions can be made about the specific role of parasite actin. The use of LatA alongside CytoD or Jas has previously been employed in *T. gondii* to determine whether phenotypic changes occur due to disruption of parasite actin, whilst controlling for effects on host cell actin (Periz et. al. 2017).

I tested the effect of CytoD (known to impair invasion of *E. tenella*: Bumstead and Tomley 2000) and LatA (not previously tested with *E. tenella*). Host cells were infected with freshly-excysted *E. tenella* sporozoites and incubated for 30 min prior to addition of CytoD, LatA or an equivalent volume of the diluent (DMSO) as control. Each test condition was performed in triplicate and two concentrations of CytoD and LatA were tested. Based on a review of previous concentrations used to disrupt actin in *Eimeria* species (Frölich and Wallach 2015, 2016), it was decided to use 200 nM CytoD and 1 µM CytoD. LatrunculinA, which has a narrower therapeutic range compared to CytoD, was used at 200 nM and 500 nM, based on evidence that these concentrations should have comparable effects on the host cell to treatment with 200 nM to 1 µM CytoD (Spector et. al. 1989).

Following treatment, samples were incubated for a further 4.5 hr, then fixed in 4% formaldehyde. Fixed cover slips were stained using Nile red, Hoechst and Phalloidin 488, the last of which labels filamentous actin. Each sample was imaged by widefield light microscopy (Fig. 4.9A to E) to quantify the percentage of sporozoites possessing anterior refractile bodies. For each sample, approximately 100 sporozoites were assessed and for each test condition, the percentage of sporozoites containing anterior refractile bodies was calculated as mean of the three samples.

In the control sample, 54.7% of sporozoites contained an anterior refractile body at 5 hr post infection (Fig. 4.9F). This number is similar to that seen in a previous experiment on the temporal dynamics of anterior refractile body loss (Fig. 4.3B). Even low concentrations of CytoD (200 nM) resulted in

a significant increase in the percentage of sporozoites retaining an anterior refractile body (80.2%) compared to the control ($p = 0.001$ One Way ANOVA and post-hoc Turkey HSD). Only high concentrations of LatA (500 nM) significantly affected the percentage of sporozoites possessing an anterior refractile body (68.3%) compared to the control ($p = 0.048$, One Way ANOVA and post-hoc Turkey HSD).

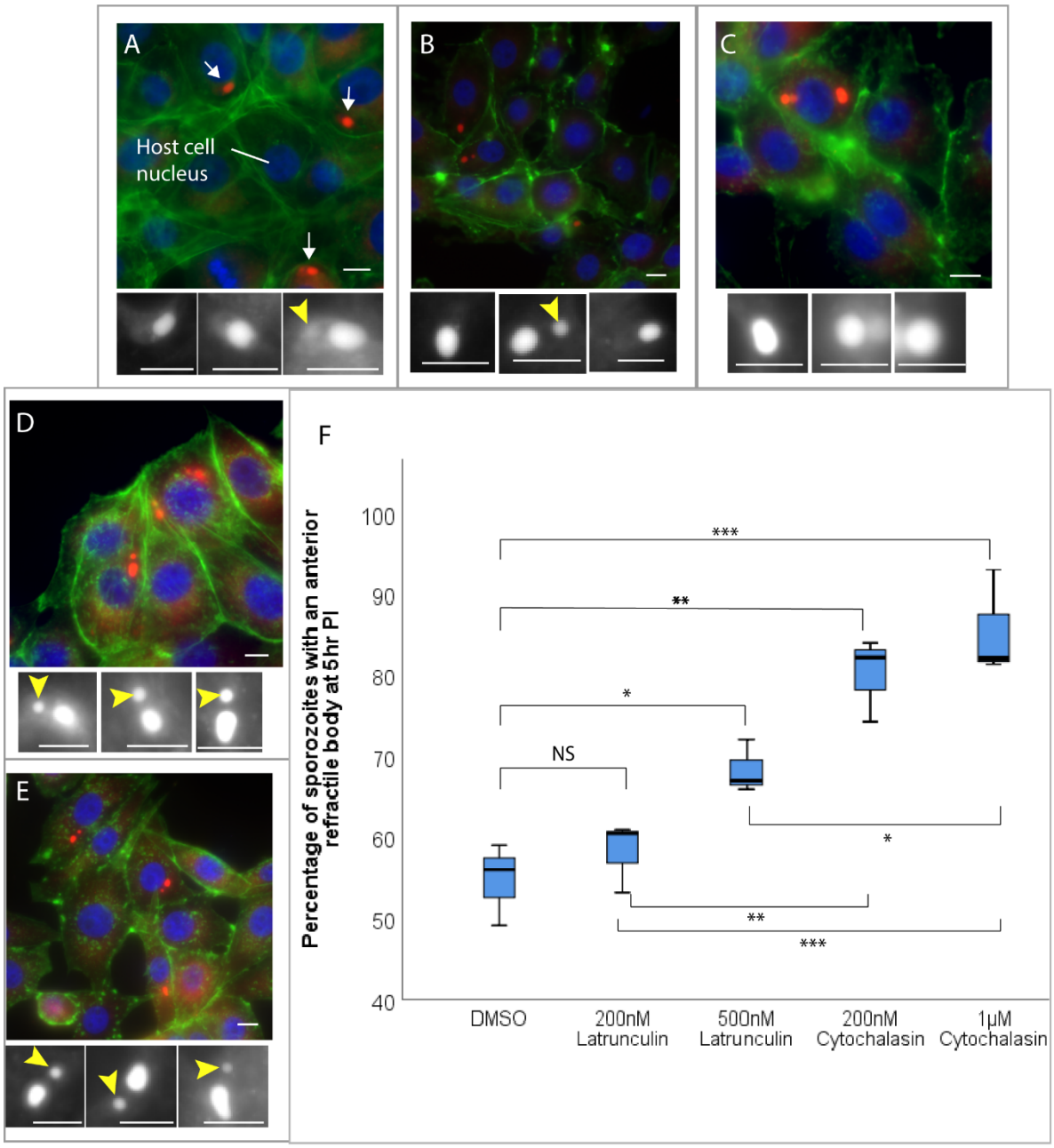


Figure 4.9. Refractile body merger is affected by disrupting sporozoite actin.

Host cells were infected with sporozoites (A - arrows) and incubated in the presence of DMSO (A), 200nM Latrunculin A (B), 500 nM Latrunculin A (C), 200 nM Cytochalasin D (D), or 1 µM Cytochalasin D (E). At 5 hr post-infection, samples were fixed and stained with Hoechst, Nile red and Phalloidin Atto 488. Sporozoites were assessed for the presence of an anterior refractile body (yellow arrowhead) using widefield microscopy. F) Following treatment with 500 nM Latrunculin A, 200 nM Cytochalasin D or 1 µM Cytochalasin D a greater percentage of sporozoites were found to contain anterior refractile bodies when compared to the DMSO controls (* = $p \leq 0.05$, ** = $p \leq 0.01$, *** = $p \leq 0.001$ - One Way ANOVA and post-hoc Turkey test). Treatment with either 200 nM Cytochalasin D or 1 µM Cytochalasin D resulted in a greater percentage of sporozoites possessing an anterior refractile body compared to those treated with 200 nM Latrunculin A. Treatment with 1 µM Cytochalasin D resulted in a greater percentage of sporozoites possessing an anterior refractile body compared to those treated with 500 nM Latrunculin A. Scale ~ 20 µm.

To examine changes to host cell actin, each sample was assessed by Phalloidin 488 staining (Fig. 4.10). Host cells in the control samples were packed with long fibres, indicative of intact actin filaments (Fig.4.10A and F). In samples treated with CytoD, host cells contained fewer intact actin filaments than in controls (Fig. 4.10B, C, G and H) and this effect was more pronounced when the higher concentration was used (Fig.4.10C and H). Host cells of samples treated with LatA showed more disruption to normal filamentous actin (Fig. 4.10D, E, I and J). The Phalloidin staining pattern of host cells treated with 200 nM LatA (Fig. 4.10D and I) was comparable to that seen in cells treated with 1 µM CytoD (Fig. 4.10C and H) and cells treated with 500 nM LatA exhibited the most disruption to actin filament structures (Fig.4.10E and J).

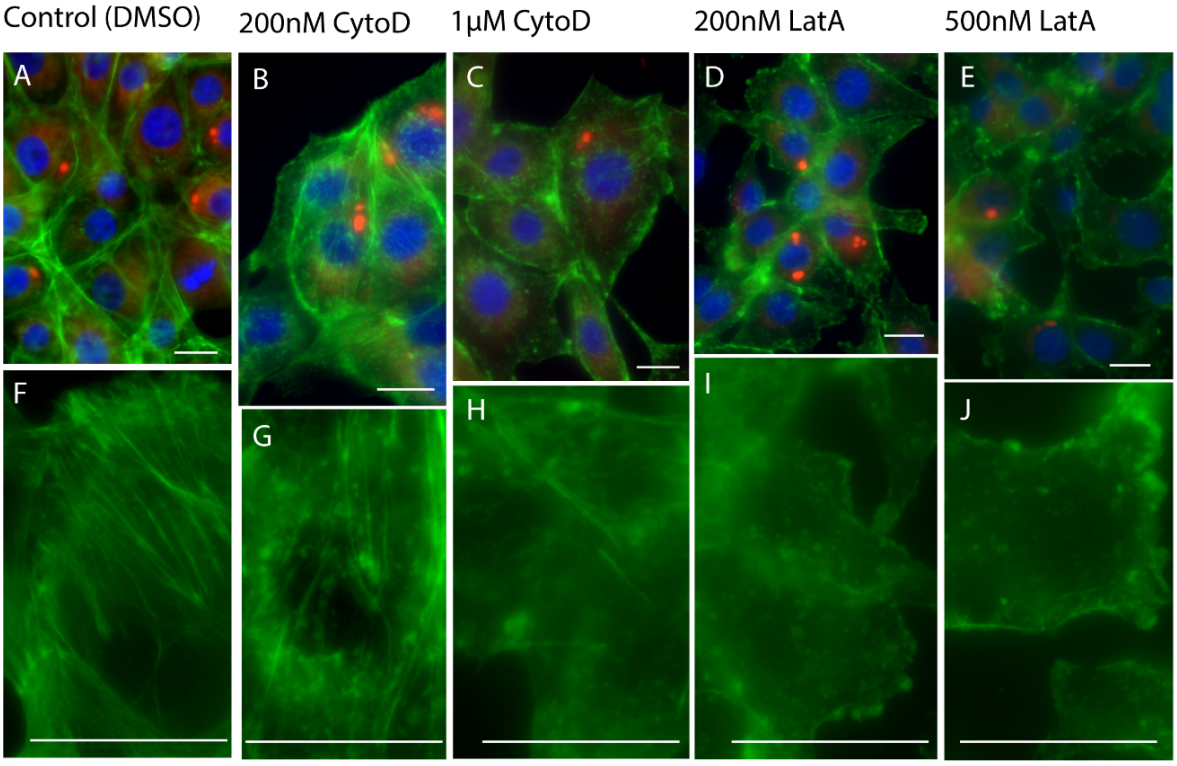


Figure 4.10. Treatment with 200 nM LatA or 1 µM CytoD cause comparable levels of host cell actin disruption.

Sporozoites and host cells were incubated in the presence of DMSO (A+F), 200 nM Cytochalasin D (B+G), 1 µM Cytochalasin D (C+H), 200 nM Latrunculin A (D+I) or 500 nM Latrunculin A (E+J). At 5 hr post-infection, samples were fixed and stained with Hoechst, Nile red and Phalloidin Atto 488. Scale bars ~ 20 µm.

Previous reports support the conclusion that the lower concentration of LatA (200 nM) should be compared to the higher concentration of CytoD (1 µM). In the study by Spector et. al. (1989), CytoD was required at 10-20 times the concentration of LatA to produce similar phenotypes.

For clarity, the effects of each treatment condition on refractile body merger and host cell actin are summarised in table 4.1. Considering all these data, it appears that LatA does not affect *E. tenella* sporozoites in the same way as CytoD (Fig. 4.9F, Table 4.1), agreeing with previous reports that LatA has little effect on apicomplexan actin (Periz et. al. 2017, Whitelaw et. al. 2017). Focusing on

the data concerning anterior refractile body presence after treatment with 200 nM LatA or 1 μM CytoD; treatment with CytoD, but not LatA, significantly reduced refractile body merger (Fig. 4.9F, Table 4.1). Although treatment with 200 nM LatA severely affected host cell actin (Fig. 4.10I), there was no significant effect on refractile body merger (Table 4.1). This suggests that specific disruption to host cell actin does not affect refractile body merger, but that disruption to both host and parasite actin significantly reduces refractile body merger. I therefore conclude that refractile body merger is at least partially dependent on the function of sporozoite actin.

Table 4.1. Effects of Cytochalasin D and Latrunculin A treatment on refractile body merger and host cell actin structure.
NA = not applicable, ARB = anterior refractile body. * data in *T. gondii* referenced corresponds to the use of 250nM rather than 200nM

Treatment	Control	200nM CytoD	1μM CytoD	200nM LatA	500nM LatA
Percentage of sporozoites containing ARB at 5hr PI	54.7%	80.2%	85.5%	58.2%	68.%
Effect on refractile body merger	NA	Severe	Severe	No significant effect	Moderate
Affects actin in *T. gondii*? (Periz et. al. 2017, Whitelaw et. al. 2017)		Yes *	Yes	No	No
Effect on host cell actin	NA	Moderate	Severe	Severe	Severe

4.6.2. **Refractile body merger is associated with cell roundness**

As described in previous sections, refractile body merger is at least partially dependent on sporozoite actin and commences from approximately 2 hr post infection. In Chapter 3, I also reported that there are significant alterations to sporozoite shape over the first 5 hr of infection. Based on these data, I hypothesised that, a) refractile body merger is associated with cell shape-change, and b) both refractile body merger and sporozoite shape-change are linked to actin cytoskeleton dynamics.

To test for an association between refractile body merger and cell shape, sporozoite lengths and widths were measured at 5 hr post infection by light microscopy (described in section 3.5.3) and scored for presence/absence of the anterior refractile-body (Fig. 4.11B, arrowhead; Fig. 4.11D).

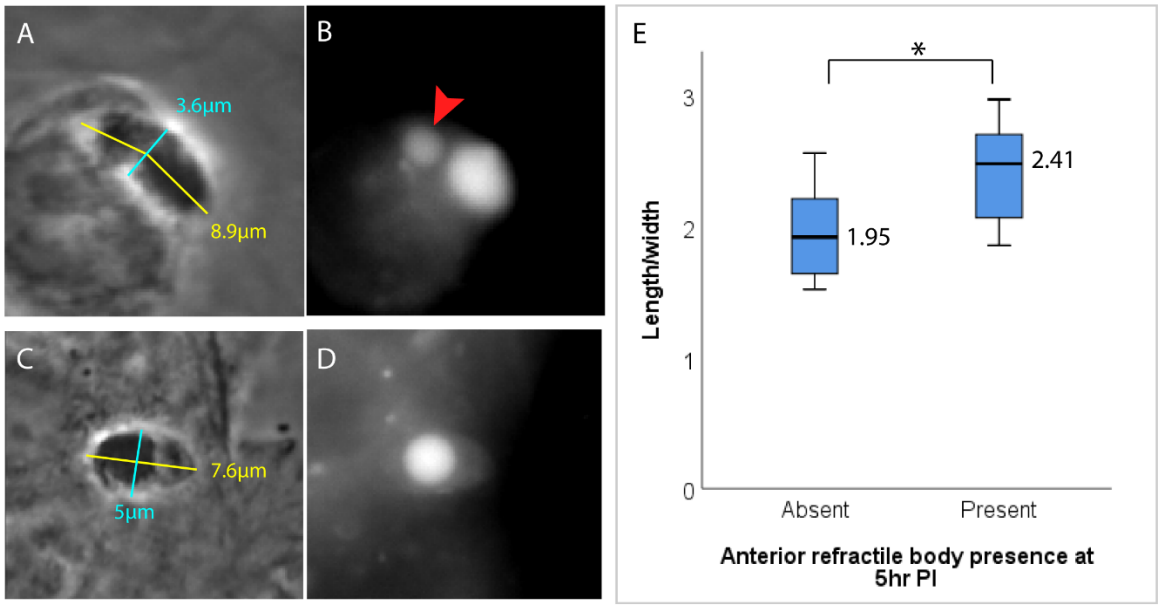


Figure 4.11. Refractile body merger is associated with an increase in sporozoite roundness.

At 5 hr post-infection of host cells, sporozoites were fixed, stained with Nile red and imaged by widefield microscopy. Cell lengths (A+C - yellow) and widths (A+C - cyan) were measured for 17 cells. Each cell was also assessed for the presence of an anterior refractile body (B - arrowhead). E) Comparison of length/width between sporozoites containing an anterior refractile body and sporozoites not containing an anterior refractile body. Statistical test = t-test, * = $p \leq 0.05$.

Mean length/width of sporozoites containing an anterior refractile body was 2.41 whereas mean length/width of sporozoites without an anterior refractile body was 1.95 ($p = 0.013$, T-test). These data suggest that the extent of sporozoite rounding (greater roundness having length/width value closer to one) is associated with refractile body merger.

To investigate whether sporozoite shape-change is associated with actin dynamics, samples prepared for the previous 'actin-inhibition' experiment (described in section 4.6.1) were re-examined. For this analysis, only the 1 µM CytoD and 200 nM LatA samples were studied as these had the most comparable effects on host cell actin filament structure and were therefore most suitable to control for off-target effects on the host (Fig.4.10). Lengths and widths were measured for 72 sporozoites following treatment with CytoD, 72 sporozoites following treatment with LatA, and 59 sporozoites from the control DMSO treated sample (Fig. 4.12).

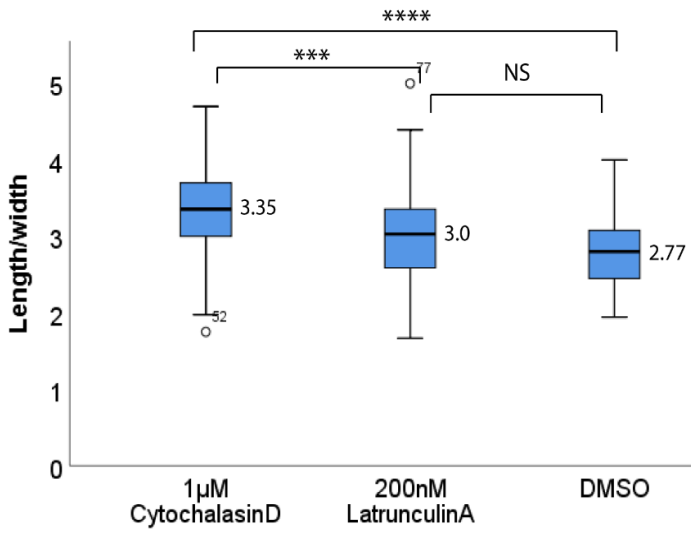


Figure 4.12. Sporozoite rounding is dependent on sporozoite actin.

At 5 hr post-infection of host cells, length/width values were calculated for 72 sporozoites from LatA and CytoD samples and 56 sporozoites from the control. Variant analysis (ANOVA) revealed significant differences between the samples which was further assessed via post-hoc Turkey HSD. Mean length/width for DMSO treated sporozoites was 2.77, mean length/width for LatA treated sporozoites was 3 and mean length/width for CytoD treated sporozoites was 3.35 (**** = $p < 0.0005$, *** = $p \leq 0.001$, NS = not significant).

For control sporozoites, mean length/width was 2.77 +/- 0.43. One-way ANOVA analysis revealed that treatment with 1 µM CytoD leads to a significant increase in length/width compared to control, with a value of 3.35 +/- 0.63 ($p < 0.0005$, post-hoc Turkey HSD). Treatment with 200 nM LatA resulted in a mean sporozoite length/width value of 3.0 +/- 0.64 which was not significantly different from the control ($p = 0.061$, one-way ANOVA with post-hoc Turkey HSD). There was also a significant difference in sporozoite length/width value between LatA-treated parasites and CytoD-treated parasites ($p = 0.001$, one-way ANOVA with post-hoc Turkey HSD) (Fig. 4.12).

As described in section 3.5.3, sporozoite 'rounding' occurs within the first few hours post infection, with mean length/width value changing from an average of 3.5 in free sporozoites to an average of 2.2 at 5 hr post-infection (Fig.3.30). In the set of experiments assessing sporozoite shape following actin inhibition, control sporozoites were significantly more rounded (lower length/width value) compared to sporozoites treated with CytoD evaluated at the same time following infection. This suggests that sporozoite rounding is associated with actin dynamics. Length/width values for sporozoites treated with LatA were significantly different to those of sporozoites treated with CytoD but were not significantly different to those of control sporozoites. As previously discussed in section 4.6.1, LatA appears not to affect sporozoite actin and has a mild effect on refractile body merger. These findings suggest that inhibition of sporozoite actin significantly affects sporozoite rounding but that specific inhibition to host-cell actin does not. I therefore conclude that both refractile body merger and sporozoite rounding are associated with sporozoite actin dynamics.

To summarise the major findings of this chapter, anterior refractile body loss in *E. tenella* predominantly occurs between 2- and 5- hr following invasion of MDBK cells in culture. Anterior refractile body loss in *E. tenella* exclusively occurs through merger between the anterior and posterior

refractile bodies, a process that takes around 60 seconds to complete. Sporozoite actin dynamics are associated with both refractile body merger and sporozoite shape-change following infection.

5. **Diversity and temporal dynamics in *E. tenella* apical complex ultrastructure**

5.1. **Introduction**

The apical complex is present, in varying forms, in invasive stages of all members of the phylum Apicomplexa (Roos 2005) and is required for important life cycle events including host cell invasion and host cell egress (Blackman and Carruthers 2013). The apical complex in species belonging to the subgroup *Coccidiasina,* is centred on a conical cage-like structure called the conoid, composed of helically-bent tubulin fibres embedded in a matrix of unknown composition (Hu et. al. 2002). These fibres are constructed from protofilaments, however, unlike microtubules, the protofilaments of conoid fibres do not form complete rings when observed in cross-section (Hu et. al. 2002). Transmission electron microscopy analysis revealed that the conoid of *T. gondii* is composed from approximately 14 fibres (Hu et. al. 2002). The level of uncertainty in this number is due to inherent difficulties in analysing such a complex structure using two-dimensional methods. The conoid of *T. gondii* performs dynamic protrusion events (Chiappino et. al. 1984, Del Carmen et. al. 2009), although the function of this conoid protrusion remains unknown. Some have hypothesised that the conoid plays a mechanical role in invasion (Hu et. al. 2006, Nichols and Chiappino 1987), acts as a regulatory 'gate-keeper' for protein secretion or invasion-related signalling pathways (Graindorge et. al. 2016, Katris et. al. 2014), or increases the chances of contact between parasite apex and host cell membrane (Carruthers and Boothroyd 2007). Comparatively more is known about the roles of secretory organelles of the apical complex compared to the conoid. Most widely studied are the micronemes and rhoptries. These organelles contain proteins essential for motility, invasion and egress. Work in *T. gondii* has revealed that both microneme and rhoptry protein secretion occurs in a tightly regulated manner from the apical tip of the parasite (Bullen et. al. 2016, Carruthers and Sibley 1997, Katris et. al. 2014, Lourido et. al. 2010). By electron microscopy, rhoptry necks can be seen within the conoid and appear to secrete via this site (Nichols et. al. 1983). In the case of micronemes, experimental studies have shown that both albumin and acetylaldehyde can induce the release of microneme proteins in *E. tenella* (Bumstead and Tomley 2000, Yan et. al. 2016). The site of microneme secretion and the physical mechanisms associated with this process are however yet to be defined. Previous hypotheses include secretion via fusion with the rhoptry necks (Bannister et. al. 2003, Scholtyseck and Mehlhorn 1970) and secretion from around the base of the conoid following conoid protrusion (Paredes-Santos et. al. 2012).

5.2. **Three-dimensional organisation of the apical complex in *E. tenella***

To investigate the three-dimensional ultrastructure of the apical complex, serial-section transmission electron tomograms were collected. Transmission electron tomography involves generating a series of images where each image views the sample from a different tilt. The data contained within the series of two-dimensional projections are then transformed into a single, three-dimensional data stack

using the IMOD software package (Kremer et. al. 1996). Each tomogram focuses on the conoid of an individual sporozoite. Figure 5.1. shows selected sections from a single serial tomogram to illustrate the three-dimensional organisation of the apical end of the sporozoite. This tomogram comprised of data from four serial resin-sections covering ~2.5 μm^3. When viewed in glancing cross-section, the conoid is seen as parallel, diagonal fibres (Fig.5.1M, insert). There are micronemes throughout the apical end (Fig.5.1A, yellow arrows), rhoptries (Fig.5.1H, R) and microtubules (Fig.5.1J, arrowheads) are present, and a set of spherical vesicals are arranged in an ordered row (Fig 5.1K, asterisks). Further details of these structures will be explained in later sections.

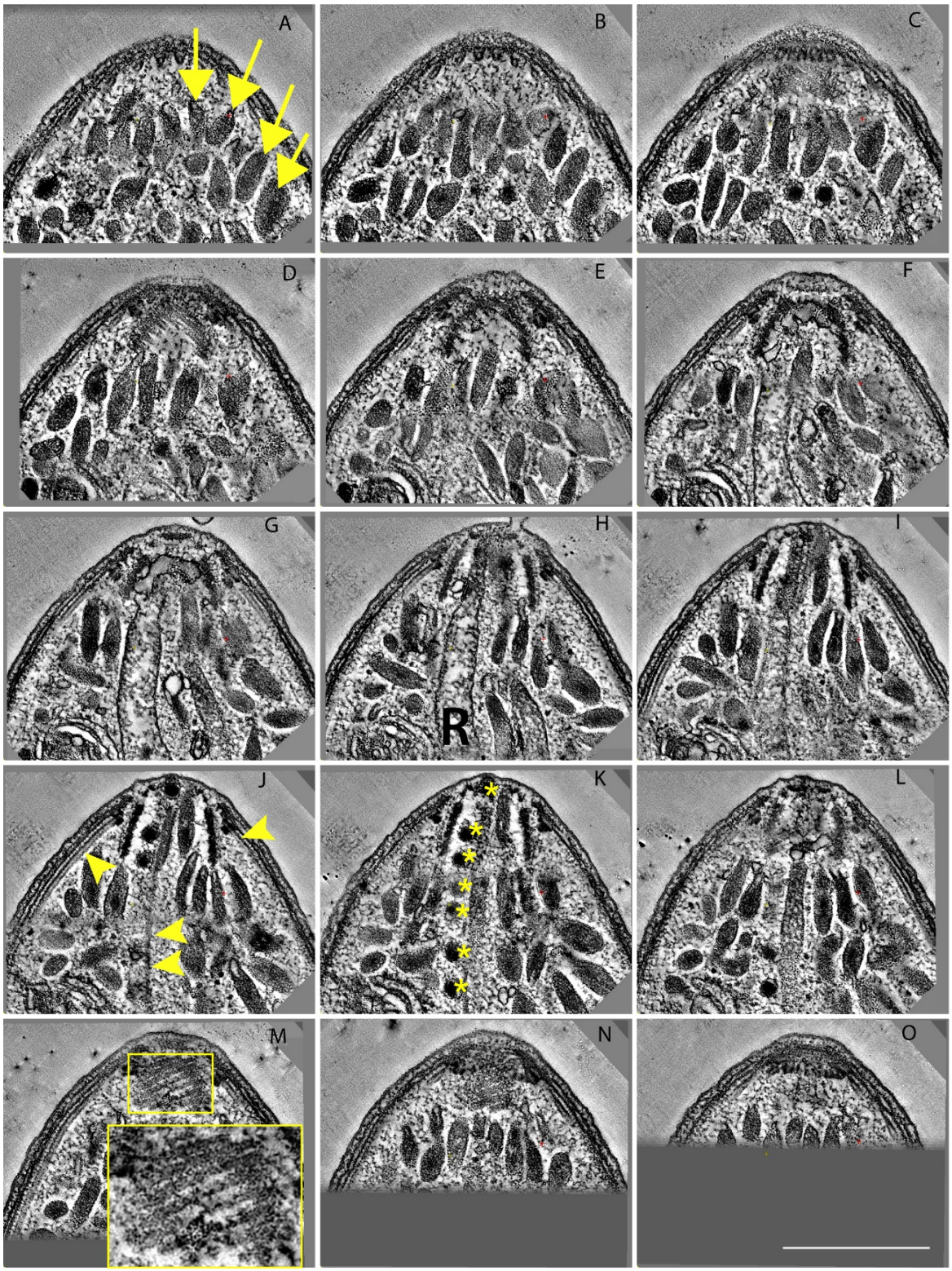


Figure 5.1. Transmission electron tomography permits detailed investigation of apical complex structures in three-dimensions.

A series of evenly spaced slices through a representative serial-section transmission electron tomogram of the *E. tenella* sporozoite apical complex. Sections are taken from tomogram 3 (see Table 5.1 for details). Arrow = microneme (A), asterisk = spherical vesicle (K), arrowheads = microtubule (J), R = rhoptry (H). Conoid fibres, insert (M). Scale ~ 500 nm.

Due to the complexity of the overall structure, parts of the apical complex are divided into 'outer ring components' (Fig.5.2A and B) and 'apical secretory organelles' (Fig.5.2D and E). Outer ring components include the conoid (Fig.5.2A, white; B, labelled), composed of helical fibres; an electron-opaque ring-shaped structure surrounding the conoid, known as the apical polar ring (APR) (Fig.5.2A, gold); subpellicular microtubules (Fig.5.2A, green), which radiate from the APR and extend towards the posterior of the cell (Fig.5.1J, single arrowheads); and two ring-shaped structures just distal to the conoid, known as pre-conoidal ring 2 (Fig.5.2A, red) and pre-conoidal ring 1 (Fig.5.2A, light blue).

When seen as a three-dimensional reconstruction (Fig.5.2A), the conoid is an open cone shape, formed from closely apposed helical fibres. As with microtubules, the helical fibres of the conoid are composed of protofilaments which are long chains of tubulin molecules (Hu et. al. 2002). In the case of microtubules, 13 protofilaments associate side by side to form a complete tube; in the case of conoid fibres, nine protofilaments associate side by side to form a curved sheet (Hu et. al. 2002) (Fig.5.2C). When viewed in cross-section, the protofilaments of microtubules form a complete ring whereas the protofilaments of conoid fibres form an open comma shape (Fig.5.2C). It has previously been postulated that the open comma arrangement of protofilaments allows the conoid fibres to exhibit the high level of curvature seen in the conoid (Hu et. al. 2002).

The functions of the pre-conoidal rings are unknown; however, in *T. gondii* the proteins TgCentrin2 (Hu et. al. 2006) and TgSAS6L (de Leon et. al. 2013) have been localised to these structures. SAS6 and centrins are widely conserved proteins associated with basal bodies/centriole formation (Aubusson-Fleury et. al. 2017, Nakazawa et. al. 2007).

The apical secretory organelles identified in *E. tenella* are of three types. Rhoptries, the largest of the three membrane-bound apical organelles and shaped like a club (Fig.5.1H and 'R', Fig.5.2D, dark blue); micronemes, which are 'rod-shaped' and present in very high numbers (Fig.5.1A, arrows, and Fig.5.2D, turquoise); and spherical vesicles, which appear as a row of electron-opaque spheres leading posteriorly from the conoid (Fig.5.1K and asterisks, Fig.5.2D, yellow). Also found within the conoid is a pair of 'intraconoid microtubules', one of which starts and terminates in line with the edges of the conoid and the other of which extends into the cell past the base of the conoid (Fig.5.1J and double arrowheads, Fig.5.2D, pink). Detailed analyses on outer/ring elements (Fig.5.2A and B) and inner/secretory elements (Fig.5.2D and E) were carried out to better understand their three-dimensional morphometrics and arrangement.

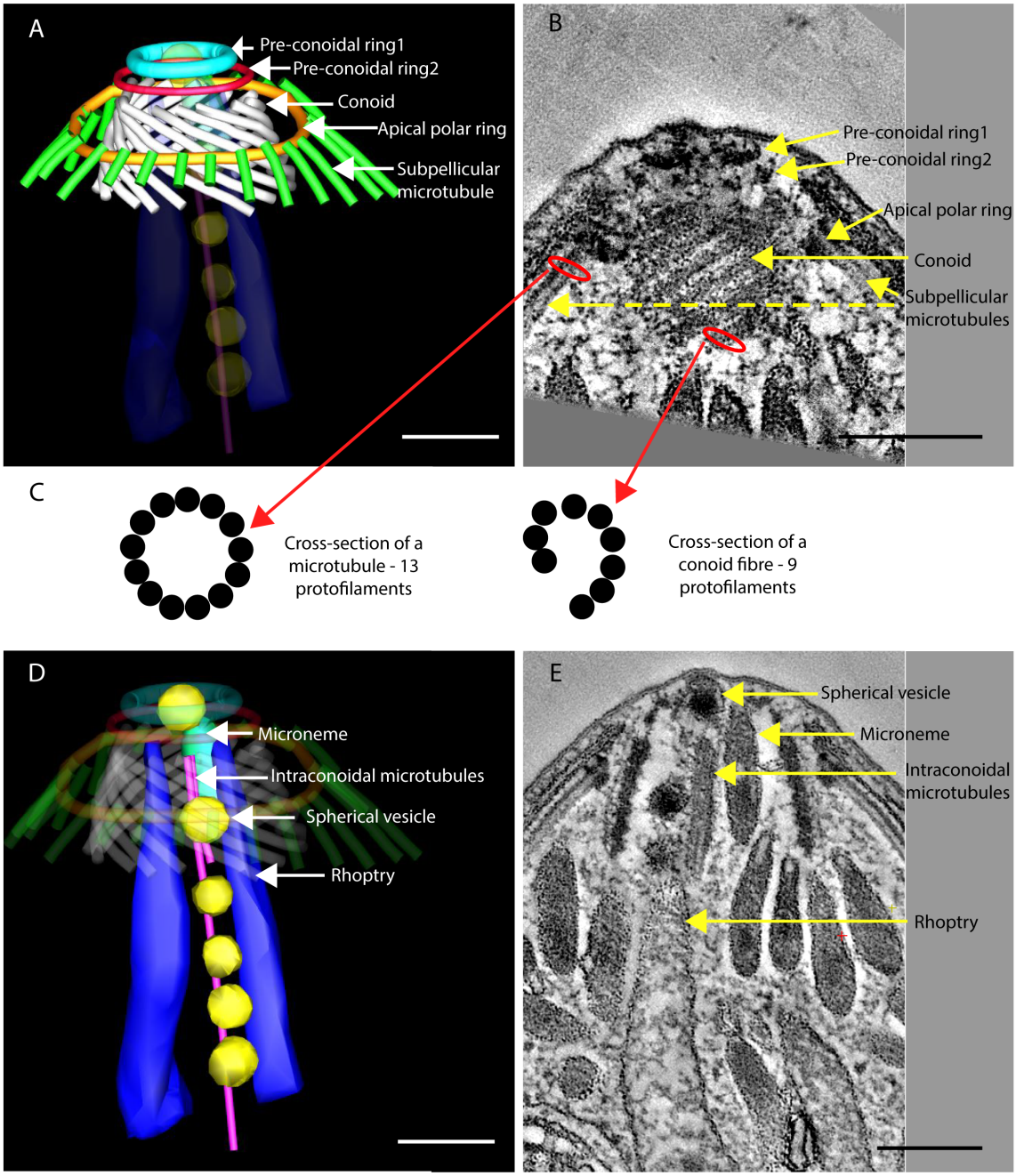


Figure 5.2. Components of the apical complex.

For clarity and ease of investigation, I have divided the apical complex into outer (A and B) and inner (D and E) components. A and B) The outer, 'ring-based', components consist of two pre-conoidal rings, the conoid and the apical polar ring (in association with minus ends of the sub-pellicular microtubules). A) Surface-rendered model from electron tomography data. B) Section from transmission electron tomogram of sporozoite apex. C) Drawings representing the arrangement of protofilaments (black spots) in cross section views of microtubules and conoid fibres. D and E) The inner components consist of apical secretory organelles (rhoptries, micronemes and secretory vesicles) and the intraconoidal microtubule pair. D) Surface-rendered model from electron tomography data. E) Section from transmission electron tomogram of sporozoite apex. Models are of 'tomogram 7' (see Table 5.1), raw data is taken from 'tomogram 3'. Scale bars ~ 200nm.

5.3. **Outer components of the apical complex**

5.3.1. **Variation in conoid fibre number**

The outer components of the apical complex act as a scaffold, conferring structural stability and spatial organisation to the inner components involved in protein secretion. Under the category of outer apical complex components, the conoid, apical polar ring (APR), subpellicular microtubules and pre-conoidal rings (Fig.5.2A and B) are included.

To quantify the number of fibres comprising the conoid of *E. tenella* sporozoites, individual conoid-fibres were segmented for each tomogram (Fig.5.3). Of the nine serial tomograms collected from freshly-excysted sporozoites (Table 5.1), one conoid contained 13 fibres, three conoids had 14 fibres, four conoids had 15 fibres and one conoid contained 16 fibres (Fig.5.3). This finding contradicts previous data on other tubulin-based organelles (such as cilia and flagella) where tubulin-fibre numbers are constant; their microtubule arrangement is even highly conserved throughout the Eukaryota (Lin et. al. 2012).

Table 5.1. Imaging settings for serial-section electron tomograms collected for freshly-excysted sporozoites

Name	Microscope	Magnification	Pixel size	Tilt parameters	Section thickness	N° serial sections	Single or dual axis
Tomogram 1	Hitachi H7650	25000	0.6nm	-60 to +60	200nm	3	dual
Tomogram 3	Hitachi H7650	25000	0.6nm	-60 to +60	150nm	4	dual
Tomogram 5	Hitachi H7650	25000	0.6nm	-60 to +60	150nm	3	dual
Tomogram 7	Hitachi H7650	25000	0.5nm	-60 to +60	90nm	5	single
Tomogram 8	Fei Tecnai Spirit	49000	1.1nm	-65 to +65	150nm	3	dual
Tomogram 9	Fei Tecnai Spirit	98000	0.55nm	-65 to +65	150nm	3	dual
Tomogram 10	Fei Tecnai G2 FEG	29000	0.37nm	-60 to +60	250nm	2	single
Tomogram 11	Fei Tecnai Spirit	98000	0.55nm	-65 to +65	150nm	3	single
Tomogram 12	Fei Tecnai Spirit	68000	0.8nm	-65 to +65	150nm	5	single

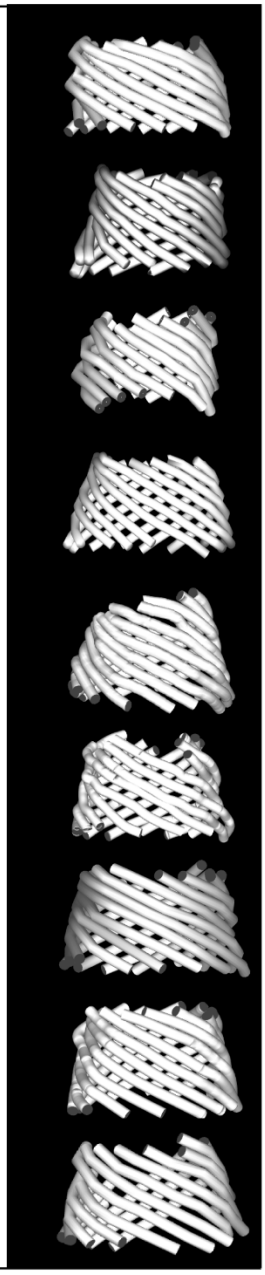
Name	Number of conoid fibres	Conoid model
Tomogram 1	15	
Tomogram 3	14	
Tomogram 5	13	
Tomogram 7	15	
Tomogram 8	15	
Tomogram 9	14	
Tomgram 10	14	
Tomogram 11	15	
Tomogram 12	16	

Figure 5.3. Conoid fibre number varies in freshly purified sporozoites.

3dmod software (University of Colorado, Boulder) was used to model individual conoid fibre from electron tomography data of freshly purified sporozoites (see Table 5.1 for tomogram details). The number of fibres making up each conoid was found to vary between 13 to 16 fibres per conoid.

The discovery of conoid variation generated several new questions, including:
a) is conoid fibre number diversity associated with variation in other morphological parameters of the apical complex?
b) is there a biological function linked to conoid fibre number variation?
c) what is the reason for this variation?

To address the first question, tomogram data was used to assess whether conoid fibre number is correlated to other morphometric parameters of the apical complex, as described in subsections 5.3.2, 5.3.3 and 5.3.4. With regards to the second and third questions, three possible hypotheses were proposed for the observed variation. The first is that during sporozoite excystation and purification, the conoid undergoes a dynamic maturation phase in preparation for host cell invasion, involving either the addition or removal of conoid fibres, and at the point of sample fixation sporozoites at various stages of maturation were present. The second hypothesis is that each sporozoite has a genetically determined conoid fibre number and that allelic variation in the population results in the range of conoid morphologies seen. The third hypothesis is that the molecular mechanism behind conoid formation allows for some plasticity in fibre number; due to stochastic processes in the cellular environment, a random number of fibres (within an acceptable range determined by other factors) are formed.

5.3.2. **Increasing conoid fibre number is associated with increasing conoid diameter**

Having found that conoid fibre numbers vary (Fig. 5.3), I hypothesised that increasing fibre number may be associated with increasing conoid size. To test the hypothesis that increasing conoid-fibre number is associated with increasing conoid size, measurements were taken of conoid base diameter (Figs. 5.4A and B, Table 5.2) (mean = 340 +/- 20 nm), conoid apex diameter (Figs. 5.4A and C, Table 5.2) (mean = 250 +/- 17 nm) and conoid height (Figs. 5.4A and D, Table 5.2) (mean = 193 +/- 35 nm).

Table 5.2. Morphometric analysis of the conoid in freshly purified sporozoites. Measurements were made on electron tomography data using 3dmod software (University of Colorado, Boulder). Continuous data was calculated as the mean of 2 measurements.

Name	Conoid fibre n°	Conoid fibre length	Conoid base diameter	Conoid apex diameter	Pre-conoidal ring 2 diameter	Pre-conoidal ring 1 diameter	Apical polar ring diameter	Conoid to apical polar ring	Conoid height	Conoid fibre width	Conoid fibre spacing	Sub-pellicular microtubule spacing
Tomogram 5	13	380	305	245	212	169	370	21	129	19	28	52
Tomogram 3	14	470	317	240	208	166	368	24	183	22	32	47
Tomogram 9	14	462	339	228	204	157	369	25	195	25	34	52
Tomogram 10	14	457	355	267	237	178	408	26	200	22	31	58
Tomogram 1	15	371	330	230	211	157	407	30	167	18	27	48
Tomogram 7	15	410	349	264	241	180	410	23	198	22	35	54
Tomogram 8	15		349	253			396	20	263	25	37	49
Tomogram 11	15	390	349	247	225	166	392	28	191	21	37	56
Tomogram 12	16	459	369	279	234	181	417	30	207	24	33	51
mean	14.6	424.9	340.2	250.3	221.5	169.3	393.0	25.2	192.6	22.0	32.7	51.9
SD	0.9	41.3	19.9	17.1	14.5	9.6	19.4	3.6	35.4	2.4	3.6	3.7

Correlation analysis revealed that variation in conoid base diameter was positively associated with conoid fibre number (correlation coefficient = 0.78) and this association was statistically significant ($p = 0.014$, Pearson correlation) (Fig. 5.4E). There were no statistically significant correlations between conoid fibre number and conoid apex diameter ($p = 0.46$, Pearson correlation) (Fig. 5.4F) or between conoid fibre number and conoid height ($p = 0.57$, Pearson correlation) (Fig. 5.4G).

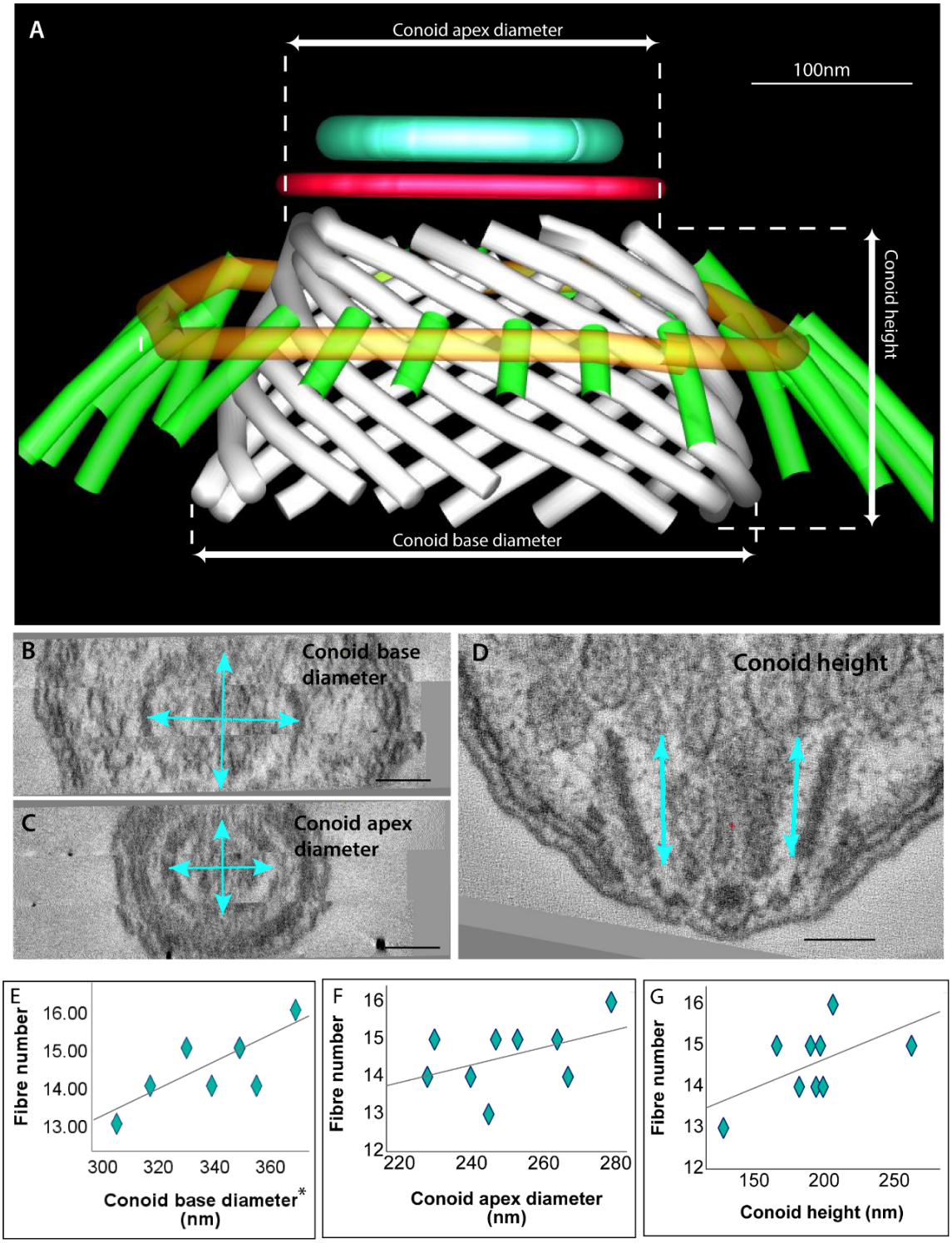


Figure 5.4. Increasing fibre number is associated with increasing conoid-base diameter.

A) Surface-rendered model of apical complex structures generated using transmission electron tomography data. B) Transmission electron tomogram section showing conoid base diameter measurement. C) Transmission electron tomogram section showing conoid apex diameter measurement. D) Transmission electron tomogram section showing conoid height measurement. Scale ~ 100nm. E) Correlation of conoid fibre number with conoid base diameter. F) Correlation of conoid fibre number with conoid apex diameter. G) Correlation of conoid fibre number with conoid height. Statistical test = Pearson correlation, * = $p \leq 0.05$.

On visual inspection, there was little variation in conoid fibre structure and arrangement between tomograms.

To quantify conoid fibre morphometrics and assess conoid fibre variation, fibre width (Fig.5.5A and B) and fibre spacing (Fig.5.5A and C) measurements were taken for each conoid.

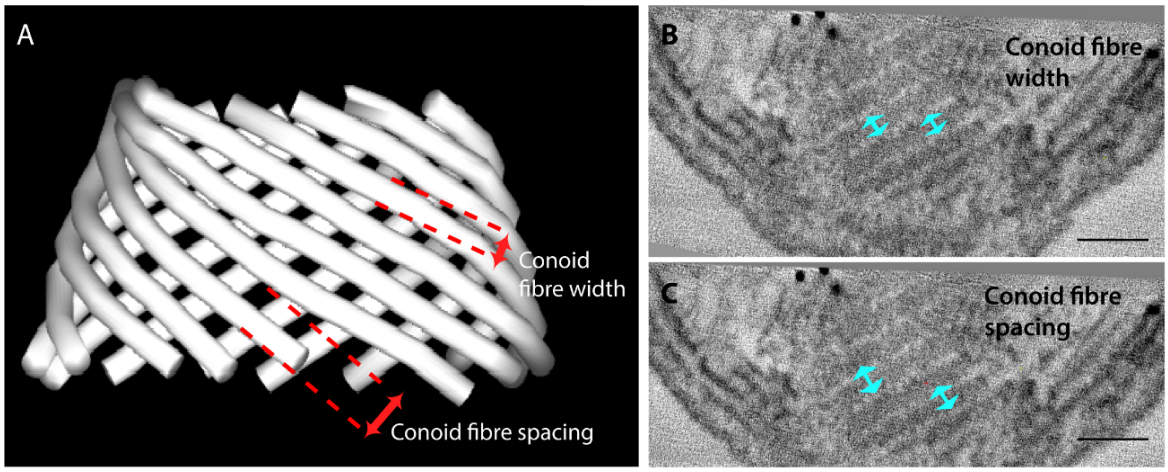


Figure 5.5. Measurement of conoid-fibre width and spacing.

A) Surface-rendered model of conoid fibres generated using electron tomography data. B and C) Transmission electron tomography section where conoid fibres are seen in cross-section. Conoid fibre width and spacing were taken as the mean of two measurements. Scale ~ 100nm.

Mean fibre width was 22 +/- 2 nm and mean fibre spacing was 33 +/- 4 nm (Table 5.2). Both fibre-spacing and fibre-width were not statistically correlated with either conoid base diameter or conoid fibre number (Pearson correlation, significance level at $p < 0.05$). These findings help to explain how increasing conoid fibre number is correlated to increasing conoid base diameter. With consistent fibre morphology and arrangement between conoids, an increase in conoid-fibre number would theoretically be associated with a larger conoid.

5.3.3. Increasing conoid fibre number is associated with increasing apical polar ring diameter

To investigate whether a sporozoite with a larger conoid base has a larger apical polar ring (APR), measurements of APR diameter and conoid-to-APR-distance were taken from each tomogram (Fig.5.6). On average, APR diameter (Fig.5.6A and C) was 393 +/- 19 nm (Table 5.2) and conoid-to-APR distance (Fig.5.6B and D) was 25 +/- 4 nm (Table 5.2).

There was greater variation in APR diameters than in APR-to-conoid distances (Table 5.2). This indicates that APR-to-conoid distance has less biological flexibility than APR diameter. Correlation analysis was carried out of APR diameter with conoid base diameter (Fig.5.6E), conoid apex diameter (Fig.5.6F) and conoid fibre number (Fig.5.6G).

Increasing APR diameter was statistically associated with increasing conoid size for each of the parameters analysed. Correlation coefficient for APR diameter and conoid base diameter was 0.76 ($p = 0.017$, Pearson correlation) (Fig.5.6E), APR diameter and conoid apex diameter correlation coefficient was 0.68 ($p = 0.044$, Pearson correlation) (Fig.5.6F) and APR diameter and conoid-fibre-number correlation coefficient was 0.76 ($p = 0.018$, Pearson correlation) (Fig.5.6G). To summarise these findings, increasing APR diameter (Fig.5.6A) is associated with increasing conoid size which may have a role in maintaining a constant APR-to-conoid distance (Fig.5.6B).

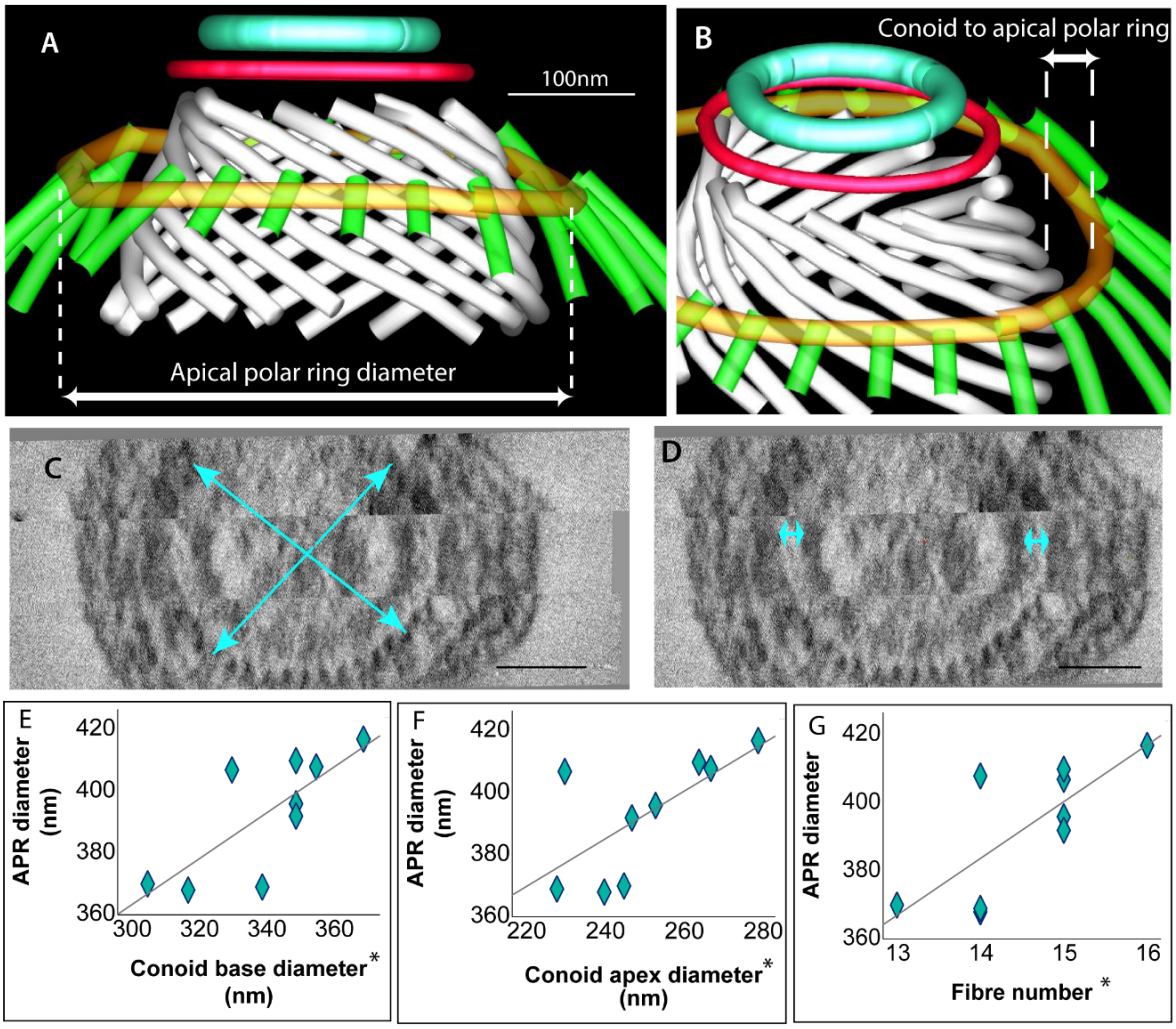


Figure 5.6. Increasing apical polar ring diameter is associated with increasing conoid-base diameter, increasing conoid apex diameter and increasing conoid-fibre number.

A and B) Surface-rendered model of components of the apical complex generated using electron tomography data from a freshly excysted sporozoite. C) Transmission electron tomography section showing apical polar ring diameter (double-ended arrows). D) Transmission electron tomography section showing conoid to apical polar ring distance (double-ended arrows). E) Correlation between apical-polar-ring diameter and conoid base diameter. F) Correlation between apical-polar-ring diameter and conoid apex diameter. G) Correlation between apical-polar-ring diameter and conoid fibre number diameter. Scale ~ 100nm.

In all tomograms, 24 subpellicular microtubules were attached to the APR leading to the hypothesis that increasing APR diameter should correlate with greater subpellicular microtubule spacing.

However, quantitative analysis revealed that average subpellicular microtubule spacing (Fig.5.7) was 52 +/- 4 nm (Table 5.2) and was not significantly correlated to APR diameter. As each subpellicular spacing is ~1/24th of the APR circumference, variation in subpellicular spacing is likely to be of a smaller scale than the variation in APR diameter. The lack of association found between APR diameter and subpellicular spacing may therefore be due to limitations in precision of the quantitation method.

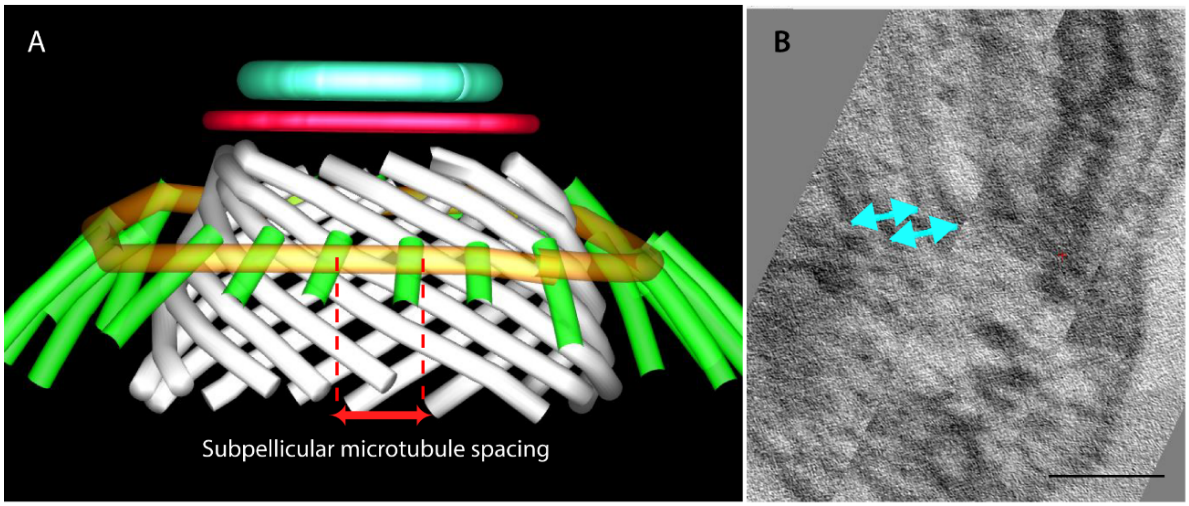


Figure 5.7. Measurement of subpellicular fibre spacing.

A) Surface-rendered model of apical complex structures generated from electron tomography data. Subpellicular microtubules are shown in green. B) Transmission electron tomography section showing subpellicular microtubules. Subpellicular microtubule spacing (double-headed arrows) was measured from the edge of one microtubule to the corresponding edge of the next microtubule, at the point of microtubule attachment to the apical polar ring. Scale ~ 100nm.

5.3.4. **Increasing conoid apex diameter is associated with increasing diameter of the pre-conoidal rings**

To investigate whether pre-conoidal-rings diameters vary in accordance with conoid size, measurements of pre-conoidal-ring-1 and pre-conoidal-ring-2 diameters were taken (Table 5.2). On average, pre-conoidal-ring-2 diameter (Fig.5.8A and B) was 221.5 +/- 14.5 nm (Table 5.2) and pre-conoidal-ring-1 diameter (Fig.5.8A and C) was 169.3 +/- 9.6 nm (Table 5.2). Pre-conoidal-ring-2 diameter was significantly correlated to both conoid base diameter (Pearson correlation = 0.74, p = 0.037) (Fig.5.8D) and conoid apex diameter (Pearson correlation = 0.9, p = 0.003) (Fig.5.8E) but not correlated to conoid fibre number (Pearson correlation = 0.5, p = 0.208) (Fig.5.8F). Pre-conoidal-ring-1 diameter was also significantly correlated to conoid apex diameter (Pearson correlation = 0.97, p<0.001) (Fig.5.8H) but not conoid base diameter (Pearson correlation = 0.54, p = 0.172) (Fig. 5.8G) or conoid fibre number (Pearson correlation = 0.3, p = 0.464) (Fig.5.8I). These findings suggest that the diameter of both pre-conoidal ring 1 and pre-conoidal ring 2 are associated with the diameter of the conoid at its apex.

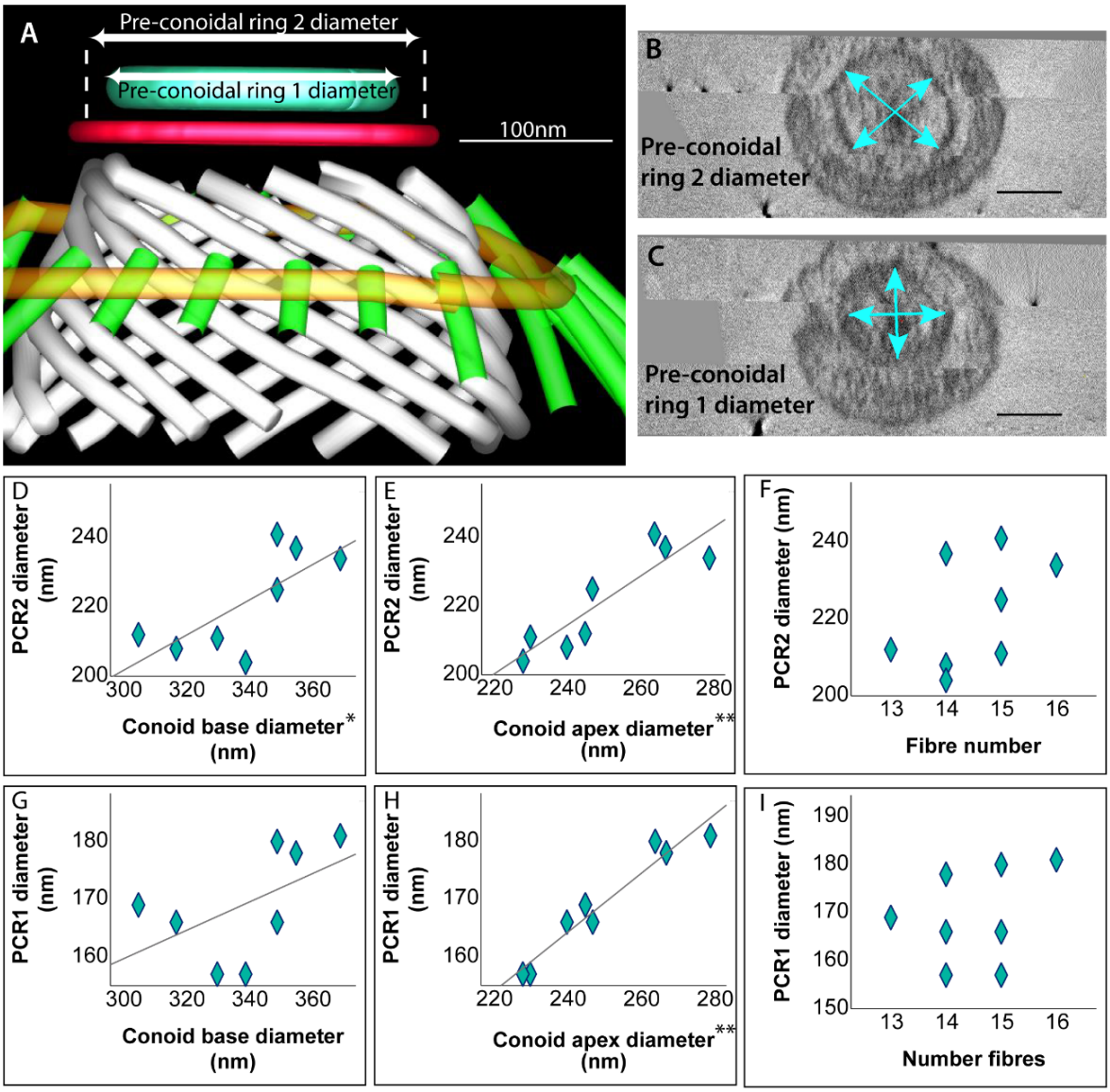


Figure 5.8. Increasing conoid diameter is associated with increasing diameters of pre-conoidal rings.

A) Surface-rendered model of apical complex structures generated from electron tomography data. Pre-conoidal ring 1 (cyan) and pre-conoidal ring 2 (red) are shown. B) Transmission electron tomography section showing pre-conoidal ring 2 diameter (double-headed arrows). C) Transmission electron tomography section showing pre-conoidal ring 1 diameter (double-headed arrows). D) Correlation of pre-conoidal ring 2 diameter and conoid base diameter. E) Correlation of pre-conoidal ring 2 diameter and conoid apex diameter. F) Correlation of pre-conoidal ring 2 diameter and fibre number. G) Correlation of pre-conoidal ring 1 diameter and conoid base diameter. H) Correlation of pre-conoidal ring 1 diameter and conoid apex diameter. I) Correlation of pre-conoidal ring 1 diameter and conoid fibre number. Statistical test = Pearson Correlation; * = $p \leq 0.05$, ** = $p \leq 0.01$. Scale ~ 100nm.

To summarise this section, increasing conoid fibre number is associated with increasing conoid base diameter; this makes logical sense in conjunction with the findings that increasing the number of conoid fibres was not associated with a reduction in either fibre width or fibre spacing. It was also found that diameters of the APR and pre-conoidal rings increase as conoid diameter increases. A possible explanation for the positive correlation between conoid diameter and diameter of associated

ring-shaped structures, is that one of these components acts as a template for subsequent formation of the other structures.

5.3.5. Conoid fibre number varies between clonal sporozoites

To address the hypothesis that variation in conoid fibre number could be due to genetic diversity, I analysed sporozoite pairs found within the same sporocyst which are genetically identical (Shirley and Harvey 1996). By capturing transmission electron tomograms of both conoids within intact sporocysts (Fig.5.9A-C), I was able to assess whether conoid fibre number is constant within these clonal pairs.

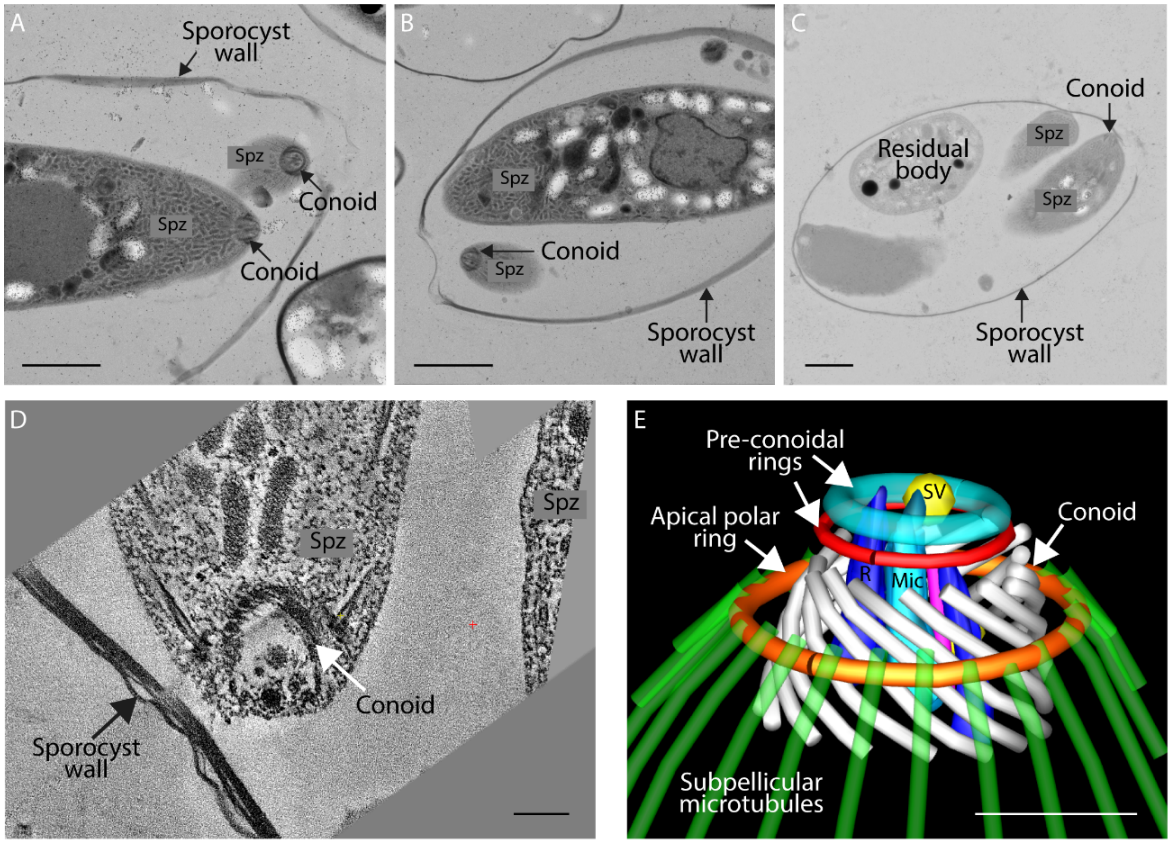


Figure 5.9. Three sporocysts were selected for investigation of conoid structure in clonal sporozoite pairs.

A to C) Transmission electron microscopy images of the three sporocysts found where both conoids were present within a series of serial sections. D) Transmission electron tomography section of an intra-sporocyst sporozoite. E) Surface-rendered model of an intra-sporocyst apical complex, generated using electron tomography data. SV = spherical vesicle, R = rhoptry, Mic = microneme. A to C) Scale ~ 1 µm. D to E) Scale ~ 200 nm.

To generate a sample containing intact sporocysts, an aliquot of post-excystation solution (containing a mixture of oocysts, sporocysts and sporozoites) was collected and processed using the single osmium protocol. Sections were post-stained with lead citrate, uranyl acetate and 10 nm gold fiducials.

Three sporocyst-conoid-pairs were captured using electron tomography. Tomogram numbers 18 and 19 (Table 5.3) were from the first sporocyst (Fig.5.9A), 20 and 21 were from the second sporocyst (Fig.5.9B) and 22 and 23 were from the third sporocyst (Fig.5.9C). As with the previous nine conoid tomograms, multiple morphometric parameters were quantified (Table 5.4).

Table 5.3. Imaging settings for serial-section electron tomograms generated from pre-excystation sporozoites (within sporocysts).

Name	Sporocyst identity	Microscope	Magnification	Pixel size	Tilt parameters	Section thickness	N° serial sections	Single or dual axis
Tomogram 18	1	FEI Talos	26000	0.37nm	-65 to +65	200nm	3	dual
Tomogram 19	1	FEI Talos	26000	0.37nm	-65 to +65	200nm	3	dual
Tomogram 20	2	FEI Talos	26000	0.37nm	-65 to +65	200nm	3	single
Tomogram 21	2	FEI Talos	26000	0.37nm	-65 to +65	200nm	2	single
Tomogram 22	3	FEI Talos	26000	0.37nm	-65 to +65	200nm	3	single
Tomogram 23	3	FEI Talos	26000	0.37nm	-65 to +65	200nm	3	single

Table 5.4. Morphometric analysis of the conoid in pre-excystation sporozoites (within sporocysts). Measurements were made on electron tomography data using 3dmod software (University of Colorado, Boulder). Continuous data was calculated as the mean of 2 measurements.

Name	Conoid fibre n°	Conoid fibre length	Conoid base diameter	Conoid apex diameter	Pre-conoidal ring 2 diameter	Pre-conoidal ring 1 diameter	Apical polar ring diameter	Conoid to apical polar ring	Conoid height	Conoid fibre width	Conoid fibre spacing	Sub-pellicular microtubule spacing
Tomogram 18	15	na	332	266	232	193	405	27	200	29	34	57
Tomogram 19	14	na	336	na	na	na	445	26	191	23	36	46
Tomogram 20	14	405	297.5	230	214	167	382	28	187	24	33	53
Tomogram 21	15	317	329	256	224	na	415	25	192	23	36	47
Tomogram 22	14	402	321	237	209	177	398	25	201	23	34	45
Tomogram 23	14	455	327	286	231	176	436	33	208	24	36	55
Mean	14.3	394.8	323.8	255.0	222.0	178.3	413.5	27.3	196.5	24.3	34.8	50.5
SD	0.5	57.3	13.8	22.5	10.2	10.8	23.7	3.0	7.8	2.3	1.3	5.1

In both the first and second sporocysts, one of the sporozoite pairs possessed a conoid containing 14 fibres whereas the other sporozoite conoid was composed of 15 fibres (Table 5.4). In the third sporocyst, both sporozoites possessed conoids composed of 14 fibres (Table 5.4). The results of this investigation therefore refute the hypothesis that conoid fibre number is genetically determined, as varying conoid fibre numbers were seen within clonal pairs. These data also suggest that conoid fibre number diversity is not a product of post-excystation/pre-invasion maturation. However, as the sample was collected following incubation in excystation fluid I cannot exclude the possibility that conoid changes occurred before the release of sporozoites from the sporocyst.

5.3.6. **Conoid fibre number varies between intracellular sporozoites**

As discussed in section 5.3.5, conoid morphometric data revealed that conoid fibre numbers vary even within clonal sporozoite pairs. To assess whether conoid fibre number diversity occurs due to a hypothetical maturation phase (associated with transition from dormant, encysted sporozoite to invasion-competent parasite), conoid fibre numbers were assessed in parasites that were fixed following invasion of host cells.

Two samples were prepared by infecting MDBK cell monolayers with freshly purified sporozoites and fixing at 30 min or 3.5 hr post infection. Following single osmium processing, sections were screened by TEM to identify intracellular sporozoites where the entire conoid could be captured. Only two suitable sporozoites were found, one for each sample (Fig.5.10). A five-serial-section tomogram was taken of the apical complex in the intracellular sporozoite fixed at 30 min post infection (Table 5.5, tomogram number 15) (Fig.5.10A-C) and a three-serial-section tomogram was taken of the apical complex in the intracellular sporozoite fixed at 3.5 hr post infection (Table 5.5, tomogram number 17) (Fig.5.10D-E).

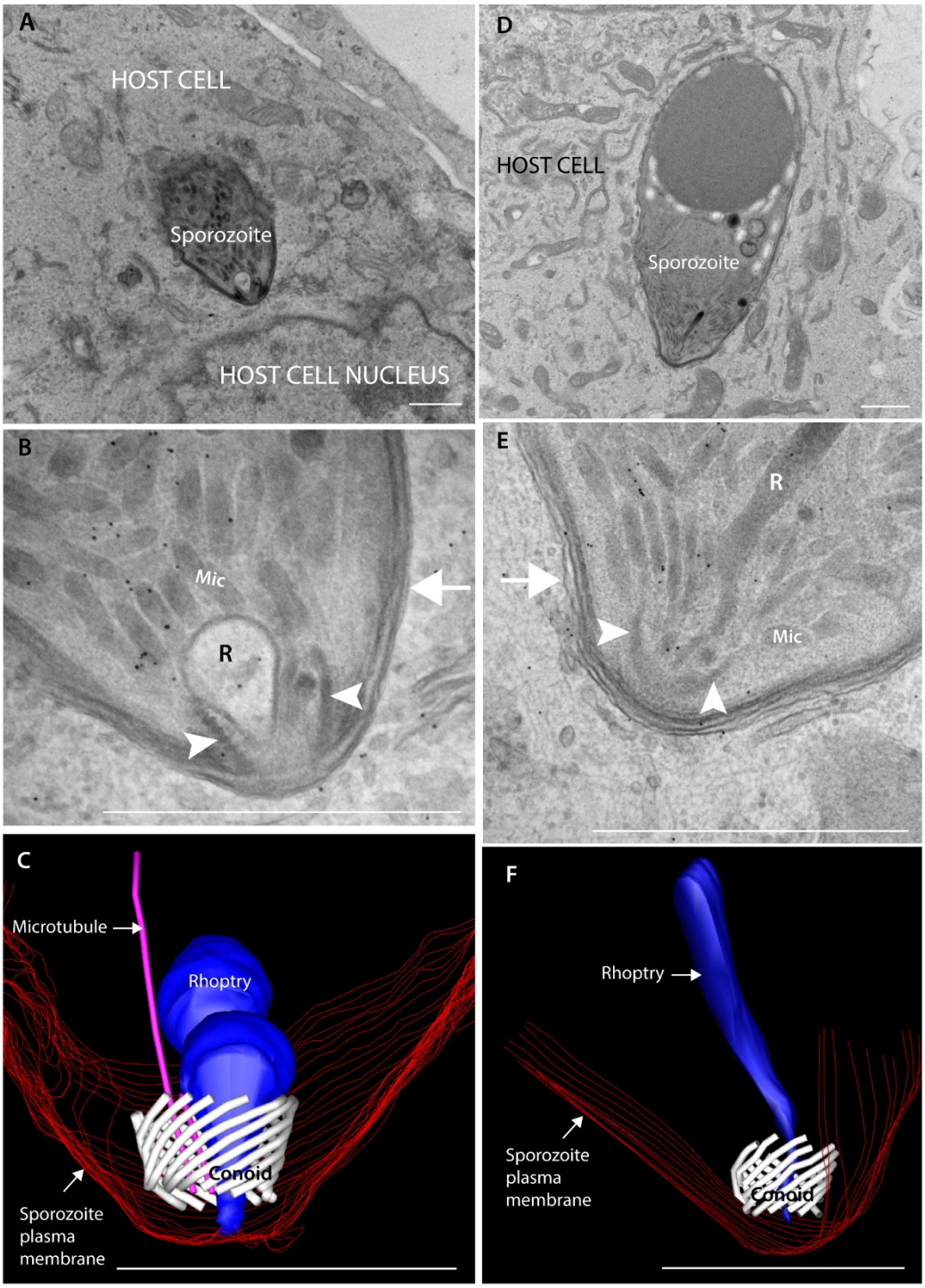


Figure 5.10. Two intracellular sporozoites were selected for electron tomography of the apical complex.

A-C) Thirty minutes post-infection sporozoite selected for electron tomography (tomogram number 15 - see Table 5.6 for details). Low (A) and high (B) magnification transmission electron microscopy images. C) Surface-rendered model created in IMOD (University of Colorado, Boulder). D-F) Three and a half hours post-infection sporozoite selected for electron tomography (tomogram number 17 - see Table 5.6 for details). Low (D) and high (E) magnification transmission electron microscopy images. F) Surface-rendered model created in IMOD. Arrow = parasitophorous vacuole membrane, arrowheads = conoid, R = rhoptry, Mic = microneme. Scale ~ 1 µm.

Table 5.5. Imaging settings for serial-section electron tomograms generated from post-invasion sporozoites

Name	Microscope	Magnification	Pixel size	Tilt parameters	Section thickness	N° serial sections	Single or dual axis
Tomogram 15	Hitachi H7650	25000	0.6nm	-60 to +60	150nm	5	dual
Tomogram 17	Hitachi H7650	20000	0.75 nm	-60 to +60	150nm	3	single

Morphometric analysis was performed on both post-invasion tomograms (Table 5.6). The conoid of the sporozoite fixed at 30 min post infection contained 16 fibres, whereas the conoid of the sporozoite fixed at 3.5 hr post infection contained 14 fibres.

Table 5.6. Morphometric analysis of the conoid in post-invasion sporozoites. Measurements were made on electron tomography data using 3dmod software (University of Colorado, Boulder). Continuous data was calculated as the mean of 2 measurements.

Name	Conoid fibre n°	Conoid fibre length	Conoid base diameter	Conoid apex diameter	Pre-conoidal ring 2 diameter	Pre-conoidal ring 1 diameter	Apical polar ring diameter	Conoid to apical polar ring	Conoid height	Conoid fibre width	Conoid fibre spacing	Sub-pellicular microtubule spacing
Tomogram 15	16	409	360	254	244	189	410	22	190	24	35	56
Tomogram 17	14	na	333	247	221	163	384	33	233	27	37	54
Mean	15.0	409.0	346.5	250.5	232.5	176.0	397.0	27.5	211.5	25.5	36.0	55.0
SD	1.4	na	19.1	4.9	16.3	18.4	18.4	7.8	30.4	2.1	1.4	1.4

Comparing conoid fibre numbers in pre-excysted sporozoite pairs (four with 14, two with 15), freshly-excysted sporozoites (one with 13, three with 14, four with 15, one with 16) and post-invasion sporozoites (one with 14, one with 16) (Fig. 5.11), it is apparent that conoids with 14 fibres are present in all samples, those with 15 fibres are present in pre- and post- excystation sporozoites, and those with 16 fibres are present in both pre- and post- invasion sporozoites.

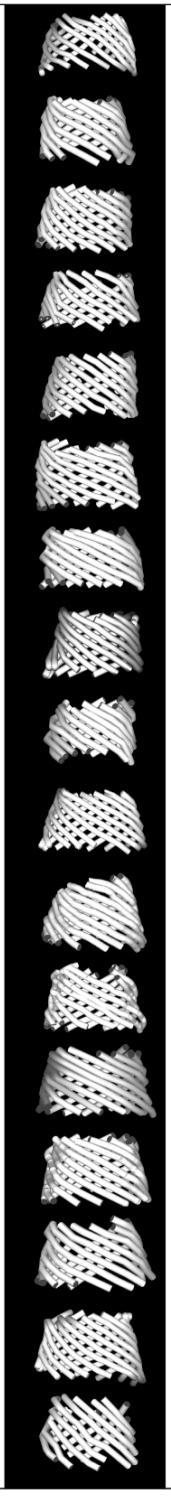
Name	Conoid fibre n°	Conoid model	Sporozoite stage
Tomogram 18	15		Within sporocyst (1)
Tomogram 19	14		Within sporocyst (1)
Tomogram 20	14		Within sporocyst (2)
Tomogram 21	15		Within sporocyst (2)
Tomogram 22	14		Within sporocyst (3)
Tomogram 23	14		Within sporocyst (3)
Tomogram 1	15		Freshly excysted
Tomogram 3	14		Freshly excysted
Tomogram 5	13		Freshly excysted
Tomogram 7	15		Freshly excysted
Tomogram 8	15		Freshly excysted
Tomogram 9	14		Freshly excysted
Tomgram 10	14		Freshly excysted
Tomogram 11	15		Freshly excysted
Tomogram 12	16		Freshly excysted
Tomogram 15	16		30min post infecton
Tomogram 17	14		3.5hr post infecton

Figure 5.11. Conoid fibre number variation is not due to either pre-invasion maturation or genetic variation.

Conoids containing 14 fibres were seen at each stage (pre-excystation, post-purification and post-invasion), conoids containing 15 fibres were seen in both pre- and post- excystation sporozoites and conoids containing 16 fibres were seen in both pre- and post- invasion sporozoites. Variation in fibre number was seen within clonal sporozoite pairs.

To summarise, the two intracellular sporozoites analysed contained different numbers of conoid fibres; thus, a specific fibre number is not required for successful parasite invasion to occur. Variations in conoid fibre number were seen in pre-excystation sporozoites, freshly-excysted sporozoites and post-invasion sporozoites (Fig.5.11), suggesting that conoid-fibre-number-variation is not a product of pre-invasion conoid-maturation.

The data presented in the subsections of section 5.3 effectively rule out genetic variation and pre-invasion maturation as causes of conoid fibre number variation. The third hypothesis, that conoid fibre number variation is a stochastic phenomenon associated with a level of flexibility in conoid formation, remains a possible explanation.

5.4. **Inner components of apical complex**

Micronemes, rhoptries, spherical vesicles and intra-conoidal microtubules are inner components of the apical complex on which this study has focused (Fig. 5.2C and D). Previously, work in *Eimeria* species and *T. gondii* have shown that proteins secreted from micronemes are involved in parasite motility, host cell invasion and egress (Bumstead and Tomley 2000, Lourido et. al. 2010). In *T. gondii*, rhoptry proteins are involved in forming the moving junction (Besteiro et. al. 2009, Lebrun et. al. 2005), a ring-shaped structure through which the parasite passes on invasion of a host cell, and in post-invasion modification of the host cell (Saeij et. al. 2007). The roles of spherical vesicles and intra-conoidal microtubules, however, are currently unknown. All that is known regarding spherical vesicles, is their appearance in electron microscopy images as a row of vesicles extending posteriorly from the conoid (Paredes-Santos et. al. 2012, Ryley 1969).

In Chapter 3, SBF-SEM imaging was used to quantify the total volumes of microneme and rhoptry organelles from a select number of sporozoites (Fig. 3.16). The use of transmission electron microscopy in the current chapter allows investigation of the apical secretory organelles at much higher resolution, however compared to SBF-SEM analysis, investigation is restricted to a limited portion of each cell.

5.4.1. **Micronemes and spherical vesicles attach to the plasma membrane in the centre of the conoid**

In all freshly-excysted-sporozoite tomograms, a single spherical vesicle and one to two micronemes were seen to be directly apposed to the plasma membrane overlying the centre of the conoid. Figure 5.12 displays sections from eight of the nine freshly-excysted-sporozoite tomograms (this excludes tomogram 8 which does not capture the apical plasma membrane overlying the conoid). Each image shows the apical end of the conoid (Fig.5.12, yellow arrowheads) and the plasma membrane overlying it.

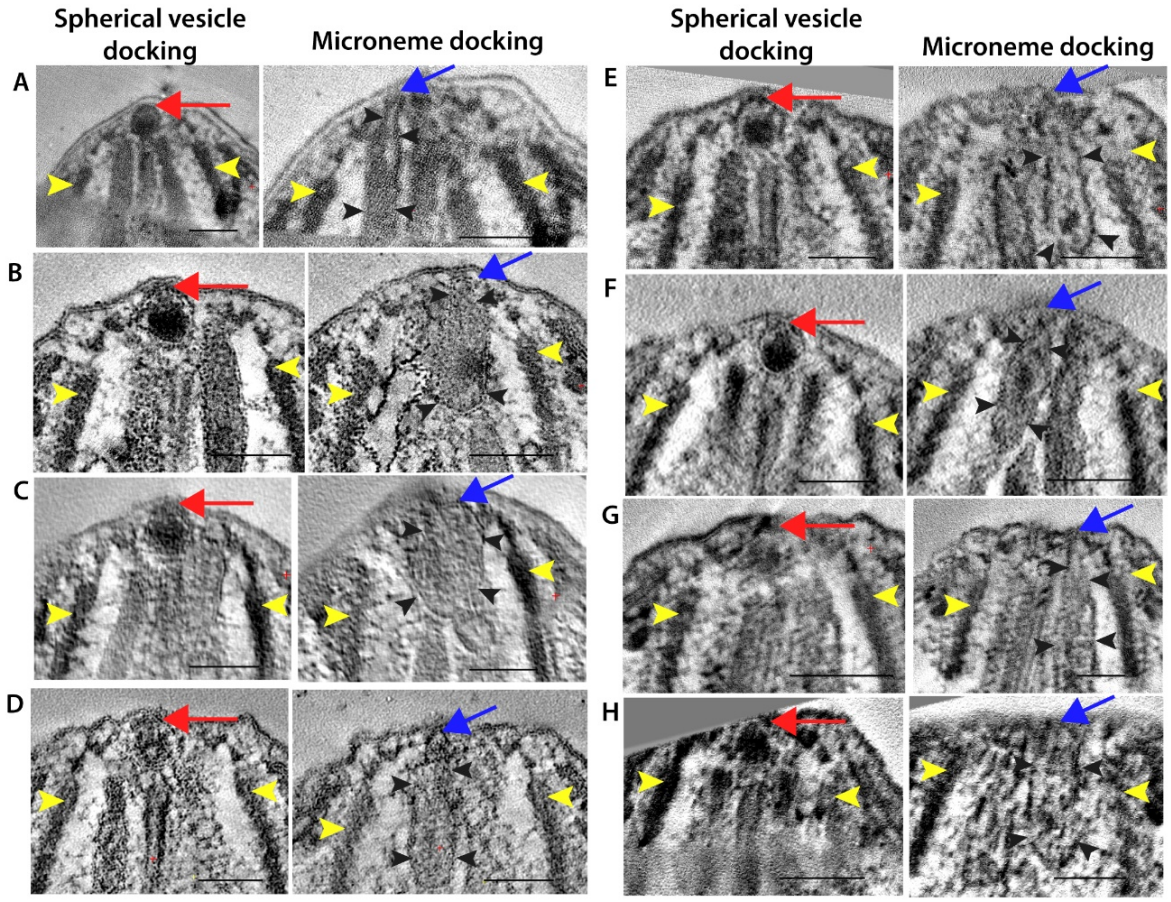


Figure 5.12. Spherical vesicles and micronemes attach to the plasma membrane overlying the conoid.

A-H) Transmission electron tomography sections of each* freshly purified sporozoite tomogram, cropped to show spherical vesicle and microneme docking within the conoid (red arrow = point of spherical vesicle/plasma membrane attachment, blue arrow = point of microneme/plasma membrane attachment, black arrowheads indicate microneme membrane, yellow arrowheads = conoid). Each line, A to H, represents data from a different sporozoite. Scale ~ 100nm.

** this excludes tomogram number 8 which finishes just short of the apical tip plasma membrane.*

Inside each conoid, there is both a spherical vesicle (Fig.5.12A-H, left image) and a microneme (Fig.5.12A-H, right image) which are in close apposition to the plasma membrane (Fig.5.12, red and blue arrows). These findings indicate that both micronemes and spherical vesicles attach to the plasma membrane prior to secretion. Based on these observations, I hypothesise that secretion of micronemes and spherical vesicles in *E. tenella* occurs through a similar mechanism to that described for secretory vesicles found in various eukaryotic cell types. Secretory vesicles release their content via a process of tethering, docking and fusion with the plasma membrane (Toonen et. al. 2006). Despite their irregular shape and unconventional biogenesis (McGovern et. al. 2018), micronemes, rhoptries and spherical vesicles are functionally analogous to secretory vesicles; all are membrane-bound protein stores destined for regulated secretion. It appears that at the time of chemical fixation, the organelles indicated in Figure 5.12 (red and blue arrows) were in the process of pre-secretory docking.

The area overlying the conoid is distinct in its structure, lacking the triple-unit pellicle arrangement found throughout the rest of the cell (Dubremetz and Torpier 1978, Scholtyseck and Mehlhorn 1970). The inner membrane complex, formed from flattened alveolar sacs, terminates at the edge of the conoid leaving only the plasma membrane separating the cytoplasm from the extracellular environment. Considering also that microneme proteins are released from the cell apex (Bumstead and Tomley 2000) it seems logical that apical organelle secretion occurs at the area devoid of the multi-unit pellicle structure. Despite extensive research into the functions of proteins secreted from apical organelles (Oakes et. al. 2013, Proellocks et. al. 2010, Tomley and Soldati 2001), this is to my knowledge, the first study providing data on the structural mechanism behind microneme secretion. Previous investigations in *T. gondii* show what may be a 'porosome analogue' at the centre of the conoid (Paredes-Santos et. al. 2012), indicating that a secretory-vesicle type system may be involved in apical organelle secretion. Porosomes are specialised structures in the plasma membrane, involved in docking and fusion of secretory vesicles (Jena 2009). In the investigation by Paredes-Santos et. al. (2012), micronemes were *not* found within the conoid and it was hypothesised that microneme secretion occurs around the extruded conoid base. My current data suggests that for *E. tenella,* microneme secretion occurs from *within* the conoid, however further work is needed to determine the precise mechanisms for other apicomplexan species such as *T. gondii*. These findings also dispute the hypothesis that microneme secretion occurs via fusion with the rhoptries, as proposed following the identification of intramembranous particles in the rhoptries of *Plasmodium falciparum* (Bannister et. al. 2000).

5.4.2. **The intra-conoidal microtubule pair is associated with secretory organelle positioning**

As depicted in Figure 5.2. (B and C) a pair of microtubules run through the centre of the conoid and extend past the conoid-base into the cytoplasm. Similar microtubules have been observed within the conoid of *T. gondii* (Hu et. al. 2002). Very little is known about the function of these microtubules; based on their location, it has been speculated that they may serve a role in secretory cargo trafficking (Hu et. al. 2006, Morrissette 2015, Qureshi et. al. 2013).

Another observation made through investigation of the high-resolution, three-dimensional structural data, was that secretory organelles are closely grouped around the intraconoid microtubule pair. Figure 5.13A shows four views of a surface-rendered model from segmentation data of 'tomogram 7' (Table 5.1). These images show that the micronemes (green), rhoptries (dark blue) and spherical vesicles (yellow) are spatially associated with the intra-conoidal microtubules (pink). An apparent spatial association between intra-conoidal microtubules and apical secretory organelles in this region was typical for surface-rendered models of the tomogram data.

To quantify spatial relationships between apical secretory organelles and intra-conoidal microtubules, measurements were taken of the distance between apical organelle and intra-conoidal

microtubule, and the distance between apical organelle and conoid. Such spatial relationships can be used to generate or support hypotheses regarding functional relationships between subcellular structures (De Brito and Scorrano 2010, Valm et. al. 2017).

Using the 'slicer' application in IMOD software (University of Colorado, Boulder), intra-conoidal micronemes, rhoptries and spherical vesicles were visualised from various planes (Fig.5.13B and C). For each of the 17 apical complex tomograms, measurements were taken of what was deemed to be the shortest distance between apical organelle membrane and conoid/microtubule (Fig.5.13B-C, double-headed arrows). In cases where two micronemes/rhoptries/spherical vesicles were present within the conoid, one was selected at random, ensuring both measurements were taken from the same organelle.

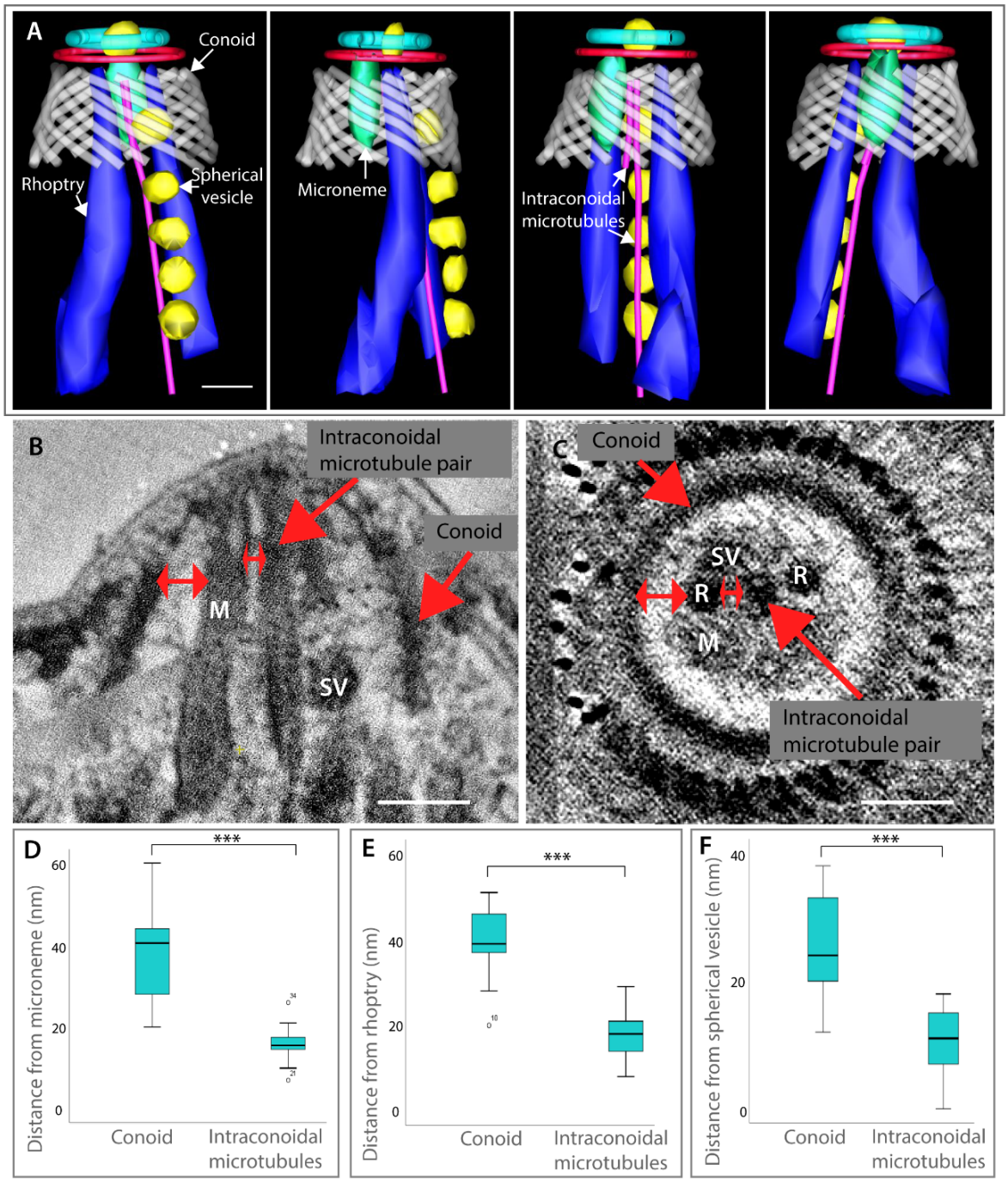


Figure 5.13. Apical organelles are spatially associated with the intraconoidal microtubule pair.

A) Series of rotational views of model created from 'tomogram 7' data (see Table 5.1) using 3dmod software (University of Colorado Boulder). Note the spatial grouping and alignment of micronemes, rhoptries and spherical vesicles with the intraconoidal microtubule pair. B and C) Electron tomography sections showing the distances from microneme (M), rhoptry (R) and spherical vesicle (SV) to the intraconoidal microtubules or conoid. Measurements were taken from what was visually deemed to be the shortest distance, edge to edge (double-headed arrows). D) Micronemes were significantly closer to the intraconoidal microtubules than to the conoid (t-test, $p < 0.0001$). E) Rhoptries were significantly closer to the intraconoidal microtubules than to the conoid (t-test, $p < 0.0001$). F) Spherical vesicles were significantly closer to the intraconoidal microtubules than to the conoid (t-test, $p < 0.0001$). Scale ~ 100 nm.

As displayed in Table 5.7 (graphically in figure 5.13D, E and F), micronemes, spherical vesicles and rhoptries are all significantly closer to the intraconoid microtubule pair than to the conoid (micronemes 15.7 +/- 4.5 nm compared to 37.9 +/- 10.1 nm, t-test, $p < 0.0001$; spherical vesicles 9.9 +/- 6.5nm compared to 25.6 +/- 8.1 nm, t-test, $p < 0.0001$; rhoptries 17.5 +/- 5.3 nm compared to 39.9 +/- 7.8 nm, t-test, $p < 0.0001$).

Table 5.7. Distances from apical organelles to intraconoidal microtubules and conoid. The distance from microneme (M), rhoptry (R) and spherical vesicle (SV) to the intraconoidal microtubules or conoid was taken from what was visually deemed to be the shortest distance, edge to edge. Measurements were made using the 'slicer' application (3dmod software - University of Colorado, Boulder). Micronemes, rhoptries and spherical vesicles were all found to be significantly closer to the intraconoidal microtubules than to the conoid (t-test, *** = p<0.0001).

Name	Microneme to conoid distance (nm)	Microneme to intraconoidal microtubule distance (nm)	Spherical vesicle to conoid distance (nm)	Spherical vesicle to intraconoidal microtubule distance (nm)	Rhoptry to conoid distance (nm)	Rhoptry to intraconoidal microtubule distance (nm)
Tomogram 1	39	10	24	0	43	10
Tomogram 3	44	15	21	11	38	11
Tomogram 5	60	21	16	12	36	22
Tomogram 7	20	7	38	18	41	14
Tomogram 8	43	15	23	15	36	19
Tomogram 9	28	16	38	7	28	18
Tomogram 10	42	18	36	0	47	14
Tomogram 11	27	16	27	16	39	21
Tomogram 12	44	14	33	17	48	23
Tomogram 15	na	na	12	0	20	17
Tomogram 17	28	10	20	0	42	8
Tomogram 18	44	17	25	13	50	20
Tomogram 19	37	15	30	18	46	29
Tomogram 20	33	15	15	8	37	16
Tomogram 21	45	19	24	11	38	16
Tomogram 22	27	17	34	9	51	18
Tomogram 23	46	26	19	13	38	22
	***		***		***	
Mean	37.9	15.7	25.6	9.9	39.9	17.5
SD	10.1	4.5	8.1	6.5	7.8	5.3

A hypothesis that accounts for these highly significant spatial dynamics, is that the apical organelles are physically tethered to the intraconoid microtubules. Moreover, this physical tethering likely has a role in apical organelle trafficking, in a similar manner to microtubule-dependent secretory vesicle trafficking that occurs in other eukaryotic cell types (Ross et. al. 2008). I thus propose a model whereby intact apical-organelles near the conoid (Fig.5.14A) attach to intra-conoidal microtubules via motor proteins such as dynein or kinesin (Fig.5.14B, red). This allows rapid, specific and targeted transport of the organelles through the conoid for attachment to the overlying plasma membrane (Fig.5.14C and G) where they dock, fuse and release their contents into the extracellular environment (Fig.5.14D). To maintain plasma membrane homoeostasis following microneme or spherical vesicle fusion, I further hypothesise that excess plasma membrane is endocytosed via the micropore and/or released into the extracellular environment as vesicles at the conoid, corresponding to membrane 'blebs' seen in some of the tomograms (Fig.5.14E and H).

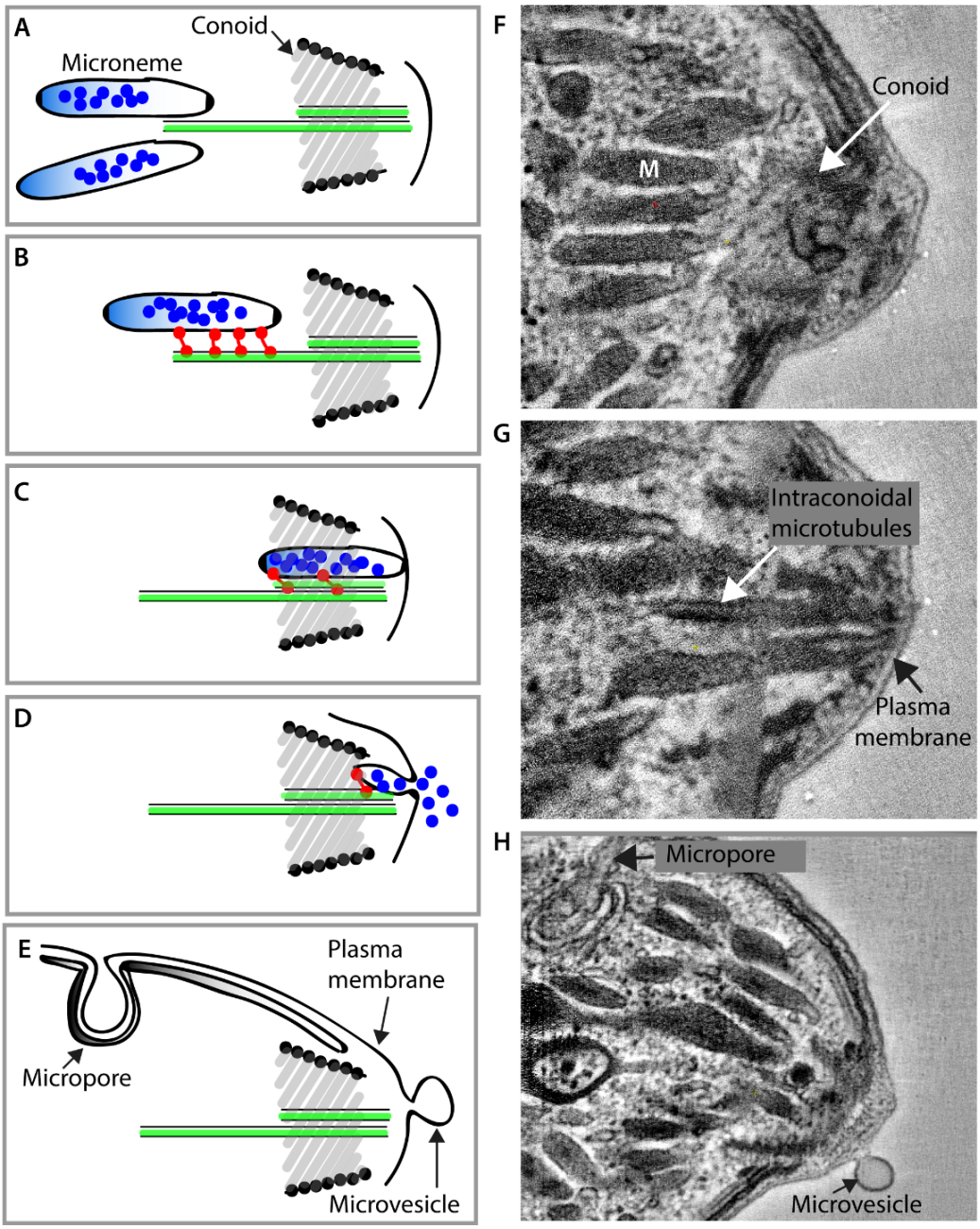


Figure. 5.14. Proposed model for microneme secretion.

A-E) Micronemes (blue) near the conoid (A) bind to the intraconoidal microtubules (green) via molecular motors (red) (B). Through action of these molecular motors, the microneme is transported through the conoid to a position where it can tether to the overlying plasma membrane (C). Following a calcium-related signal cascade, the microneme fuses with the plasma membrane and a fusion pore is created allowing release of microneme proteins (blue dots) (D). Following the addition of microneme membrane material, the plasma membrane maintains homeostasis by endocytosis via the micropore or through microvesicle release (E). F) Electron tomography data of a freshly-excysted sporozoite showing micronemes (M) near the conoid. G) Electron tomography data showing microneme docking. H) Electron tomography data showing the micropore and microvesicle release. Scale ~ 100nm.

Additional data to support this model is the finding of a conoid-localised dynein protein (TgDLC8a) in *T. gondii* (Hu et. al. 2006, Qureshi et. al. 2013). Another piece of supporting data can be found in

the electron microscopy study of the *T. gondii* cytoskeleton by Nichols and Chiappino (1987). Here it was reported that 'large, dense arms (of electron opaque material) are consistently associated with the internal microtubules, and the arms are in contact with adjacent organelles (i.e. conoid, rhoptries, and pellicular microtubules)'. This description would be fitting for the appearance of molecular motors. A couple of hypotheses were made regarding the roles of these 'dense arms' which differ slightly from my proposed model. Nichols and Chiapinno (1987) suggested that through connection with the intraconoid microtubules, they may provide 'structural stability to the rhoptries during secretion' or that they may bring about intraconoid microtubule movement as a way of 'advancing or retracting the pre-conoidal ring'.

5.4.3. **Intracellular sporozoites interact directly with the host cell cytoplasm via a break in the parasitophorous vacuole membrane (preliminary data)**

To add to the novel findings to come out of this tomography study, preliminary data were generated which indicate that intracellular sporozoites interact directly with the host cell cytoplasm via a break in the parasitophorous vacuole membrane (PVM).

Tomogram 15 (Table 5.5) shows the apical complex of an intracellular sporozoite fixed at 30 min post infection (Fig.5.15A). A membrane-bound structure, resembling that described by Saffer et. al. (1992) as an 'empty rhoptry' via immuno-electron microscopy, is visible and appears to be continuous with the parasite plasma membrane and attached at its apex to a hole in the PVM (Fig.5.15B and C). This appears to create a channel passing through both the parasite plasma membrane and the PVM, connecting the 'empty rhoptry' contents directly with host cell cytoplasm (Fig.5.15C). Similar events have been captured by thin-section electron microscopy, for example the 'empty rhoptry' of a *T. gondii* tachyzoite (Nichols et. al. 1983). Based on their electron microscopy image (Fig.5.15D) a channel between rhoptry contents and host cytoplasm can almost be resolved.

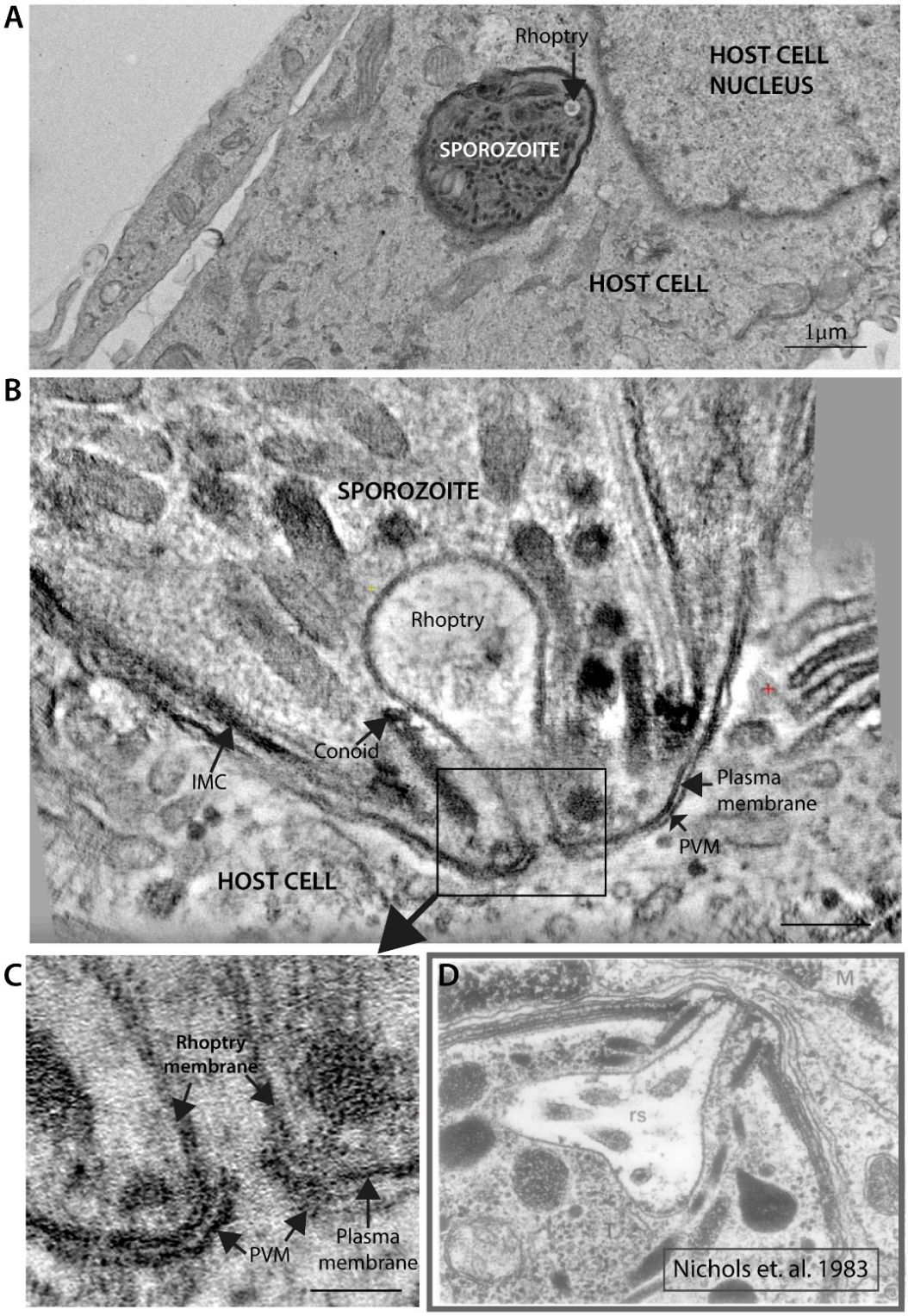


Figure 5.15. Rhoptry contents communicate directly with host cell cytoplasm via a break in the parasitophorous vacuole membrane (PVM).

A) Transmission electron microscopy image of an intracellular *E. tenella* sporozoite fixed at 30 min post infection of an MDBK cell monolayer (tomogram number 15 - see Table 5.6 for details). B) Section from transmission electron tomogram 15 (same cell as shown in (A)). Scale ~ 100 nm. C) Enlarged area from (B) showing direct communication between rhoptry contents and host cell cytoplasm via a break in the PVM. Scale ~ 50 nm. D) Transmission electron microscopy image of an intracellular *T. gondii* tachyzoite (Nichols et. al. 1983).

The observation of a direct connection between host cell cytoplasm and rhoptry contents may have significant implications in re-shaping what is understood about the parasitophorous vacuole (PV); the current view of the apicomplexan PVM is one of a sealed encasing, requiring insertion of parasite-derived pores for the transport of molecules between host cell cytoplasm and intra-vacuolar space (Gold et. al. 2015, Marino et. al. 2018). As previously mentioned, this is preliminary data, collected from a single tomogram, however hopefully it will inspire a more extensive study to confirm or refute this phenomenon.

To summarise the major findings of this chapter, the conoid of *E. tenella* varies in its fibre number. The analysed data suggests that this variation is not associated with either dynamic structural changes to the conoid or genetic differences between sporozoites. Conoid fibre number is associated with conoid base diameter and apical polar ring diameter and furthermore conoid diameter is associated with the diameters of the two pre-conoidal rings. I have discovered, and quantified, the spatial relationships of micronemes, rhoptries and spherical vesicles with the intra-conoidal microtubules which suggests a physical connection, potentially involved in vesicle positioning or secretion.

6. **Discussion**

The aim of this PhD project was to apply high-resolution microscopy to investigate the sub-cellular structure and spatio-temporal organelle dynamics of *Eimeria tenella.* It was expected that the new knowledge generated would contribute to increased understanding of the changes that occur during parasite life-cycle progression from sporozoite excystation, through the process of host cell invasion and endogenous development.

This aim was achieved, with the generation of a three-dimensional model of the *Eimeria tenella* sporozoite that provides novel insights into the subcellular morphology of this parasite stage. Through analysis of cellular components at single-cell resolution it was discovered that *E. tenella* sporozoites exhibit significant variation in their size and structure. By comparing organelle morphometrics between freshly-purified and intracellular sporozoites, novel data regarding the processes that occur during early intracellular development have been generated. In addition, a novel investigation of apical complex structure has been completed using transmission electron tomography, resulting in precise quantification of conoid morphometrics. High-resolution microscopy analysis of apical complex structures inspired several hypotheses regarding the physical and molecular processes involved in apicomplexan invasion.

6.1. **Organelle morphometrics in *E. tenella*.**

Serial block face SEM data from sporozoites processed in double osmium without thiocarbohydrazide, and sporozoites processed with a single osmium incubation, were used for ultrastructural morphometric analysis. Whole cell, refractile bodies, nucleus, amylopectin granules, mitochondria and acidocalcisomes were each analysed for 19 sporozoites. Of the sporozoites imaged by SBF-SEM, four cells were used for microneme volumetric analysis and three cells were used for rhoptry volumetric analysis.

This is the first time that volumetric organelle analysis has been performed for a species of *Eimeria*. Organelle morphometrics have been analysed for the coccidian *T. gondii*. One study employed stereological methods to provide population average volumes for dense granules, micronemes and rhoptries in *T. gondii* tachyzoites (Paredes et. al. 2011). Another study used serial section electron microscopy to calculate mitochondrial volume for two individual *T. gondii* tachyzoites (Melo et. al. 2000). Organelle morphometrics have also been analysed for *Cryptosporidium parvum* sporozoites using serial section transmission electron microscopy (Tetley et. al. 1998). This data on *C. parvum* organelle morphometrics involves total organelle volumes from one excysted sporozoite and four intra-oocyst sporozoites.

6.1.1. **Absence of dense granules in *E. tenella***

When comparing previous data on apicomplexan morphometrics with this new data on organelle morphometrics in freshly-excysted *E. tenella* sporozoites, several distinctions are apparent. In both

T. gondii and *C. parvum*, secretory organelles known as dense granules are present (Tetley et. al. 1998, Paredes et. al. 2011). These are spherical structures, several times larger than the micronemes, with a similar level of electron opacity to that of micronemes and rhoptries when processed for electron microscopy (Tetley et. al. 1998, Paredes et. al. 2011). No structures resembling dense granules were observed in the electron microscopy investigations of *E. tenella* described in this thesis.

6.1.2. **Rhoptries were found throughout the sporozoite**

In the three-dimensional investigation of *C. parvum* sporozoites (Tetley et. al. 1998) a single rhoptry was found for each cell. For *T. gondii*, six to 14 rhoptries were observed per tachyzoite (Paredes et. al. 2011). For both *T. gondii* and *C. parvum*, rhoptries were consistently positioned with the neck portion extending towards or into the conoid (Tetley et. al. 1998, Paredes et. al. 2011). In my analysis of three-dimensional *E. tenella* sporozoite structure, rhoptries with the neck portion extending towards the conoid were observed. Unlike in *T. gondii* or *C. parvum* however, structures resembling rhoptries were also found in the central or posterior parts of the sporozoite and were randomly orientated with respect to the conoid (Fig 3.16C).

6.1.3. **Microneme morphology and volume**

Microneme volumes have been calculated for both *C. parvum* sporozoites (Tetley et. al. 1998) and *T. gondii* tachyzoites (Paredes et. al. 2011). In extracellular *T. gondii* tachyzoites, micronemes occupied 0.21% of the total cell volume (Paredes et. al. 2011). In an extracellular *C. parvum* sporozoite, 167 micronemes were counted and in total occupied 0.8% of the cell volume (Tetley et. al. 1998). For extracellular *E. tenella* sporozoites, I found that micronemes occupied 5% of total cell volume (Fig. 3.17) and were elongated ovoid in structure. This is similar to what is reported for *T. gondii* tachyzoites (Paredes et. al. 2011) but differs from the spherical appearance of micronemes observed in *C. parvum* sporozoites (Melo et. al. 1998). A possible explanation for the discrepancy in microneme morphology could be due to differences in sample preparation procedure. In the work by Melo et. al. (1998), *C. parvum* sporozoites were initially fixed using cryofixation whereas the sporozoites involved in my investigation and the *T. gondii* tachyzoites examined by Paredes et. al. (2011) were initially fixed using chemical methods.

6.1.4. ***E. tenella* sporozoites possess multiple mitochondria**

Three-dimensional ultrastructural analysis of *T. gondii* tachyzoites revealed that a single mitochondrion is present in each cell and occupies approximately 3.7% to 3.8% of total cell volume (Melo et. al. 2000). For *C. parvum* sporozoite, no structures resembling mitochondria were identified (Tetley at. al. 1998). In this study on *E. tenella* sporozoites, multiple mitochondria were observed within each sporozoite. On average, sporozoites contained 14 mitochondria (Fig. 3.14E) that together occupied 2% of the total cell volume (Fig.3.17).

6.1.5. **Evaluation of organelle quantification using SBF-SEM imaging**

Due to their sub-micron scale, analyses of the structures comprising the apical complex (such as micronemes, rhoptries and the conoid) were particularly challenging following SBF-SEM imaging. This was partly due to incompatibility of the sample with osmium-intense preparation protocols. Samples containing large amounts of elements with high atomic number are more resistant to electron charging artifacts (Peddie and Collinson 2014); this means a greater probe current or a higher vacuum setting can be used resulting in greater signal to noise ratio of the image data, which could have improved segmentation of structures such as the micronemes. Another limitation of SBF-SEM imaging is the axial resolution. In the system used at Oxford Brookes University, sectioning was limited to 60 nm, resulting in under-sampling of the apical-complex structures.

By using three-dimensional, whole-cell data, it was possible to quantify organelle volumes at single-cell resolution. For each cell, these measurements are likely to be accurate at sub-micron resolution; imaging voxel sizes were in the range of 3×10^{-7} μm^3 to 5×10^{-6} μm^3 (or 300 nm^3 to 5,000 nm^3). A small level of inaccuracy is expected, caused by slight structural change on chemical fixation and human error during segmentation. By collecting data over multiple cells, it has been possible to calculate mean volumetric values as well as providing insights into the spread of sporozoite morphometrics over a population. The ability to automatically collect data encompassing multiple whole cells within a matter of hours means that SBF-SEM has a significant advantage compared to other three-dimensional electron microscopy techniques. Serial section transmission electron microscopy is another method used to collect data encompassing entire cells. As demonstrated in this thesis investigation, this technique generates high-resolution ultrastructural data, however it is technically more challenging and time-consuming compared to SBF-SEM.

These quantitative, descriptive data may be useful to many aspects of coccidiosis research; for example, in predicting organelle, molecule or chemical quantities per unit of cells. The use of ultrastructural morphological data in calculations of molecule quantity has previously been demonstrated; for example, in constructing the molecular anatomy of secretory vesicles (Takamori et. al. 2006) and in determining the insulin content of pancreatic β-cells (Shomorony et. al. 2015).

The quantitative model of *E. tenella* sporozoite anatomy could also be used as a reference for studies exploring the changes associated with life cycle progression or experimental perturbation. I have used this approach to evaluate changes to sporozoites in the initial hours after invasion.

The limitations of SBF-SEM imaging for analysis of poorly-contrasted or sub-100 nm structures, inspired us to investigate alternative imaging modalities. I predicted that transmission electron tomography would be more suitable for structural analysis of the apical complex. This technique can be used to produce sub-nanometre resolution, three-dimensional data; however, it is much less suited to imaging large volumes (for example greater than 5 μm^2) compared to SBF-SEM. Although the use of transmission electron microscopy to analyse microneme and rhoptry volumes over multiple

whole cells would be challenging (and not within the scope of this project), I hypothesised that transmission electron tomography would allow us to investigate precise morphometrics of the apical complex. To my knowledge, transmission electron tomography has never been used to investigate the conoid and associated structures.

6.2. **Cell-to-cell morphometric variation.**

Various experiments throughout this project involved detailed analyses of structures at single-cell resolution. Although most research questions are interested in average results from a population of test subjects, valuable insights can be gained by considering data on an individual-subject basis. One such insight is in calculating the degree to which variation exists within the sample. Interpreting data variation can be complex and is associated with the reliability of the method used. In many cases of research, variation in the results occurs due to lack of reliability of the data collection method. In most studies, it is important to discover the population norm and researchers focus on average values in the analyses. When working with controlled biological systems, data variation (either side of the average) is commonly assumed to be a consequence of limitations in reliability of the analytical method used.

The use of high-resolution, electron microscopy techniques, combined with high-precision measurements, meant that I had confidence in the reliability of the individual cell data-points examined in this thesis. When considering natural variation, there was an additional advantage of working with a population of cells in a non-dividing state (freshly-excysted sporozoites). All freshly-excysted sporozoites were in a dormant (sporulated-oocyst) life-cycle stage immediately prior to excystation and fixation. A subsequent batch of parasites was also tested for strain specificity by researchers at the Royal Veterinary College. This test involved sequencing of a microneme protein (AMA1) and confirmed that parasites were of the *E. tenella* wis strain.

6.2.1. **Variation in cell shape and volume**

Within populations of freshly-excysted sporozoites, there was considerable variation in cell volume and shape; the smallest sporozoite recorded was 36 μm^2 in volume and the largest sporozoite was 72 μm^2 in volume. There were also $\geq$ 2-fold volume variations for each organelle analysed (nuclei, refractile bodies, mitochondria, amylopectin granules and acidocalcisomes).

An association between cell size and organelle content was also discovered. Larger cells were found to be associated with greater nucleus volume (Fig. 3.11D), greater refractile bodies volume (Fig.3.12E) and greater mitochondria volume (Fig.3.14D).

In terms of the cell-to-cell variation seen in whole cell and organelle volumes, I hypothesise that this occurs due to asymmetric cell division. The phenomenon of asymmetric cell division has been well characterised in model organisms such as *Saccharomyces cerevisiae* and *Caenorhabditis elegans*. Several molecular mechanisms involved in the formation of different-sized daughter cells are

covered in the review by Neumüller and Knoblich (2009). Whilst within the *E. tenella* oocyst, a single diploid zygote undergoes mitotic and meiotic cell divisions (Cornelissen et. al. 1984) to form eight sporozoites (Fig. 1.2), although the exact sequence of development is poorly understood. Asymmetric organelle and cytoplasm segregation during these divisions could hypothetically lead to the sporozoite morphometric variation that was observed.

6.2.2. **Variation in conoid fibre number**

Perhaps even more interesting, was the variation seen in conoid structure between freshly-excysted sporozoites of the same population. The number of fibres comprising the conoid was found to range from 13 (for example in Fig. 6.1A) to 16 (for example in Fig. 6.1B) per sporozoite. Through investigation of clonal individuals and intracellular parasite stages, I was able to confirm that conoid structure variation is not due to genetic diversity and that it is present among individuals at various points in the life-cycle.

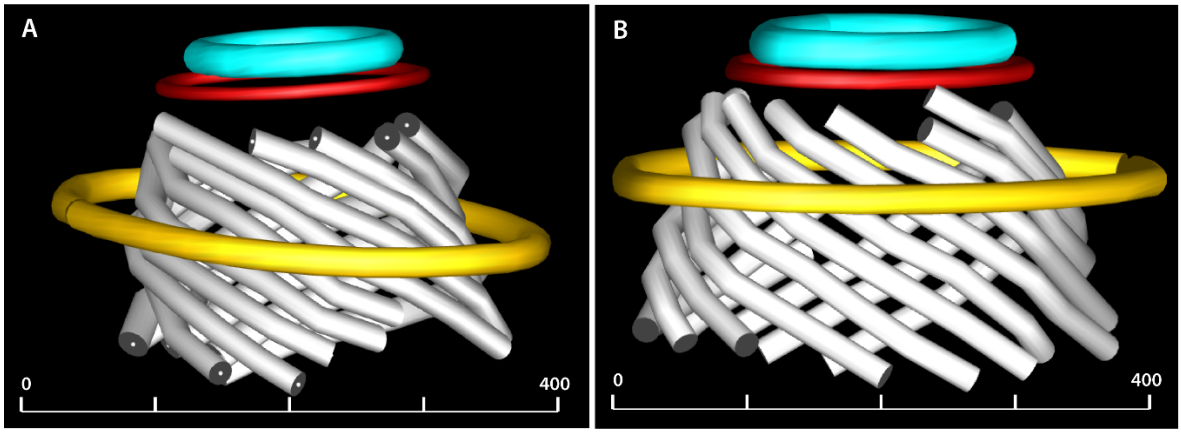


Figure 6.1. Scaled comparison of a conoid containing 13 fibres and a conoid containing 16 fibres.

A) Three-dimensional model generated from transmission electron tomography data of a conoid which contains 13 fibres. B) Three-dimensional model generated from transmission electron tomography data of a conoid which contains 16 fibres. Conoid fibres shown in silver, apical polar ring shown in gold, pre-conoidal ring one shown in cyan and pre-conoidal ring two shown in red. Scale is in nanometres.

6.2.3. **Associated morphometric parameters of the apical complex ring structures**

Following the discovery of conoid fibre number variation, morphometric parameters of apical complex structures were assessed for correlation with conoid fibre number. Greater conoid base diameter and greater apical polar ring diameter were both statistically associated with a greater conoid fibre number (Fig.5.4E, Fig.5.6G). This suggests that both conoid and apical polar ring increase in diameter to accommodate a greater number of conoid fibres. When comparing a conoid with 13 fibres (Fig.6.1A) with a conoid with 16 fibres (Fig.6.1B) differences in apical polar ring and conoid diameters are apparent.

There was also a positive correlation between conoid fibre number and conoid apex diameter, but this was not a statistically significant association (Fig. 5.4F). Greater conoid apex diameter was, however, statistically associated with greater pre-conoidal ring 2 diameter (Fig.5.7E) and greater pre-conoidal ring 1 diameter (Fig.5.7H). This suggests that during formation of the conoid and pre-conoidal rings, there is an association between the apical end of the conoid and the pre-conoidal rings. For example, the conoid may be synthesised first which then acts as a template for the formation of the pre-conoidal rings. Again, by comparing the apical complex structure for a sporozoite with 13 fibres (Fig. 6.1A) with a sporozoite with 16 conoid fibres (Fig. 6.1B) the relationship between conoid apex diameter and diameters of the pre-conoidal rings is apparent.

6.2.4. **Sporozoite morphometric variation and single-cell heterogeniety**

These findings all indicate that *E. tenella* parasites exhibit natural variation and morphological heterogeneity. In recent years, there has been increased interest into the phenomenon of single-cell heterogeneity; discussions on this topic can be found in several reviews (Ackermann 2013, 2015, Avery 2006, Hellweger et. al. 2016, Martins and Locke 2015). These reviews highlight both the possible causes for single-cell heterogeneity, such as asymmetric cell division (Martins and Locke 2015), stochastic metabolism (Avery 2006, Hellweger et. al. 2016) and epigenetic modifications (Avery 2006, Hellweger et. al. 2016), and the potential evolutionary advantage of 'noisy' phenotypes (Ackermann 2013, Martins and Locke 2015). One such advantage can be explained by the strategy of 'bet-hedging' (Ackermann 2013). This strategy involves the development of a proportion of the population which are sub-optimally suited to the current environment but are more likely to survive a change in conditions. This ensures population survival in a naturally fluctuating environment. Previous examples of single-cell heterogeneity have mainly focused on molecular or functional traits; a table of key examples is displayed in the review by Avery (Avery 2006, Table 1) . My work contributes to existing knowledge of single-cell heterogeneity by approaching the topic from a structural perspective.

With the conoid being a complex structure built from tubulin protofilaments organised into fibres, one might expect its formation to be precisely regulated. Morphological studies of similar structures

built from microtubules (also formed from tubulin protofilaments) have shown little variation in microtubule numbers between individuals or species. A good example is the flagellum, which is highly conserved in both number and arrangement of microtubules (Lin et. al. 2012).

The finding of conoid structure heterogeneity, even between individuals of the same strain of parasites, evokes several interesting questions. It has been hypothesised that the conoid evolved from basal bodies/flagella components (de Leon et. al. 2013). If this is the case, then changes associated with its evolution must have allowed for the appearance of morphological flexibility. This concept of morphological flexibility, at a subcellular level, is likely to be associated with the complex cascades involved in de-novo conoid organelle formation, where the role of check-points, molecular thresholds, or initial structure templates are not fully understood. I hypothesise that intrinsic to the formation of the conoid, there exists a range of fibre numbers which can successfully fulfil necessary interactions with the template or nucleation-units from which it is formed. In the case of basal-body or centriole formation, nine-fold symmetry is laid down early in its nucleation which ensures little deviation in the final structure (Nakazawa et. al. 2007). Until more is known about the molecular sequence of conoid formation, the reasons behind morphological flexibility in this structure are unlikely to be fully understood.

To summarise, morphometric data on the fine structures of *E. tenella* sporozoites indicate the presence of single-cell heterogeneity. Based on the data so far, it is not possible to determine whether variation in conoid structure or cell and organelle volumes offers any evolutionary advantage. Due to the variable and dynamic nature of the chicken intestinal lumen, single-cell heterogeneity may be more effective at ensuring successful infection than a 'one size fits all' approach.

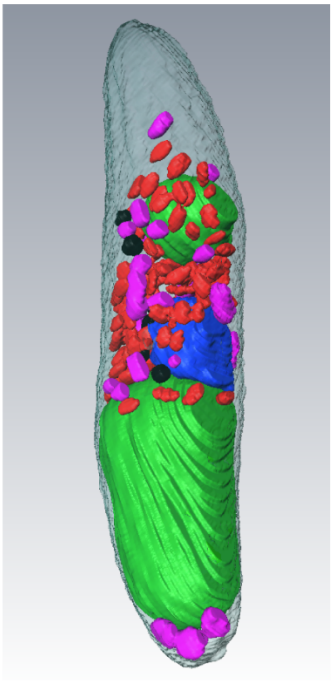
6.3. **Morphological changes associated with early intracellular development**

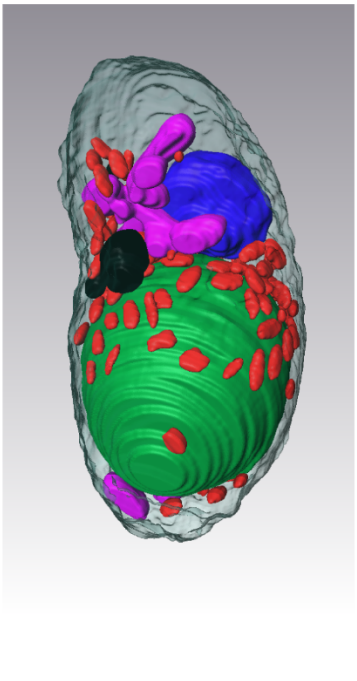
Another general finding from this thesis is the extent to which sporozoites develop during the first few hours after invasion of host cells. SBF-SEM investigation of morphometric differences between freshly-excysted and intracellular sporozoites, along with light microscopy investigations of refractile body and cell-shape dynamics, revealed that *E. tenella* sporozoites go through substantial structural changes within the first 5 hr of infection.

Although previous studies have indicated that early intracellular development may be important for the development of a protective immune response *in vivo* (Jenkins et. al. 1991, Jeurissen et. al. 1996, McDonald et. al. 1986), our understanding of the developmental processes of this stage is far from complete. The next morphologically recognisable developmental stage to succeed the sporozoite (the trophozoite) is not seen until ~ 35 hr post-infection (Pacheco et. al. 1975), and there has been a general assumption that newly invaded sporozoites essentially represent a 'resting' phase with minimal structural changes occurring in the first few hours. This study has shown that this is not the case.

6.3.1. **Cell and organelle shape and volume changes**

By 2.5 hr post infection there is a 21% increase in cell volume, a 55% increase in nuclear volume, a 29% increase in refractile bodies volume and a 45% increase in mitochondrial volume (Fig. 6.2). During this time, there were noticeable changes to both cell shape and mitochondrial morphology (Fig. 6.2). Quantification of cell-shape-change via light microscopy revealed that sporozoites change from sickle to rounded in shape over the first 5 hr of infection; cell length decreases by 29% and cell width increases by 45% (Fig. 6.2). By analysing morphometrics of sporozoites incubated in the absence of host cells, it was also confirmed that these changes are partially dependent on parasite interaction with the host cell.





	Extracellular sporozoite		Intracellular sporozoite
Cell volume	61.27 µm³	↑	(+ 21%) 70.64 µm³
Cell shape	Sickle		Rounded
Cell length	11.12 µm³	↓	(- 29%) 7.94 µm³
Cell width	3.25 µm³	↑	(+ 13%) 3.67 µm³
Nucleus volume	2.3 µm³	↑	(+ 55%) 3.4 µm³
Total refractile body volume	22.1 µm³	↑	(+ 29%) 26.9 µm³
Refractile body number (median)	2	↓	1
Mitochondria volume	1.14 µm³	↑	(+ 45%) 1.6 µm³
Mitochondrial morphology	Small, globular		Large, branched
Amylopectin granules volume	2.66 µm³		2.06 µm³
Acidocalcisomes volume	0.32 µm³		0.4 µm³
Micronemes volume	3.18 µm³		NA
Rhoptries volume	0.26 µm³		NA

Figure 6.2. Morphometric changes associated with early intracellular development.

Summary of findings associated with sporozoite morphometric changes following invasion. Mean values for quantitative morphometric parameters are displayed, this excludes refractile body number which is given as a median. Up arrows represent a positive direction of change whereas down arrows represent a negative direction of change. Cell length and width data refer to changes between 0 hr and 5 hr post infection. All other data refer to changes between 0 hr and 2.5 hr post infection.

6.3.2. **Loss of the anterior refractile body**

Due to their large volume in relation to other *E. tenella* sporozoite organelles, and the lack of understanding regarding their function, I was especially interested in the changes observed for the refractile bodies. Compared to the two refractile bodies seen in most of the freshly-excysted sporozoites, the majority of intracellular sporozoites contained a single refractile body (Fig. 6.2). I was surprised to find that the majority of sporozoites at 2.5 hr post infection contained just one refractile body since development of the *E. tenella* trophozoite (a parasite stage possessing a single refractile body which forms through development of intracellular sporozoites) has been described as occurring from around 35 hr post infection (Pacheco et. al. 1975). Further reading around refractile body dynamics revealed a study where loss of the anterior refractile body occurred earlier than 35 hr after infection. Fayer (1969) found that 58% of *E. meleagrimitis* sporozoites contained only a posterior refractile body at 6 hr post infection and 53% of *E. adenoeids* were found to contain only a posterior refractile body by 3 hr post infection. Fayer describes that loss of the anterior refractile body occurs following its posterior translocation and subsequent fusion with the posterior refractile body. Alternative methods of anterior refractile body loss have also been described. Clark and Hammond (1969) and Roberts et. al. (1970) observed fragmentation and shrinkage of the anterior refractile body in both *E. auburnensis* and *E. callospermophili*.

6.3.3. **Increase in refractile bodies volume**

A significant finding from my investigation was that the volume of the refractile bodies increases during the first few hours of infection, despite a loss of the anterior refractile body. The mechanism of refractile body fusion described by Fayer would explain why loss of the anterior refractile body is *not* associated with a *decrease* in total refractile body volume. I therefore hypothesised that anterior refractile body loss in *E. tenella* occurs through merger as opposed to fragmentation or shrinkage. Although Fayer has temporally described the process of anterior refractile body loss in *E. meleagrimitis* and *E. adenoeids* I was unable to find any temporal analysis on anterior refractile body loss in *E. tenella*.

6.3.4. **Temporal regulation of anterior refractile body loss**

Through analysis of sporozoites fixed at various time points, it was found that by 5 hr post infection, 78% (experiment1) or 44% (experiment2) of sporozoites have lost the anterior refractile body. Averaging findings from both experiments, 48.4% of sporozoites had lost the anterior refractile body between 2 hr and 5 hr post infection. A limitation of this study was the lack of data regarding change in anterior refractile body presence at time points later than 5 hr post infection. Further experiments could be performed to investigate whether all intracellular sporozoites eventually lose the anterior refractile body. Time-lapse live-cell imaging could also be employed to investigate the fate of

sporozoites containing an anterior refractile body at 5 hr post infection and assess the hypothesis that refractile body merger is essential for further parasite development.

6.3.5. **Anterior refractile body loss occurs through fusion of the refractile bodies**

By analysing live-cell microscopy data, it was found that the process of anterior refractile body loss in *E. tenella* occurred exclusively through refractile body merger (fusion of the anterior and posterior refractile bodies) (Fig. 4.6). These data build on the single prior study of refractile body merger carried out 50 years ago (Fayer 1969); by exploiting advances in light microscopy technology since then, it was possible to generate large amounts of time-lapse data with high lateral, axial and temporal resolution. After comprehensive assessment of every case of anterior refractile body loss within my dataset (Fig. 4.6) it was possible to demonstrate that completion of merger (as determined by smooth outline of the posterior refractile body) occurs within 60 seconds of initial contact. By analysing refractile body numbers in parasites incubated in the absence of host cells, it was possible to conclude that refractile body merger is dependent on host-cell presence (Fig. 4.3).

6.3.6. **Role of actin in cell shape change and refractile body merger**

Inspired by findings that similar 'membrane-less' structures exhibit actin-dependent fusion dynamics (Feric and Brangwynne 2013), I investigated the role of actin in refractile body merger. By testing actin-disrupting agents that have a differential impact on host or parasite actin, it was possible to conclude that refractile body merger is at least partially dependent on the function of parasite actin but independent to the function of host actin (Table 4.1). As refractile body merger is coincident with changes to cell shape, I hypothesised that these two dynamics are linked. By comparing length and width measurements from sporozoites with or without the anterior refractile body (all at 5 hr post infection) it was concluded that loss of the anterior refractile body was associated with a decrease in length/width ratio (Fig. 4.11E). This indicates that refractile body merger and sporozoite shape change are indeed linked. Based on these findings, I further hypothesised that sporozoite shape change is also dependent on parasite actin dynamics and by comparing cell length and width for control cells with those for samples treated with Latrunculin A or Cytochalasin D, it was possible to generate data which supported this conclusion (Fig. 4.12).

In extracellular sporozoites, an array of microtubules is present beneath the plasma membrane and inner membrane complex (Russell and Sinden 1982). It is likely that the arrangement of these microtubules confers structural stability to the elongated shape of the sporozoite (Fig. 6.3A). For sporozoite rounding to occur, I hypothesise that the spatial arrangement of these subpellicular microtubules alters. I hypothesise that the microtubules remain fixed in position at the apical polar ring (supported by the finding that subpellicular microtubule spacing in intracellular sporozoites (Table 5.6) was like that of freshly-excysted sporozoites (Table 5.2)) but that the spacing between the distal ends of the microtubules increase, much like ribs of an umbrella upon opening. In my

investigation of the role of actin in sporozoite morphological changes, actin dynamics were found to be associated with sporozoite rounding. Following invasion, actin may be involved in constriction of the cell length (Fig. 6.3Bi). This may increase the intracellular pressure leading to passive spreading of the subpellicular microtubule cytoskeleton. Alternatively, actin may be directly associated with widening the spaces between the distal ends of the subpellicular microtubules (Fig. 6.3Bii). The resultant increase in sporozoite cell width could lead to a passive reduction in cell length, with movement of material towards the cell apex due to increased pressure on the plasma membrane and decreased pressure within the cell.

For an increase in cell roundness to occur there may also be changes to the inner membrane complex. It is not yet clear whether this complex of alveolar sacs has enough flexibility to accommodate the observed changes to cell shape, or whether inner membrane complex disruption occurs to permit sporozoite rounding. Previous studies have shown that around 35 hr after invasion, much of the inner membrane complex structure is lost (Pacheco et. al. 1975), so it is possible that changes to the inner membrane complex are initiated during the first few hours after invasion.

A third potential scenario for increased cell roundness is that there is detachment of the subpellicular microtubules from the surrounding pellicle membrane which allows passage of cytoplasmic material into the space between the microtubule scaffold and cell-surface pellicle (Fig. 6.3Biii). In this scenario, changes to sporozoite shape may occur without any changes to the shape of the microtubule scaffold. A caveat of this scenario is that the distal ends of the microtubule scaffold could interfere with the smooth surface shape of the large posterior refractile body as it becomes more spherical in shape and is positioned closer to the apex of the cell. No such deformation of the posterior refractile body was observed via SBF-SEM analysis of intracellular sporozoites (Fig. 3.22). If microtubule scaffold detachment from the pellicle was coupled with depolymerisation of the free microtubule ends however, this could account for the absence of any shape deformation observed in the posterior refractile body.

Regarding the molecular mechanism behind refractile body merger, figure 6.3C shows two potential hypotheses. Refractile body merger may be a passive event (Fig. 6.3Ci). Actin-driven changes in cell shape may cause spatial re-organisation of the organelles. This could lead to closer association of the refractile bodies. Analyses of other membrane-less organelles have demonstrated that they exist due to phase-separation (Uversky 2017). This is where two liquids do not readily mix with one another, for example the separation that occurs in a mixure of oil and water. If, as hypothesised, refractile bodies also exist due to phase-separation, contact between two bodies is likely to result in a fusion event. An alternative hypothesis involves direct interaction between actin filaments and refractile bodies (Fig. 6.3Cii). Actin filaments may attach to the anterior refractile body; actin-filament polymerisation or actin-associated molecular motor interactions could therefore result in anterior refractile body relocation and fusion with the posterior refractile body.

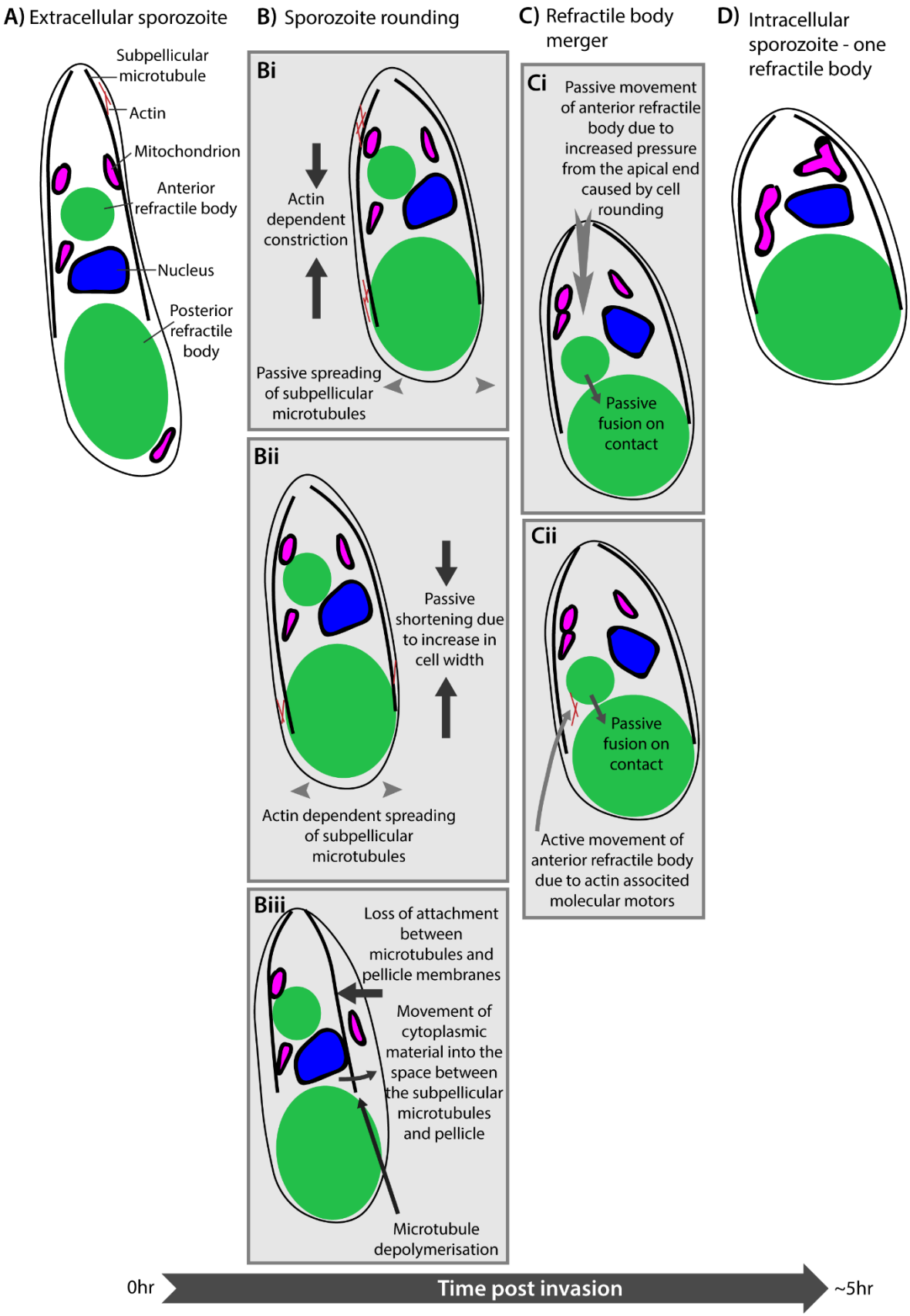


Figure 6.3. Potential molecular mechanisms underlying refractile body merger.

A) Diagramatic representation of a freshly-excysted *E. tenella* sporozoite. B) Three potential mechanisms for the increase in sporozoite roundness observed during the first few hours post invasion. C) Two potential mechanisms for refractile body merger. D) Diagramatic representation of a typical sporozoite seen at ~ 5 hr post invasion containing a single refractile body.

With developments in genetic modification of *Eimeria* species (Clark et. al. 2008), future studies, combining transgenics, targeted molecule disruption and microscopy analysis, could be employed to investigate which processes are essential for refractile body merger and how they might be targeted. Being unique organelles (not found in vertebrate host cells) I believe that these organelles represent potential targets for vaccines or pharmaceuticals. It is possible that disrupting refractile body merger may affect subsequent parasite development, although this remains to be tested. Genetic modification of *E. tenella* could be used to assess the hypothesis that refractile bodies play an essential role in parasite survival.

We also propose that the refractile bodies should be classified as a 'proteinaceous, membrane-less organelles' (PMLO). Based on the current understanding and observations of these structures, they fulfil the defined criteria and characteristics; they express fluid-like properties and maintain their structure in the absence of a limiting membrane.

6.4. **Structural insights into apical organelle secretion**

In the concluding stages of this project, the first ever three-dimensional investigation of conoid architecture in an apicomplexan species was performed. By using serial-section cellular electron tomography, I was able to generate precise measurements on apical complex component numbers, sizes and spatial relationships. Precise morphometric quantitation is useful for understanding the biomechanics of a complex structure such as the conoid. My high-resolution three-dimensional data on the morphology and spatial relationships of the conoid, appendages and apical secretory organelles, have also allowed me to generate hypotheses regarding apical organelle secretion.

Prior to this investigation, knowledge about conoid structure was based on two-dimensional cross-sections and projections through collapsed, whole conoids, following detergent extraction and negative staining. In some papers, the conoid is described as having 14 fibres (Heaslip et. al. 2009, Hu et. al. 2006, Nichols and Chiappino 1987); however, as Hu et. al. states (2002), issues involved in quantifying conoid fibre number from these types of data means a level of uncertainty at around +/-1 fibre. Other issues arise when studying such a complex three-dimensional structure using two-dimensional methods. Measurements obtained based on cross-sections can be significantly skewed if the cross-section is not in the precise plane appropriate for the measurement. Analyses based on cytoskeleton preparations must be interpreted with some caution, as detergent extraction will drastically alter the structure from its natural state. As shown in Chapter 5, transmission electron tomography was used to quantify conoid morphometrics in non- detergent-extracted specimens. Precise and reliable data from multiple cells were obtained and revealed the phenomenon of conoid fibre number variation.

6.4.1. **Site of secretion for the apical organelles**

Previous investigations into microneme and rhoptry dynamics have included electron microscopy, light microscopy and molecular techniques. The coccidian apical organelles have not previously been investigated using a technique with such high spatial resolution as transmission electron tomography. By applying this technique to study the apical secretory organelles, I have provided clear evidence that micronemes and spherical vesicles travel through the conoid and dock to the overlying plasma membrane prior to secretion (Fig. 5.12). Based on previous reports regarding apicomplexan parasites, there appears to be uncertainty regarding both the structural mechanism and location of microneme secretion. Conclusions regarding microneme secretion include the hypothesis that microneme secretion occurs by fusion with the rhoptries (Bannister et. al. 2003) and the hypothesis that micronemes secrete from around the base of the conoid at a site revealed following conoid extrusion (Paredes-Santos et. al. 2012). Other researchers believe that the micronemes are most likely to secrete following fusion with the extreme apical membrane (Blackman and Carruthers 2013); however, as Dubremetz states in his 2007 review, 'microneme exocytosis by fusion of the organelle to the apical plasma membrane has not been clearly visualized, neither has any docking characterized prior to exocytosis' (Dubremetz 2007). As such, my data provides an important novel clarification. The relevance of further investigations into the mechanism of microneme exocytosis is clearly stated in a recent review by Dubois and Soldati-Favre (2019). In the concluding remarks, they state that 'some of the many interesting avenues of research topics to broach would be the fusion event itself and the mechanisms underpinning the controlled secretion and replenishment of micronemes at the apical tip of the parasites' (Dubois and Soldati-Favre 2019).

In my own search of the literature, I found one paper where visualisation of microneme docking in *Toxoplasma* was claimed (Carruthers and Sibley 1999). In my opinion, the data presented in this paper does not clearly show microneme docking or fusion with the apical plasma membrane. In the two images provided where the conoid is visible, the structures in close apposition to the overlying plasma membrane appear analogous to spherical vesicles rather than micronemes.

6.4.2. **Docking and secretion of a single microneme**

Analysis of my serial-section electron tomograms also revealed that only one microneme appears to be docked for each cell. This suggests that only one microneme secretes at a time. Given the vast numbers of micronemes found within the cell, this hypothesis may seem counter-intuitive. Perhaps the use of high-resolution live cell fluorescent microscopy could be used to study the temporal dynamics of microneme exocytosis and test this hypothesis? Allowing only single-microneme secretion in a sequential manner may have a beneficial role in regulating microneme-protein release and ensuring persistence of microneme secretion whilst navigating the complex intra-intestinal environment in search of a site for invasion. At this point it is important to note that the sporozoites used in this analysis were collected following excystation and were not incubated in the presence of

cells or in conditions where microneme secretion is chemically induced. This could lead to structural or spatial changes in microneme arrangement that are not accounted for in this analysis.

6.4.3. **Role of intraconoidal microtubules in apical organelle trafficking**

Another aspect of apical organelle secretion explored in this project, was the interaction between apical organelles and the intra-conoidal microtubule pair. Quantitative analysis revealed a spatial association of the microtubule pair with micronemes, rhoptries and spherical vesicles (Fig. 5.13). I hypothesise that these microtubules have a direct role in apical organelle trafficking, into and through the conoid. This potential function has already been hypothesised by other researchers (Hu et. al. 2006, Morrissette 2015, Qureshi et. al. 2013) however until now, no evidence of a physical link between the intra-conoidal microtubules and apical organelles was described. In support of this theory, dynein (a microtubule-associated molecular motor) has been localised to the area of the conoid in *T. gondii* (Hu et. al. 2006, Qureshi et. al. 2013). Interestingly, genetic perturbation of dynein light chain 8 did not affect invasion rates in *T. gondii* (Qureshi et. al. 2013). Although I acknowledge this data as evidence against my theory, I believe further investigation on the roles of molecular motors is required before concluding that the intra-conoidal microtubules are unlikely to function in apical organelle transport.

Bringing these findings together, I propose a model of microneme secretion whereby organelles are individually transported through the conoid via interaction with the intra-conoidal microtubules (Fig. 5.14B and C). Fusion between microneme and plasma membranes allow secretion of the contents (Fig. 5.14D). Following the addition of membranous material from microneme fusion, plasma membrane homeostasis is maintained by either release of vesicles from the apical tip or by endocytosis, as seen by the formation of a 'micropore' (Fig. 5.14E). This concept of 'membrane flow', with the addition of material from the apical end coupled with endocytic removal elsewhere, has previously been proposed (Gras et. al. 2018).

6.4.4. **Role and dynamics of the spherical vesicles**

The organelles with strongest spatial association to the intra-conoidal microtubules were the spherical vesicles (Fig. 5.13A). These vesicles have been poorly studied and are currently without any attributed function. Structures resembling empty spherical vesicles have been hypothesised to be the result of membrane reabsorption following microneme discharge (Carruthers and Sibley 1999). In my analysis, spherical vesicles were found in non-activated sporozoites, prior to excystation from sporocyst casings, suggesting they are formed independently of microneme secretion. Based on their location at the apical complex and apparently primed for secretion, I hypothesise that spherical vesicles play a role in motility or invasion. It would be very interesting to understand the contents of these structures. Potential experiments could include immuno-electron microscopy to confirm the presence or absence of known microneme proteins. It may also be possible to purify these structures

via density gradient fractionation, a method which was previously applied to isolate and investigate the micronemes (Dubremetz et. al. 1989, Tomley et. al. 1991).

6.4.5. **Interaction between rhoptry contents and host cell cytoplasm**

One of the most exciting findings of this project, although unfortunately the aspect with the least scientific weight due to a sample size of one, was the observation of a direct connection between rhoptry contents and host cell cytoplasm in a fully-invaded parasite (Fig. 5.15). This work builds on previous data indicating direct injection of *Toxoplasma* rhoptry contents into host cell cytoplasm via a break in the host cell membrane during invasion (Håkansson et. al. 2001, Nichols et. al. 1983). Direct connection between internal parasite components and host cell cytoplasm has also been evidenced in transmission electron microscopy data of invading *Cryptosporidium* sporozoites (Lumb et. al. 1988). In contrast to the previous data on host cell – rhoptry interaction, I have provided evidence that direct communication between host cell and rhoptry contents occurs in what appears to be a fully-invaded parasite. By using transmission electron tomography, I was able to generate data with high spatial resolution in three-dimensions. This enables us to view the channel formed through both the parasite outer membrane and parasitophorous vacuole membrane in multiple planes. I was able to confirm the process described by Nichols *et. al.* (1983), whereby rhoptries fuse to the parasite membrane and breakdown of both the parasite and parasitophorous vacuole membranes occurs at this site (Fig. 5.15C).

For *T. gondii* tachyzoites, it is generally believed that direct injection of rhoptry contents into host cell cytoplasm is a transient event occurring only in the initial stages of infection, i.e. attachment and invasion (Bougdour et. al. 2013, Carruthers and Sibley 1997, Dubremetz 2007, Gilbert et. al. 2007, Håkansson et. al. 2001, Shen and Sibley 2012). *Toxoplasma gondii* rhoptry proteins, ROP16 and TgPP2C-hn, have been shown to translocate to the nucleus of infected cells and the mechanism behind this efficient translocation remains unknown (Gilbert et. al. 2007, Saeij et. al. 2007). Referring to rhoptry ROP proteins in *T. gondii*, Boothroyd and Dubremetz state that 'how these proteins enter the host cell is a mystery'. It is possible that a direct connection between host cell cytoplasm and rhoptry contents of intracellular *T. gondii* tachyzoites exists, like that observed in my *E. tenella* sporozoite. Transmission electron microscopy of intracellular *T. gondii* tachyzoites could be employed to answer this question.

Sporozoite invasion through a breach in the host cell plasma membrane has been described for several apicomplexan species; as summarised in the review by Morta and Rodrigues (2001). In these cases, a direct interaction between the parasite and host cytosol would therefore be present. It is generally believed that host cell invasion via plasma membrane disruption does not result in intracellular development of *T. gondii*, *Eimeria* or *Plasmodium* species sporozoites, as parasite replication is invariably observed within parasitophorous vacuoles (Beyer et. al. 2002, Entzeroth et. al. 1998, Mota and Rodriguez 2001, Speer et. al. 1997). In my electron tomography data, a

parasitophorous vacuole membrane can be seen surrounding the same intracellular sporozoite where a direct connection between host cytoplasm and sporozoite contents is observed. The presence of a parasitophorous vacuole membrane, broken only at the point where the sporozoite rhoptry is fused with the parasite plasma membrane, indicates that invasion of this sporozoite occurred in the classical manner, involving invagination of the host cell plasma membrane rather than entry through a hole in the host plasma membrane.

The interaction between apicomplexan parasites and host cells is exceedingly complex and many questions regarding the process of invasion and nature of the parasitophorous vacuole over the various apicomplexan species and life-cycle stages remain.

6.5. **Future work**

In addition to addressing specific objectives set out in the introduction of this thesis (see section 1.8), the observations and analyses made during the completion of this PhD have inspired novel testable hypotheses and ideas for further experimental work.

To further the investigations into refractile body dynamics, a key experiment would be to **quantify sporozoites possessing an anterior refractile body at 6 hr and 10 hr post infection**. The purpose of this would be to assess whether loss of the anterior refractile body plateaus by around 5 hr post infection or whether the percentage of sporozoites possessing an anterior refractile body decreases further between 5 hr and 10 hr post infection.

In a second experiment, **time-lapse microscopy** could be used **to track refractile body merger and parasite development** in living sporozoites over the first two days of intracellular development. If all schizonts develop from sporozoites which formerly underwent refractile body merger, this would support the hypothesis that refractile body merger is essential for schizont development. If schizonts are found to develop from sporozoites where no refractile body merger has occurred, this would refute the hypothesis that refractile body merger is essential for schizogony.

To further the investigations into apical complex organelles and ultrastructure, a key experiment would be to **generate multiple transmission electron tomograms of intracellular sporozoites from 30 min to 1 hr post infection.** These tomograms could be used to build on the preliminary data regarding sporozoite-host interaction in the early stages of intracellular development. As shown in figure 5.15, my data suggests that intra-sporozoite components communicate directly with host cell cytoplasm, however analysis of multiple cells is required to give scientific weight to this finding.

To **elucidate whether host-cell material is endocytosed by the sporozoite** during this intimate interaction, **immuno- electron microscopy** could be employed. Intracellular sporozoites could be processed and sectioned for electron microscopy. Sections could be labelled with antibodies against either rhoptry bulb proteins or host cytosol proteins and incubated with secondary antibodies conjugated with gold. In sections labelled against host cell proteins, positive gold labelling within

the ‘empty rhoptries’ would indicate endocytosis. In sections labelled against rhoptry proteins, positive labelling in the host cytosol near to the parasite apex would suggest that the ‘empty rhoptry’ is associated with rhoptry secretion.

Immuno- electron microscopy could also be used to analyse the origin of spherical vesicles. Sporozoites prepared and sectioned for electron microscopy could be labelled with antibodies against microneme or rhoptry proteins then incubated with secondary antibodies conjugated with gold. The presence or absence of gold labelling in the spherical vesicles can be used to assess the hypotheses that they are formed from microneme or rhoptry organelles.

An alternative method for the **investigation of spherical vesicle contents** could involve **cell fractionation and spherical vesicle purification**. **Two-dimensional gel electrophoresis followed by mass spectroscopy** could be used to separate and analyse proteinaceous contents of the spherical vesicles. This approach was successfully used in *E. tenella* to investigate protein content of the refractile bodies (de Venevelles et. al. 2006).

References

Ackermann M (2013) Microbial individuality in the natural environment. *The ISME journal* 7(3): 465.

Ackermann M (2015) A functional perspective on phenotypic heterogeneity in microorganisms. *Nature Reviews Microbiology* 13(8): 497.

Adl SM, Leander BS, Simpson AG, Archibald JM, Anderson OR, Bass D, Bowser SS, Brugerolle G, Farmer MA and Karpov S (2007) Diversity, nomenclature, and taxonomy of protists. *Systematic Biology* 56(4): 684–689.

Aikawa M, Miller LH, Johnson J and Rabbege J (1978) Erythrocyte entry by malarial parasites. A moving junction between erythrocyte and parasite. *The Journal of cell biology* 77(1): 72–82.

Alexander DL, Mital J, Ward GE, Bradley P and Boothroyd JC (2005) Identification of the moving junction complex of Toxoplasma gondii: a collaboration between distinct secretory organelles. *PLoS pathogens* 1(2): e17.

Allen PC and Fetterer R (2002) Recent advances in biology and immunobiology of Eimeria species and in diagnosis and control of infection with these coccidian parasites of poultry. *Clinical microbiology reviews* 15(1): 58–65.

Andenmatten N, Egarter S, Jackson AJ, Jullien N, Herman J-P and Meissner M (2013) Conditional genome engineering in Toxoplasma gondii uncovers alternative invasion mechanisms. *Nature methods* 10(2): 125.

Aubusson-Fleury A, Balavoine G, Lemullois M, Bouhouche K, Beisson J and Koll F (2017) Centrin diversity and basal body patterning across evolution: new insights from Paramecium. *Biology open* 6(6): 765–776.

Avery SV (2006) Microbial cell individuality and the underlying sources of heterogeneity. *Nature Reviews Microbiology* 4(8): 577.

Banani SF, Lee HO, Hyman AA and Rosen MK (2017) Biomolecular condensates: organizers of cellular biochemistry. *Nature reviews Molecular cell biology* 18(5): 285.

Bannister L, Hopkins J, Fowler R, Krishna S and Mitchell G (2000) Ultrastructure of rhoptry development in Plasmodium falciparum erythrocytic schizonts. *Parasitology* 121(3): 273–287.

Bannister LH, Hopkins JM, Dluzewski AR, Margos G, Williams IT, Blackman MJ, Kocken CH, Thomas AW and Mitchell GH (2003) Plasmodium falciparum apical membrane antigen 1 (PfAMA-1) is translocated within micronemes along subpellicular microtubules during merozoite development. *Journal of cell science* 116(18): 3825–3834.

Besteiro S, Dubremetz J and Lebrun M (2011) The moving junction of apicomplexan parasites: a key structure for invasion. *Cellular microbiology* 13(6): 797–805.

Besteiro S, Michelin A, Poncet J, Dubremetz J-F and Lebrun M (2009) Export of a Toxoplasma gondii rhoptry neck protein complex at the host cell membrane to form the moving junction during invasion. *PLoS pathogens* 5(2): e1000309.

Beyer TV, Svezhova NV, Radchenko AI and Sidorenko NV (2002) Parasitophorous vacuole: morphofunctional diversity in different coccidian genera (a short insight into the problem). *Cell biology international* 26(10): 861–871.

Bissati K, Levigne P, Lykins J, Adlaoui EB, Barkat A, Berraho A, Laboudi M, El Mansouri B, Ibrahimi A and Rhajaoui M (2018) Global initiative for congenital toxoplasmosis: an observational and international comparative clinical analysis. *Emerging microbes & infections* 7(1): 1–14.

Blackman MJ and Carruthers VB (2013) Recent insights into apicomplexan parasite egress provide new views to a kill. *Current opinion in microbiology* 16(4): 459–464.

Blake DP and Tomley FM (2014) Securing poultry production from the ever-present Eimeria challenge. *Trends in parasitology* 30(1): 12–19.

Boucher LE and Bosch J (2015) The apicomplexan glideosome and adhesins–Structures and function. *Journal of structural biology* 190(2): 93–114.

Bougdour A, Durandau E, Brenier-Pinchart M-P, Ortet P, Barakat M, Kieffer S, Curt-Varesano A, Curt-Bertini R-L, Bastien O and Coute Y (2013) Host cell subversion by Toxoplasma GRA16, an exported dense granule protein that targets the host cell nucleus and alters gene expression. *Cell host & microbe* 13(4): 489–500.

Brown KM, Lourido S and Sibley LD (2016) Serum albumin stimulates protein kinase G-dependent microneme secretion in Toxoplasma gondii. *Journal of Biological Chemistry* 291(18): 9554–9565.

Bullen HE, Jia Y, Yamaryo-Botté Y, Bisio H, Zhang O, Jemelin NK, Marq J-B, Carruthers V, Botté CY and Soldati-Favre D (2016) Phosphatidic acid-mediated signaling regulates microneme secretion in Toxoplasma. *Cell host & microbe* 19(3): 349–360.

Bumstead J and Tomley F (2000) Induction of secretion and surface capping of microneme proteins in Eimeria tenella. *Molecular and biochemical parasitology* 110(2): 311–321.

Bushong EA, Johnson DD, Kim K-Y, Terada M, Hatori M, Peltier ST, Panda S, Merkle A and Ellisman MH (2015) X-ray microscopy as an approach to increasing accuracy and efficiency of serial block-face imaging for correlated light and electron microscopy of biological specimens. *Microscopy and Microanalysis* 21(1): 231–238.

Butler NJ, Furtado JM, Winthrop KL and Smith JR (2013) Ocular toxoplasmosis II: clinical features, pathology and management. *Clinical & experimental ophthalmology* 41(1): 95–108.

Carey KL, Westwood NJ, Mitchison TJ and Ward GE (2004) A small-molecule approach to studying invasive mechanisms of Toxoplasma gondii. *Proceedings of the National Academy of Sciences* 101(19): 7433–7438.

Carreno RA, Matrin DS and Barta JR (1999) Cryptosporidium is more closely related to the gregarines than to coccidia as shown by phylogenetic analysis of apicomplexan parasites inferred using small-subunit ribosomal RNA gene sequences. *Parasitology research* 85(11): 899–904.

Carruthers V and Boothroyd JC (2007) Pulling together: an integrated model of Toxoplasma cell invasion. *Current opinion in microbiology* 10(1): 83–89.

Carruthers VB and Sibley L (1997) Sequential protein secretion from three distinct organelles of Toxoplasma gondii accompanies invasion of human fibroblasts. *European journal of cell biology* 73(2): 114–123.

Carruthers VB and Sibley LD (1999) Mobilization of intracellular calcium stimulates microneme discharge in Toxoplasma gondii. *Molecular microbiology* 31(2): 421–428.

Cha JO, Zhao J, Yang MS, Kim WI, Cho HS, Lim CW and Kim B (2018) Oocyst-Shedding Patterns of Three Eimeria Species in Chickens and Shedding Pattern Variation Depending on the Storage Period of Eimeria tenella Oocysts. *Journal of Parasitology* 104(1): 18–23.

Chapman H (2014) Milestones in avian coccidiosis research: a review. *Poultry science* 93(3): 501–511.

Charron AJ and Sibley LD (2004) Molecular partitioning during host cell penetration by Toxoplasma gondii. *Traffic* 5(11): 855–867.

Chiappino ML, Nichols BA and O'Connor GR (1984) Scanning Electron Microscopy of Toxoplasma gondii: Parasite Torsion and Host-Cell Responses during Invasion 1. *The Journal of protozoology* 31(2): 288–292.

Chobotar B and Entzeroth R (1993) Parasite-Host-Cell Interactions of Eimeria papillata Sporozoites with Cultured Cells A Freeze-Fracture Study. *Archiv für Protistenkunde* 143(4): III–IV.

Chobotar B and Scholtyseck E (1982) General ultrastructural features of the motile stages 102. *The Biology of the Coccidia* 101.

Clark JD, Billington K, Bumstead JM, Oakes RD, Soon PE, Sopp P, Tomley FM and Blake DP (2008) A toolbox facilitating stable transfection of Eimeria species. *Molecular and biochemical parasitology* 162(1): 77–86.

Clark WN and Hammond DM (1969) Development of Eimeria auburnensis in cell cultures. *The Journal of protozoology* 16(4): 646–654.

Coppin A, Dzierszinski F, Legrand S, Mortuaire M, Ferguson D and Tomavo S (2003) Developmentally regulated biosynthesis of carbohydrate and storage polysaccharide during differentiation and tissue cyst formation in Toxoplasma gondii. *Biochimie* 85(3–4): 353–361.

Cornelissen A, Overdulve J and Van der Ploeg M (1984) Determination of nuclear DNA of five eucoccidian parasites, Isospora (Toxoplasma) gondii, Sarcocystis cruzi, Eimeria tenella, E. acervulina and Plasmodium berghei, with special reference to gamontogenesis and meiosis in I.(T.) gondii. *Parasitology* 88(3): 531–553.

Courchaine EM, Lu A and Neugebauer KM (2016) Droplet organelles? *The EMBO journal* 35(15): 1603–1612.

Crane M, Goggin B, Pellegrino R, Ravino O, Lange C, Karkhanis Y, Kirk K and Chakraborty P (1991) Cross-protection against four species of chicken coccidia with a single recombinant antigen. *Infection and Immunity* 59(4): 1271–1277.

Danforth H and Augustine P (1989) Eimeria tenella: Use of a monoclonal antibody in determining the intracellular fate of the refractile body organelles and the effect on in vitro development. *Experimental parasitology* 68(1): 1–7.

Darling AL, Liu Y, Oldfield CJ and Uversky VN (2018) Intrinsically Disordered Proteome of Human Membrane-Less Organelles. *Proteomics* 18(5–6): 1700193.

Darzynkiewicz Z, Juan G and Srour EF (2004) Differential staining of DNA and RNA. *Current Protocols in Cytometry* 30(1): 7–3.

Daugschies A and Najdrowski M (2005) Eimeriosis in cattle: current understanding. *Journal of Veterinary Medicine, Series B* 52(10): 417–427.

De Brito OM and Scorrano L (2010) An intimate liaison: spatial organization of the endoplasmic reticulum–mitochondria relationship. *The EMBO journal* 29(16): 2715–2723.

Del Carmen MG, Mondragon M, Gonzalez S and Mondragon R (2009) Induction and regulation of conoid extrusion in Toxoplasma gondii. *Cellular microbiology* 11(6): 967–982.

Denk W and Horstmann H (2004) Serial block-face scanning electron microscopy to reconstruct three-dimensional tissue nanostructure. *PLoS biology* 2(11): e329.

Dobrowolski JM, Carruthers VB and Sibley LD (1997) Participation of myosin in gliding motility and host cell invasion by Toxoplasma gondii. *Molecular microbiology* 26(1): 163–173.

Dobrowolski JM and Sibley LD (1996) Toxoplasma invasion of mammalian cells is powered by the actin cytoskeleton of the parasite. *Cell* 84(6): 933–939.

Docampo R (2016) The origin and evolution of the acidocalcisome and its interactions with other organelles. *Molecular and biochemical parasitology* 209(1–2): 3–9.

Dubois DJ and Soldati-Favre D (2019) Biogenesis and secretion of micronemes in Toxoplasma gondii. *Cellular microbiology* e13018.

Dubremetz J, Ferreira E and Dissous C (1989) Isolation and partial characterization of rhoptries and micronemes fromEimeria nieschulzi zoites (Sporozoa, Coccidia). *Parasitology research* 75(6): 449–454.

Dubremetz J and Torpier G (1978) Freeze fracture study of the pellicle of an eimerian sporozoite (Protozoa, Coccidia). *Journal of ultrastructure research* 62(2): 94–109.

Dubremetz JF (2007) Rhoptries are major players in Toxoplasma gondii invasion and host cell interaction. *Cellular microbiology* 9(4): 841–848.

Duszynski DW (2001) Eimeria. *e LS*.

Edgar S (1954) Effect of temperature on the sporulation of oocysts of the protozoan, Eimeria tenella. *Transactions of the American Microscopical Society* 73(3): 237–242.

Entzeroth R, Mattig F and Werner-Meier R (1998) Structure and function of the parasitophorous vacuole in Eimeria species. *International journal for parasitology* 28(7): 1015–1018.

Entzeroth Rolf, Stefen C, Chobotar B and Dubremetz JF (1993) Evidence of secretion of an internal antigen of Eimeria papillata into cultured cells. *Archiv für Protistenkunde* 143(4): 347–351.

Fallahi S, Rostami A, Shiadeh MN, Behniafar H and Paktinat S (2018) An updated literature review on maternal-fetal and reproductive disorders of Toxoplasma gondii infection. *Journal of gynecology obstetrics and human reproduction* 47(3): 133–140.

Fantham H (1910) The Morphology and Life-History of Eimeria (Coccidium) avium: a Sporozoö causing a fatal disease among young Grouse. paper presented at the Proceedings of the Zoological Society of London. Wiley Online Library, 672–691.

Farrell A, Thirugnanam S, Lorestani A, Dvorin JD, Eidell KP, Ferguson DJ, Anderson-White BR, Duraisingh MT, Marth GT and Gubbels M-J (2012) A DOC2 protein identified by mutational profiling is essential for apicomplexan parasite exocytosis. *Science* 335(6065): 218–221.

Fayer R (1969) Refractile body changes in sporozoites of poultry coccidia in cell culture. paper presented at the Proc. helminth. Soc. Wash, 224–231.

Fayer R and Hammond DM (1969) Morphological changes in Eimeria bovis sporozoites during their first day in cultured mammalian cells. *The Journal of parasitology* 398–401.

Ferguson D, Belli SI, Smith NC and Wallach MG (2003) The development of the macrogamete and oocyst wall in Eimeria maxima: immuno-light and electron microscopy. *International journal for parasitology* 33(12): 1329–1340.

Feric M and Brangwynne CP (2013) A nuclear F-actin scaffold stabilizes ribonucleoprotein droplets against gravity in large cells. *Nature cell biology* 15(10): 1253.

Frandsen JC (1968) Eimeria stiedae: cytochemical identification of acid and alkaline phosphatases, carboxylic ester hydrolases, and succinate, lactate, and glucose-6-phosphate dehydrogenases in endogenous stages from rabbit tissues. *Experimental parasitology* 23(3): 398–411.

Frénal K, Dubremetz J-F, Lebrun M and Soldati-Favre D (2017) Gliding motility powers invasion and egress in Apicomplexa. *Nature Reviews Microbiology* 15(11): 645.

Friedman PL and Ellisman MH (1981) Enhanced visualization of peripheral nerve and sensory receptors in the scanning electron microscope using cryofracture and osmium-thiocarbohydrazide-osmium impregnation. *Journal of neurocytology* 10(1): 111–131.

Frölich S and Wallach M (2015) F-actin distribution and function during sexual development in Eimeria maxima. *Parasitology* 142(7): 855–864.

Frölich S and Wallach M (2016) Use of fluorescent nanoparticles to investigate nutrient acquisition by developing Eimeria maxima macrogametocytes. *Scientific reports* 6: 29030.

Gavin MA, Wanko T and Jacobs L (1962) Electron microscope studies of reproducing and interkinetic Toxoplasma. *The Journal of protozoology* 9(2): 222–234.

Gilbert LA, Ravindran S, Turetzky JM, Boothroyd JC and Bradley PJ (2007) Toxoplasma gondii targets a protein phosphatase 2C to the nuclei of infected host cells. *Eukaryotic cell* 6(1): 73–83.

Gjurčević E, Kužir S, Baždarić B, Matanović K, Debelić I, Marino F, Drašner K and Rosenthal BM (2017) New data on Eimeria dicentrarchi (Apicomplexa: Eimeriidae), a common parasite of farmed European sea bass (Dicentrarchus labrax) from the mid-eastern Adriatic. *Vet Arh* 87: 77–86.

Golemansky V (2015) Checklist of Haemosporidian and Piroplasmid Parasites (Apicomplexa: Haemospororida and Pirolasmorida) of Man and Animals in Bulgaria. *Acta Zoologica Bulgarica* 67(4): 453–460.

Gonzalez V, Combe A, David V, Malmquist NA, Delorme V, Leroy C, Blazquez S, Ménard R and Tardieux I (2009) Host cell entry by apicomplexa parasites requires actin polymerization in the host cell. *Cell host & microbe* 5(3): 259–272.

Graindorge A, Frénal K, Jacot D, Salamun J, Marq JB and Soldati-Favre D (2016) The conoid associated motor MyoH is indispensable for Toxoplasma gondii entry and exit from host cells. *PLoS pathogens* 12(1): e1005388.

Gras S, Jackson A, Woods S, Pall G, Whitelaw J, Leung JM, Ward GE, Roberts CW and Meissner M (2017) Parasites lacking the micronemal protein MIC2 are deficient in surface attachment and host cell egress, but remain virulent in vivo. *Wellcome open research* 2.

Gras S, Jimenez-Ruiz E, Klinger CM, Lemgruber L and Meissner M (2018) Apicomplexan motility depends on the operation of an endocytic-secretory cycle. *BioRxiv* 450080.

Grattepanche J, Walker LM, Ott BM, Paim Pinto DL, Delwiche CF, Lane CE and Katz LA (2018) Microbial diversity in the eukaryotic SAR clade: Illuminating the darkness between morphology and molecular data. *BioEssays* 40(4): 1700198.

Gubbels M-J and Duraisingh MT (2012) Evolution of apicomplexan secretory organelles. *International journal for parasitology* 42(12): 1071–1081.

Guigue N, Léon L, Hamane S, Gits-Muselli M, Le Strat Y, Alanio A and Bretagne S (2018) Continuous Decline of Toxoplasma gondii Seroprevalence in Hospital: A 1997–2014 Longitudinal Study in Paris, France. *Frontiers in microbiology* 9.

Håkansson S, Charron AJ and Sibley LD (2001) Toxoplasma evacuoles: a two-step process of secretion and fusion forms the parasitophorous vacuole. *The EMBO journal* 20(12): 3132–3144.

Hamid PH, Hirzmann J, Kerner K, Gimpl G, Lochnit G, Hermosilla CR and Taubert A (2015) Eimeria bovis infection modulates endothelial host cell cholesterol metabolism for successful replication. *Veterinary research* 46(1): 100.

Hammond DM and Long PL (1973) The coccidia. Eimeria, Isospora, Toxoplasma, and related genera. *The coccidia. Eimeria, Isospora, Toxoplasma, and related genera.*

Heaslip AT, Ems-McClung SC and Hu K (2009) TgICMAP1 is a novel microtubule binding protein in Toxoplasma gondii. *PLoS One* 4(10): e7406.

Hellweger FL, Clegg RJ, Clark JR, Plugge CM and Kreft J-U (2016) Advancing microbial sciences by individual-based modelling. *Nature Reviews Microbiology* 14(7): 461.

Hu K, Johnson J, Florens L, Fraunholz M, Suravajjala S, DiLullo C, Yates J, Roos DS and Murray JM (2006) Cytoskeletal components of an invasion machine—the apical complex of Toxoplasma gondii. *PLoS pathogens* 2(2): e13.

Hu K, Roos DS and Murray JM (2002) A novel polymer of tubulin forms the conoid of Toxoplasma gondii. *The Journal of cell biology* 156(6): 1039–1050.

Hughes L, Borrett S, Towers K, Starborg T and Vaughan S (2017) Patterns of organelle ontogeny through a cell cycle revealed by whole-cell reconstructions using 3D electron microscopy. *J Cell Sci* 130(3): 637–647.

Hutchison W, Dunachie J, Siim JC and Work K (1970) Coccidian-like nature of Toxoplasma gondii. *Br Med J* 1(5689): 142–144.

Jena BP (2009) Porosome: the secretory portal in cells. *Biochemistry* 48(19): 4009–4018.

Jenkins M, Augustine P, Danforth H and Barta J (1991) X-irradiation of Eimeria tenella oocysts provides direct evidence that sporozoite invasion and early schizont development induce a protective immune response (s). *Infection and immunity* 59(11): 4042–4048.

Jensen JB and Hammond DM (1975) Ultrastructure of the invasion of Eimeria magna sporozoites into cultured cells. *The Journal of protozoology* 22(3): 411–415.

Jeurissen S, Janse E, Vermeulen A and Vervelde L (1996) Eimeria tenella infections in chickens: aspects of host-parasite: interaction. *Veterinary Immunology and Immunopathology* 54(1–4): 231–238.

Jirků M, Modrý D, Šlapeta JR, Koudela B and Lukeš J (2002) The phylogeny of Goussia and Choleoeimeria (Apicomplexa; Eimeriorina) and the evolution of excystation structures in coccidia. *Protist* 153(4): 379–390.

Katris NJ, van Dooren GG, McMillan PJ, Hanssen E, Tilley L and Waller RF (2014) The apical complex provides a regulated gateway for secretion of invasion factors in Toxoplasma. *PLoS pathogens* 10(4): e1004074.

Kheysin YM (2013) *Life cycles of coccidia of domestic animals*. Elsevier.

Kopko S and Martin D (2000) Responses of chickens to a recombinant refractile body antigen of Eimeria tenella administered using various immunizing strategies. *Poultry Science* 79(3): 336–342.

Koster AJ, Grimm R, Typke D, Hegerl R, Stoschek A, Walz J and Baumeister W (1997) Perspectives of molecular and cellular electron tomography. *Journal of structural biology* 120(3): 276–308.

Kremer JR, Mastronarde DN and McIntosh JR (1996) Computer visualization of three-dimensional image data using IMOD. *Journal of structural biology* 116(1): 71–76.

Lai L, Bumstead J, Liu Y, Garnett J, Campanero-Rhodes MA, Blake DP, Palma AS, Chai W, Ferguson DJ and Simpson P (2011) The role of sialyl glycan recognition in host tissue tropism of the avian parasite Eimeria tenella. *PLoS pathogens* 7(10): e1002296.

Lal K, Bromley E, Oakes R, Prieto JH, Sanderson SJ, Kurian D, Hunt L, Yates III JR, Wastling JM and Sinden RE (2009) Proteomic comparison of four Eimeria tenella life-cycle stages: Unsporulated oocyst, sporulated oocyst, sporozoite and second-generation merozoite. *Proteomics* 9(19): 4566–4576.

Lane CE and Archibald JM (2008) The eukaryotic tree of life: endosymbiosis takes its TOL. *Trends in ecology & evolution* 23(5): 268–275.

Lebrun M, Michelin A, El Hajj H, Poncet J, Bradley PJ, Vial H and Dubremetz JF (2005) The rhoptry neck protein RON4 relocalizes at the moving junction during Toxoplasma gondii invasion. *Cellular microbiology* 7(12): 1823–1833.

Lekutis C, Ferguson DJ, Grigg ME, Camps M and Boothroyd JC (2001) Surface antigens of Toxoplasma gondii: variations on a theme. *International journal for parasitology* 31(12): 1285–1292.

Lemgruber L and Lupetti P (2012) Crystalloid body, refractile body and virus-like particles in Apicomplexa: what is in there? *Parasitology* 139(3): 285–293.

de Leon JC, Scheumann N, Beatty W, Beck JR, Tran JQ, Yau C, Bradley PJ, Gull K, Wickstead B and Morrissette NS (2013) A SAS-6-like protein suggests that the Toxoplasma conoid complex evolved from flagellar components. *Eukaryotic cell* 12(7): 1009–1019.

Levine ND (1977) Taxonomy of Toxoplasma. *The Journal of protozoology* 24(1): 36–41.

Levine ND (1980) Some corrections of coccidian (Apicomplexa: Protozoa) nomenclature. *The Journal of parasitology* 66(5): 830–834.

Levine ND (1984) Nomenclatural corrections and new taxa in the apicomplexan protozoa. *Transactions of the American Microscopical Society* 195–204.

Li P, Banjade S, Cheng H-C, Kim S, Chen B, Guo L, Llaguno M, Hollingsworth JV, King DS and Banani SF (2012) Phase transitions in the assembly of multivalent signalling proteins. *Nature* 483(7389): 336.

Lim L and McFadden GI (2010) The evolution, metabolism and functions of the apicoplast. *Philosophical Transactions of the Royal Society B: Biological Sciences* 365(1541): 749–763.

Lin J, Heuser T, Carbajal-González BI, Song K and Nicastro D (2012) The structural heterogeneity of radial spokes in cilia and flagella is conserved. *Cytoskeleton* 69(2): 88–100.

Lourido S and Moreno SN (2015) The calcium signaling toolkit of the Apicomplexan parasites Toxoplasma gondii and Plasmodium spp. *Cell Calcium* 57(3): 186–193.

Lourido S, Shuman J, Zhang C, Shokat KM, Hui R and Sibley LD (2010) Calcium-dependent protein kinase 1 is an essential regulator of exocytosis in Toxoplasma. *Nature* 465(7296): 359.

Luft BJ, Brooks RG, Conley FK, McCabe RE and Remington JS (1984) Toxoplasmic encephalitis in patients with acquired immune deficiency syndrome. *Jama* 252(7): 913–917.

Lumb R, Smith K, O'donoghue P and Lanser J (1988) Ultrastructure of the attachment of Cryptosporidium sporozoites to tissue culture cells. *Parasitology research* 74(6): 531–536.

Martins BM and Locke JC (2015) Microbial individuality: how single-cell heterogeneity enables population level strategies. *Current opinion in microbiology* 24: 104–112.

Martins-Duarte ÉS, Carias M, Vommaro R, Surolia N and de Souza W (2016) Apicoplast fatty acid synthesis is essential for pellicle formation at the end of cytokinesis in Toxoplasma gondii. *J Cell Sci* 129(17): 3320–3331.

Matsubayashi M, Hatta T, Miyoshi T, Sasai K, Shimura K, Isobe T, Kita K and Tsuji N (2013) High-throughput RNA sequencing profiles and transcriptional evidence of aerobic respiratory enzymes in sporulating oocysts and sporozoites of Eimeria tenella. *Infection, Genetics and Evolution* 18: 269–276.

McAllister CT, Duszynski DW, Fisher RN and Austin CC (2014) A new species of Eimeria Schneider, 1875 (Apicomplexa: Eimeriidae) from the Solomon ground skink, Sphenomorphus solomonis (Boulenger)(Sauria: Scincidae) from Papua New Guinea. *Systematic parasitology* 87(1): 83–86.

McAllister CT, Motriuk-Smith D, Seville RS, Connior MB, Trauth SE and Robison HW (2017) Coccidian Parasites (Apicomplexa: Eimeriidae) of Arkansas Herpetofauna: A Summary with Two New State Records. *Journal of the Arkansas Academy of Science* 71: 143.

McDonald V, Rose ME and Jeffers T (1986) Eimeria tenella: immunogenicity of the first generation of schizogony. *Parasitology* 93(1): 1–7.

McDonald V, Wisher M, Rose ME and Jeffers T (1988) Eitneria tenella: immunological diversity between asexual generations. *Parasite immunology* 10(6): 649–660.

McDonald Vincent and Rose ME (1987) Eimeria tenella and E. necatrix: a third generation of schizogony is an obligatory part of the developmental cycle. *The Journal of parasitology* 617–622.

McDougald L and Jeffers T (1976) Comparative in vitro development of precocious and normal strains of Eimeria tenella (Coccidia). *The Journal of protozoology* 23(4): 530–534.

McGovern OL, Rivera-Cuevas Y, Kannan G, Narwold Jr AJ and Carruthers VB (2018) Intersection of endocytic and exocytic systems in Toxoplasma gondii. *Traffic* 19(5): 336–353.

McLaren DJ (1969) Observations on the fine structural changes associated with schizogony and gametogony in Eimeria tenella. *Parasitology* 59(3): 563–574.

Megía-Palma R, Martínez J, Acevedo I, Martín J, García-Roa R, Ortega J, Peso-Fernández M, Albaladejo G, Cooper RD and Paranjpe DA (2015) Phylogeny of the reptilian Eimeria: are Choleoeimeria and Acroeimeria valid generic names? *Zoologica Scripta* 44(6): 684–692.

Melo E, Attias M and De Souza W (2000) The single mitochondrion of tachyzoites of Toxoplasma gondii. *Journal of structural biology* 130(1): 27–33.

Mercier C and Cesbron-Delauw M-F (2015) Toxoplasma secretory granules: one population or more? *Trends in parasitology* 31(2): 60–71.

Mikula S and Denk W (2015) High-resolution whole-brain staining for electron microscopic circuit reconstruction. *Nature methods* 12(6): 541.

Miranda K, de Souza W, Plattner H, Hentschel J, Kawazoe U, Fang J and Moreno SN (2008) Acidocalcisomes in Apicomplexan parasites. *Experimental parasitology* 118(1): 2–9.

Mondragon R and Frixione E (1996) Ca2+-dependence of conoid extrusion in Toxoplasma gondii tachyzoites. *Journal of Eukaryotic Microbiology* 43(2): 120–127.

Mordue DG, Håkansson S, Niesman I and Sibley LD (1999) Toxoplasma gondii resides in a vacuole that avoids fusion with host cell endocytic and exocytic vesicular trafficking pathways. *Experimental parasitology* 92(2): 87–99.

Morisaki JH, Heuser JE and Sibley LD (1995) Invasion of Toxoplasma gondii occurs by active penetration of the host cell. *Journal of cell science* 108(6): 2457–2464.

Morrissette N (2015) Targeting Toxoplasma tubules: tubulin, microtubules, and associated proteins in a human pathogen. *Eukaryotic cell* 14(1): 2–12.

Mota MM and Rodriguez A (2001) Migration through host cells by apicomplexan parasites. *Microbes and infection* 3(13): 1123–1128.

Münter S, Sabass B, Selhuber-Unkel C, Kudryashev M, Hegge S, Engel U, Spatz JP, Matuschewski K, Schwarz US and Frischknecht F (2009) Plasmodium sporozoite motility is modulated by the turnover of discrete adhesion sites. *Cell host & microbe* 6(6): 551–562.

Nakai Y and Ogimoto K (1987) Relationship between amylopectin and infectivity of Eimeria tenella sporozoite. *Nihon juigaku zasshi. The Japanese journal of veterinary science* 49(3): 447–452.

Nakazawa Y, Hiraki M, Kamiya R and Hirono M (2007) SAS-6 is a cartwheel protein that establishes the 9-fold symmetry of the centriole. *Current Biology* 17(24): 2169–2174.

Neumüller RA and Knoblich JA (2009) Dividing cellular asymmetry: asymmetric cell division and its implications for stem cells and cancer. *Genes & development* 23(23): 2675–2699.

Nichols Babara A and Chiappino ML (1987) Cytoskeleton of Toxoplasma gondii 1. *The Journal of protozoology* 34(2): 217–226.

Nichols Barbara A, Chiappino ML and O'Connor GR (1983) Secretion from the rhoptries of Toxoplasma gondii during host-cell invasion. *Journal of ultrastructure research* 83(1): 85–98.

Nott TJ, Craggs TD and Baldwin AJ (2016) Membraneless organelles can melt nucleic acid duplexes and act as biomolecular filters. *Nature chemistry* 8(6): 569.

Nott TJ, Petsalaki E, Farber P, Jervis D, Fussner E, Plochowietz A, Craggs TD, Bazett-Jones DP, Pawson T and Forman-Kay JD (2015) Phase transition of a disordered nuage protein generates environmentally responsive membraneless organelles. *Molecular cell* 57(5): 936–947.

Oakes RD, Kurian D, Bromley E, Ward C, Lal K, Blake DP, Reid AJ, Pain A, Sinden RE and Wastling JM (2013) The rhoptry proteome of Eimeria tenella sporozoites. *International journal for parasitology* 43(2): 181–188.

Okamoto N and Keeling PJ (2014) The 3D structure of the apical complex and association with the flagellar apparatus revealed by serial TEM tomography in Psammosa pacifica, a distant relative of the Apicomplexa. *PloS one* 9(1): e84653.

Ortega YR and Sanchez R (2010) Update on Cyclospora cayetanensis, a food-borne and waterborne parasite. *Clinical Microbiology Reviews* 23(1): 218–234.

Pacheco ND, Vetterling JM and Doran DJ (1975) Ultrastructure of cytoplasmic and nuclear changes in Eimeria tenella during first-generation schizogony in cell culture. *The Journal of parasitology* 61(1): 31–42.

Paredes-Santos TC, de Souza W and Attias M (2012) Dynamics and 3D organization of secretory organelles of Toxoplasma gondii. *Journal of structural biology* 177(2): 420–430.

Parkinson DY, McDermott G, Etkin LD, Le Gros MA and Larabell CA (2008) Quantitative 3-D imaging of eukaryotic cells using soft X-ray tomography. *Journal of structural biology* 162(3): 380–386.

Peddie CJ and Collinson LM (2014) Exploring the third dimension: volume electron microscopy comes of age. *Micron* 61: 9–19.

Pereira-Chioccola VL, Vidal JE and Su C (2009) Toxoplasma gondii infection and cerebral toxoplasmosis in HIV-infected patients. *Future microbiology* 4(10): 1363–1379.

Periz J, Whitelaw J, Harding C, Gras S, Minina MIDR, Latorre-Barragan F, Lemgruber L, Reimer MA, Insall R and Heaslip A (2017) Toxoplasma gondii F-actin forms an extensive filamentous network required for material exchange and parasite maturation. *Elife* 6: e24119.

Peterson JR and Mitchison TJ (2002) Small molecules, big impact: a history of chemical inhibitors and the cytoskeleton. *Chemistry & biology* 9(12): 1275–1285.

Pinali C and Kitmitto A (2014) Serial block face scanning electron microscopy for the study of cardiac muscle ultrastructure at nanoscale resolutions. *Journal of molecular and cellular cardiology* 76: 1–11.

Preiser P, Kaviratne M, Khan S, Bannister L and Jarra W (2000) The apical organelles of malaria merozoites: host cell selection, invasion, host immunity and immune evasion. *Microbes and Infection* 2(12): 1461–1477.

Proellocks NI, Coppel RL and Waller KL (2010) Dissecting the apicomplexan rhoptry neck proteins. *Trends in parasitology* 26(6): 297–304.

Qureshi BM, Hofmann NE, Arroyo-Olarte RD, Nickl B, Hoehne W, Jungblut PR, Lucius R, Scheerer P and Gupta N (2013) Dynein light chain 8a of Toxoplasma gondii, a unique conoid-localized β-strand-swapped homodimer, is required for an efficient parasite growth. *The FASEB Journal* 27(3): 1034–1047.

Reid AJ, Blake DP, Ansari HR, Billington K, Browne HP, Bryant J, Dunn M, Hung SS, Kawahara F and Miranda-Saavedra D (2014) Genomic analysis of the causative agents of coccidiosis in domestic chickens. *Genome research* 24(10): 1676–1685.

Riglar DT, Richard D, Wilson DW, Boyle MJ, Dekiwadia C, Turnbull L, Angrisano F, Marapana DS, Rogers KL and Whitchurch CB (2011) Super-resolution dissection of coordinated events during malaria parasite invasion of the human erythrocyte. *Cell host & microbe* 9(1): 9–20.

Robert-Gangneux F, Murat J-B, Fricker-Hidalgo H, Brenier-Pinchart M-P, Gangneux J-P and Pelloux H (2011) The placenta: a main role in congenital toxoplasmosis? *Trends in parasitology* 27(12): 530–536.

Roberts WL and Hammond DM (1970) Ultrastructural and cytologic studies of the sporozoites of four Eimeria species. *The Journal of protozoology* 17(1): 76–86.

Roberts WL, Hammond DM, Anderson LC and Speer CA (1970) Ultrastructural study of schizogony in Eimeria callospermophili. *The Journal of protozoology* 17(4): 584–592.

Roberts WL, Speer CA and Hammond DM (1971) Penetration of Eimeria larimerensis sporozoites into cultured cells as observed with the light and electron microscopes. *The Journal of parasitology* 615–625.

Rohloff P, Miranda K, Rodrigues JC, Fang J, Galizzi M, Plattner H, Hentschel J and Moreno SN (2011) Calcium uptake and proton transport by acidocalcisomes of Toxoplasma gondii. *PLoS One* 6(4): e18390.

Roos DS (2005) Themes and variations in apicomplexan parasite biology. *Science* 309(5731): 72–73.

Rose ME, Lawn A and Millard B (1984) The effect of immunity on the early events in the life-cycle of Eimeria tenella in the caecal mucosa of the chicken. *Parasitology* 88(2): 199–210.

Ross JL, Ali MY and Warshaw DM (2008) Cargo transport: molecular motors navigate a complex cytoskeleton. *Current opinion in cell biology* 20(1): 41–47.

Russell D and Sinden R (1982) Three-dimensional study of the intact cytoskeleton of coccidian sporozoites. *International journal for parasitology* 12(2–3): 221–226.

Ryley JF (1969) Ultrastructural studies on the sporozoite of Eimeria tenella. *Parasitology* 59(1): 67–72.

Sabin AB (1939) Biological and immunological identity of Toxoplasma of animal and human origin. *Proceedings of the Society for Experimental Biology and Medicine* 41(1): 75–80.

Saeij J, Coller S, Boyle J, Jerome M, White M and Boothroyd J (2007) Toxoplasma co-opts host gene expression by injection of a polymorphic kinase homologue. *Nature* 445(7125): 324.

Saffer LD, Mercereau-Puijalon O, Dubremetz JF and Schwartzman JD (1992) Localization of a Toxoplasma gondii rhoptry protein by immunoelectron microscopy during and after host cell penetration. *The Journal of protozoology* 39(4): 526–530.

Sakaguchi M, Miyazaki N, Fujioka H, Kaneko O and Murata K (2016) Three-dimensional analysis of morphological changes in the malaria parasite infected red blood cell by serial block-face scanning electron microscopy. *Journal of structural biology* 193(3): 162–171.

Schmitz S, Grainger M, Howell S, Calder LJ, Gaeb M, Pinder JC, Holder AA and Veigel C (2005) Malaria parasite actin filaments are very short. *Journal of molecular biology* 349(1): 113–125.

Schneider MP, Liu B, Glock P, Suttie A, McHugh E, Andrew D, Batinovic S, Williamson N, Hanssen E and McMillan P (2017) Disrupting assembly of the inner membrane complex blocks Plasmodium falciparum sexual stage development. *PLoS pathogens* 13(10): e1006659.

Scholtyseck E and Mehlhorn H (1970) Ultrastructural study of characteristic organelles (paired organelles, micronemes, micropores) of sporozoa and related organisms. *Zeitschrift für Parasitenkunde* 34(2): 97–127.

Scott M, Chen C-C, Mecklenburg M, Zhu C, Xu R, Ercius P, Dahmen U, Regan B and Miao J (2012) Electron tomography at 2.4-ångström resolution. *Nature* 483(7390): 444.

Sheffield HG and Melton ML (1968) The fine structure and reproduction of Toxoplasma gondii. *The Journal of parasitology* 209–226.

Shen B and Sibley LD (2012) The moving junction, a key portal to host cell invasion by apicomplexan parasites. *Current opinion in microbiology* 15(4): 449–455.

Shirley M and Harvey D (1996) Eimeria tenella: infection with a single sporocyst gives a clonal population. *Parasitology* 112(6): 523–528.

Shomorony A, Pfeifer C, Aronova M, Zhang G, Cai T, Xu H, Notkins A and Leapman R (2015) Combining quantitative 2D and 3D image analysis in the serial block face SEM: application to secretory organelles of pancreatic islet cells. *Journal of microscopy* 259(2): 155–164.

Sibley LD (1995) Invasion of vertebrate cells by Toxoplasma gondii. *Trends in cell biology* 5(3): 129–132.

Sibley LD (2004) Intracellular parasite invasion strategies. *Science* 304(5668): 248–253.

Skillman KM, Diraviyam K, Khan A, Tang K, Sept D and Sibley LD (2011) Evolutionarily divergent, unstable filamentous actin is essential for gliding motility in apicomplexan parasites. *PLoS pathogens* 7(10): e1002280.

Smith C and Strout R (1980) Eimeria tenella: effect of narasin, a polyether antibiotic on the ultrastructure of intracellular sporozoites. *Experimental parasitology* 50(3): 426–436.

Soares Medeiros LC, Gomes F, Maciel LRM, Seabra SH, Docampo R, Moreno S, Plattner H, Hentschel J, Kawazoe U and Barrabin H (2011) Volutin granules of Eimeria parasites are acidic compartments and have physiological and structural characteristics similar to acidocalcisomes. *Journal of Eukaryotic Microbiology* 58(5): 416–423.

Sologub L, Kuehn A, Kern S, Przyborski J, Schillig R and Pradel G (2011) Malaria proteases mediate inside-out egress of gametocytes from red blood cells following parasite transmission to the mosquito. *Cellular microbiology* 13(6): 897–912.

Song H, Qiu B, Yan R, Xu L, Song X and Li X (2013) The protective efficacy of chimeric SO7/IL-2 DNA vaccine against coccidiosis in chickens. *Research in veterinary science* 94(3): 562–567.

Spector I, Shochet NR, Blasberger D and Kashman Y (1989) Latrunculins—novel marine macrolides that disrupt microfilament organization and affect cell growth: I. Comparison with cytochalasin D. *Cell motility and the cytoskeleton* 13(3): 127–144.

Speer C, Dubey J, Blixt J and Prokop K (1997) Time lapse video microscopy and ultrastructure of penetrating sporozoites, types 1 and 2 parasitophorous vacuoles, and the transformation of sporozoites to tachyzoites of the VEG strain of Toxoplasma gondii. *The Journal of parasitology* 83(4): 565–574.

Speer CA and Hammond DM (1970) Nuclear divisions and refractile-body changes in sporozoites and schizonts of Eimeria callospermophili in cultured cells. *The Journal of parasitology* 461–467.

Starborg T, Kalson NS, Lu Y, Mironov A, Cootes TF, Holmes DF and Kadler KE (2013) Using transmission electron microscopy and 3View to determine collagen fibril size and three-dimensional organization. *Nature protocols* 8(7): 1433.

Szabo EK and Finney CA (2017) Toxoplasma gondii: one organism, multiple models. *Trends in parasitology* 33(2): 113–127.

Tafti AK and Mansourian M (2008) Pathologic lesions of naturally occurring coccidiosis in sheep and goats. *Comparative Clinical Pathology* 17(2): 87–91.

Takamori S, Holt M, Stenius K, Lemke EA, Grønborg M, Riedel D, Urlaub H, Schenck S, Brügger B and Ringler P (2006) Molecular anatomy of a trafficking organelle. *Cell* 127(4): 831–846.

Tapia JC, Kasthuri N, Hayworth KJ, Schalek R, Lichtman JW, Smith SJ and Buchanan J (2012) High-contrast en bloc staining of neuronal tissue for field emission scanning electron microscopy. *Nature protocols* 7(2): 193.

Tenter AM, Barta JR, Beveridge I, Duszynski DW, Mehlhorn H, Morrison DA, Thompson RA and Conrad PA (2002) The conceptual basis for a new classification of the coccidia. *International Journal for Parasitology* 32(5): 595–616.

Tenter AM, Heckeroth AR and Weiss LM (2000) Toxoplasma gondii: from animals to humans. *International journal for parasitology* 30(12–13): 1217–1258.

Tenter AM and Johnson AM (1997) Phylogeny of the tissue cyst-forming coccidia. *Advances in Parasitology*. Elsevier, 69–139.

Titze B and Denk W (2013) Automated in-chamber specimen coating for serial block-face electron microscopy. *Journal of microscopy* 250(2): 101–110.

Tomley FM, Clarke LE, Kawazoe U, Dijkema R and Kok JJ (1991) Sequence of the gene encoding an immunodominant microneme protein of Eimeria tenella. *Molecular and biochemical parasitology* 49(2): 277–288.

Tomley FM and Soldati DS (2001) Mix and match modules: structure and function of microneme proteins in apicomplexan parasites. *Trends in parasitology* 17(2): 81–88.

Toonen RF, Kochubey O, de Wit H, Gulyas-Kovacs A, Konijnenburg B, Sørensen JB, Klingauf J and Verhage M (2006) Dissecting docking and tethering of secretory vesicles at the target membrane. *The EMBO journal* 25(16): 3725–3737.

Tosetti N, Pacheco NDS, Soldati-Favre D and Jacot D (2019) Three F-actin assembly centers regulate organelle inheritance, cell-cell communication and motility in Toxoplasma gondii. *eLife* 8: e42669.

Tyzzer EE (1929) Coccidiosis in gallinaceous birds. *American Journal of Epidemiology* 10(2): 269–383.

Uboldi AD, McCoy JM, Blume M, Gerlic M, Ferguson DJ, Dagley LF, Beahan CT, Stapleton DI, Gooley PR and Bacic A (2015) Regulation of starch stores by a Ca2+-dependent protein kinase is essential for viable cyst development in Toxoplasma gondii. *Cell Host & Microbe* 18(6): 670–681.

Uversky VN (2017) Intrinsically disordered proteins in overcrowded milieu: membrane-less organelles, phase separation, and intrinsic disorder. *Current opinion in structural biology* 44: 18–30.

Valm AM, Cohen S, Legant WR, Melunis J, Hershberg U, Wait E, Cohen AR, Davidson MW, Betzig E and Lippincott-Schwartz J (2017) Applying systems-level spectral imaging and analysis to reveal the organelle interactome. *Nature* 546(7656): 162.

de Venevelles P, Chich JF, Faigle W, Lombard B, Loew D, Péry P and Labbé M (2006) Study of proteins associated with the Eimeria tenella refractile body by a proteomic approach. *International journal for parasitology* 36(13): 1399–1407.

Vermeulen A, Kok J, Van den Boogaart P, Dijkema R and Claessens J (1993) Eimeria refractile body proteins contain two potentially functional characteristics: transhydrogenase and carbohydrate transport. *FEMS microbiology letters* 110(2): 223–229.

Vidal JC, Alcantara C de L, de Souza W and Cunha-e-Silva NL (2016) Loss of the cytostome-cytopharynx and endocytic ability are late events in Trypanosoma cruzi metacyclogenesis. *Journal of structural biology* 196(3): 319–328.

Vrba V and Pakandl M (2015) Host specificity of turkey and chicken Eimeria: controlled cross-transmission studies and a phylogenetic view. *Veterinary parasitology* 208(3–4): 118–124.

Wagenbach GE (1969) Purification of Eimeria tenella sporozoites with glass bead columns. *The Journal of parasitology* 833–838.

Wagenbach GE and Burns WC (1969) Structure and respiration of sporulating Eimeria stiedae and E. tenella oocysts. *The Journal of protozoology* 16(2): 257–263.

Waller RF, Ralph SA, Reed MB, Su V, Douglas JD, Minnikin DE, Cowman AF, Besra GS and McFadden GI (2003) A type II pathway for fatty acid biosynthesis presents drug targets in Plasmodium falciparum. *Antimicrobial Agents and Chemotherapy* 47(1): 297–301.

West SA, Reece SE and Read AF (2001) Evolution of gametocyte sex ratios in malaria and related apicomplexan (protozoan) parasites. *Trends in parasitology* 17(11): 525–531.

Whitelaw JA, Latorre-Barragan F, Gras S, Pall GS, Leung JM, Heaslip A, Egarter S, Andenmatten N, Nelson SR and Warshaw DM (2017) Surface attachment, promoted by the actomyosin system of Toxoplasma gondii is important for efficient gliding motility and invasion. *BMC biology* 15(1): 1.

Yan X, Tao G, Liu X, Ji Y and Suo X (2016) Calcium-dependent microneme protein discharge and in vitro egress of Eimeria tenella sporozoites. *Experimental parasitology* 170: 193–197.

Zaslavsky BY, Ferreira LA, Darling AL and Uversky VN (2018) The solvent side of proteinaceous membrane-less organelles in light of aqueous two-phase systems. *International journal of biological macromolecules* 117: 1224–1251.